

STRUCTURAL STUDY OF Pb(II) AND Sb(V) ADSORPTION ON THE
HYDROXYLATED HEMATITE(1102) SURFACE

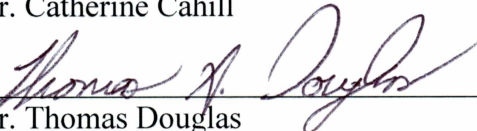
By

Canrong Qiu

RECOMMENDED:



Dr. Catherine Cahill



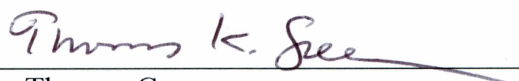
Dr. Thomas Douglas



Dr. William Simpson

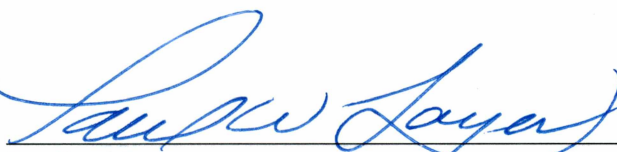


Dr. Thomas Trainor
Advisory Committee Chair

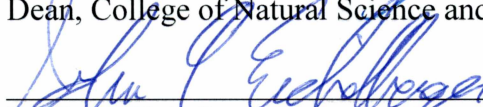


Dr. Thomas Green
Chair, Department of Chemistry and Biochemistry

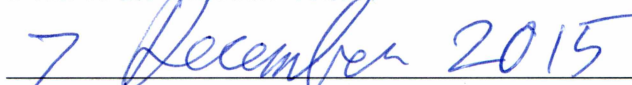
APPROVED:



Dr. Paul Layer
Dean, College of Natural Science and Mathematics



Dr. John Eichelberger
Dean of the Graduate School



Date

STRUCTURAL STUDY OF Pb(II) AND Sb(V) ADSORPTION ON THE
HYDROXYLATED HEMATITE($1\bar{1}02$) SURFACE

A

DISSERTATION

Presented to the Faculty
of the University of Alaska Fairbanks

in Partial Fulfillment of the Requirements
for the Degree of

DOCTOR OF PHILOSOPHY

By

Canrong Qiu, M.S.

Fairbanks, AK

December 2015

Abstract

Surface complexation reactions at mineral-water interface play a key role in dictating the mobility and bioavailability of aqueous species in the environment, considering the minerals (like iron-(oxyhydr)oxides), ubiquitous in nature, are usually of high specific surface area and contain a lot of potentially reactive surface sites for binding ions. Thus, the fundamental understanding of surface complexation reactions is essential to better model the environmental fate and transport of toxic aqueous species.

In the current study, the hematite ($1\bar{1}02$) surface was selected as a model substrate for iron-(oxyhydr)oxides commonly found in the environment to investigate the surface complexation reactions of Pb(II) and Sb(V) using the crystal truncation rod (CTR) surface diffraction. The hematite ($1\bar{1}02$) surface displays two surface terminations, the half layer termination (HLT) and the full layer termination (FLT) depending on sample preparation schemes. Previous CTR studies of clean hydrated hematite ($1\bar{1}02$) surface indicated that the chemically mechanical polishing procedure favors a HLT surface, while an annealing procedure favors the FLT surface. Our CTR results on the clean annealed hematite ($1\bar{1}02$) surface provides structural evidence that the substrate annealed in air undergoes a surface termination transformation that occurs through the projection of the near surface Fe atoms from original lattice sites to occupy top vacant Fe sites.

The adsorption of Pb(II) on the hydrated hematite($1\bar{1}02$) surface was also studied using CTR diffraction. Our findings demonstrate that aqueous Pb(II) adsorbs at two types of bidentate edge-sharing sites on the HLT surface, whereas the surface adsorption of Pb(II) occurs only at one type of edge-sharing site on the FLT surface. The site preference could be rationalized through comparing O-Fe-O bond angles for different edge-sharing binding sites. It was found that Pb

binding at edge-sharing sites with relatively large O-Fe-O bond angles ($>100^\circ$) is unfavorable as a result of forming a Pb complex species with extremely long (weak) Pb-O bonds ($>2.5\text{\AA}$). On the contrary, an edge-sharing site with relatively small O-Fe-O bond angles would be more favorable for binding Pb(II) species, since it would give rise to a surface complex species with reasonable Pb-O bond lengths ($\sim 2.25\text{\AA}$).

Differing from the case of Pb(II), the Sb(V) adsorption on the hematite ($1\bar{1}02$) surface with the HLT occurs only at a tridentate site in a binuclear edge-sharing/corner-sharing binding mode. The bidentate binding configurations are apparently not favorable due to the steric constraints caused by the Sb-bonded hydroxyl groups, which are abnormally close to the surface oxygen groups.

The molecular scale structural details presented in this study improve the understanding of the surface adsorption of Pb(II) and Sb(V) on the hematite($1\bar{1}02$) surface. Our findings also give evidence that the surface reactivity is largely determined by the surface structure through steric constraints as a function of sorbate type.

Table of Contents

	Page
Signature Page	i
Title Page	iii
Abstract	v
Table of Contents	vii
List of Figures	xiii
List of Tables	xxi
Acknowledgements and Dedications	xxiii
Chapter 1 Introduction	1
1.1 Different methods for studying surface complexation reactions	2
1.2 Reviews of surface adsorption of Pb and Sb on different substrates	6
1.2.1 Pb adsorption on different substrates.....	6
1.2.2 Sb adsorption on different substrates.....	9
1.3 Heterogeneity of surface termination of hematite	10
1.4 Research objectives	12
1.5 Summary of each thesis chapter	13
1.6 References	15
Chapter 2 Structural Study of the Hematite ($1\bar{1}02$) Surface Annealed at High Temperature: Interfacial Water Structure and the Surface Termination Transformation	21
Abstract	21
2.1 Introduction	22
2.2 Methods	25

2.2.1 Sample preparation	25
2.2.2 Scattering measurements	26
2.3 Structure and termination of hematite ($1\bar{1}02$) surface	27
2.4 Data Analysis	29
2.4.1 CTR theory	29
2.4.2 CTR structural model	29
2.4.3 Fitting algorithm and bond valence constraints.....	31
2.5 Results and discussion	33
2.5.1 Constraints of termination weights used in a multi-termination model	33
2.5.2 Surface relaxation	34
2.5.3 Interfacial water network.....	36
2.5.4 Bond valence analysis of the best fit model structure	41
2.5.5 Mechanisms of surface transformation and implications of the domain size	42
2.6 Conclusions	44
2.7 Acknowledgements	45
2.8 References	46
 Chapter 3 Structural Study of the Surface Complexation of Pb(II) on the Hydrated	
Hematite ($1\bar{1}02$) Surface	61
Abstract	61
3.1 Introduction	62
3.2 Methods and experiments	66
3.2.1 Sample preparations	66
3.2.2 CTR data collection	67

3.2.3 Structure and termination of hematite ($1\bar{1}02$) surface	68
3.2.4 Potential binding sites on the hematite ($1\bar{1}02$) surface	70
3.2.5 Description of the CTR analysis	71
3.2.6 Incorporation of bond valence constraints in the CTR analysis	73
3.3 CTR modeling results	75
3.3.1 Model trials based on a single type of sorption site	75
3.3.2 Model trials based on two edge-sharing sites assigned to two termination surfaces ...	77
3.3.3 Model trials based on two types of edge-sharing site on the same termination surface	78
3.3.4 Influence of interfacial waters	79
3.4 Discussions	80
3.4.1 Description of best-fit model	80
3.4.1.1 Relaxation of surface structure	80
3.4.1.2 Surface complex structure of Pb(II) on hematite surface	81
3.4.2 Relationship between the site coverage and the sorbate-sorbate distance	84
3.4.3 Surface complexation reactions of Pb(II) on hematite ($1\bar{1}02$) surface	86
3.5 Conclusions	89
3.6 Acknowledgements	91
3.7 References	91
Chapter 4 Structural Study of Surface Complexation of Pb(II) on Annealed and Hydroxylated Hematite($1\bar{1}02$) Surface	111
Abstract	111
4.1 Introduction	112

4.2 Methods and experiments	116
4.2.1 Sample preparation.....	116
4.2.2 Beamline experiments	117
4.2.3 Structure and terminations of hematite ($1\bar{1}02$) surface.....	118
4.2.4 Surface functional groups in the hematite ($1\bar{1}02$) surface.....	119
4.2.5 Potential binding sites on hematite ($1\bar{1}02$) surface.....	120
4.2.6 Description of the CTR analysis.....	121
4.2.6.1 Calculation of structure factor for a multi-unit cell model	121
4.2.6.2 Procedure of CTR model refinement.....	122
4.2.6.3 Bond valence constraint in the CTR analysis	124
4.3 CTR modeling results	127
4.4 Discussion	128
4.4.1 Description of best-fit model.....	128
4.4.1.1 Relaxation of surface structure	128
4.4.1.2 Pb complex structure on the FLT	129
4.4.2 Bond valence analysis and the surface complexation reaction stoichiometry	130
4.4.3 Exploration of the relationship between surface reactivity and structure	132
4.5 Conclusions	135
4.6 Acknowledgements	137
4.7 References	137
Chapter 5 Structural Study of Sb(V) Adsorption on Hematite ($1\bar{1}02$) Using Crystal Truncation Rod X-ray Scattering	155
Abstract	155

5.1 Introduction	156
5.2 Methods and experiments	160
5.2.1 Sample preparation	160
5.2.2 Beamline experiments	162
5.2.3 Hematite (1 $\bar{1}$ 02) crystallographic property	163
5.2.4 Potential binding sites and the step features on the hematite surface	165
5.2.5 CTR theory	165
5.2.6 CTR analysis	167
5.2.6.1 Structure factor calculation in a multi-unit cell model	167
5.2.6.2 Constraints on the fitting parameters	168
5.2.6.3 Incorporation of bond valence constraint into CTR analysis	170
5.3 CTR modeling results	172
5.3.1 Description of CTR profiles based on different models	172
5.3.1.1 Models regarding to Sb-bonded FLT	172
5.3.1.2 Models regarding to Sb-bonded HLT	173
5.3.1.3 Description of best fit structure model	174
5.4 Discussions	175
5.4.1 Implications of the mechanism controlling the surface binding configuration	175
5.4.2 Comparison to previous DFT and XAFS studies	177
5.4.3 Protonation schemes of interfacial oxygen	179
5.4.4 Relationship between site coverage and the inter-site distance	181
5.5 Conclusions	183
5.6 Acknowledgements	184

5.7 References	184
Chapter 6 Conclusions	201
6.1 Surface termination transformation mechanism from the HLT to the FLT	201
6.2 Surface adsorption mechanism of Pb(II) and Sb(V) on the hematite (1$\bar{1}$02)	202
6.2.1 Influence of substrate structure on the surface binding mechanism.....	203
6.2.2 Surface binding mechanism of Sb(V) to the hematite (1 $\bar{1}$ 02) surface	207
6.3 Implication of site coverage simulation results	209
6.4 The future direction in the environmental interfacial chemistry	211
6.5 References	212

List of Figures

	Page
Figure 2.1 Comparison of surface functional groups in the half layer termination (A, C) and the full layer termination (B, D) from both the side view (A, B) and the top view (C, D). Note that each atom layer was uniquely labeled as “ <i>Layer-n M</i> ”, where <i>n</i> represents the layer number, and <i>M</i> represents for the associated element symbol (either Fe or O). Left superscripts on the labeled oxygens indicate the iron coordination numbers. Red balls are oxygen atoms, while blue balls are iron atoms. The surface-layer iron atoms are shown in octahedrons with the rest not shown for clarity in the top-view surface structures. The position of the <i>b_s</i> glide plane symmetry is highlighted in both surface terminations.....	54
Figure 2.2 Comparison of layer heights from the present study under different O-O separation cutoff limits (red solid circle) to the other two studies by Catalano et al. (Catalano et al., 2007a)(blue solid circle) and Tanwar et al. (Tanwar et al., 2007a) (green solid circle). The uncertainties were illustrated as error bars for each point. The black solid lines show the atom layer heights in the ideal surface structure. The red dot lines are drawn based on the results from the current study at 2.5 Å O-O separation cutoff limit for comparison purpose.	55
Figure 2.3 Comparison of the top layer Fe (Layer-3 Fe) local structure derived from this study (A), Tanwar’s study (B) and the ideal case (C). The Fe atoms are represented as blue spheres, while the O atoms are red spheres. The numbers are the associated bond lengths in Å.	56
Figure 2.4 Experimental structure factors (blue open circles) (F_{HKL}) as a function of perpendicular momentum transfer (<i>L</i> , in reciprocal lattice units) for the hematite ($1\bar{1}02$) surface annealed at 550°C in air for 24 hours. The red solid lines represent the calculated CTR profiles based on the best fit structural model containing interfacial water structure (2.75 Å cutoff for O-O separations).	57
Figure 2.5 Interfacial water structure of the full layer termination surface based on the best fit model structure with 2.75 Å O-O separation cutoff limit (A). As a comparison, the interfacial water structure proposed by Catalano et al. (Catalano et al., 2007a) is also presented (B). Note the dashed lines represent the possible H-bond network according to the associated O-O separations that are shown as well. The O-O _{water} -O angles are shown to compare the distortion of the tetrahedral H-bonded water structure. The interfacial structure contains two adsorbed water layers (1 st layer in green ball and 2 nd layer in blue balls), surface O atoms (red balls) and Fe atoms (blue balls).	58
Figure 2.6 AFM image of annealed hematite surface (A) and the step heights distribution profile based on the AFM image (B). The calculated root-mean-square surface roughness is 1.75 Å. Although it is impossible to directly map the surface terminations (C, D, E) to the AFM images due to the lateral resolution of AFM measurement, the roughness calculated from the best fit CTR structural model containing three different termination surfaces is at first approximation in good agreement with the value calculated based on AFM data (see text for detail).	59

Figure 2.7 A schematic diagram of the mechanism of surface termination transformation from the HLT to the FLT when the hematite ($1\bar{1}02$) is annealed in air. In this diagram, the surface termination of the same type (chemically and crystallographically equivalent) are painted in the same color. The initial weight in percentage of each termination surface is arbitrary and we assume a 100% conversion of the HLT to the FLT for simplicity. The surface termination pattern of a CMP-prepared surface is illustrated as Panel A, where two symmetry related domains are present in an equal weight. The top four atom layers are shown to illustrate the atom rearrangement during annealing. The projection of Layer-5 Fe to occupy the Layer-3 vacant Fe sites leads to the termination transformation, which produces a long FLT and a short FLT with an equal weight (20%), as shown in Panel B. Note that although the surface termination transformation result in an unequal weight for two types of FLT on each domain, the total weight of each type of FLT is equivalent to each other when the summation is performed over two symmetry domains. Our best fit structure model supports a surface morphology, which is characterized by the presence of domains, which are separated by steps with $Nc/2$ offset (N is any integer), as illustrated in Panel C and Panel D. On each domain, there are multiple surface terminations with characteristic termination heights. After the surface termination transformation, the domain feature does not change but the surface morphology within each domain becomes more complicated due to the appearance of the third type of surface termination (long FLT), as shown in Panel D. The rule for summing over the structure factors within domain size follows coherent addition while the structure factors over the domain size are summed up based on incoherent addition rule. 60

Figure 3.1 (A) Layer stacking sequence along the C_s axis for the full layer termination surface of hematite ($1\bar{1}02$); (B) Layer stacking sequence along the C_s axis for the half layer termination surface of hematite ($1\bar{1}02$); (C) polyhedral representation of the oxygen-terminated full layer termination surface of hematite ($1\bar{1}02$) (second octahedral layer and those beneath are not shown for clarity) ; (D) polyhedral representation of the oxygen-terminated half layer termination surface of hematite ($1\bar{1}02$) (second octahedral layer and those beneath are not shown for clarity). Lengths for unit cell edges are $a=5.038 \text{ \AA}$, $b=5.434 \text{ \AA}$ and $c=7.3707 \text{ \AA}$. The $^{\text{III}}\text{O}$, $^{\text{II}}\text{O}$, and $^{\text{I}}\text{O}$ represent oxygen triply, doubly and singly coordinated to iron, respectively. Each atom layer is labelled as “Layer- n E”, where n is integer from 1 and E is the element symbol for either O or Fe..... 102

Figure 3.2 (A) Schematic diagram of surface topographic pattern (bottom part) formed by overlapping the termination fine steps (top part) on a surface with terraces of relatively large size (middle part). Step heights are numerical values demonstrating the relative height of steps without physical meaning. (B) A closer view of the step patterns on the CMP-hematite ($1\bar{1}02$) surface showing the relative step height difference between two symmetrically related terraces (Terrace A and Terrace B) as well as the rules for summing over the structure factors among different domains. 103

Figure 3.3 Schematic diagram of fitting parameters of Pb and distal oxygen in a bidentate edge-sharing binding mode. The Pb complex trigonal pyramid could rotate about axis A1A2 (A1 and A2 are positions for two anchored oxygen atoms) by ϕ , while the dihedral angle θ (A1OA2, O is the position of Pb atom) could vary in a range from 60° to 90° . To consider the distortion of Pb complex structure, Pb atom is allowed to slide along vector OA1, and distal oxygen could rotate freely on the OBC plane (B is the ideal position of the distal oxygen, and C is the center of

A1A2). Red spheres are the surface oxygens, the gray sphere is Pb, the green sphere is the distal oxygen not directly bonded at substrate surface. Fe coordination structure is represented in an octahedral. 104

Figure 3.4 Experimental structure factors (F_{HKL}) as a function of perpendicular momentum transfer (L , in reciprocal lattice units) for the hematite ($1\bar{1}02$) surface reacted with 200 μM Pb(II) at pH 5.5. The dash lines in green represent the calculated CTR profiles based on the best fit model O1O2, the solid lines in green represent the calculated CTR profiles based on the best fit model O1O3, the dash lines in red represent the calculated CTR profiles based on the best fit model O5O6, and the solid lines in red represent the calculated CTR profiles based on the best fit model O5O7. 105

Figure 3.5 Experimental structure factors (F_{HKL}) as a function of perpendicular momentum transfer (L , in reciprocal lattice units) for the hematite ($1\bar{1}02$) surface reacted with 200 μM Pb(II) at pH 5.5. The dash lines in green represent the calculated CTR profiles based on the best fit model O1O3_O5O7, the solid lines in green represent the calculated CTR profiles based on the best fit model O1O3_O5O8, the dash lines in red represent the calculated CTR profiles based on the best fit model O1O4_O5O7, and the solid lines in red represent the calculated CTR profiles based on the best fit model O1O4_O5O8. 106

Figure 3.6 Experimental structure factors (F_{HKL}) as a function of perpendicular momentum transfer (L , in reciprocal lattice units) for the hematite ($1\bar{1}02$) surface reacted with 200 μM Pb(II) at pH 5.5. The red solid lines represent the calculated CTR profiles based on the optimized model O1O3_O1O4 without interfacial water, and the green dashed lines represent the calculated CTR profiles based on the optimized model O5O7_O5O8. 107

Figure 3.7 Comparison of layer heights of top six atomic layers for the clean (labeled as clean_HL) and Pb bonded HLT (labeled as Pb_HLT_1 for O1O3 site and Pb_HLT_2 for O1O4 site) based on the best fit structural from this study as well as those presented in Tanwar's best fit model (Tanwar et al., 2007b). The solid lines are based on the ideal atomic layer height in the un-relaxed structure. The dash lines in red are drawn based on the layer heights for Pb_HLT_1 and the dash lines in blue are drawn based on layer heights presented in Tanwar's mode. 108

Figure 3.8 Structures of surface complex species with two types of edge-sharing binding configurations on the HL termination surface based on the best fit model. The top view of the interfacial structure for cases of Pb binding at site O1O3 (A) and site O1O4 (C) with first Fe layer visualized as octahedral and the local structure of surface complex species as ball and stick with green balls representing for distal oxygen, red balls surface binding oxygen, gray balls the Pb atom. Note that the symmetry related sites were not shown for clarity. The detailed structural information of the surface complex species at site O1O3 (B) and site O1O4 (D) in terms of bond angles ($^\circ$) and bond lengths (\AA). The near neighbor Fe atoms (blue balls) was showed as well. And the local structure of trigonal pyramid was oriented properly for a better view of geometric relationships. 109

Figure 3.9 (A) The trend of simulated site coverage (%) as a function of cutoff Pb-Pb distances (\AA) using the CTR derived reacted surface sites consisting of two pair of symmetric sites (embedded in A). The blue dash lines tracks the overall trend of simulated coverage over the

cutoff Pb-Pb distance. (B) The inter site distances identified from a fully occupied super cell through drawing a variety of co-centered coordinated circles with radius representing the associated inter site distances. (C) An example of site occupation with a super lattice forming but still satisfying the cutoff Pb-Pb distance of 5.42 Å (see text for more explanation). Horizontal dash line in red marks the CTR derived site occupancies. (D) The simulated site occupation pattern associated with the cutoff Pb-Pb distance of 5.42 Å, where the circles in different colors highlight the adjacent sites of same type aligned vertically. 110

Figure 4.1 (A) Layer stacking sequence along the c_s axis for the HLT surface of hematite ($1\bar{1}02$); (B) Layer stacking sequence along the c_s axis for the FLT surface of hematite ($1\bar{1}02$); (C) polyhedral representation of the oxygen-terminated HLT surface of hematite ($1\bar{1}02$) (second octahedral layer and those beneath are not shown for clarity) ; (D) polyhedral representation of the oxygen-terminated FLT surface of hematite ($1\bar{1}02$) (second octahedral layer and those beneath are not shown for clarity). Lengths for unit cell edges are $a=5.038$ Å, $b=5.434$ Å and $c=7.3707$ Å. The ^{III}O , ^{II}O , and ^{I}O represent oxygen triply, doubly and singly coordinated to iron, respectively. Top six atomic layers are labeled. Note Layer-1 O and Layer-3 Fe belong to FLT only, while the other four atomic layers are shared by both terminations. The surface functional groups are named as “ O_n ” with the subscripts n starting from 1. The red dash lines represent for the b_s glide planes. 147

Figure 4.2 A schematic diagram of the mechanism of surface termination transformations on an annealed hematite ($1\bar{1}02$) based on the best fit model for the clean annealed hematite ($1\bar{1}02$) surface. In this diagram, the surface terminations of the same type (chemically and crystallographically equivalent) are painted in the same color. The surface termination pattern of an annealed surface is illustrated as Panel A and Panel B, which represent for two symmetry related domains with equivalent weight percentage (50%). The weights for different terminations are denoted on each domain. Note that although the surface termination transformation result in an unequal weight for two types of FLT on each domain, the total weight of each type of FLT is equivalent to each other when the summation is performed across two symmetry domains. Our best fit model supports a surface morphology, which is characterized by presence of domains, which are separated by steps with $Nc/2$ offset (N is any integer, and c is the lattice parameter), as illustrated in Panel C. On each domain, there are multiple surface terminations with characteristic termination heights. The rule for summing over the structure factors within domain size follows coherent addition while the structure factors over the domain size are summed up based on incoherent addition rule. 148

Figure 4.3 Schematic diagram of fitting parameters of Pb and distal oxygen in a bidentate edge-sharing binding mode. The Pb complex trigonal pyramid could rotate about axis A1A2 (A1 and A2 are positions for two anchored oxygen atoms) by φ , while the dihedral angle θ (A1OA2, O is the position of Pb atom) could vary in a range from 60° to 90° . To consider the distortion of Pb complex structure, Pb atom is allowed to slide along vector A1O, and distal oxygen could rotate freely on the OBC plane (B is the ideal position of the distal oxygen, and C is the center of A1A2). Red spheres are the surface oxygens, the gray sphere is Pb, the green sphere is the distal oxygen not directly bonded at substrate surface. Fe coordinative structure is represented in an octahedral. 149

Figure 4.4 Experimental structure factors (blue open circles) (F_{HKL}) as a function of perpendicular momentum transfer (L , in reciprocal lattice units) for the annealed hematite ($1\bar{1}02$) surface reacted with $200 \mu\text{M}$ Pb(II) at pH 5.5. The green dash lines represent the calculated CTR profiles based on the optimized model CS, the black dash lines represent the calculated CTR profiles based on the optimized model ES1, and the red solid lines represent the calculated CTR profiles based on the optimized model ES2 (best fit model). 150

Figure 4.5 Comparison of atomic layer heights for the Pb-bonded FLT surface (Pb_FLT), clean FLT surface (clean_FLT) in this study and the clean FLT surface reported by Tanwar et al. (Tanwar et al., 2007a) (clean_FLT_Tanwar). The uncertainties were illustrated as error bars for each point. The black solid lines show the atom layer heights in the ideal surface structure. For comparison purpose, the red dot lines are drawn based on the results of Pb_FLT from the current study, and blue dot lines are based on Tanwar's model. 151

Figure 4.6 (A) The top view of the best fit model structure of Pb surface complex species binding at ES2 sites on the FLT surface within a 2 by 2 unit cells. The top Fe layers are displayed as octahedron, and deeper atoms are not shown for clarity. The cations are labeled as element symbols, while the oxygen anions are represented as red balls for surface oxygen groups as well as green balls for distal oxygen atoms. Some O-O separations are highlighted at the surface as dashed lines. (B) The structural details of the surface complex species at ES2 sites in terms of bond angles and bond lengths. The near neighbor Fe atoms (blue balls) was shown as well. And the local structure of trigonal pyramid was oriented properly for a better view of geometric relationships. 152

Figure 4.7 Structural comparison of Pb(II) binding to ES1 sites (B and D) and ES2 sites (A and C) assuming an unrelaxed FLT surface in the geometrical constraints of Pb-O bonds of 2.26 \AA as well as a 0° rotation angle (see text for details). Four adjacent surface Fe octahedral units are shown on the top view in Panel C and Panel D, where the O-O separations (dashed lines) between the distal oxygen (green balls) and two terminal oxygens are shown to highlight the potential steric constraints. Panel A and Panel B display the geometrical relationship between the Pb surface complex species and the associated Fe octahedral in terms of O-Pb-O bond angles, the Pb-O bond length, O-O edge lengths and Pb-Fe separations. The structure is properly oriented for better visibility. Cations (Fe and Pb) are labeled as the associated element symbols, the structural surface oxygen atoms are shown as red balls. 153

Figure 5.1 Layer stacking sequence along the C_s axis for the stoichiometric termination surface of hematite ($1\bar{1}02$) (A) and the half layer termination surface of hematite ($1\bar{1}02$) (B). Polyhedral representation of the oxygen-terminated full layer termination surface of hematite ($1\bar{1}02$) (C) and half layer termination surface of hematite ($1\bar{1}02$) (D) (second octahedral layer and those beneath are not shown for clarity). Lengths for unit cell are $\mathbf{a}=5.038 \text{ \AA}$, $\mathbf{b}=5.434 \text{ \AA}$ and $\mathbf{c}=7.3707 \text{ \AA}$. The $^{\text{III}}\text{O}$, $^{\text{II}}\text{O}$, and $^{\text{I}}\text{O}$ represent oxygen triply, doubly and singly coordinated to iron in the structure, respectively. Names of surface functional groups were shown for both half layer termination surface (O_1 to O_6) and the stoichiometric termination surface (O_6 to O_8). Note that the first atom layer in the stoichiometric termination surface overlaps with the fourth atom layer in the half layer termination surface, and thus O_5 and O_6 represent either atoms in the fourth atom layer in the half layer termination surface or atoms in the first atom layer in the stoichiometric termination surface. 193

Figure 5.2 Schematic diagram of surface topographic pattern (C) formed by a mixture of HLT and FLT on different terraces (either DomainA or DomainB). The DomainA is symmetry related to DomainB. The weight percentage for each termination is based on the results of the best fit model..... 194

Figure 5.3 (A) Geometrical solution of Sb position in a bidentate edge-sharing binding mode (O1O2 as the binding site) through two angles, rotation angle ϕ (rotating about O1O2 axis), dihedral angle θ (angle O1-Sb-O2 floated in a range from 80° to 100° during model refinement). (B) Geometrical solution of Sb position in a tridentate binding mode (A1A2A3 as the binding site). A bisecting plane through center point of A1A2 (**o**) is used to find a dummy point A3', which forms an equilateral triangle with A1 and A2, and is nearest to A3. To locate A3', a circle centering at **o** on the bisecting plane is drawn with a radius, which makes each point on the circle form an equilateral triangle with A1 and A2. Then A3 is projected on the bisecting plane to point A3_{prj}, which is connected to point **o**. Then **o**A3_{prj} will cross the dummy point A3' on the circle. With dummy point A3' computed, the position for Sb (shown as blue ball labeled as M) as well as positions for the other three distal oxygens (not shown) could be calculated by knowing the dihedral angles (O-Sb-O) is 90° 195

Figure 5.4 Experimental (gray circles) and model-based structure factors (F_{HKL}) as a function of perpendicular momentum transfer (L, in reciprocal lattice units) for the hematite ($1\bar{1}02$) surface reacted with $200 \mu\text{M}$ Sb(V) at pH 5.5. The solid lines in green represent the calculated CTR profiles based on the best fit model Model1, the solid lines in blue represent the calculated CTR profiles based on the best fit model Model2, the solid lines in red represent the calculated CTR profiles based on the best fit model Model3. 196

Figure 5.5 Experimental (gray circles) and model-based structure factors (F_{HKL}) as a function of perpendicular momentum transfer (L, in reciprocal lattice units) for the hematite ($1\bar{1}02$) surface reacted with $200 \mu\text{M}$ Sb(V) at pH 5.5. The solid lines in green represent the calculated CTR profiles based on the best fit model Model4, the solid lines in blue represent the calculated CTR profiles based on the best fit model Model6, the solid lines in red represent the calculated CTR profiles based on the best fit model Model5. 197

Figure 5.6 (A) Octahedral local structure of Sb(V) surface complex in the best fit model structure; (B) bond lengths of the Sb(V) surface complex;(C)Atom layer spacing values for Sb(V) modified half layer termination surface based on the best fit model structure for Model5. Sb octahedral structure in (A) and (B) were oriented properly for better visualization compared to that in (C). 198

Figure 5.7 Results of site simulation test with (A)a bar chart showing the trend of simulated site coverages over the cutoff Sb-Sb distance, (B) radical chart of co-centered circles showing all cutoff Sb-Sb distances tested in the site simulation, (C) site occupation pattern obtained for the cutoff limit of 5.03 \AA corresponding to the CTR derived site occupancy, (D) a subset of the site occupation pattern from (C) with the atomic structure of the substrate being visurized, (E) top view of an atomic structure of a surface with the theoretical mono layer saturation, (F) hypythetical mechanism for the re-organization of atoms to relieve steric strain by sharing one oxygen for the adjacent Sb(V) species aligned along the y direction. Note that the red dash line highlights the site coverage derived from the CTR analysis. 199

Figure 6.1 Topographic structure of the HLT surface with different types of surface binding sites identified, consisting of the bidentate edge-sharing site of type 1 (ES₁) and type 2 (ES₂), the bidentate corner-sharing site (CS), the face-sharing tridentate site (FS) and the tridentate site bridging ES₁ and CS site. One unit cell was highlighted with dash lines in black. The dash line in red represented the **b_s** glide plane. The top Fe atoms are visualized as octahedral in blue, the green spheres are singly coordinated oxygen groups, and the purple spheres are doubly coordinated oxygen groups. The other atoms and Fe-O bonds are shown as points and lines for clarity. 216

Figure 6.2 Topographic structure of the FLT surface with different types of surface binding sites identified, consisting of the bidentate edge-sharing site of type 1 (ES₁) and type 2 (ES₂), the bidentate corner-sharing site (CS), the face-sharing tridentate site (FS) and the tridentate site bridging ES₁ and CS site. One unit cell was highlighted with dash lines in black. The dash line in red represented the **b_s** glide plane. The top Fe atoms are visualized as octahedral in blue; the green spheres are singly coordinated oxygen groups, and the pink spheres are triply coordinated oxygen groups. The other atoms and Fe-O bonds are shown as points and lines for clarity..... 217

Figure 6.3 Schematic diagrams of Pb(II) binding at the ES₂ site on the FLT under two different situations with (A) in a geometrical constraint of reasonable Pb-O bond length (2.25 Å) and (B) in a geometrical constraint of reasonable O-Pb-O bond angle (79°) and Pb-Fe separation (3.33 Å) derived from XAFS studies. 218

List of Tables

	Page
Table 2.1 Best fit parameters based on CTR analysis of multi-unit cell model structure.....	50
Table 2.2 Comparison of atom relaxations and layer spacings (in Å) for top six atom layers in the full layer termination surface structure based on results from three different studies	52
Table 2.3 Results of bond valence analysis on the ideal and the best fit model structure	53
Table 3.1 A complete description of different model trials in terms of binding sites, binding modes and possible protonation schemes	98
Table 3.2 Best fit parameters based on CTR analysis on the model O1O3_O1O4	99
Table 3.3 Bond valence analysis of sorbate, distal oxygen and surface functional groups based on the best fit model structure (valence in v.u.).....	101
Table 4.1 A complete list of structural models tested in the surface modeling	143
Table 4.2 Atomic displacements, Debye Waller factors and occupancies for different domains in the best fit model structure.....	144
Table 4.3 The results of bond valence analysis of the best fit model structure (valence in v.u.)	146
Table 5.1 Potential binding sites on hematite ($1\bar{1}02$) surface and goodness-of-fit for different models.....	189
Table 5.2 Best fit structural parameters based on the model with tridentate corner-sharing/edge-sharing binding mode.....	190
Table 5.3 Bond valence analysis of surface species based on the best fit structure model.....	192

Acknowledgements and Dedications

On Aug. 19, 2010, I together with my wife, after 24-hour flight, made it all the way from Xiamen, China to Fairbanks, Alaska, a strange place which made me a little scared about the harsh winter there at first, but turns out to be one nothing short of amazing. Many people deserve my sincere gratitude for their tireless assistance and great support from different perspectives, which lead to the final completion of this project.

The past five years have not been an easy ride, both academically and personally. When I started my research here, I realized that the project I was going to do is a great challenge, since I didn't have any background on the technique I would need to conduct the associated experiments. Enormous thanks are owed to my advisor, Dr. Tom Trainor, who is a clever, inventive, patient mentor steering clear of a lot of obstacles in front of me through encouragements and tireless teaching on the CTR theory in my first academic year. Tom's great effort and time put into my "pre-board" study finally got me on board at the end of my first year here. Tom is such a wonderful advisor that he never pushed me too hard creating too much pressure in me, rather he gave me a lot of freedom to crank out the project. However, I can always count on him to be around providing insightful suggestions on my current status as well as answering any question I may have. I can feel his backup all the time even when he is not around. Thus a lot of times, he just stepped back to leave behind a free atmosphere, where I can build up my independence and confidence on doing scientific research. His hands are free on me, but always reachable for assistance whenever I need. I would also like to thank the other committee members, Dr. Bill Simpson for his encouragements and valuable questions and comments posed at my annual committee meetings, Dr. Tom Douglas for his sense of humor

which makes me think that doing scientific research could be a lot of fun, Dr. Catherine Cahill for her caring and great questions which are of super help in guiding me forward.

There are some other people, who also contributed directly or indirectly to the success in this project. First person I want to mention here is Matts Björck, who wrote the GenX program for modeling CTR data. I am grateful to Matts for his tireless email response to my questions on GenX program, which help me better understand the work flow of algorithms used in GenX for fitting CTR data. With his help, I was able to customize the original version of GenX to one incorporating new features for surface modeling. Speaking of coding assistance, Frank Heberling is another person I want to thank here. Frank is an ingenious Python expert, who wrote a whole Python package to deal with the RAXR modeling. I am extremely indebted to Frank for his generous time on replying my email to answer a lot (really a lot) of questions about how to use the RAXR package he wrote. Frank provided great help in the process of my attempt to update GenX to be able to consider for RAXR modeling besides CTR modeling. For numerous times, he provided detailed solutions to my specific questions, which contribute to the final success in adding RAXR modeling function as a plug-in into GenX package.

If Matts and Frank are two persons helping me a great deal in setting up computer scripts, Franta Majas, who used to work in Trainor's group as a postdoc fellow, deserves incredible gratitude for his help with my beamtime experiments at APS. He contributed a lot of time and effort to grind and polish hematite crystal samples with good surface quality suited to being used for CTR experiments. Besides his help in preparing hematite substrates, he always accompanied with me to APS, Chicago to conduct beamline experiments. When we were in Chicago, he played different kinds of roles, such as a reliable driver to drive me anywhere (I was scared of driving in a big city like Chicago at that moment), a great laboratory technician helping a lot

ranging from doing dishes to making solutions, an experienced beamline experimenter helping me line up the sample and collect high quality data at the beamline, and also a humorous friend always making jokes, which make me forget about the fatigue during crazy, and sometimes overwhelming, beamtime.

Two beamline scientists (Peter Eng and Joanne Stubbs) at GSECARS (sector 13), APS, Chicago, deserve a great deal of credits in the completion of this project. Both Peter and Joanne are so experienced in performing surface diffraction experiments that my beamtime trips were always productive and rewarding. They are not just beamline scientists providing technical support at the beamline, but also my coworkers getting involved in the modeling work after the on-site beamtime experiments. For quite a few times, Peter and Joanne contributed their private time (+3 hours each time) going through my modeling work via video communication, during which they provided valuable feedbacks to make me move on to improve my modeling results. They helped me move further than I thought I could go.

People sitting at the Help Desk from Arctic Super Computer Center (ARSC) at UAF are acknowledged for their great help for getting my MPI codes written in Python running successful on the super computer system. Running CTR models on the super computer system greatly expedites my modeling process, which takes as short as ~30 min for running one single model compared to several days when it is ran on a desktop computer.

My academic success cannot be achieved without so many other people, to whom I owe many thanks for their moral support and good friendship with me. Here I want to first thank folks working in both the current and the past Trainor's group, including Amanda Barker (for her help at the several beamtime trips; good luck to her PhD project's completion on time), Anastasia Ilgen (for her encouragements and sharing with me a lot of her experience about how to do

scientific research more effectively; and I am glad to see that Nasia is now becoming an outstanding female scientist at Sandia National Laboratory making a firm seat in the geochemistry community; best wishes to her and her family in New Mexico), Peter Peterson (for his help in setting up Linux machine and sharing some tips of writing Python scripts), and Chris Iceman (for his help in showing me the directions for visualizing molecular structures using DS Viewer software). In addition, I want to also thank my current officemates (Nicole Knight, Terilyn Stephen and Kristin Gagne), who not only share an office with me but also share a lot of cool things happening in their lives, which add a lot of fun to my office hours. I am also thankful to staffs (Jacy Pietsch, Emily Reiter, Mist D'June-Gussak, Jessica Armstrong) working in the Department of Chemistry and Biochemistry for their hard work to have a lot of things running smoothly. Mist was our guardian to help us with all the administrative paper work. After Mist left for Anchorage, Jessica continues her work here providing great service (like emailing us reminder of important deadlines, posting job opportunities) to us students. Jacy and Emily are my mentor for my work as a teaching assistant for several semesters. I really appreciate for their work to give me such a wonderful teaching experience. Those TA meetings led by Emily are so helpful to get me refreshed on the coming experiment. Jacy is thanked for her nice and hard work to set up experiment materials prior to each experiment.

In addition, I want to express my sincere gratitude to my faith family at University of Baptize Church for their encouragement and support in my spiritual growth in Jesus Christ. The amazing grace coming from our Heavenly Father opens up my mind to see what's unseen before, leads me to safe places, on which I can rest with peace and joy in my heart. God always watches me on my way to the Holy righteousness and gives me blessings, which are countless.

Last but not least, I am indebted a lot to my wife, Lingqun Wu, for her unselfish love on me and huge moral support on my research. She sacrificed her time to stay home being a fulltime housewife taking care of my daily life. Whenever I arrive home at the meal time, I can smell the delicious dishes she prepared even at the door. When my academic work is in chaos, she knows how to comfort me. Without her being here with me, my life would become much more difficult. Our son, Ethan W. Qiu, was born in 2012. Also our daughter, Elena L. Qiu, was born this year. I am so thankful to their birth, which adds a lot of joys in my life. I would like to also thank my parents in China, my father Youde Qiu and my mother Jiumei Lai, for their constant support and unconditional love. I love you all dearly.

“The fear of the LORD is the beginning of knowledge, but fools despise wisdom and discipline.” ---Proverbs 1:7

Chapter 1 Introduction

Iron-(oxyhydr)oxides occur in the natural environment with great abundance and they usually exist as fine particles (particle size typically ranging from nm to μm) or coatings on other minerals. Therefore, iron oxides commonly found in soil and sediment environments have a high specific surface area and numerous reactive surface functional groups exposed to solution. Iron (oxyhydr)oxides surfaces show a strong affinity for binding aqueous ions, and thus play a key role in dictating the mobility and chemical speciation of environmental contaminants in different aquatic systems (Gadde and Laitinen, 1974; Kinniburgh et al., 1976; McKenzie, 1980; Tessier et al., 1985; Johnson, 1986; Bowell, 1994; Benjamin et al., 1996; Cornell and Schwertmann, 2003). Hence, a comprehensive characterization of the interfacial reactions with respect to various aqueous species at the surface of different iron-(oxyhydr)oxides is essential for developing robust models to predict their geochemical and environmental behaviors.

Surface adsorption has been extensively studied using macroscale batch experiments which are focused on solute uptake as a function of pH, concentration and ionic strength. The sorption data is then typically fit using different types of models including empirical models (e.g. Langmuir model), and surface complexation models (stern layer model, triple layer model etc.). The modeling work based on macroscale sorption data provides valuable information on the surface complexation from the perspectives of thermodynamics (Venema et al., 1996). However, a fundamental understanding of the interfacial reactions relies on techniques capable of resolving structural details on a molecular scale (Brown and Sturchio, 2002). In recent decades significant advances in surface analysis has been made using synchrotron X-ray techniques, such as X-ray adsorption fine structure (XAFS) (Koningsberger and Prins, 1988; Brown et al., 1995), X-ray reflectivity (XR) and crystal truncation rod (CTR) diffraction (Robinson and Tweet, 1992). The

wide application of synchrotron X-ray techniques in the field of surface adsorption chemistry have shed light into fundamental understandings of the heterogeneous reactions occurring at mineral water interface over wide range of environmental conditions (Brown et al., 1998; Brown et al., 1999; Brown and Sturchio, 2002; Fenter, 2002; Fenter and Sturchio, 2004).

1.1 Different methods for studying surface complexation reactions

The complexity of heterogeneous reactions at mineral-water interfaces has been a major challenge in developing a fundamental understandings of the associated interfacial chemistry as there is no single technique capable of deriving a comprehensive picture of interfacial reactions and molecular structures. In this section, a brief review will be given to compare two different categories of methods for studying surface adsorption chemistry; surface complexation modeling (SCM) and methods based on synchrotron X-ray techniques.

The theory of SCMs dates back to 1970s when Stumm, Schindler and colleagues developed the initial versions of the constant capacitance model and diffuse layer model (Stumm et al., 1970; Schindler and Gamsjäger, 1972; Huang and Stumm, 1973). After the pioneering work of Stumm and Schindler, SCM experienced a great deal of development by numerous researchers who proposed a variety of specialized modifications such as the triple-layer model (Davis and Leckie, 1978), 1-pK basic Stern model (Van Riemsdijk et al., 1986; Westall, 1986) and charge distribution-multisite surface complexation model (Hiemstra et al., 1989; Hiemstra and Riemsdijk, 1996). All surface complexation models are based on common principles: (1) surface adsorption is described using mass law equations; (2) the adsorption of ions occurs at specific sites, which could be inner-sphere sites when ions directly bond to surface functional groups, or outer-sphere sites when ions associate with the surface via hydrogen bonding or specific charge-

charge associations; (3) the charging behavior is explicitly considered through mathematic definition of static planes carrying electric charge as well as the electrical diffuse layer; (4) electrostatic effect on ion binding is taken into account through a term that accounts for the work required to move ions to a charged surface. The SCM has been successfully applied to study ion adsorption on different oxide surfaces over broad experimental conditions. However, SCM could lead to ambiguity for following two reasons. Firstly, it does not directly relate to the surface binding structure, which, however, is required to define physically realistic surface complex species. In addition, it involves some physical or chemical parameters (like site density and equilibrium constants for different surface complexation reactions) which are not attained through experiments but solely through model fitting. A desirable fitting to experimental data could usually be made even under different prerequisites (like surface site density, surface complexation reactions) at the cost of biasing some model parameters. As a consequence, modeling results derived from one specific set of experimental conditions usually could not be extrapolated over a wide experimental conditions (Dyer, Trivedi, Scrivner, et al., 2003). Therefore, conducting SCM studies without the knowledge of the molecular scale surface binding structure could be problematic in deriving unambiguous surface complexation reactions.

On the other hand, a variety of modern synchrotron X-ray based techniques provide the capability to resolve molecular structure of surface binding, which could serve as molecular-scale structural constraints to develop the realistic reaction stoichiometry. X-ray adsorption fine structure (XAFS) is one such technique, which has been well developed and is capable of deriving molecular scale structure information surrounding the sorbate element, such as coordination number, interatomic distances, and chemical identity of near neighboring atoms (Koningsberger and Prins, 1988; Brown et al., 1995). Based on the derived structural

information, the binding configuration of an ion could be deduced with good certainty. However, it should be noted that XAFS spectra are damped due to the intrinsic thermal vibration of composing atoms in the system and that limits the probing range of XAFS to about 5 Å. In light of that, the XAFS technique usually cannot resolve the geometrical relationship between a sorbate and the substrate, especially when the surface structure of the substrate is not well characterized, which is usually the case for environmental samples. Therefore, the analyses of XAFS spectra often result in multiple plausible surface binding configurations based on the derived cation-cation separation. A relatively small cation-cation separation is usually assigned to a surface complex species with an edge-sharing or face-sharing binding mode, whereas a larger cation-cation separation corresponds to a monodentate or bidentate corner-sharing binding mode. However, a full distinction between the monodentate binding mode and the corner-sharing binding mode is sometimes impossible if the associated cation-cation separations are fairly close to each other. In addition, a site-specific analysis of surface complexation under bidentate edge-sharing mode is also difficult when there are multiple bidentate edge-sharing sites on the substrate surface.

The disadvantages of using XAFS technique could be overcome by a technique which could resolve the interfacial structure with a longer probing range for a better characterization of the geometrical relationship between the sorbate and the substrate surface. CTR diffraction is one such technique which can be used to probe the entire mineral-water interfacial structure and thus is well suited to studying the surface complexation reactions of aqueous species at mineral-water interfaces. CTRs are diffuse streaks of scattering intensities running along a direction parallel to the normal of substrate surface (Robinson and Tweet, 1992). The CTR intensities are contributed by the interference of the diffracted signal coming from both the bulk structure as well as the

surface slab. While the bulk structure of the substrate has been well characterized and maintains throughout the experiment, the surface slab is subject to different interfacial processes, such as atomic relaxation/contraction, hydrogen bonding reaction, and surface complexation reactions. However, the negative sides of using CTR technique lies in its requirement of single crystal samples with high quality surfaces, which limits its usage in studying model systems, like hematite sample.

In this study, we used CTR diffraction to resolve the molecular structural details associated with surface complexations of Pb(II) and Sb(V) at hematite ($1\bar{1}02$) surface. The Pb(II) and Sb(V) were selected as the target species in this study for following reasons. Firstly, both Pb and Sb find wide use in commercial applications. Applications of Pb include the historic usage as anti-knocking fuel additive (Nriagu, 1990) and paint pigment (Sandalinas et al., 2006) and its current application is seen widely in the battery industry (Piper and Restrepo, 2013) and in ammunition (Scheuhammer and Norris, 1995; Lin, 1996; Craig et al., 1999). The major industrial use of Sb is its use as alloy hardener for production of the lead-antimony alloy, which are used for solder, ammunition, covering for electrical cables and lead storage batteries (Filella et al., 2002; Wilson et al., 2010). In addition, antimony (Sb_2O_3) has some other minor uses in the manufacture of brake pads, glass, ceramics and the production of plastics (Filella et al., 2002; Varrica et al., 2013). Secondly, both Pb and Sb are of environmental concerns since they are toxic and could pose a high risk to health when found at elevated concentration levels (Goyer, 1993; Verma and Dubey, 2003; Sundar and Chakravarty, 2010). Furthermore, both Pb and Sb are elements have a relative high atomic number (82 and 51 for Pb and Sb, respectively), and thus correspond to a higher signal-to-noise level for CTR data allowing for CTR modeling with good certainty.

1.2 Reviews of surface adsorption of Pb and Sb on different substrates

The sorption of Pb(II) and Sb(V) on a variety of different substrates has been extensively studied using both methods based on batch sorption and XAFS spectroscopy. These studies serve as a background upon which our CTR model structural details can be compared to present deeper insight into the surface complexation reactions at the mineral water interface. In this section a review of Pb and Sb adsorption chemistry on different substrate surfaces (focus on iron oxy-(hydr)oxides) is presented to identify the knowledge gaps regarding the surface complexation reactions in different systems.

1.2.1 Pb adsorption on different substrates

Surface adsorption of Pb(II) has been extensively studied on different iron-(oxyhydr)oxides, such as hematite (Christl and Kretzschmar, 1999; Lenhart et al., 2001; Mason et al., 2009; Barton et al., 2011; Grover et al., 2012), goethite (Hayes and Leckie, 1987; Roe et al., 1991; Müller and Sigg, 1992; Müller and Sigg, 1992; Gunneriusson et al., 1994; Palmqvist et al., 1997; Abdel-Samad and Watson, 1998; Palmqvist et al., 1999; Kovačević et al., 2000; Ponthieu et al., 2006), ferrihydrite (Dyer, Trivedi, Sanders, et al., 2003; Dyer, Trivedi, Scrivner, et al., 2003; Trivedi et al., 2003; Gustafsson et al., 2011; Tiberg et al., 2013), hydrous ferric oxide (Reich et al., 2010) as well as on natural soils (Appel and Ma, 2002; Serrano et al., 2009; Shaheen, 2009), using a variety of approaches, such as macroscale batch sorption experiments, density functional theory, and spectroscopic techniques including FTIR, XPS and XAFS.

In those published results there is a general observation of strong surface binding of Pb(II) in an inner-sphere mode. However, a detailed binding configuration as well as surface complexation stoichiometry range widely from different studies. For example, Müller et al

(Müller and Sigg, 1992) investigated Pb(II) adsorption on goethite powder using a constant capacitance model, and found two surface complexation stoichiometries; Pb(II) binding in a monodentate mode and Pb(II) binding in a bidentate mode. The Pb species under the bidentate binding mode was not observed in an earlier study by Hayes et al. (Hayes and Leckie, 1987), who used a triple layer model to study the Pb(II) adsorption on the goethite surface and found it only required a single monodentate surface complexation stoichiometry to fit the experimental batch uptake data. A handful of later batch uptake studies of the Pb(II)/goethite system also present evidence of Pb(II) binding at goethite surface via a monodentate mode (Gunneriusson et al., 1994; Palmqvist et al., 1997; Abdel-Samad and Watson, 1998; Kovačević et al., 2000). However, recent XAFS studies (Ostergren et al., 2000a; Ostergren et al., 2000b) suggest the sorption of Pb(II) on the goethite surface occurs via two types of bidentate modes; bidentate corner-sharing mode (Fe-Pb separation is ~ 3.9 Å) and a bidentate edge-sharing binding mode (Fe-Pb separation is ~ 3.3 Å). Different binding configurations of a surface Pb complex were also found in studies based on ferrihydrite. For example, an XAFS study undertaken by Trivedi et al (Trivedi et al., 2003) suggest a pH dependence of Pb(II) adsorption on ferrihydrite with a higher pH (pH>5) favoring the bidentate edge-sharing mode and a lower pH (pH 4.5) favoring both the edge-sharing and corner-sharing binding modes. A surface complexation modeling study of Pb(II) sorption on colloidal hematite sample was undertaken by Christl et al. (Christl and Kretzschmar, 1999) who proposed the surface complexation reactions consisting of surface species in both outer-sphere and inner-sphere monodentate binding modes. These results differ substantially from two XAFS studies (Bargar et al., 1997; Lenhart et al., 2001), where a bidentate edge-sharing binding mode was proposed to explain the Pb(II) sorption on hematite.

Besides the sorbate binding configuration, the proton stoichiometry upon Pb(II) adsorption is also under debate. It is commonly accepted that Pb(II) binding on the substrate surface would release one or two protons depending on the binding mode, and one extra proton may be released if the adsorbed Pb also undergoes hydrolysis. Conducting surface complexation modeling on a metal/substrate system could deduce a set of surface complexation reactions with proton stoichiometry defined therein. However, deduction of a unique surface complexation stoichiometry is usually difficult, since the goodness of using SCM is based on what experimental constraints are available, such as site density, realistic surface complexation reaction stoichiometries. For example, Gustafsson et al. (Gustafsson et al., 2011) applied CD-MUSIC model to fit the Pb adsorption data on ferrihydrite surface, and they found ambiguity of proton stoichiometry in the surface complexation reaction; a statistically equivalent fit to batch uptake data could be achieved whether or not considering proton release upon Pb(II) adsorption. In addition, there is no consensus opinion in terms of the hydrolysis of the adsorbed Pb. Previous surface complexation modeling studies usually proposed the surface complexation reaction stoichiometry with different hydrolysis statuses of the adsorbed Pb complex. A XPS study of Pb(II) sorption on goethite (Abdel-Samad and Watson, 1998) provided spectroscopic evidence that the protonation schemes of surface functional groups as well as the hydrolysis state of adsorbed Pb is related to solution pH. They found that low pH would favor the protonation of Pb-bonded surface oxygen functional group as well as Pb surface species without being hydroxylated, whereas the deprotonation of surface functional groups and the hydrolysis of adsorbed Pb surface complex was observed when the solution pH gradually increases.

The pH dependence of protonation/deprotonation of surface functional groups as well as hydrolysis state of a Pb surface complex would probably lead to a pH dependence of surface

complexation reactions, as found by Dyer et al. (Dyer, et al., 2003), who applied surface complexation model to study the Pb adsorption on the ferrihydrite surface and found that it is necessary to make corrections accordingly to the surface complexation constants as a function of solution pH. In addition, the difference of proton affinity for different types of surface oxygen groups could be an important factor in dictating the surface binding configuration of aqueous ions as a function of pH. At lower pH, a surface oxygen group with high proton affinity could be protonated without further bonding to aqueous metal ions, and as a result, some new binding site could open up for binding sorbates. For example, it was found in an XAFS study (Ostergren et al., 2000a) that a new binding mode (bidentate corner-sharing binding mode) was observed for Pb adsorption on the goethite surface under a relatively low pH (pH 5.0) as compared to dominantly edge-sharing binding configuration at pH>6.5. It was claimed that the bidentate corner-sharing binding sites becoming reactive at pH 5.0 due to a higher proton affinity for the ^{III}O group, which is one of the composing oxygen group for the bidentate edge-sharing site.

1.2.2 Sb adsorption on different substrates

It is generally believed that surface adsorption on natural substrates is one of the main mechanism controlling the fate and transport of Sb in soil and aquatic environments (Mitsunobu et al., 2010; Resongles et al., 2013). In recent years, numerous studies have focused on Sb(V) adsorption (the most common environmental form of Sb) using experimental approaches based on both batch adsorption experiments and X-ray absorption spectroscopic techniques (XAFS). The studies using batch adsorption experiments indicate that Sb(V) adsorption occurred on iron hydroxides via an inner-sphere binding mode and that the Sb uptake was significantly affected by solution pH (Tighe et al., 2005; Leuz et al., 2006; Martínez-Lladó et al., 2008; Vithanage et

al., 2013). The binding mode deduced from batch adsorption experiments was consistent with that revealed by XAFS studies, which provided further information on the binding structure. For example, Guo et al. (Guo et al., 2014) propose a bidentate edge-sharing mode for Sb(V) adsorption on hydrous ferric oxide based on a relatively short Sb-Fe distance (3.0-3.19 Å). Such an edge-sharing binding mode was also found in a study using a goethite/ferrihydrite substrate with a Fe-Sb distance of 3.08-3.11 Å (Mitsunobu et al., 2010). In that study, in addition to the edge-sharing, a corner-sharing binding mode was also observed on ferrihydrite sample based on a longer Sb-Fe distance (3.51-3.55 Å). XAFS analysis of Sb in a shooting range soil sample (Scheinost et al., 2006) and in downstream sediments close to a historic Sb mining site (Ritchie et al., 2013) also found Sb(V) as a surface complex species with both edge-sharing and corner-sharing binding configurations probably due to a mixture of different types of iron oxides coexisting in the soil sample. Two such binding modes pertaining to Sb(V) adsorption on the iron hydroxide surfaces could be the reason responsible for different desorption rates observed by McComb et al. (McComb et al., 2007), who conducted a desorption test of Sb(V) from amorphous iron oxide particle sample and speculated the presence of at least two binding sites with different binding strength.

1.3 Heterogeneity of surface termination of hematite

A single crystal substrate could terminate differently on different crystalline planes displaying a unique surface morphology. For example, hematite has two dominant growth faces (the (0001) plane and the (1 $\bar{1}$ 02) plane) in nature (Cornell and Schwertmann, 2003); and the hematite of both crystalline planes was found to have two different surface terminations, as observed in previous CTR studies (Trainor et al., 2004; Tanwar et al., 2007b). Specifically, the

hematite (0001) surface displays a combination of an O-terminating surface and a Fe-terminating surface with the terminated Fe octahedral as islands decking on top of stoichiometric O-terminating surface (Trainor et al., 2004). As for the hematite ($1\bar{1}02$) surface there are two surface terminations; one is consistent with the stoichiometric atomic layer sequence (named as FLT) and the second has a surface structure with the top layer Fe atoms missing as compared to the stoichiometric atom layer sequence (named as HLT) (Tanwar et al., 2007b). Interestingly, the surface termination transformation of the hematite ($1\bar{1}02$) surface could be made through a wet chemical mechanical polishing procedure (CMP) (favoring the HLT) or an annealing procedure (favoring the FLT) (Tanwar et al., 2007a).

The presence of multiple terminations at a mineral surface would potentially change the physical/chemical properties of the surface compared to single-termination surfaces. For example, a recent study of surface potential at the hematite (0001) surface indicated that the presence of multiple terminations would lead to the failure in using SCM method for modelling the experimental surface potential data (Lützenkirchen et al., 2013). It was also claimed that a more sophisticated SCM method is needed to account for the potential gradient between different surface terminations. That study, although not directly dealing with the surface adsorption reactions, presented an important indication that the heterogeneity of a surface termination should not be ignored when developing models of surface complexation reactions. In addition, a different surface termination could display different chemical properties at the substrate surface since the difference in the number and identities of surface moieties is an important factor in determining binding configurations of sorbates. Therefore, the heterogeneity of surface terminations must be considered properly in order to utilize the SCM method for deriving

physically realistic surface complexation reactions, which are essential for better modeling the environmental fate and transport of aqueous metal ions in the aquatic system.

Based on these previous studies it is hypothesized that the hematite ($1\bar{1}02$) surface will show different affinity for binding aqueous species depending on which termination is dominant. In the HLT surface, there exist three types of oxygen groups, $^{\text{I}}\text{O}$, $^{\text{II}}\text{O}$ and $^{\text{III}}\text{O}$, whereas the FLT surface contains only $^{\text{I}}\text{O}$ and $^{\text{III}}\text{O}$ groups. Therefore, a further investigation on the adsorption of aqueous ions at different surface terminations of hematite ($1\bar{1}02$) is a promising way to explore the relationship between the surface structure and the surface reactivity, which leads to the research questions stated in next section.

1.4 Research objectives

In this study, the hematite ($1\bar{1}02$) surface was chosen as a model substrate since it has a tunable surface termination pattern which allows for studying the adsorption chemistry on different terminations. This study focuses on the surface complexation reactions of Pb(II) and Sb(V) at the hematite ($1\bar{1}02$) surface with an aim to improve the understanding of the associated surface adsorption chemistry as a function of adsorbate type as well as surface termination. Specifically, we want to address the following questions: (1) what are the structural details of Pb(II) and Sb(V) sorption on hematite ($1\bar{1}02$) surface with both HLT and FLT? (2) what is the potential mechanism controlling the binding configuration? (3) what's the relationship between the binding configuration of ions and the surface substrate structure? We believed that the structural models presented here could serve as a basis to aid in predicting the adsorption of various contaminant species onto iron (hydr)oxide substrates, since all iron (hydr)oxide substrates share a common Fe octahedral structural unit (octahedral coordination with distortion

to different extents), which results in a limited set of Fe-(hydr)oxo moieties exposed at mineral fluid interface.

1.5 Summary of each thesis chapter

This thesis is divided into six chapters with the first and the last chapters as the general introduction and general conclusion, respectively. The other four chapters, from Chapter 2 to Chapter 5, are the main body of this thesis that present CTR modeling results regarding surface complexation reactions at hematite ($1\bar{1}02$) surface under different conditions. All those chapters comprising the core of this thesis will be submitted for publication to different journals.

Chapter 2 present CTR modeling results of the clean air annealed hematite ($1\bar{1}02$) to describe the surface termination transformation induced by high temperatures. The structural details indicated that surface atom relaxations along the surface normal direction are comparable to published results (Catalano et al., 2007; Tanwar et al., 2007a). In addition, two water layers were identified with both lateral and vertical ordering, which gave rise to a unique hydrogen bond network bridging the substrate surface and the bulk solution. Our best fit model structure implies a model for the surface transformation from the HLT to the FLT by the projection of 5th layer Fe atoms to vacant 3rd layer Fe sites.

In Chapter 3, the structural details of Pb(II) sorption on the CMP-prepared hematite ($1\bar{1}02$) surface was elucidated based on CTR modeling. It was found that Pb(II) sorption occurs at two different types of surface sites, both with a bidentate edge-sharing binding configuration. The local structure of both Pb surface species is a distorted trigonal pyramid with Pb-O bonds of similar lengths (~ 2.26 Å) but significantly different nearest Pb-Fe separations (3.32 and 3.64 Å, respectively). Site preference for Pb(II) binding at edge-sharing sites observed in this study could

be attributed to more feasible steric constraints as well as the potential hydrogen bond effect in the edge-sharing binding configuration.

The CTR modeling results presented in Chapter 4 is a continuation of the work presented in Chapter 3. Here we designed a similar adsorption experiment but using a hematite ($1\bar{1}02$) substrate with a different surface termination, produced through annealing the CMP-prepared substrate. By comparing the difference in the Pb(II) adsorption on the same substrate but with different surface terminations, we aim to provide deeper insight into the relationship between the surface structure and the surface reactivity. Interestingly, the best fit CTR model indicated that Pb(II) adsorption on an annealed hematite ($1\bar{1}02$) surface occurred only at one type of edge-sharing site. By comparing the structure of two types of possible edge-sharing sites on the hematite ($1\bar{1}02$) substrate surface (FLT surface), we found that the chemically inert edge-sharing sites as observed on the FLT surface bear O-O edges too long to make a stable Pb complex species.

In Chapter 5, we switched to a different system to explore the Sb(V) sorption on a CMP-prepared hematite ($1\bar{1}02$) surface. Sb(V) exists as an oxyanion species in the aqueous solution with an octahedral coordinative structure. The best fit CTR model demonstrated that Sb(V) sorption on the HLT hematite($1\bar{1}02$) surface occurred at a tridentate corner-sharing/edge-sharing site. Such a binding structure produces an Sb-Fe separation (3.05 Å) comparable to those published XAFS results based on soil samples (Mitsunobu et al., 2010; Ritchie et al., 2013; Guo et al., 2014). However, those published results suggested an edge-sharing binding mode based on the Sb-Fe separation. Therefore, our CTR work presented here indicated that knowledge of the local structure of an adsorbate, but without knowledge of the entire interfacial structure, could lead to ambiguity for deriving the surface binding structure.

1.6 References

- Abdel-Samad H. and Watson P. R. (1998) An XPS study of the adsorption of lead on goethite (α -FeOOH). *Appl. Surf. Sci.* **136**, 46–54.
- Appel C. and Ma L. (2002) Concentration, pH, and surface charge effects on cadmium and lead sorption in three tropical soils. *J. Environ. Qual.* **31**, 581–589.
- Bargar J. R., Brown G. E. and Parks G. A. (1997) Surface complexation of Pb(II) at oxide-water interfaces: II. XAFS and bond-valence determination of mononuclear Pb(II) sorption products and surface functional groups on iron oxides. *Geochim. Cosmochim. Acta* **61**, 2639–2652. Available at: <http://www.sciencedirect.com/science/article/pii/S0016703797001257>.
- Barton L. E., Grant K. E., Kosel T., Quicksall A. N. and Maurice P. A. (2011) Size-Dependent Pb Sorption to Nanohematite in the Presence and Absence of a Microbial Siderophore. *Environ. Sci. Technol.* **45**, 3231–3237. Available at: <http://pubs.acs.org/doi/abs/10.1021/es1026135>.
- Benjamin M. M., Sletten R. S., Bailey R. P. and Bennett T. (1996) Sorption and filtration of metals using iron-oxide-coated sand. *Water Res.* **30**, 2609–2620.
- Bowell R. J. (1994) Sorption of arsenic by iron oxides and oxyhydroxides in soils. *Appl. Geochemistry* **9**, 279–286.
- Brown G. E., Henrich V. E., Casey W. H., Clark D. L., Eggleston C., Felmy A., Goodman D. W., Grätzel M., Maciel G., McCarthy M. I., Nealon K. H., Sverjensky D. A., Toney M. F. and Zachara J. M. (1999) Metal Oxide Surfaces and Their Interactions with Aqueous Solutions and Microbial Organisms. *Chem. Rev.* **99**, 77–174. Available at: <http://pubs.acs.org/doi/abs/10.1021/cr980011z>.
- Brown G. E. J., Parks G. A., Bargar J. R. and Towle S. N. (1998) Use of X-ray Absorption Spectroscopy To Study Reaction Mechanisms at Metal Oxide--Water Interfaces. In *Mineral-Water Interfacial Reactions* pp. 14–36. Available at: <http://pubs.acs.org/doi/abs/10.1021/bk-1998-0715.ch002>.
- Brown G. E., Parks G. A. and O'Day P. A. (1995) Sorption at mineral-water interfaces: macroscopic and microscopic perspectives. *Miner. Surfaces* **5**.
- Brown G. E. and Sturchio N. C. (2002) An overview of synchrotron radiation applications to low temperature geochemistry and environmental science. *Rev. Mineral. Geochemistry* **49**, 1–115.
- Catalano J. G., Fenter P. and Park C. (2007) Interfacial water structure on the (0 1 2) surface of hematite: Ordering and reactivity in comparison with corundum. *Geochim. Cosmochim. Acta* **71**, 5313–5324.
- Christl I. and Kretzschmar R. (1999) Competitive sorption of copper and lead at the oxide-water interface: Implications for surface site density. *Geochim. Cosmochim. Acta* **63**, 2929–2938. Available at: <http://www.sciencedirect.com/science/article/pii/S0016703799002665>.

- Cornell R. M. and Schwertmann U. (2003) *The iron oxides: structure, properties, reactions, occurrences and uses.*, John Wiley & Sons.
- Craig J. R., Rimstidt J. D., Bonnaffon C. A., Collins T. K. and Scanlon P. F. (1999) Surface water transport of lead at a shooting range. *Bull. Environ. Contam. Toxicol.* **63**, 312–319.
- Davis J. A. and Leckie J. O. (1978) Surface ionization and complexation at the oxide/water interface II. Surface properties of amorphous iron oxyhydroxide and adsorption of metal ions. *J. Colloid Interface Sci.* **67**, 90–107.
- Dyer J. A., Trivedi P., Scrivner N. C. and Sparks D. L. (2003) Lead Sorption onto Ferrihydrite. 2. Surface Complexation Modeling. *Environ. Sci. Technol.* **37**, 915–922. Available at: <http://pubs.acs.org/doi/abs/10.1021/es025794r>.
- Fenter P. A. (2002) X-ray Reflectivity as a Probe of Mineral-Fluid Interfaces: A User Guide. *Rev. Mineral. Geochemistry* **49**, 149–221. Available at: <http://ring.geoscienceworld.org/content/49/1/149.short>.
- Fenter P. and Sturchio N. C. (2004) Mineral--water interfacial structures revealed by synchrotron X-ray scattering. *Prog. Surf Sci.* **77**, 171–258. Available at: <http://www.sciencedirect.com/science/article/pii/S0079681605000031>.
- Filella M., Belzile N. and Chen Y.-W. (2002) Antimony in the environment: a review focused on natural waters: I. Occurrence. *Earth-Science Rev.* **57**, 125–176.
- Gadde R. R. and Laitinen H. A. (1974) Heavy metal adsorption by hydrous iron and manganese oxides. *Anal. Chem.* **46**, 2022–2026.
- Goyer R. A. (1993) Lead toxicity: current concerns. *Environ. Health Perspect.* **100**, 177.
- Grover V. A., Hu J., Engates K. E. and Shipley H. J. (2012) Adsorption and desorption of bivalent metals to hematite nanoparticles. *Environ. Toxicol. Chem.* **31**, 86–92.
- Gunneriusson L., Lövgren L. and Sjöberg S. (1994) Complexation of Pb (II) at the goethite (α -FeOOH)/water interface: The influence of chloride. *Geochim. Cosmochim. Acta* **58**, 4973–4983.
- Guo X., Wu Z., He M., Meng X., Jin X., Qiu N. and Zhang J. (2014) Adsorption of antimony onto iron oxyhydroxides: Adsorption behavior and surface structure. *J. Hazard. Mater.* **276**, 339–345.
- Gustafsson J. P., Tiberg C., Edkymish A. and Kleja D. B. (2011) Modelling lead(II) sorption to ferrihydrite and soil organic matter. *Environ. Chem.* **8**, 485–492.
- Hayes K. F. and Leckie J. O. (1987) Modeling ionic strength effects on cation adsorption at hydrous oxide/solution interfaces. *J. Colloid Interface Sci.* **115**, 564–572.
- Hiemstra T. and Riemsdijk W. H. Van (1996) A Surface Structural Approach to Ion Adsorption: The Charge Distribution (CD) Model. *J. Colloid Interface Sci.* **179**, 488–508. Available at: <http://www.sciencedirect.com/science/article/pii/S0021979796902428>.
- Hiemstra T., Van Riemsdijk W. H. and Bolt G. H. (1989) Multisite proton adsorption modeling at the solid/solution interface of (hydr) oxides: A new approach: I. Model description and evaluation of intrinsic reaction constants. *J. Colloid Interface Sci.* **133**, 91–104.

- Huang C. P. and Stumm W. (1973) Specific adsorption of cations on hydrous γ -Al₂O₃. *J. Colloid Interface Sci.* **43**, 409–420. Available at: <http://www.sciencedirect.com/science/article/pii/0021979773903871>.
- Johnson C. A. (1986) The regulation of trace element concentrations in river and estuarine waters contaminated with acid mine drainage: The adsorption of Cu and Zn on amorphous Fe oxyhydroxides. *Geochim. Cosmochim. Acta* **50**, 2433–2438.
- Kinniburgh D. G., Jackson M. L. and Syers J. K. (1976) Adsorption of alkaline earth, transition, and heavy metal cations by hydrous oxide gels of iron and aluminum. *Soil Sci. Soc. Am. J.* **40**, 796–799.
- Koningsberger D. C. and Prins R. (1988) X-ray absorption: principles, applications, techniques of EXAFS, SEXAFS, and XANES.
- Kovačević D., Pohlmeier A., Özbaş G., Narres H.-D. and Kallay M. J. N. (2000) The adsorption of lead species on goethite. *Colloids Surfaces A Physicochem. Eng. Asp.* **166**, 225–233.
- Lenhart J. J., Bargar J. R. and Davis J. A. (2001) Spectroscopic Evidence for Ternary Surface Complexes in the Lead(II)–Malonic Acid–Hematite System. *J. Colloid Interface Sci.* **234**, 448–452. Available at: <http://www.sciencedirect.com/science/article/pii/S0021979700973454>.
- Leuz A.-K., Mönch H. and Johnson C. A. (2006) Sorption of Sb (III) and Sb (V) to goethite: influence on Sb (III) oxidation and mobilization. *Environ. Sci. Technol.* **40**, 7277–7282.
- Lin Z. (1996) Secondary mineral phases of metallic lead in soils of shooting ranges from Örebro County, Sweden. *Environ. Geol.* **27**, 370–375. Available at: <http://dx.doi.org/10.1007/BF00766707>.
- Lützenkirchen J., Preočanin T., Stipić F., Heberling F., Rosenqvist J. and Kallay N. (2013) Surface potential at the hematite (001) crystal plane in aqueous environments and the effects of prolonged aging in water. *Geochim. Cosmochim. Acta* **120**, 479–486. Available at: <http://www.sciencedirect.com/science/article/pii/S0016703713003773>.
- Martínez-Lladó X., de Pablo J., Giménez J., Ayora C., Martí V. and Rovira M. (2008) Sorption of antimony(V) onto synthetic goethite in carbonate medium. *Solvent Extr. Ion Exch.* **26**, 289–300.
- Mason S. E., Iceman C. R., Tanwar K. S., Trainor T. P. and Chaka A. M. (2009) Pb (II) Adsorption on Isostructural Hydrated Alumina and Hematite (0001) Surfaces: A DFT Study. *J. Phys. Chem. C* **113**, 2159–2170.
- McComb K. A., Craw D. and McQuillan A. J. (2007) ATR-IR Spectroscopic Study of Antimonate Adsorption to Iron Oxide. *Langmuir* **23**, 12125–12130. Available at: <http://pubs.acs.org/doi/abs/10.1021/la7012667>.
- McKenzie R. M. (1980) The adsorption of lead and other heavy metals on oxides of manganese and iron. *Soil Res.* **18**, 61–73.
- Mitsunobu S., Takahashi Y. and Terada Y. (2010) μ -XANES Evidence for the Reduction of Sb(V) to Sb(III) in Soil from Sb Mine Tailing. *Environ. Sci. Technol.* **44**, 1281–1287.

- Müller B. and Sigg L. (1992) Adsorption of lead(II) on the goethite surface: Voltammetric evaluation of surface complexation parameters. *J. Colloid Interface Sci.* **148**, 517–532. Available at: <http://www.sciencedirect.com/science/article/pii/002197979290187Q>.
- Nriagu J. O. (1990) The rise and fall of leaded gasoline. *Sci. Total Environ.* **92**, 13–28.
- Ostergren J. D., Brown G. E., Parks G. A. and Persson P. (2000a) Inorganic Ligand Effects on Pb(II) Sorption to Goethite (α -FeOOH): II. Sulfate. *J. Colloid Interface Sci.* **225**, 483–493. Available at: <http://www.sciencedirect.com/science/article/pii/S0021979799967024> [Accessed November 13, 2015].
- Ostergren J. D., Trainor T. P., Bargar J. R., Brown G. E. and Parks G. A. (2000b) Inorganic Ligand Effects on Pb(II) Sorption to Goethite (α -FeOOH): I. Carbonate. *J. Colloid Interface Sci.* **225**, 466–482. Available at: <http://www.sciencedirect.com/science/article/pii/S0021979799967012> [Accessed November 13, 2015].
- Palmqvist U., Ahlberg E., Lövgren L. and Sjöberg S. (1999) Competitive metal ion adsorption in goethite systems using in situ voltammetric methods and potentiometry. *J. Colloid Interface Sci.* **218**, 388–396.
- Palmqvist U., Ahlberg E., Lövgren L. and Sjöberg S. (1997) In Situ Voltammetric Determinations of Metal Ions in Goethite Suspensions: Single Metal Ion Systems. *J. Colloid Interface Sci.* **196**, 254–266.
- Piper D. and Restrepo J. F. C. (2013) Lead and Cadmium: Priorities for action from UNEP's perspective for addressing risks posed by these two heavy metals. *E3S Web Conf* **1**, 30004. Available at: <http://dx.doi.org/10.1051/e3sconf/20130130004>.
- Ponthieu M., Juillot F., Hiemstra T., Van Riemsdijk W. H. and Benedetti M. F. (2006) Metal ion binding to iron oxides. *Geochim. Cosmochim. Acta* **70**, 2679–2698.
- Reich T. J., Das S., Koretsky C. M., Lund T. J. and Landry C. J. (2010) Surface complexation modeling of Pb (II) adsorption on mixtures of hydrous ferric oxide, quartz and kaolinite. *Chem. Geol.* **275**, 262–271.
- Resongles E., Casiot C., Elbaz-Poulichet F., Freydier R., Bruneel O., Piot C., Delpoux S., Volant A. and Desoeuvre A. (2013) Fate of Sb(V) and Sb(III) species along a gradient of pH and oxygen concentration in the Carnoules mine waters (Southern France). *Environ. Sci. Impacts* **15**, 1536–1544.
- Van Riemsdijk W. H., Bolt G. H., Koopal L. K. and Blaakmeer J. (1986) Electrolyte adsorption on heterogeneous surfaces: adsorption models. *J. Colloid Interface Sci.* **109**, 219–228.
- Ritchie V. J., Ilgen A. G., Mueller S. H., Trainor T. P. and Goldfarb R. J. (2013) Mobility and chemical fate of antimony and arsenic in historic mining environments of the Kantishna Hills district, Denali National Park and Preserve, Alaska. *Chem. Geol.* **335**, 172–188.
- Robinson I. K. and Tweet D. J. (1992) Surface x-ray diffraction. *Reports Prog. Phys.* **55**, 599. Available at: <http://stacks.iop.org/0034-4885/55/i=5/a=002>.

- Roe A. L., Hayes K. F., Chisholm-Brause C., Brown G. E. J., Parks G. A., Hodgson K. O. and Leckie J. O. (1991) In situ X-ray absorption study of lead ion surface complexes at the goethite-water interface. *Langmuir* **7**, 367–373.
- Sandalinas C., Ruiz-Moreno S., López-Gil A. and Miralles J. (2006) Experimental confirmation by Raman spectroscopy of a Pb--Sn--Sb triple oxide yellow pigment in sixteenth-century Italian pottery. *J. Raman Spectrosc.* **37**, 1146–1153.
- Scheinost A. C., Rossberg A., Vantelon D., Xifra I., Kretschmar R., Leuz A.-K., Funke H. and Johnson C. A. (2006) Quantitative antimony speciation in shooting-range soils by EXAFS spectroscopy. *Geochim. Cosmochim. Acta* **70**, 3299–3312. Available at: <http://www.sciencedirect.com/science/article/pii/S0016703706001451>.
- Scheuhammer A. M. and Norris S. L. (1995) A review of the environmental impacts of lead shotshell ammunition and lead fishing weights in Canada. *Occas. Pap. Can. Wildl. Serv.* **1995**.
- Schindler P. W. and Gamsjäger H. (1972) Acid—base reactions of the TiO₂ (Anatase)—water interface and the point of zero charge of TiO₂ suspensions. *Kolloid-Zeitschrift und Zeitschrift für Polym.* **250**, 759–763.
- Serrano S., O'Day P. A., Vlassopoulos D., García-González M. T. and Garrido F. (2009) A surface complexation and ion exchange model of Pb and Cd competitive sorption on natural soils. *Geochim. Cosmochim. Acta* **73**, 543–558. Available at: <http://www.sciencedirect.com/science/article/pii/S0016703708006844>.
- Shaheen S. M. (2009) Sorption and lability of cadmium and lead in different soils from Egypt and Greece. *Geoderma* **153**, 61–68.
- Stumm W., Huang C. P. and Jenkins S. R. (1970) Specific chemical interaction affecting stability of dispersed systems. *Croat. Chem. Acta* **42**, 223.
- Sundar S. and Chakravarty J. (2010) Antimony toxicity. *Int. J. Environ. Res. Public Health* **7**, 4267–4277.
- Tanwar K. S., Catalano J. G., Petitto S. C., Ghose S. K., Eng P. J. and Trainor T. P. (2007a) Hydrated α -Fe₂O₃ surface structure: Role of surface preparation. *Surf Sci.* **601**, L59–L64.
- Tanwar K. S., Lo C. S., Eng P. J., Catalano J. G., Walko D. A., Brown G. E. J., Waychunas G. A., Chaka A. M. and Trainor T. P. (2007b) Surface diffraction study of the hydrated hematite surface. *Surf Sci.* **601**, 460–474. Available at: <http://www.sciencedirect.com/science/article/pii/S0039602806010739>.
- Tessier A., Rapin F. and Carignan R. (1985) Trace metals in oxic lake sediments: possible adsorption onto iron oxyhydroxides. *Geochim. Cosmochim. Acta* **49**, 183–194.
- Tiberg C., Sjöstedt C., Persson I. and Gustafsson J. P. (2013) Phosphate effects on copper (II) and lead (II) sorption to ferrihydrite. *Geochim. Cosmochim. Acta* **120**, 140–157.
- Tighe M., Lockwood P. and Wilson S. (2005) Adsorption of antimony(V) by floodplain soils, amorphous iron(III) hydroxide and humic acid. *J. Environ. Monit.* **7**, 1177–1185.

- Trainor T. P., Chaka A. M., Eng P. J., Newville M., Waychunas G. A., Catalano J. G. and Brown G. E. J. (2004) Structure and reactivity of the hydrated hematite (0001) surface. *Surf. Sci.* **573**, 204–224. Available at: <http://www.sciencedirect.com/science/article/pii/S0039602804012531>.
- Trivedi P., Dyer J. A. and Sparks D. L. (2003) Lead Sorption onto Ferrihydrite. 1. A Macroscopic and Spectroscopic Assessment. *Environ. Sci. Technol.* **37**, 908–914. Available at: <http://pubs.acs.org/doi/abs/10.1021/es0257927>.
- Varrica D., Bardelli F., Dongarrà G. and Tamburo E. (2013) Speciation of Sb in airborne particulate matter, vehicle brake linings, and brake pad wear residues. *Atmos. Environ.* **64**, 18–24.
- Venema P., Hiemstra T. and van Riemsduik W. H. (1996) Comparison of different site binding models for cation sorption: description of pH dependency, salt dependency, and cation--proton exchange. *J. Colloid Interface Sci.* **181**, 45–59. Available at: <http://www.sciencedirect.com/science/article/pii/S0021979796903550>.
- Verma S. and Dubey R. S. (2003) Lead toxicity induces lipid peroxidation and alters the activities of antioxidant enzymes in growing rice plants. *Plant Sci.* **164**, 645–655.
- Vithanage M., Rajapaksha A. U., Dou X., Bolan N. S., Yang J. E. and Ok Y. S. (2013) Surface complexation modeling and spectroscopic evidence of antimony adsorption on iron-oxide-rich red earth soils. *J. Colloid Interface Sci.* **406**, 217–224.
- Westall J. C. (1986) Reactions at the oxide-solution interface: Chemical and electrostatic models. In *Geochemical processes at mineral surfaces* American Chemical Society Washington, DC. pp. 54–78.
- Wilson S. C., Lockwood P. V, Ashley P. M. and Tighe M. (2010) The chemistry and behaviour of antimony in the soil environment with comparisons to arsenic: a critical review. *Environ. Pollut. (Oxford, U. K.)* **158**, 1169–1181.

Chapter 2 Structural Study of the Hematite ($1\bar{1}02$) Surface Annealed at High Temperature: Interfacial Water Structure and the Surface Termination Transformation¹

Abstract

The interfacial structure of an annealed hematite ($1\bar{1}02$) surface in contact with water was investigated using crystal truncation rod X-ray diffraction to address two questions: the ordering of interfacial waters at the mineral fluid interface and the mechanism of the surface termination transformation during annealing. The best fit surface structure model was compared to previously published results; we observe general agreement in both the out-of-plane relaxations and the in-plane displacements of atomic layers (comparable within model errors). Two adsorbed interfacial water layers were identified on the annealed hematite ($1\bar{1}02$) surface with both lateral and vertical ordering. Based on the positions of oxygen atoms we infer that the 1st layer interfacial waters are bound with two ¹O groups from adjacent unit cells through H-bonding interaction with O-O separations of 2.75 Å. In addition, the 2nd layer waters appear to be hydrogen-bonded with the 1st layer adsorbed water. The inferred interfacial hydrogen bonding network formed by the adsorbed waters was found to be consistent with the results of the bond valence analysis. In this study, we propose a chemical pathway for the termination transformation of the annealed hematite substrate. Our model proposes that the projection of near-surface substrate Fe atoms to occupy the surface Fe vacancy sites is the key step in the transformation from half-layer dominated to full-layer dominated surface termination. The

¹ Qiu C., Eng P. J., Stubbs J. and Trainor T. P. (2015) Structural Study of the Hematite ($1\bar{1}02$) Surface Annealed at High Temperature: Interfacial Water Structure and the Surface Termination Transformation. Prepared for submission to Surface Science.

proposed pathway for the redistribution of Fe atoms also results in a characteristic surface morphology, which was further confirmed in the AFM image of an annealed hematite ($1\bar{1}02$) surface.

2.1 Introduction

Iron-(hydr)oxides, abundant in the Earth crust, play a significant role in the fate and transport of environmental contaminants due to their extraordinary surface properties such as high specific surface area, and surface functional groups which are highly reactive with respect to the complexation of heavy metals (Bargar et al., 1997; Bargar et al., 1999; Christl and Kretzschmar, 1999; Bargar et al., 2000; Lenhart et al., 2001; Bargar et al., 2004; Catalano et al., 2005; Catalano et al., 2006; Ha et al., 2009) and some anionic species (Catalano et al., 2007b; Catalano et al., 2008; Brechbühl et al., 2012). Hematite, a common iron oxide, is often found as nanoparticles or as surface coatings on other substrates playing a key role in attenuation of trace metals in certain soil or aquatic environments (Madden and Hochella, 2005). In addition to its geochemical and environmental significance the physiochemical properties of hematite, such as high theoretical capacity, high inherent density, high resistance to corrosion, and desirable band gap (~ 2.2 eV), also make it a material widely used in industrial applications. For example, hematite has proven to be an effective photoanode material for the water splitting reaction to produce molecular oxygen and hydrogen (Cesar et al., 2006; Cesar et al., 2009; Sivula et al., 2010; Tilley et al., 2010; Ling et al., 2011); hematite has also long been recognized as catalysts or catalyst precursor for a range of different chemical reactions such as the combustion of methyl-ethyl ketone (Escobar et al., 2004), Friedel-Crafts acylation of benzene (Sharghi et al., 2010) and dehydrogenation of ethylbenzene to styrene (Muhler et al., 1990). There has also been

recent focus on the potential of using nano-hematite incorporated on the surface of graphene sheets for producing a promising anode in Li-ion batteries (Bai et al., 2012).

Significant research effort has focused on understanding how the size and morphology of (nano-)particulate oxides influence substrate reactivity (Waychunas et al., 2005). Temperature is often a controlling factor dictating (nano-)particle size and morphology during synthesis. For example, a field-emission scanning electron microscopy study of an electrodeposited iron oxide thin films (Tamboli et al., 2012) found an increase in annealing temperature from 400 to 700°C is responsible for the transition from nano-sheets to elongated dumbbell shaped nanoparticles, which correlates with a change in the optical band gap. Interestingly, the influence of temperature on substrate structure was also found in some surface specific experimental studies (Catalano et al., 2007a; Tanwar et al., 2007a), which provided evidence of the annealing-induced surface termination transformation of the hematite ($1\bar{1}02$) substrate. Tanwar et al. (Tanwar et al., 2007a; Tanwar et al., 2007b) used crystal truncation rod (CTR) X-ray diffraction to study the hydrated hematite ($1\bar{1}02$) surface and found two chemically distinct surface terminations co-existing with a ratio depending on the sample preparation scheme. When the substrate is prepared through a wet chemical and mechanical polishing (CMP) procedure the surface was dominant by a half-layer termination (>70%), which has a Fe vacancy at the surface relative to the stoichiometric termination. Interestingly, the transformation of the surface termination to a stoichiometric layer stacking sequence was observed after the substrate was annealed in the air at 500 °C for 3 hrs. Such a termination transformation was also observed in an X-ray reflectivity (XR) study undertaken by Catalano et al. (Catalano et al., 2007a). Although previous CTR and XR studies are consistent in the surface termination transformation of the hematite ($1\bar{1}02$) induced by annealing, neither study had proposed a mechanism. In the present study, we

explicitly incorporate multiple types of unit cells representing the different surface terminations and optimize each independently. The CTR modeling results were further coupled with analysis of AFM images of an annealed hematite ($1\bar{1}02$) surface to propose a potential mechanism describing the surface termination transformation induced by annealing.

Besides the surface termination transformation, the present study also focuses on the ordering of interfacial water at the substrate surface. In previous studies of water sorption on oxides surfaces the ordering of interfacial waters was found to be damping quickly away from the substrate surface; within a length scale of less than 10 Å any surface induced order had decayed to bulk like water structure (Cheng et al., 2001; Geissbühler et al., 2004; Catalano et al., 2007a; Catalano, 2010; Heberling et al., 2011). The ordering of interfacial water will likely change the dielectric constant relative to the bulk solution (Catalano et al., 2007a; Catalano et al., 2009), which would exert some influence on the associated electrostatic interactions at mineral water interface (Oliveira et al., 2004). Based on the multi-unit cell structure, the interfacial water structure and the associated water ordering was characterized in the present study. Our best fit model structure indicates a potential interfacial water structure at the annealed hematite ($1\bar{1}02$) surface. The resolved interfacial water structure in this study consists of two adsorbed water layers with a H-bonding network consistent with the 1st layer adsorbed water bridging two ¹O atoms from adjacent unit cells and the 2nd layer adsorbed water H-bonded to the 1st layer adsorbed water only.

2.2 Methods

2.2.1 Sample preparation

A natural single crystal hematite sample was cut parallel to the $(1\bar{1}02)$ plane and made to a round shape with a surface area of $\sim 1 \text{ cm}^2$ and thickness of $\sim 2 \text{ mm}$. The sample surface was then polished following the CMP procedures as described by Tanwar et al. (Tanwar et al., 2007b). Briefly, the sample was first polished for 20 min using commercial colloidal silica suspension ($0.06 \mu\text{m}$ diameter) (TED PELLA, USA), which was adjusted to pH 11.5 using a NaOH solution. The polishing suspension was then switched to the raw colloidal silica suspension (pH 10.0) to continue polishing the surface for another 10 min. Following the polishing the sample was base washed for 1 hour (NaOH solution of pH 10.5) followed by a 4-hour acid wash (HNO_3 solution of pH 2.0). Following this preparation method the sample used in this study was found to have a miss-cut of less than 0.03° and a suitable surface quality for use in surface scattering experiment. The CMP-prepared sample was annealed for 24 hours in a furnace preheated to 550°C under an ambient atmosphere. After annealing, the hematite sample was transferred to a dessicator and stored overnight. The sample was then mounted in a liquid cell designed for *in situ* surface scattering. The liquid cell was described in detail elsewhere (Heberling et al., 2011). The sample cell was filled with de-ionized water that had been purged for two hours with pure N_2 gas ($>99.999\%$) after boiling. The de-ionized water was adjusted to pH $5.5(\pm 0.2)$ in a N_2 filled glove box using HCl. The solution was then withdrawn in a syringe which was used to introduce the solution into the liquid cell. After introduction of the solution into the liquid cell the sample was allowed to equilibrate for 30 minutes with a thick film of water ($> 5 \text{ mm}$) before generating a thin film (by adjusting film gap) trapped between the sample surface and a several-micron thick Kapton film. The quality of the liquid film was monitored through observing the

film surface, which should exhibit clear Newton rings if the liquid film is thin and has a relatively uniform thickness (several microns). To avoid dehydration of the liquid film due to water escaping through the Kapton film, the liquid cell was capped with a Kapton film dome with water-saturated He (relative humidity >90%) flowing through the dome headspace.

2.2.2 Scattering measurements

The CTR measurements were performed at the undulator beamline 13IDC at the Advanced Photon Source (APS), Argonne National Laboratory. The energy of incoming beam was fixed at 13 keV using a liquid nitrogen cooled double-crystal silicon (111) monochromator. The incoming beam was focused and collimated to $10\ \mu\text{m} \times 100\ \mu\text{m}$ using rhodium coated horizontal and the vertical mirrors as well as a set of horizontal and vertical slits. A Kappa geometry Newport diffractometer (4S+2D) was used for sample and detector orientation with angles and diffractometer coordinates defined according to You (You, 1999). X-ray intensity prior to the sample was monitored using a N_2 gas filled ion-chamber and scattered intensity was measured using a Dectris PILATUS 100K 2D pixel array detector with 195×487 pixels (vertical \times horizontal) (Eikenberry et al., 2003). Nine CTRs, including the specular rod, were collected in order to probe both the lateral and vertical electron density of the surface. To collect non-specular CTR data, the incident angle of the beam relative to the sample surface was fixed at 2° , while an Omega scan was used to scan the specular rod with the surface normal of the sample constrained to lie within the lab frame horizontal plane.

The structure factor (magnitude) of each data point was extracted from the associated Pilatus image using TDL software package (<http://cars9.uchicago.edu/ifeffit/tld>). Each data point is subject to background subtraction, followed by corrections for active area, polarization, and

Lorentz factors to account for the variance of the intercept between Ewald-sphere and CTR as a function of Q according to the method outlined by Schlepütz et al. (Schlepütz et al., 2005).

Potential beam-induced damage to the sample surface was checked by repeating the collection of a CTR segment several times throughout the course of the measurements. We observed that “check rod” intensities remained within experimental errors throughout the course of data collection indicative of no substantial surface damage.

2.3 Structure and termination of hematite ($1\bar{1}02$) surface

Hematite (α -Fe₂O₃), belongs to the space group R-3c, and has lattice parameters of (5.035 Å, 13.747 Å, 90°, 90°, 120°) (Finger and Hazen, 1980). The oxygen atoms in the hematite structure are hexagonal close-packed with iron atoms occupying two-thirds of the octahedral holes. The Fe octahedral unit in the hematite bulk structure are slightly distorted making two sets of Fe-O bonds with bond lengths of 1.95 Å and 2.11 Å, respectively (Finger and Hazen, 1980). For convenience, the hematite ($1\bar{1}02$) surface can be re-indexed by defining a pseudo unit cell (5.038 Å, 5.434 Å, 7.3707 Å, 90°, 90°, 90°) as described in detail by Trainor et al. (Trainor et al., 2002). The main advantage of the pseudo-cell is it places the c-axis parallel to the surface normal (**c_s**), with the **a_s** and **b_s** axes defined within the plane of the surface. The re-indexed unit cell contains ten atomic layers with a stoichiometric layer sequence of (**O₂-Fe₂-O₂-Fe₂-O₂-O₂-Fe₂-O₂-Fe₂-O₂-**R**) along the **c_s** axis, where **R** represents the stoichiometric (Fe₂O₃) repeat of the bulk material. The bottom five atom layers are symmetry related to the top five layers via a glide plane (**c_s** glide). This result in two symmetry related surface unit cells which are chemically equivalent but crystallographically distinct. In addition, another glide plane symmetry (**b_s** glide) is found in the surface structure running along a **b_s** direction crossing the surface lattice point ($\frac{3}{4}, 0$) based on**

the re-indexed unit cell. As depicted in Figure 2.1 (C and D), hematite ($1\bar{1}02$) surface (both the HLT and the FLT) displays a topographical pattern with surface atoms zigzagging along a direction parallel to the \mathbf{b}_s axis. Two types of Fe octahedral units with different orientations are related by the \mathbf{b}_s glide plane.

The termination of the hematite ($1\bar{1}02$) has been extensively studied using both experimental and theoretical approaches (Henderson et al., 1998; Catalano et al., 2007a; Tanwar et al., 2007a; Tanwar et al., 2007b; Lo et al., 2007). In these previous studies it was observed that the chemical identity of the termination is largely determined by the sample preparation scheme. For example, the stoichiometric (1×1) hematite ($1\bar{1}02$) sample prepared under ultra-high vacuum annealing at 950 K is observed to produce a reduced (2×1) surface (Henderson et al., 1998). However, when prepared using a wet chemical mechanical polishing (CMP) procedure the surface is observed to be terminated largely with a so-called half-layer termination (HLT); similar to the stoichiometric (1×1) surface but with the Layer-3 Fe sites vacant (Figure 2.1) (Tanwar et al., 2007b).

Interestingly, after the CMP-prepared surface was annealed at 500 °C in an ambient atmosphere for 3 hours the surface was observed to be dominated by a (hydrated) stoichiometry termination (>70%), as found by Tanwar et al. (Tanwar et al., 2007a). This implies a termination transformation from the HLT to the stoichiometry termination (called full layer termination (FLT) hereafter) via mobilization of the Layer-5 Fe atoms to the vacant Layer 3 sites (Figure 2.1) (Tanwar et al., 2007a). In this paper, we build upon these previous results by analyzing the (air) annealed surface using a multi-unit cell structural model to gain further insight into the surface transformation mechanism using mass balance constraints.

2.4 Data Analysis

2.4.1 CTR theory

Crystal truncation rods are diffuse streaks of X-ray scattering intensity running parallel to the surface normal direction, which are caused by the abrupt termination of a crystal structure (Robinson, 1986). The total CTR structure factor is expressed as

$$F_T = SR(F_b F_{CTR} + F_{sc}) \quad (2.1)$$

where the S is the overall scale factor, R is a roughness factor (calculated using the β model described by Robinson (Robinson, 1986) in this study), F_b is the structure factor of the bulk unit cell and F_{sc} is the structure factor of the surface unit cell, F_{CTR} is the CTR form factor (Robinson, 1986; Vlieg, 2000; Fenter, 2002). The bulk cell structure factor is computed as

$$F_b = \sum_{j=1}^n \theta_j f_j \exp(i\mathbf{Q} \cdot \mathbf{r}_j) \exp[-B_j(|\mathbf{Q}|/4\pi)^2] \quad (2.2)$$

and depends on the momentum transfer (\mathbf{Q}), atomic form factor (f_j), site occupancy (θ_j), fractional coordinates (\mathbf{r}_j), and isotropic Debye Waller factor (B_j) of each atom j in the unit cell. The CTR form factor (F_{CTR}) arises from the semi-infinite stacking of bulk unit cells along the surface normal direction and is a function only of the perpendicular momentum transfer (L)

$$F_{CTR} = \frac{1}{1 - e^{-i2\pi L}} \quad (2.3)$$

2.4.2 CTR structural model

Structure models of the surface unit cell are refined against the CTR data by optimizing atomic displacements, occupancies and isotropic Debye Waller factors. The modeling was performed in two phases. In the first phase a single-unit cell structural model was used with an atom layer sequence (projected along the surface normal direction) of **O₂-Fe₂-O₂-Fe₂-O₂-O₂-**

Fe₂-O₂-Fe₂-O₂-O₂-R, where **R** represents the stoichiometric (Fe₂O₃) repeat unit of the bulk. We explicitly consider two symmetry equivalent domains (with a 1:1 weight ratio) in the calculation of the structure factor by performing an incoherent summation of the structure factors of two chemically equivalent but crystallographically distinct unit cells. Because of the symmetry relationship (*c_s* glide plane symmetry) of the two unit cells, there are only one set of independent parameters. In the second phase different terminations (the HLT and the FLT) on each domain was incorporated to build a multi-unit cell structural model. The termination weights are constrained from the optimized model in the first phase. The atomic displacements for the FLT surface and the HLT surface were fit independently considering they are chemically distinct. After the surface modeling in the second phase, two oxygen layers were added to each constituent termination to simulate the adsorbed interfacial water layers. Another run of model refinement was performed to specifically optimize the interfacial water with all the other fitting parameters frozen to the values obtained in the second phase.

To decrease the total fitting parameters, atoms within the same atom layer were constrained to have equivalent occupancies, Debye Waller factors, and out-of-plane motions. In-plane displacements of atoms within the same layer were constrained so that the glide plane symmetry along the **b_s** axis will be maintained during the fitting. We limited each model run to refining 30 fitting parameters at most. As a result, successive runs were done until the refinement of fitting parameters became self-consistent.

2.4.3 Fitting algorithm and bond valence constraints

The structural model was refined to fit the experimental data using the differential evolution (DE) algorithm, an effective global optimization algorithm as described in detail elsewhere (Björck, 2011). The figure of merit (FOM), based on the normalized χ^2 value

$$\chi^2 = \sum_{i=1}^N \frac{\left[\frac{F_i - F_{i,c}}{e_i} \right]^2}{N-p} \quad (2.4)$$

was minimized in the process of model refinement. In Equation 2.4, F_i is the experimental value for the structure factor (magnitude), $F_{i,c}$ is the calculated structure factor (magnitude), e_i is the error of i^{th} data point, N is the number of data points, p is the number of fitting parameters.

A bond valence constraint was also used to help guide the fitting to structurally plausible models. According to the bond valence rule, each atom in a crystal structure should have its formal charge balanced by the sum of bond valence contributions from its coordinated members (Pauling, 1929). An empirical expression, developed by Brown et al. (Brown and Altermatt, 1985; Brown, 2009), relates a bond length to the bond valence,

$$s = e^{\frac{(r_0 - r)}{B}} \quad (2.5)$$

where r_0 is tabulated for different Metal-O bonds, B is a constant value 0.37 representing the softness of the interaction between the two atoms, and r is the actual bond length. A bond valence penalty factor is calculated in the process of model refinement by

$$P = 1 + \sum_{j=1}^n |x_j - f_j| \quad (2.6)$$

where f_j represents the formal charge of atom j and x_j represents the bond valence sum calculated for atom j . The bond valence penalty factor, associated with a net deficit (under-saturation) or net excess (over-saturation) of bond valence for the surface atoms being considered, was used to scale the original FOM value through $P \times \text{FOM}$. It is apparent that a structural model with all

atoms having a saturated bond valence values will give rise to a bond valence penalty factor equaling 1 making no effect on the original FOM. Whereas a model containing some atoms with under/over-saturation will produce a penalty factor greater than 1, increasing the FOM value.

It should be noted that the bond valence constraints would be incomplete without including the contribution of the covalent hydrogen bond (H-O) and the weak hydrogen bond (H \cdots O). However, H atoms do not contribute significantly to the CTR scattering intensity, thus their positions are not refined in the CTR modeling. Instead, the protonation states as well as the possible hydrogen bond interactions for each surface functional group are inferred in the model refinement process through exhaustively testing different combinations. The bond valence contribution of a typical covalent bound hydrogen and a weak hydrogen bond are constrained to lie in the range of 0.68-0.88 v.u. and 0.13-0.25 v.u., respectively, as suggested by Bargar et al. (Bargar et al., 1997). During model refinement the valence for each hydrogen bond (covalent and weak) is floating within the range mentioned above. A covalent hydrogen and/or a hydrogen bond will be assigned to an oxygen atom only if such an assignment could give rise to a total valence sum closer to bond valence saturation.

Our observation is that the enforcement of the bond valence constraint in the process of surface modeling is highly effective in attaining an optimized structure, which not only produces a desirable fit to the experimental data but also is physically reasonable in terms of coordination structure. However, we also realized that the model errors for the bond valence is difficult to evaluate, since the bond valence sum is directly related to the bond lengths that have errors determined by the associated atom positions. In light of that, an arbitrary tolerance level (0.2 v.u.) was applied in the calculation of the bond valence penalty factor, and the atom with a bond

valence sum consistent with its atomic valence within the tolerance level will make no contribution ($|x_j - f_j|$ in Equation 2.6 is set to 0) to the bond valence penalty factor P.

2.5 Results and discussion

2.5.1 Constraints of termination weights used in a multi-termination model

The annealing-induced termination transformation will produce a surface morphology corresponding to a mixture of different surface terminations. We noticed that there is only one possible route of atom rearrangement to transform the HLT to the FLT under the mass balance constraint, *i.e.* the projection of near-surface Fe atoms from one HLT unit cell to occupy the surface Fe vacancies in a different HLT unit cell, as illustrated in Figure 2.7A. As a result, both the HLT unit cell releasing Fe atoms and the one receiving Fe atoms will turn into a FLT unit cell but with a half unit cell height offset ($c/2$), as shown in Figure 2.7B. If the Fe projection occurs within the same domain, a different type of termination (the long FLT) emerges after the termination transformation producing a surface with a mixture of the HLT, the short FLT and the long FLT. The surface morphology will degenerate to one containing only the short FLT and the long FLT if assuming a 100% transformation rate from the HLT to the FLT, as shown in Figure 2.7B. To obtain surface proportions for different terminations, we built a single-unit cell structural model (in the first phase of surface modeling) with the occupancy of top five atomic layers being constrained accordingly. As compared in Figure 2.1, the Layer-1 O and the Layer-3 Fe belong to the long FLT only, while the other layers (Layer-2 O, Layer-4 O and Layer-5 Fe) are shared by both the long FLT and the HLT. Therefore, in the first phase of the model refinement we linked the occupancy of Layer-1 O and Layer-3 Fe to a same value ($\text{Occ_O}_1\text{Fe}_3$), and set equivalent the occupancies of the other three atomic layers ($\text{Occ_O}_2\text{O}_4\text{Fe}_5$). Apparently,

under this constraint, we could physically interpret the single-unit cell structural model as one equivalent to a multi-unit cell structural model that consists of the HLT (termination weight of $\text{Occ_O}_2\text{O}_4\text{Fe}_5\text{-Occ_O}_1\text{Fe}_3$), the long FLT ($\text{Occ_O}_1\text{Fe}_3$), and the short FLT ($1\text{-Occ_O}_2\text{O}_4\text{Fe}_5$). To arrive at reasonable occupancies, $\text{Occ_O}_2\text{O}_4\text{Fe}_5$ has to be greater than or equivalent to $\text{Occ_O}_1\text{Fe}_3$ corresponding to a presence (a partial termination transformation) or an absence (a complete termination transformation) of the HLT, respectively. The optimized model obtained in the first phase gave rise to an occupancy for Layer-1 O and Layer-3 Fe equivalent to 27%, and an occupancy for the other three atomic layers equivalent to 43%. Therefore, using the rule described above, the termination weights for different surface unit cells are computed corresponding to 16% HLT, 27% long FLT and 57% short FLT. The termination weights obtained from the first phase were further optimized in the second phase of surface modeling, but the variances (<2%) are within model errors. Therefore, termination weights derived in the first phase of surface modeling were fixed throughout the course of the surface refinement in the second phase.

2.5.2 Surface relaxation

The best fit modeling results are listed in Table 2.1, including the atomic displacements, isotropic Debye Waller factors, occupancies and weight factors. CTR modeling based on multi-unit cell structure provides an opportunity to compare the surface structures of different surface terminations; however, the uncertainties of fitting parameters will become substantially larger when one termination unit cell has a relatively small weight. In the present study, the weight for the HLT on each domain is $16(\pm 3)\%$, significantly less than that for the FLT ($84(\pm 3)\%$), and therefore results in high uncertainties of atom positions (up to 0.3 \AA). However, we noticed that

the best fit model structure of the HLT surface is consistent to previously published results by Tanwar et al. (Tanwar et al., 2007b) within model errors. The discussion below will focus on the atomic relaxation found in the FLT surface, which is the dominant surface termination taking up more than 80% of the surface.

According to our best fit model, a slight layer spacing expansion ($<0.04 \text{ \AA}$) was observed for Layer 2-3, Layer 3-4 and Layer 5-6 as opposed to Layer 1-2, where the inter-layer spacing expanded by 0.12 \AA mainly due to the large out-of-plane relaxation of Layer-1 O, as shown in Table 2.2. On the contrary, the Layer 4-5 is subject to a contraction of 0.08 \AA , which is caused by the recess of Layer-4 O into the bulk structure as well as the Layer-5 Fe moving towards the surface. The atom layer spacings (Table 2.2) obtained from this study were compared to those previously determined by Tanwar et al. (Tanwar et al., 2007a) and Catalano et al. (Catalano et al., 2007a), who also investigated the annealed and hydrated hematite ($1\bar{1}02$) surface. As shown in Table 2.2, the layer spacing pattern presented in this study is in good agreement with those reported in Tanwar's model although the layer spacings for Layer 2-3 and Layer 4-5 are slightly different between two studies with a difference of $<0.1 \text{ \AA}$. In addition, some differences in the layer spacings were also seen in Catalano's best fit model compared to our best fit model. For example, Catalano's model gave rise to a slight contraction of Layer 1-2 (0.04 \AA) instead of an expansion of 0.12 \AA found in our study. In addition, a larger expansion (0.16 \AA) was observed for Layer 3-4 in Catalano's model compared to that (0.02 \AA) found in our best fit model. In spite of the differences of the layer spacing pattern among three different studies, the layer heights of the top six atom layers deduced from this study are comparable to the other two studies within the model uncertainties, as illustrated in Figure 2.2. The convergence of atom layer heights

confirms the average electron density distribution along the direction of surface normal is comparable in all three studies.

The inclusion of off-specular data in the CTR analysis allows for the examination of in-plane displacements of surface atoms. According to the results from the present study, the in-plane motion along the \mathbf{a}_s direction of Layer-1 O and Layer-2 O anions are close to those reported in Tanwar's study (within 0.05\AA), whereas the atom movement along the \mathbf{b}_s direction are different from two studies. As shown in Table 2.2, Tanwar's best fit model gave rise to a 0.16\AA larger \mathbf{b}_s displacement for the Layer-1 O anions than that derived in this study. However, they are consistent within model errors. In addition, compared to our best fit model, Tanwar's model gave rise to a Layer-2 O which displayed a $0.10 (\pm 0.05)\text{\AA}$ smaller displacement along the \mathbf{b}_s direction. Despite these small differences, as shown in Figure 2.3, the bond length for Fe-O bonds calculated from the best fit model in the current study are in good agreement with that calculated according to Tanwar's best fit model (within 0.1\AA). In addition, we calculated the bond valence sum for the Layer-3 Fe using the Fe-O bond lengths derived in both Tanwar's and our best fit model, and we found that in both studies the bond valence sum (2.9 v.u. for this study and 2.8 v.u. for Tanwar's model) is close to the atomic valence of Fe(III) suggesting a near bond valence saturation for Layer-3 Fe atoms.

2.5.3 Interfacial water network

Interfacial water is a transition zone bridging the substrate surface and the bulk solution. As mentioned above, a model trial was initially run using a multi-unit cell structural model without interfacial waters in the second phase of surface modeling. As shown in Figure 2.4, the water-free model produced some anti-Bragg valleys significantly lower than experimental values, such

as (0 0 2.5), (2 0 2.1) and (2 0 -2.1), which could be due to the incomplete model without involving adsorbed interfacial waters. To investigate the structure of interfacial adsorbed water layers, two extra oxygen layers were included in the optimized water-free structure model. The presence of two water molecules within one unit cell results in a water density in the interfacial region close to the value for the bulk water solution (0.033 \AA^{-3}) assuming an inter-water layer spacing of 2 \AA .

To make the refinement more robust, we placed a constraint on the interfacial water positions by setting a set of cutoff limits for reasonable O-O separation (between two water molecules or between one water molecule and one surface oxygen group) ranging from 2.5 \AA to 2.8 \AA with a 0.5 \AA increment, which are arbitrary but close to values ($\sim 2.7 \text{ \AA}$) obtained through bond valence analysis of the repulsion between two oxygens involving in the hydrogen bonding interaction (Brown, 1976). The modeling results at different cutoff limits indicated that the optimized heights of interfacial water layers increase with the cutoff limit although the fitting qualities are statistically the same according to the Hamilton R-ratio test at a 95% confidence level. At the cutoff limit of 2.5 \AA , the optimized model give rise to two water layers with layer heights of $1.72 (-0.01, +0.2) \text{ \AA}$ and $3.06 (-0.2, +0.1) \text{ \AA}$, respectively, significantly lower than the case when the model is run at the cutoff limit of 2.8 \AA , where the best fit associated layer heights are $2.17 (-0.1, +0.1) \text{ \AA}$ and $3.29 (-0.04, +0.14) \text{ \AA}$, respectively.

The plausible dipole orientation of adsorbed interfacial waters could be predicted via the constraint of the tetrahedral hydrogen bonded water structure that could be distorted somehow (Marcus, 2009). Under this geometric constraint, we propose the most probable dipole orientation based on the knowledge of best fit oxygen positions. As shown in Figure 2.5, the 1st water molecule would act as H-bond acceptor by bridging two ^1O atoms from two adjacent unit

cells, and at the same time such a water molecule also acts as a H-bond donor by coordinating with two of the 2nd layer water molecules. Not surprisingly, the interfacial water structure under different O-O cutoff limit are slightly different. The 1st layer water molecules in the structure model ran under the 2.5 Å O-O cutoff limit exhibit a tetrahedral coordination structure with a high distortion bearing a range of O-O distances from 2.5 Å to 3.1 Å. Interestingly, the distortion was found to be gradually alleviated as we increase the O-O cutoff limit. The modeling results also indicated that the 1st layer interfacial water displays a tetrahedral coordination structure with equivalent O-O separations when the model refinements were performed at a O-O cutoff limit greater than 2.65 Å. In light of that, we speculate that it is more likely to have a interfacial H-bonding network with O-O separation of >2.65 Å on the annealed hematite (1 $\bar{1}$ 02) surface, since that will give rise to a less distorted tetrahedral coordination structure with equivalent O-O separations as well as reasonable O-O_{water}-O angles (^IO-O_{water1}-^IO angle and O_{water2}-O_{water1}-O_{water2} angle), as shown in Figure 2.5.

The interfacial water structure on an annealed hematite (1 $\bar{1}$ 02) surface has also been investigated by Catalano et al. (Catalano et al., 2007a) using X-ray reflectivity. The layer heights of two water layers in the reflectivity study are consistent within model error to those found in our study when the model is refined at the 2.5 Å cutoff limit for O-O separation. However, the optimized 1st layer water heights at cutoff limits >2.5 Å are significantly greater than that reported by Catalano et al., as illustrated in Figure 2.2. Catalano et al. suggested that a plausible interfacial water structure would require the 1st layer water bridges two ^{III}O atoms while the 2nd layer water bridges two ^IO atoms. However, we notice that such a bridging structure proposed by Catalano is sterically infeasible, since the 1st layer water molecule would be too close to one of ^IO atoms (~2.2 Å) although it is far away enough from the ^{III}O atoms (Figure 2.5B). In addition,

the associated $^{\text{III}}\text{O}-\text{O}_{\text{water}}-^{\text{III}}\text{O}$ angles ($<60^\circ$) in that H-bonding configuration proposed by Catalano are significantly smaller than the ideal value (109.5°) making a seriously distorted tetrahedral coordination structure. As opposed to the 1st layer waters, the positions of the 2nd layer water based on Catalano's model is consistent with that obtained from our best fit model at all cutoff limits, as shown in Figure 2.2. However, Catalano's model indicated that the 2nd layer water should bridge two $^{\text{I}}\text{O}$ atoms from the same unit cell, which would again lead to an unreasonably small bond angle of $^{\text{I}}\text{O}-\text{O}_{\text{water}}-^{\text{I}}\text{O}$ ($\sim 60^\circ$). According to the comparison of interfacial water structures from two different studies, we realized that the weak scattering feature could make it a challenge to resolve the interfacial water structure with certainty solely based on model fitting to experimental data. And the structural and the steric considerations (O-O separations and O-O_{water}-O bond angles) of interfacial waters could serve as useful constrains to provide further insights into the interfacial water structure. The interfacial water structure proposed in the current study is probably more realistic than that proposed in Catalano's study, since it is sterically more feasible in terms of both the O-O separations and the O-O_{water}-O bond angles. However, we are unclear of the exact reason causing the difference in the layer height of the 1st adsorbed water layer in Catalano's results, which could be induced by different experimental conditions (like pH) or related to different ways in setting up the interfacial water structure (Catalano's model involve layered water structure, which was not modeled in this study).

To date, interfacial water structure has been extensively studied on numerous substrate surfaces, such as mica, calcite, corundum, and goethite and these studies show that different substrates usually induce a distinct interfacial water structure. For example, in an X-ray reflectivity study of interfacial water structure at the mica (001) surface, Cheng et al. (Cheng et al., 2001) identified one adsorbed water layer at a layer height of $1.3(2) \text{ \AA}$ above the terminal

oxygen and an oscillatory layered water structure extending above the adsorbed water layer. The calcite(104) surface displayed a much simpler water structure including only two water layers without the subsequent oscillatory layered water structure, as found in two CTR studies (Geissbühler et al., 2004; Heberling et al., 2011). In both calcite studies, the 1st layer adsorbed water was believed to complete the octahedral coordination structure of calcium atom but with a position being distorted from the ideal position. In another CTR study of the hematite (0001) surface by Trainor et al. (Trainor et al., 2004), two chemically distinct domains were identified with an interfacial structure consisting of only one water layer with similar layer heights (2.0(3) Å and 1.9(3) Å). Comparing the interfacial water structure proposed in the current study and those reported in published studies mentioned above, we see some generic trend about the interfacial water structure. (1) The first water layer usually occupies a position templating the bulk structure through completing the surface metal coordination structure, as seen consistently in both this study and the other studies mentioned above. (2) The next adsorbed water layer is likely to present above the substrate surface at a characteristic layer height, which is probably related to the lattice structure of the substrate surface. A substrate surface with a cavity feature (like mica (001)) or a surface feature with a large interstitial space (like hematite ($1\bar{1}02$)) tend to have a second adsorbed layer water occupying above the cavity or the interstitial space with relatively low layer height. On the contrary, a substrate with a surface of relatively packed surface atom arrangement (like calcite (104) and hematite (0001)) would be more likely to induce a second adsorbed water with a much higher layer in order to make reasonable O-O separations. (3) The damping oscillatory structure of layered water may or may not exist depending on the ordering of the top one or two adsorbed water layers.

2.5.4 Bond valence analysis of the best fit model structure

Bond valence analysis was performed to deduce plausible protonation schemes of the surface oxygen functional groups. As listed in Table 2.3, both $^{\text{I}}\text{O}$ and $^{\text{III}}\text{O}$ groups on the FLT surface could achieve a bond valence saturation state within 0.10 v.u. after proper assignment of protonation schemes. The $^{\text{I}}\text{O}$ group requires to associate with two covalent protons, each contributing a valence of 0.76 v.u., to give rise to a bond valence saturation (2.00 v.u.). The $^{\text{III}}\text{O}$ group only needs one covalent hydrogen bond contributing a bond valence of 0.68 v.u. to reach a (slightly over) saturated bond valence sum of 2.08 v.u.. Interestingly, no hydrogen bonds were required to arrive at bond valence saturation for both the $^{\text{I}}\text{O}$ and the $^{\text{III}}\text{O}$ groups, suggesting only a hydrogen-bond donor character to the surface.

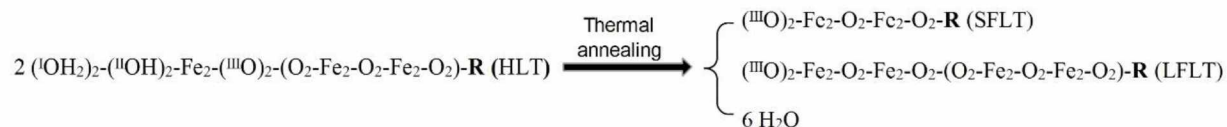
According to the H-bond network proposed above, the protonated $^{\text{I}}\text{O}$ group should donate H-bond to the first adsorbed water molecules. The relatively low bond valence (0.68 v.u.) contributed from the proton associating with $^{\text{III}}\text{O}$ group will result in a stronger hydrogen bond donor character (0.32 v.u.) associated with this group. We could not find the proper acceptor for such a strong hydrogen bond from the interfacial waters based on the H-bonding network proposed above. As discussed above, a consideration of H-bond interaction between $^{\text{III}}\text{O}$ group and the first layer water will end up with a greatly distorted tetrahedral coordination structure of the first layer adsorbed water molecule due to the small O-O-O angle ($<60^\circ$). Interestingly, if we reassign the protonation scheme of the $^{\text{I}}\text{O}$ group by considering a weaker covalent hydrogen bond (0.60 v.u.), then the $^{\text{I}}\text{O}$ group will open up a bond valence deficit of 0.32 v.u., which could be balanced by accepting the hydrogen bond contributed from the $^{\text{III}}\text{O}$ group. It should be pointed out that a bond valence of 0.60 v.u. for a covalent hydrogen bond falls slightly outside the range (0.68-0.88 v.u.) suggested by Bargar et al. (Bargar et al., 1997). Therefore, the

consideration of the hydrogen bond interaction between ^IO and ^{III}O groups will render the ^IO group a stronger Bronsted acid with a higher potential to release protons due to the weak H-O bonds.

2.5.5 Mechanisms of surface transformation and implications of the domain size

The best fit CTR modeling results based on the multi-unit cell structural models provide some insights into the surface morphology of an annealed surface. The domains in the CTR model could be physically related to surface terraces, as shown in Figure 2.7C. It should be noted that the incoherent rule applied for summing structure factors from different domains does not allow for a further investigation of the histogram distribution of surface terraces that is the main factor dictating the global surface roughness. In addition, the terminations within each terrace, as inferred from the best fit CTR model, represents the fine structural feature regionally. We speculate that the CMP procedure provides external chemical/mechanical force to produce terraces on the surface, which should be maintained when the surface is subject to the annealing. The annealing probably affect the surface structure locally through termination transformation that leads to a variation of the fine structural feature within a surface terrace, as shown in Figure 2.7D.

We propose that the pathway for termination transformation involves the mobilization of Layer-5 Fe in the HLT unit cell to occupy empty Layer-3 Fe sites resulting in the FLT unit cell (Figure 2.7). This pathway would result in the formation of two chemically equivalent FLT's with a half unit cell ($c/2$) step height offset, one associated with the vacating Layer-5 Fe and another unit cell associated with the filled Layer-3 Fe (Figure 2.7(AB)). A possible stoichiometric reaction is listed as follows,



where **R** is the stoichiometric repeated atom layer sequence. Note the protonation schemes of surface oxygens in the HLT are based on the bond valence analysis results (Table 2.3). In addition, the protonation or the hydroxylation of products (the short FLT(SFLT) and the long FLT(LFLT)) are not involved in the reaction stoichiometry, although it could occur when the sample is cooled down in the air and further reacts with water in the liquid cell.

The best fit model gave rise to a surface of two symmetry related domains with each domain containing 16% HLT, 27% long FLT and 57% short FLT. The deduction of unequal termination weights for two symmetry related terminations (the long FLT and the short FLT) appears to be a thermodynamically unreasonable scenario, since chemically equivalent surface terminations bear equivalent Gibbs free energy, and thus should be equivalently distributed on the surface.

However, it should be noted that the multi-unit cell model contains two symmetry related domains with a $\text{Nc}/2$ domain height offset, and thus the long FLT (short FLT) on one domain is crystallographically equivalent to the short FLT (long FLT) on its symmetry counterpart domain, as illustrated in Figure 2.7B. In light of that, the termination weights of two types of FLT are equal across the surface, although they are distinct on each constituent domain.

To confirm the termination features on an annealed hematite ($1\bar{1}02$) surface derived in the CTR modeling, AFM images were collected on the surface. The AFM image (Figure 2.6A) indicated a smooth surface with a root-mean-square roughness (σ_{RMS}) of 1.75 Å computed within the scan size (3 μm by 3 μm), which is roughly consistent with that ($\sigma_{\text{RMS}}=1.61$ Å) calculated based on a single domain structure (Figure 2.6 (CDE)) derived from the best fit CTR structural model. However, the real surface roughness is not only determined by the identity and proportion

of surface terminations on each domain but also by the domain steps, which could vary significantly depending on the physical/chemical history on the sample surface. In this study, we applied an incoherent addition rule to sum structure factors from different domains, and thus the roughness beyond the domain size could not be inferred from the modeling results.

The consistency of surface roughness calculated from the AFM image and that computed based on the CTR-derived domain structure suggests that the scan size of the AFM image (3 μm by 3 μm) should be comparable to or smaller than the domain size of the annealed surface, since a mixture of more than two coherently separated domains within the AFM image scan range would probably result in a much larger root-mean-square roughness considering the domain steps are relatively large. The typical coherence length found in a third generation synchrotron X-ray beamline is around 5 μm if assuming 1 \AA X-ray (Als-Nielsen and McMorrow, 2011). Hence, a domain size should be smaller than the coherence length of a modern synchrotron X-ray beam, which further suggests that the AFM image shown in Figure 2.6A is most likely to represent the surface height distribution pattern within a domain.

2.6 Conclusions

The mineral-water interfacial structure of the hematite ($1\bar{1}02$) surface, subject to ambient atmosphere annealing, was probed using crystal truncation rod X-ray diffraction. The results show a dominant FLT surface, which has small out-of-plane relaxation for the top six atom layers relative to the bulk structure, in good agreement with previous results (within model uncertainties). The best fit model structure gives rise to two adsorbed water layers with both the lateral and vertical ordering. We proposed a possible dipole orientation for the interfacial water structure using both the steric and structural constraints, and the proposed dipole orientation

suggests that the 1st layer water acts as a H-bond acceptor bridging two adjacent ¹⁶O oxygens as well as a H-bond donor making connection to the 2nd layer water. The multi-unit cell structural model implies a surface morphology characterized by a mixture of HLT, long FLT and short FLT on coherently separated surface terraces, which is also supported in the analysis of the AFM image. The CTR-derived multi-unit cell surface structure also provides insights into the chemical route for the annealing-induced surface termination transformation from the HLT to the FLT, which occurs via the projection of Layer-5 Fe to occupy vacant Layer-3 Fe sites.

2.7 Acknowledgements

This project is funded by DoD SERDP grant ER-1770. All the associated experiments were performed at beamline 13IDC of GeoSoilEnviroCARS (Sector 13), Advanced Photon Source (APS), Argonne National Laboratory. GSECARS is supported by the National Science Foundation - Earth Sciences (EAR-1128799) and Department of Energy - Geosciences (DE-FG02-94ER14466). Use of the Advanced Photon Source was supported by the U. S. Department of Energy, Office of Science, Office of Basic Energy Sciences, under Contract No. DE-AC02-06CH11357. We would also like to thank the Arctic Super Computer Center (ARSC) at University of Alaska Fairbanks for providing computation resource used in the surface modeling. Last but not least, we also want to appreciate Sang Soo Lee at Argonne National Laboratory for his help in collecting AFM images of annealed hematite samples.

2.8 References

- Als-Nielsen J. and McMorrow D. (2011) *Elements of modern X-ray physics.*, John Wiley & Sons.
- Bai S., Chen S., Shen X., Zhu G. and Wang G. (2012) Nanocomposites of hematite ($\alpha\text{-Fe}_2\text{O}_3$) nanospindles with crumpled reduced graphene oxide nanosheets as high-performance anode material for lithium-ion batteries. *RSC Adv.* **2**, 10977–10984.
- Bargar J. R., Brown G. E. and Parks G. A. (1997) Surface complexation of Pb(II) at oxide-water interfaces: II. XAFS and bond-valence determination of mononuclear Pb(II) sorption products and surface functional groups on iron oxides. *Geochim. Cosmochim. Acta* **61**, 2639–2652. Available at: <http://www.sciencedirect.com/science/article/pii/S0016703797001257>.
- Bargar J. R., Reitmeyer R. and Davis J. A. (1999) Spectroscopic Confirmation of Uranium(VI)-Carbonato Adsorption Complexes on Hematite. *Environ. Sci. Technol.* **33**, 2481–2484. Available at: <http://pubs.acs.org/doi/abs/10.1021/es990048g>.
- Bargar J. R., Reitmeyer R., Lenhart J. J. and Davis J. A. (2000) Characterization of U(VI)-carbonato ternary complexes on hematite: EXAFS and electrophoretic mobility measurements. *Geochim. Cosmochim. Acta* **64**, 2737–2749. Available at: <http://www.sciencedirect.com/science/article/pii/S0016703700003987>.
- Bargar J. R., Trainor T. P., Fitts J. P., Chambers S. A. and Brown G. E. (2004) In Situ Grazing-Incidence Extended X-ray Absorption Fine Structure Study of Pb(II) Chemisorption on Hematite (0001) and (1-102) Surfaces. *Langmuir* **20**, 1667–1673.
- Björck M. (2011) Fitting with differential evolution: an introduction and evaluation. *J. Appl. Crystallogr.* **44**, 1198–1204. Available at: <http://dx.doi.org/10.1107/S0021889811041446>.
- Brechbühl Y., Christl I., Elzinga E. J. and Kretzschmar R. (2012) Competitive sorption of carbonate and arsenic to hematite: Combined ATR-FTIR and batch experiments. *J. Colloid Interface Sci.* **377**, 313–321. Available at: <http://www.sciencedirect.com/science/article/pii/S0021979712002937>.
- Brown I. D. (1976) Geometry of O-H...O hydrogen bonds. *Acta Crystallogr. Sect. A Cryst. Physics, Diffraction, Theor. Gen. Crystallogr.* **A32, Pt. 1**, 24–31.
- Brown I. D. (2009) Recent Developments in the Methods and Applications of the Bond Valence Model. *Chem. Rev.* **109**, 6858–6919. Available at: <http://pubs.acs.org/doi/abs/10.1021/cr900053k>.
- Brown I. D. and Altermatt D. (1985) Bond-valence parameters obtained from a systematic analysis of the Inorganic Crystal Structure Database. *Acta Crystallogr. Sect. B* **41**, 244–247. Available at: <http://dx.doi.org/10.1107/S0108768185002063>.
- Catalano J. G. (2010) Relaxations and Interfacial Water Ordering at the Corundum (110) Surface. *J. Phys. Chem. C* **114**, 6624–6630. Available at: <http://pubs.acs.org/doi/abs/10.1021/jp100455s>.

- Catalano J. G., Fenter P. and Park C. (2007a) Interfacial water structure on the (0 1 2) surface of hematite: Ordering and reactivity in comparison with corundum. *Geochim. Cosmochim. Acta* **71**, 5313–5324.
- Catalano J. G., Fenter P. and Park C. (2009) Water ordering and surface relaxations at the hematite (110)--water interface. *Geochim. Cosmochim. Acta* **73**, 2242–2251.
- Catalano J. G., Park C., Fenter P. and Zhang Z. (2008) Simultaneous inner- and outer-sphere arsenate adsorption on corundum and hematite. *Geochim. Cosmochim. Acta* **72**, 1986–2004.
- Catalano J. G., Trainor T. P., Eng P. J., Waychunas G. A. and Brown Jr G. E. (2005) CTR diffraction and grazing-incidence EXAFS study of U (VI) adsorption onto α -Al₂O₃ and α -Fe₂O₃(1-102) surfaces. *Geochim. Cosmochim. Acta* **69**, 3555–3572.
- Catalano J. G., Zhang Z., Fenter P. and Bedzyk M. J. (2006) Inner-sphere adsorption geometry of Se (IV) at the hematite (100)--water interface. *J. Colloid Interface Sci.* **297**, 665–671. Available at: <http://www.sciencedirect.com/science/article/pii/S0021979705012038>.
- Catalano J. G., Zhang Z., Park C., Fenter P. and Bedzyk M. J. (2007b) Bridging arsenate surface complexes on the hematite(0 1 2) surface. *Geochim. Cosmochim. Acta* **71**, 1883–1897.
- Cesar I., Kay A., Gonzalez Martinez J. A. and Graetzel M. (2006) Translucent Thin Film Fe₂O₃ Photoanodes for Efficient Water Splitting by Sunlight: Nanostructure-Directing Effect of Si-Doping. *J. Am. Chem. Soc.* **128**, 4582–4583.
- Cesar I., Sivula K., Kay A., Zboril R. and Gratzel M. (2009) Influence of Feature Size, Film Thickness and Silicon Doping on the Performance of Nanostructured Hematite Photoanodes for Solar Water Splitting. *J. Phys. Chem. C* **113**, 772–782.
- Cheng L., Fenter P., Nagy K. L., Schlegel M. L. and Sturchio N. C. (2001) Molecular-scale density oscillations in water adjacent to a mica surface. *Phys. Rev. Lett.* **87**, 156103.
- Christl I. and Kretzschmar R. (1999) Competitive sorption of copper and lead at the oxide-water interface: Implications for surface site density. *Geochim. Cosmochim. Acta* **63**, 2929–2938. Available at: <http://www.sciencedirect.com/science/article/pii/S0016703799002665>.
- Eikenberry E. F., Brönnimann C., Hülsen G., Toyokawa H., Horisberger R., Schmitt B., Schulze-Briese C. and Tomizaki T. (2003) PILATUS: a two-dimensional X-ray detector for macromolecular crystallography. *Nucl. Instruments Methods Phys. Res. Sect. A Accel. Spectrometers, Detect. Assoc. Equip.* **501**, 260–266.
- Escobar G. P., Beroy A. Q., Iritia M. P. P. and Huerta J. H. (2004) Kinetic study of the combustion of methyl-ethyl ketone over α -hematite catalyst. *Chem. Eng. J.* **102**, 107–117. Available at: <http://www.sciencedirect.com/science/article/pii/S1385894703002730>.
- Fenter P. A. (2002) X-ray Reflectivity as a Probe of Mineral-Fluid Interfaces: A User Guide. *Rev. Mineral. Geochemistry* **49**, 149–221. Available at: <http://ring.geoscienceworld.org/content/49/1/149.short>.
- Finger L. W. and Hazen R. M. (1980) Crystal structure and isothermal compression of Fe₂O₃, Cr₂O₃, and V₂O₃ to 50 kbars. *J. Appl. Phys.* **51**, 5362–5367.

- Geissbühler P., Fenter P., DiMasi E., Srajer G., Sorensen L. B. and Sturchio N. C. (2004) Three-dimensional structure of the calcite--water interface by surface X-ray scattering. *Surf. Sci.* **573**, 191–203.
- Ha J., Trainor T. P., Farges F. and Brown G. E. J. (2009) Interaction of Aqueous Zn(II) with Hematite Nanoparticles and Microparticles. Part 1. EXAFS Study of Zn(II) Adsorption and Precipitation. *Langmuir* **25**, 5574–5585.
- Heberling F., Trainor T. P., Lützenkirchen J., Eng P., Denecke M. A. and Bosbach D. (2011) Structure and reactivity of the calcite--water interface. *J. Colloid Interface Sci.* **354**, 843–857. Available at: <http://www.sciencedirect.com/science/article/pii/S0021979710012336>.
- Henderson M. A., Joyce S. A. and Rustad J. R. (1998) Interaction of water with the (1×1) and (2×1) surfaces of α -Fe₂O₃(0 1 2). *Surf. Sci.* **417**, 66–81. Available at: <http://www.sciencedirect.com/science/article/pii/S0039602898006621>.
- Lenhart J. J., Bargar J. R. and Davis J. A. (2001) Spectroscopic Evidence for Ternary Surface Complexes in the Lead(II)–Malonic Acid–Hematite System. *J. Colloid Interface Sci.* **234**, 448–452. Available at: <http://www.sciencedirect.com/science/article/pii/S0021979700973454>.
- Ling Y., Wang G., Wheeler D. A., Zhang J. Z. and Li Y. (2011) Sn-Doped Hematite Nanostructures for Photoelectrochemical Water Splitting. *Nano Lett.* **11**, 2119–2125.
- Lo C. S., Tanwar K. S., Chaka A. M. and Trainor T. P. (2007) Density functional theory study of the clean and hydrated hematite (1-102) surfaces. *Phys. Rev. B* **75**, 75425. Available at: <http://link.aps.org/doi/10.1103/PhysRevB.75.075425>.
- Madden A. S. and Hochella M. F. (2005) A test of geochemical reactivity as a function of mineral size: Manganese oxidation promoted by hematite nanoparticles. *Geochim. Cosmochim. Acta* **69**, 389–398.
- Marcus Y. (2009) Effect of ions on the structure of water: structure making and breaking. *Chem. Rev.* Available at: <http://pubs.acs.org/doi/pdf/10.1021/cr8003828> [Accessed November 22, 2015].
- Muhler M., Schütze J., Wesemann M., Rayment T., Dent A., Schlögl R. and Ertl G. (1990) The nature of the iron oxide-based catalyst for dehydrogenation of ethylbenzene to styrene: I. Solid-state chemistry and bulk characterization. *J. Catal.* **126**, 339–360. Available at: <http://www.sciencedirect.com/science/article/pii/0021951790900033>.
- Oliveira Jr. O. N., Riul Jr. A. and Leite V. B. P. (2004) Water at interfaces and its influence on the electrical properties of adsorbed films. *Brazilian J. Phys.* **34**, 73–83. Available at: http://www.scielo.br/scielo.php?script=sci_arttext&pid=S0103-97332004000100011&lng=en&nrm=iso&tlng=en [Accessed November 18, 2015].
- Pauling L. (1929) The principles determining the structure of complex ionic crystals. *J. Am. Chem. Soc.* **51**, 1010–1026.
- Robinson I. K. (1986) Crystal truncation rods and surface roughness. *Phys. Rev. B* **33**, 3830–3836. Available at: <http://link.aps.org/doi/10.1103/PhysRevB.33.3830>.

- Schleppütz C. M., Herger R., Willmott P. R., Patterson B. D., Bunk O., Brönnimann C., Henrich B., Hülsen G. and Eikenberry E. F. (2005) Improved data acquisition in grazing-incidence X-ray scattering experiments using a pixel detector. *Acta Crystallogr. Sect. A Found. Crystallogr.* **61**, 418–425.
- Sharghi H., Jokar M., Doroodmand M. M. and Khalifeh R. (2010) Catalytic Friedel–Crafts Acylation and Benzoylation of Aromatic Compounds Using Activated Hematite as a Novel Heterogeneous Catalyst. *Adv. Synth. Catal.* **352**, 3031–3044. Available at: <http://dx.doi.org/10.1002/adsc.201000319>.
- Sivula K., Zboril R., Le Formal F., Robert R., Weidenkaff A., Tucek J., Frydrych J. and Gratzel M. (2010) Photoelectrochemical Water Splitting with Mesoporous Hematite Prepared by a Solution-Based Colloidal Approach. *J. Am. Chem. Soc.* **132**, 7436–7444.
- Tamboli S. H., Rahman G. and Joo O.-S. (2012) Influence of potential, deposition time and annealing temperature on photoelectrochemical properties of electrodeposited iron oxide thin films. *J. Alloys Compd.* **520**, 232–237. Available at: <http://www.sciencedirect.com/science/article/pii/S092583881200076X>.
- Tanwar K. S., Catalano J. G., Petitto S. C., Ghose S. K., Eng P. J. and Trainor T. P. (2007a) Hydrated α -Fe₂O₃ surface structure: Role of surface preparation. *Surf. Sci.* **601**, L59–L64.
- Tanwar K. S., Lo C. S., Eng P. J., Catalano J. G., Walko D. A., Brown G. E. J., Waychunas G. A., Chaka A. M. and Trainor T. P. (2007b) Surface diffraction study of the hydrated hematite surface. *Surf. Sci.* **601**, 460–474. Available at: <http://www.sciencedirect.com/science/article/pii/S0039602806010739>.
- Tilley S. D., Cornuz M., Sivula K. and Gratzel M. (2010) Light-Induced Water Splitting with Hematite: Improved Nanostructure and Iridium Oxide Catalysis. *Angew. Chemie, Int. Ed.* **49**, 6405–6408.
- Trainor T. P., Chaka A. M., Eng P. J., Newville M., Waychunas G. A., Catalano J. G. and Brown G. E. J. (2004) Structure and reactivity of the hydrated hematite (0001) surface. *Surf. Sci.* **573**, 204–224. Available at: <http://www.sciencedirect.com/science/article/pii/S0039602804012531>.
- Trainor T. P., Eng P. J. and Robinson I. K. (2002) Calculation of crystal truncation rod structure factors for arbitrary rational surface terminations. *J. Appl. Crystallogr.* **35**, 696–701. Available at: <http://dx.doi.org/10.1107/S0021889802013985>.
- Vlieg E. (2000) ROD: a program for surface X-ray crystallography. *J. Appl. Crystallogr.* **33**, 401–405. Available at: <http://dx.doi.org/10.1107/S0021889899013655>.
- Waychunas G. A., Kim C. S. and Banfield J. F. (2005) Nanoparticulate iron oxide minerals in soils and sediments: unique properties and contaminant scavenging mechanisms. *J. Nanoparticle Res.* **7**, 409–433.
- You H. (1999) Angle calculations for a 4S+2D six-circle diffractometer. *J. Appl. Crystallogr.* **32**, 614–623.

Table 2.1 Best fit parameters based on CTR analysis of multi-unit cell model structure

Layer	el	x	y	z	Δx (Å)	Δy (Å)	Δz (Å)	B_{iso} (Å ²)	Occ
Half layer termination surface with weight of 8% (-3%, +2%)									
Layer-i2	O	0.763	0.225	1.312	(-1E-1, 1E-1)	(-2E-1, 6E-1)	(-9E-1, 5E-2)	0.81(-1E-2,9E0)	0.27(-3E-1,3E-1)
	O	0.737	0.725	1.312	(-1E-1, 1E-1)	(-2E-1, 6E-1)	(-9E-1, 5E-2)	0.81(-1E-2,9E0)	0.27(-3E-1,3E-1)
Layer-i1	O	0.173	0.571	1.147	(-4E-2, 5E-2)	(-9E-1, 4E-2)	(-3E-1, 1E-1)	0.82(-2E-2,9E0)	0.60(-5E-1,1E-3)
	O	0.327	1.071	1.147	(-5E-2, 4E-2)	(-9E-1, 4E-2)	(-3E-1, 1E-1)	0.82(-2E-2,9E0)	0.60(-5E-1,1E-3)
Layer-2	O	0.672	0.944	0.911	0.097 (-2E-1, 1E-1)	-0.157 (-6E-2, 3E-1)	0.060 (-2E-1, 1E-1)	0.40	1.00
	O	0.828	0.444	0.911	-0.097 (-2E-1, 1E-1)	-0.157 (-6E-2, 3E-1)	0.060 (-2E-1, 1E-1)	0.40	1.00
Layer-4	O	0.298	0.608	0.775	-0.039 (-1E-1, 9E-2)	0.016 (-2E-1, 2E-1)	0.182 (-3E-1, 4E-2)	0.40	1.00
	O	0.202	0.107	0.775	0.039 (-1E-1, 9E-2)	0.016 (-2E-1, 2E-1)	0.182 (-3E-1, 4E-2)	0.40	1.00
Layer-5	Fe	0.513	0.868	0.670	-	-	0.182 (-4E-2, 8E-3)	0.32	1.00
	Fe	-0.013	0.367	0.670	-	-	0.182 (-4E-2, 8E-3)	0.32	1.00
Layer-6	O	0.847	0.737	0.613	-	-	0.120 (-3E-2, 3E-3)	0.40	1.00
	O	0.653	0.236	0.613	-	-	0.120 (-3E-2, 3E-3)	0.40	1.00
Layer-7	O	0.347	0.904	0.393	-	-	-0.077 (-4E-2, 4E-2)	0.40	1.00
	O	0.153	0.403	0.393	-	-	-0.077 (-4E-2, 4E-2)	0.40	1.00
Layer-8	Fe	0.000	0.761	0.371	-	-	0.115 (-2E-2, 2E-3)	0.32	1.00
	Fe	0.500	0.260	0.371	-	-	0.115 (-2E-2, 2E-3)	0.32	1.00
Long full layer termination surface with weight of 13.5% (-3%, +2%)									
Layer-i2	O	0.368	0.583	1.436	(-3E-2, 3E-2)	(-4E-2, 3E-2)	(-4E-2, 1E-1)	4.03(-3E0, 6E0)	0.40(-2E-1, 2E-1)
	O	0.132	1.083	1.436	(-3E-2, 3E-2)	(-4E-2, 3E-2)	(-4E-2, 1E-1)	4.03(-3E0, 6E0)	0.40(-2E-1, 2E-1)
Layer-i1	O	0.655	0.959	1.281	(-3E-2, 2E-2)	(-3E-2, 2E-2)	(-5E-2, 2E-1)	8.60(-8E0, 1E0)	0.13(-1E-1, 1E-1)
	O	0.845	1.459	1.281	(-2E-2, 3E-2)	(-3E-2, 2E-2)	(-5E-2, 2E-1)	8.60(-8E0, 1E0)	0.13(-1E-1, 1E-1)
Layer-1	O	0.122	0.831	1.113	-0.155 (-5E-2, 5E-2)	0.134 (-1E-1, 8E-2)	0.117 (-6E-2, 2E-2)	0.40	1.00
	O	0.378	0.331	1.113	0.155 (-5E-2, 5E-2)	0.134 (-1E-1, 8E-2)	0.117 (-6E-2, 2E-2)	0.40	1.00
Layer-2	O	0.657	0.997	0.903	0.022 (-4E-2, 3E-2)	0.133 (-5E-2, 7E-2)	-0.002 (-4E-2, 4E-2)	0.40	1.00
	O	0.843	0.497	0.903	-0.022 (-4E-2, 3E-2)	0.133 (-5E-2, 7E-2)	-0.002 (-4E-2, 4E-2)	0.40	1.00
Layer-3	Fe	0.000	0.829	0.850	-	-	-0.034 (-1E-2, 2E-2)	0.32	1.00
	Fe	0.500	0.329	0.850	-	-	-0.034 (-1E-2, 2E-2)	0.32	1.00

Table 2.1 Continued

Layer-4	O	0.306	0.605	0.742	-	-	-0.062 (-3E-2, 4E-2)	0.40	1.00
	O	0.194	0.104	0.742	-	-	-0.062 (-3E-2, 4E-2)	0.40	1.00
Layer-5	Fe	0.500	0.880	0.647	-	-	0.017 (-1E-2, 1E-2)	0.32	1.00
	Fe	0.000	0.379	0.647	-	-	0.017 (-1E-2, 1E-2)	0.32	1.00
Layer-6	O	0.847	0.737	0.595	-	-	-0.014 (-2E-2, 4E-2)	0.40	1.00
	O	0.653	0.236	0.595	-	-	-0.014 (-2E-2, 4E-2)	0.40	1.00

The coordinates are fractional based on the re-indexed unit cell parameters ($a=5.038 \text{ \AA}$, $b=5.434 \text{ \AA}$, $c=7.3707 \text{ \AA}$, $\alpha=90^\circ$, $\beta=90^\circ$, $\gamma=90^\circ$). Δx , Δy , and Δz are atomic displacements in \AA along directions of \mathbf{a}_s axis, \mathbf{b}_s axis, and \mathbf{c}_s axis respectively. The B_{iso} are isotropic Debye-Waller factors and Occ are occupancy parameters. The occupancies of all surface atoms were fixed at 100% in each individual domain with the domain weight being optimized during the modeling. Numbers inside a parenthesis are the ranges of errors for the best fit parameter values calculated at a 95% confidence level. Note that those errors written in scientific notation do not follow a normal distribution, which is an intrinsic feature for the differential evolution algorithm. Note the results for the short full layer termination (domain weight=28.5%) was not listed in the table, since the short full layer termination is symmetrically related to the long full layer termination via glide plane symmetry, as detailed in text. In addition, each termination surface mentioned above has a symmetry related termination on the symmetry related domain with equal weights, which were not listed either. Layer-i1 and Layer-i2 are two interfacial water layers on top of each termination surface. The best fit water positions are based on the 2.75 \AA O-O cutoff limit.

Table 2.2 Comparison of atom relaxations and layer spacings (in Å) for top six atom layers in the full layer termination surface structure based on results from three different studies

Layers	This study			Tanwar's study			Catalano's Study
	dx	dy	dz	dx	dy	dz	dz
Layer-1 O	-0.16(0.05)	0.13(-0.10,0.08)	0.12(-0.06, 0.02)	-0.12(0.35)	0.29(0.16)	0.16(0.05)	-0.02(0.1)
Layer-2 O	0.02(-0.04,0.03)	0.13(-0.05,0.07)	0.00(0.04)	0.04(0.05)	0.03(0.05)	-0.03(0.07)	0.02(0.3)
Layer-3 Fe	-	-	-0.03(-0.01, 0.02)	0.00(0.20)	-0.06(0.22)	0.01(0.05)	0.00(0.07)
Layer-4 O	-	-	-0.06(-0.03,0.04)	0.00(0.30)	-0.03(0.27)	-0.01(0.05)	-0.16(0.1)
Layer-5 Fe	-	-	0.02(0.01)	0.00(0.05)	0.00(0.05)	-0.02(0.03)	-0.03(0.06)
Layer-6 O	-	-	-0.01(-0.02,0.04)	0.04(0.15)	-0.04(0.11)	-0.05(0.06)	-0.03(0.06)
Layer spacings	Ideal layer spacing (L)		dL (This study)	dL (Tanwar's study)		dL (Catalano's study)	
Layer 1-2 (O-O)	1.42		0.12(-0.10, 0.06)	0.19(0.12)		-0.04(0.40)	
Layer 2-3 (O-Fe)	0.35		0.03(-0.06, 0.05)	-0.04(0.12)		0.02(0.37)	
Layer 3-4 (Fe-O)	0.78		0.03(-0.05, 0.05)	0.02(0.10)		0.16(0.17)	
Layer 4-5 (O-Fe)	0.78		-0.08(-0.04, 0.05)	0.01(0.08)		-0.13(0.16)	
Layer 5-6 (Fe-O)	0.35		0.03(-0.05, 0.03)	0.03(0.09)		0.00(0.12)	

Note the model uncertainties are listed inside the parenthesis. The uncertainty with a single value means that the error follows a symmetric normal distribution, while an uncertainty defined with two numbers (in this study) indicates that the model error follows an asymmetric distribution with the boundaries defined by those two numbers.

Table 2.3 Results of bond valence analysis on the ideal and the best fit model structure

	Layer-1	Layer-2	Layer-3	Layer-4	Layer-5
FLT surface					
Surface species	^I O	^{III} O	^{VI} Fe	^{IV} O	^{VI} Fe
Ideal structure	0.60	1.37	2.95	1.98	2.96
Best fit model	0.48	1.40	2.89	2.03	2.98
Protonation scheme	2H (0.76)	1H (0.68)	-	-	-
Bond valence sum	2.00	2.08	2.89	2.03	2.98
HLT surface					
Surface species	x	^I O	x	^{II} O	^{VI} Fe
Ideal structure	x	0.38	x	0.99	2.96
Best fit model	x	0.53	x	0.93	2.82
Protonation scheme	x	2H (0.74)	x	1H+1HB(0.87+0.20)	-
Bond valence sum	x	2.00	x	2.00	2.82

The protonation scheme was assigned to those under-saturated oxygen groups by assuming the contribution of the valence (0.68-0.88 v.u.) and (0.13-0.25 v.u.) from a covalent hydrogen bond (H) and a weak hydrogen bond (HB), respectively, as suggested by Bargar et al. (Bargar et al., 1997).

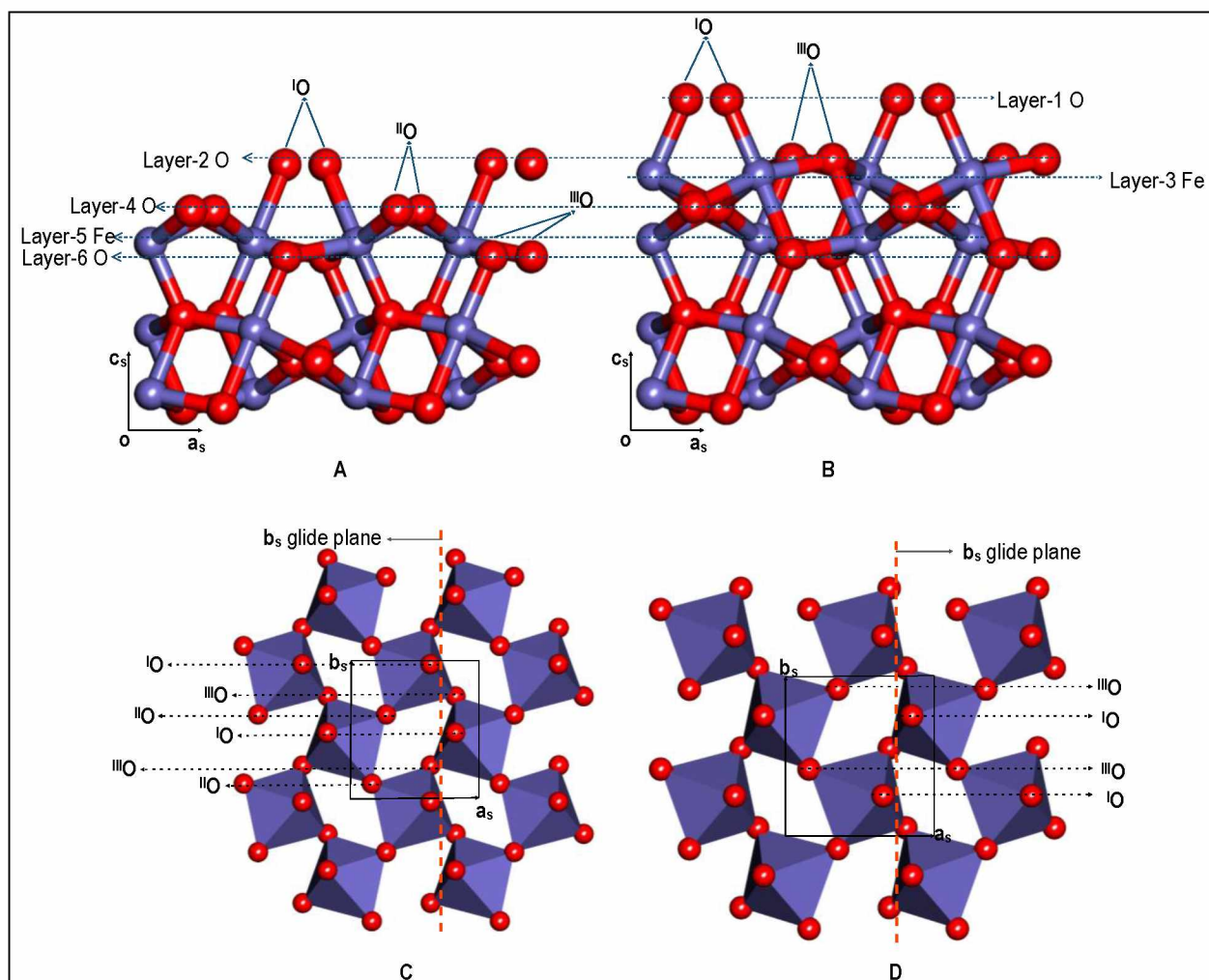


Figure 2.1 Comparison of surface functional groups in the half layer termination (A, C) and the full layer termination (B, D) from both the side view (A, B) and the top view (C, D). Note that each atom layer was uniquely labeled as “*Layer- n M* ”, where n represents the layer number, and M represents for the associated element symbol (either Fe or O). Left superscripts on the labeled oxygens indicate the iron coordination numbers. Red balls are oxygen atoms, while blue balls are iron atoms. The surface-layer iron atoms are shown in octahedrons with the rest not shown for clarity in the top-view surface structures. The position of the b_s glide plane symmetry is highlighted in both surface terminations.

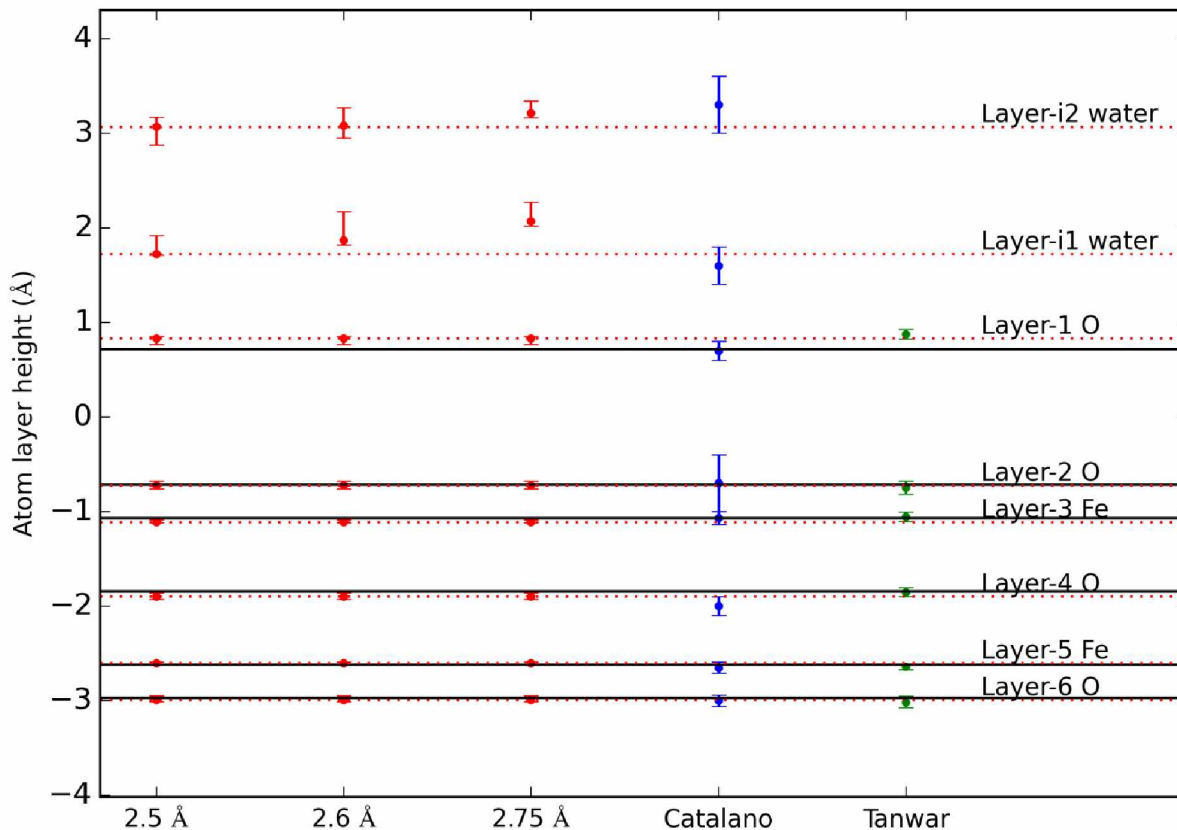


Figure 2.2 Comparison of layer heights from the present study under different O-O separation cutoff limits (red solid circle) to the other two studies by Catalano et al. (Catalano et al., 2007a) (blue solid circle) and Tanwar et al. (Tanwar et al., 2007a) (green solid circle). The uncertainties were illustrated as error bars for each point. The black solid lines show the atom layer heights in the ideal surface structure. The red dot lines are drawn based on the results from the current study at 2.5 Å O-O separation cutoff limit for comparison purpose.

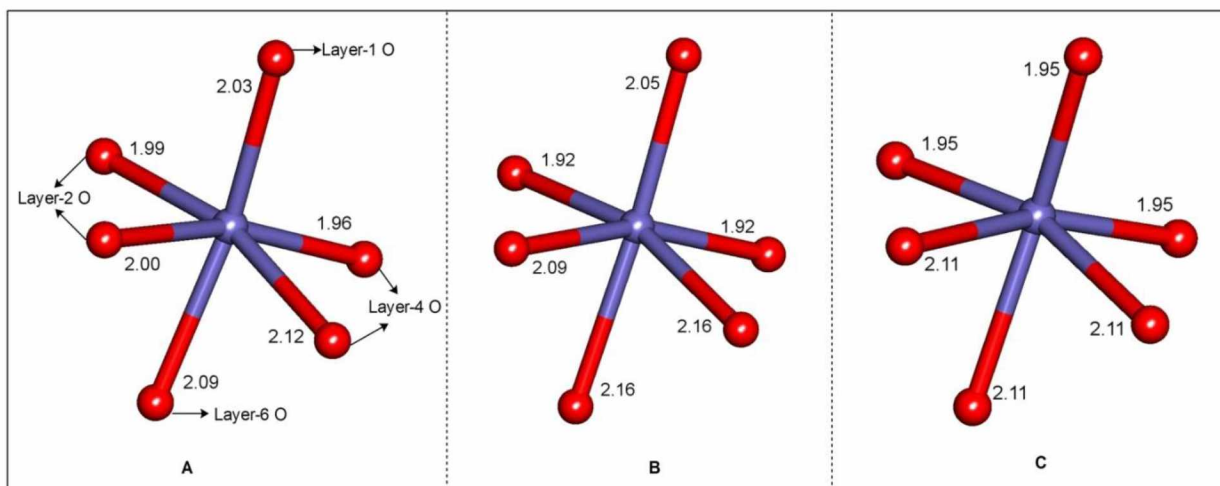


Figure 2.3 Comparison of the top layer Fe (Layer-3 Fe) local structure derived from this study (A), Tanwar's study (B) and the ideal case (C). The Fe atoms are represented as blue spheres, while the O atoms are red spheres. The numbers are the associated bond lengths in Å.

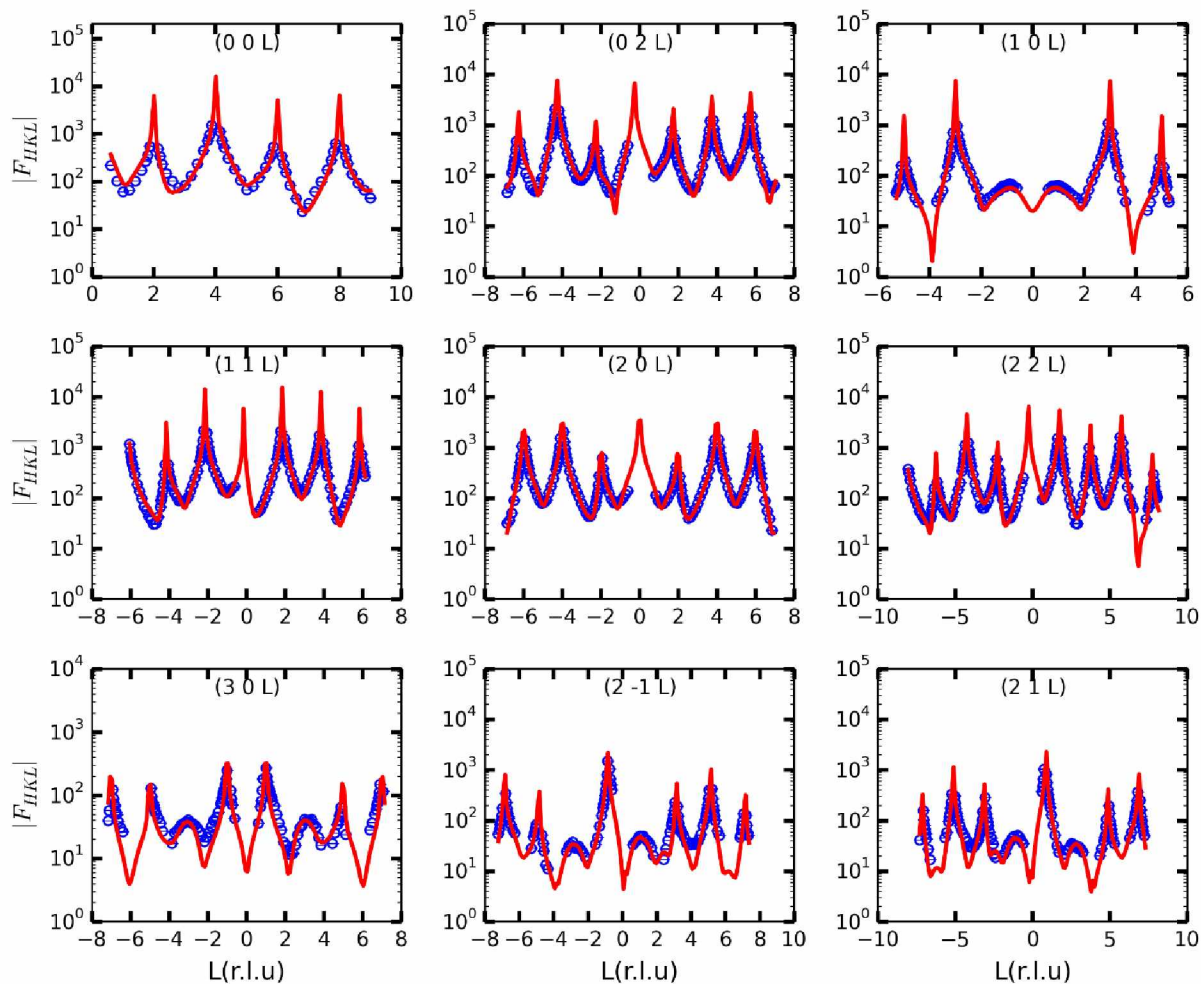


Figure 2.4 Experimental structure factors (blue open circles) (F_{HKL}) as a function of perpendicular momentum transfer (L , in reciprocal lattice units) for the hematite ($1\bar{1}02$) surface annealed at 550°C in air for 24 hours. The red solid lines represent the calculated CTR profiles based on the best fit structural model containing interfacial water structure (2.75 \AA cutoff for O-O separations).

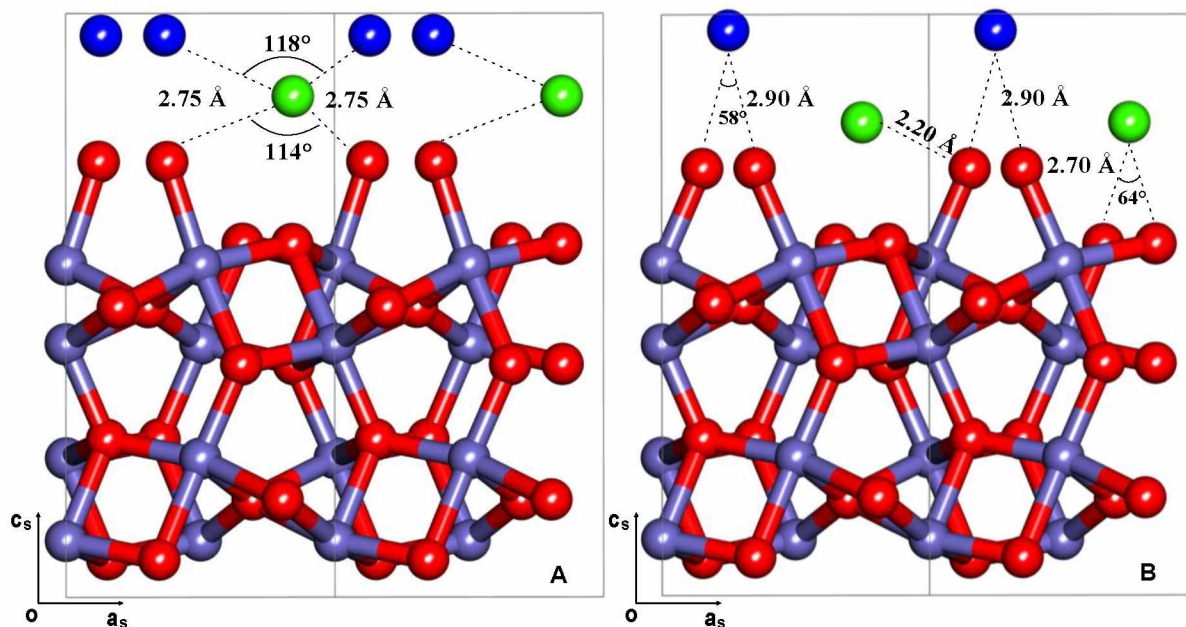


Figure 2.5 Interfacial water structure of the full layer termination surface based on the best fit model structure with 2.75 Å O-O separation cutoff limit (A). As a comparison, the interfacial water structure proposed by Catalano et al. (Catalano et al., 2007a) is also presented (B). Note the dashed lines represent the possible H-bond network according to the associated O-O separations that are shown as well. The O-O_{water}-O angles are shown to compare the distortion of the tetrahedral H-bonded water structure. The interfacial structure contains two adsorbed water layers (1st layer in green ball and 2nd layer in blue balls), surface O atoms (red balls) and Fe atoms (blue balls).

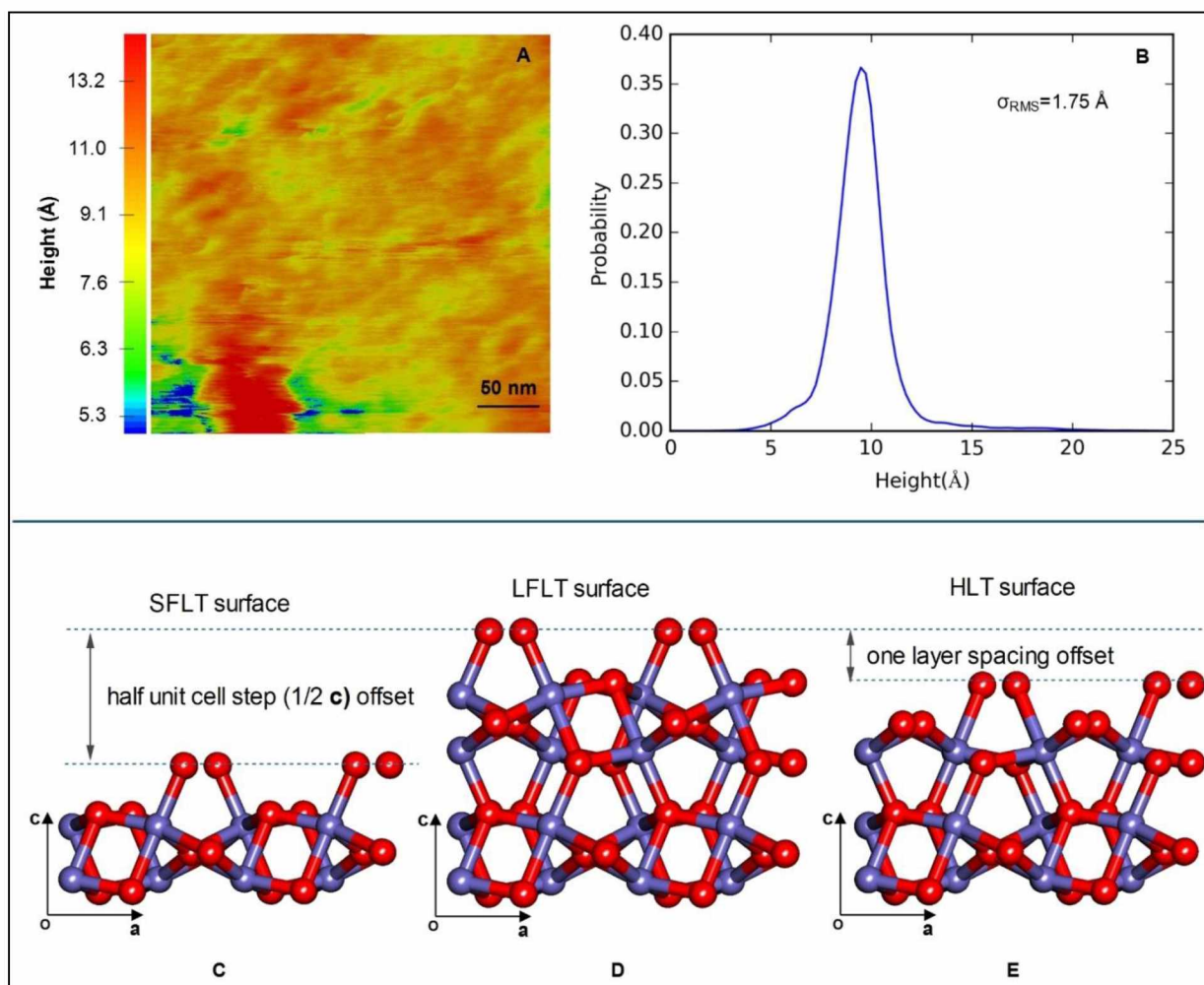


Figure 2.6 AFM image of annealed hematite surface (A) and the step heights distribution profile based on the AFM image (B). The calculated root-mean-square surface roughness is 1.75 Å. Although it is impossible to directly map the surface terminations (C, D, E) to the AFM images due to the lateral resolution of AFM measurement, the roughness calculated from the best fit CTR structural model containing three different termination surfaces is at first approximation in good agreement with the value calculated based on AFM data (see text for detail).

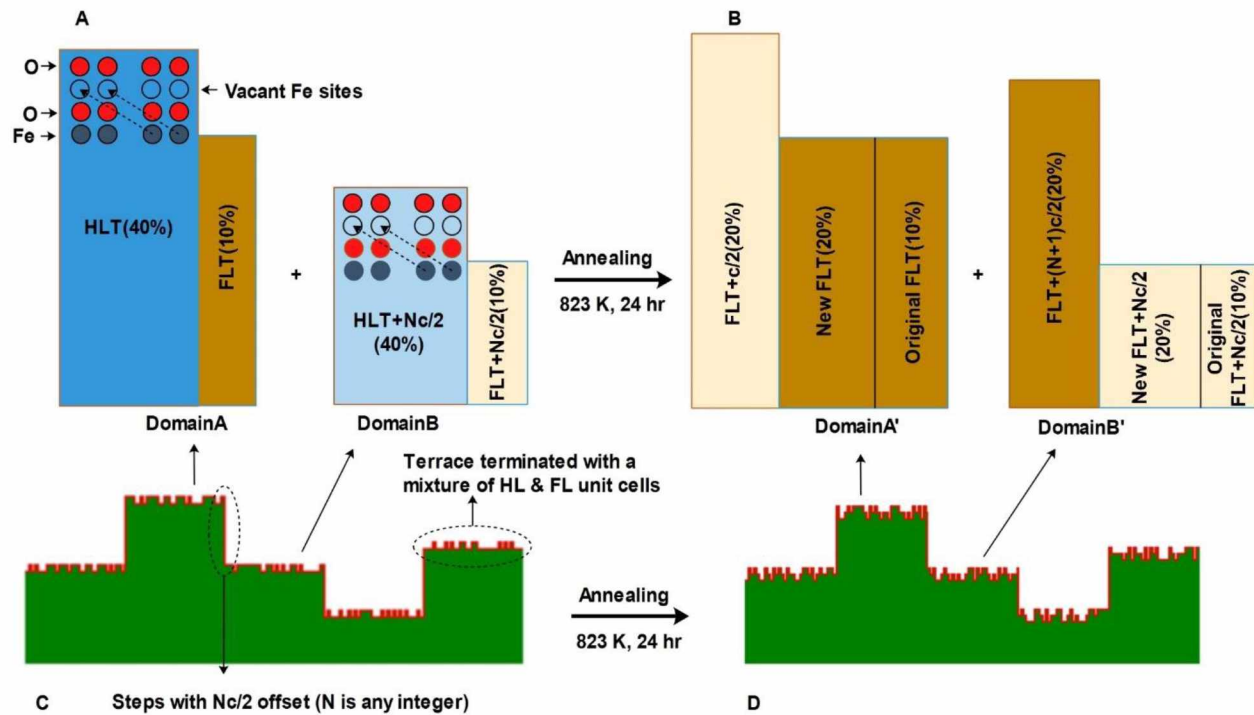


Figure 2.7 A schematic diagram of the mechanism of surface termination transformation from the HLT to the FLT when the hematite ($1\bar{1}02$) is annealed in air. In this diagram, the surface termination of the same type (chemically and crystallographically equivalent) are painted in the same color. The initial weight in percentage of each termination surface is arbitrary and we assume a 100% conversion of the HLT to the FLT for simplicity. The surface termination pattern of a CMP-prepared surface is illustrated as Panel A, where two symmetry related domains are present in an equal weight. The top four atom layers are shown to illustrate the atom rearrangement during annealing. The projection of Layer-5 Fe to occupy the Layer-3 vacant Fe sites leads to the termination transformation, which produces a long FLT and a short FLT with an equal weight (20%), as shown in Panel B. Note that although the surface termination transformation result in an unequal weight for two types of FLT on each domain, the total weight of each type of FLT is equivalent to each other when the summation is performed over two symmetry domains. Our best fit structure model supports a surface morphology, which is characterized by the presence of domains, which are separated by steps with $Nc/2$ offset (N is any integer, and c is the lattice parameter), as illustrated in Panel C and Panel D. On each domain, there are multiple surface terminations with characteristic termination heights. After the surface termination transformation, the domain feature does not change but the surface morphology within each domain becomes more complicated due to the appearance of the third type of surface termination (long FLT), as shown in Panel D. The rule for summing over the structure factors within domain size follows coherent addition while the structure factors over the domain size are summed up based on incoherent addition rule.

Chapter 3 Structural Study of the Surface Complexation of Pb(II) on the Hydrated Hematite ($1\bar{1}02$) Surface¹

Abstract

A structural study of the surface complexation of Pb(II) on the ($1\bar{1}02$) surface of hematite was undertaken using crystal truncation rod X-ray diffraction (CTR) under *in situ* conditions. The best fit model indicates that the substrate surface consists of 71% half layer termination (HLT) and 29% full layer termination (FLT), consistent with the results reported in a previous CTR study on a clean hematite ($1\bar{1}02$) surface. The sorbed Pb was found to be bound at two types of edge-sharing sites on the HLT surface in an inner-sphere binding mode. The best fit structural model resulted in a distorted trigonal pyramid local structure with an average Pb-O bond length of $\sim 2.26 \text{ \AA}$ and two characteristic Pb-Fe separations of 3.32 \AA and 3.64 \AA , respectively, in good agreement with previous XAFS studies. In light of the site multiplicity on the HLT, Pb(II) exhibited a selectivity for edge-sharing binding sites implying a difference in reactivity of potential surface sites. In addition, a site coverage simulation test was developed to predict the site coverage as a function of sorbate-sorbate distance. The simulation results give rise to a realistic Pb-Pb distance (5.42 \AA) with the simulated site coverage best matching the CTR-derived occupancy. Based on the structural results we proposed a stoichiometry of the surface complexation reaction of Pb(II) on the hematite ($1\bar{1}02$) surface and used bond valence analysis to assign the protonation schemes of surface oxygens. The surface reaction

¹ Qiu C., Majs F., Eng P. J., Stubbs J. and Trainor T. P. (2015) Structural Study of the Surface Complexation of Pb(II) on the Hydrated Hematite ($1\bar{1}02$) Surface. Prepared for submission to *Geochimica et Cosmochimica Acta*.

stoichiometry reveals that the primary source of proton release in the course of surface complexation is due to the deprotonation of the Pb-bound ^1O group as well as the hydrolysis of the distal oxygen.

3.1 Introduction

Surface complexation reactions occurring at the mineral water interface are a key process controlling the fate and dispersion of trace metals in the environment (Stumm et al., 1976; Davis and Leckie, 1978; Dzombak and Morel, 1990; Robertson and Leckie, 1997; Wang et al., 1997; Koretsky, 2000). Iron-(oxyhydr)oxides are ubiquitous in the environment and usually of high specific surface area with abundant reactive sites capable of binding aqueous metal species (McKenzie, 1980; Cornell and Schwertmann, 2003), and hence are among the most important environmental substrates. The reactivity of a particular mineral surface is largely dependent upon both the composition and structure of the surface, the latter being dictated by the type(s) of the growth, cleavage or fracture surfaces, the stoichiometry of the termination and other factors such as steric effects associated with a given surface structure. Therefore, understanding the reactivity of a mineral surface relies on a detailed knowledge of molecular scale surface structure. This information however is generally limited due to the difficulty in probing surface structure directly using traditional experimental approaches.

Environmental Pb contamination is of serious environmental concern due to its notorious toxic effect on a diversity of organisms (Goyer, 1993; Verma and Dubey, 2003). Sources of Pb include the historic usage as an anti-knocking fuel additive (Nriagu, 1990) and Pb pigment in paints (Sandalinas et al., 2006) and its current application seen widely in the battery industry (Piper and Restrepo, 2013) and the manufacture of ammunition (Scheuhammer and Norris, 1995;

Lin, 1996; Craig et al., 1999). The environmental concerns of Pb comes from its potential mobility under a variety of geochemical conditions (Lee et al., 1997; Jordan et al., 1997; Smuda et al., 2007). To better model the environmental fate and transport of Pb, we need to fully characterize the surface complexation of Pb at mineral-water interface that serves as a major mechanism for reducing Pb contamination (Brown, 2001; Brown and Sturchio, 2002).

To date, there have been extensive reports of Pb(II) adsorption on a variety of iron-(oxyhydr)oxides under different experimental conditions. The majority of the published results have focused on Pb(II) sorption behavior based on macroscale uptake experiments coupling with different surface complexation models (SCMs) (Müller and Sigg, 1992; Christl and Kretzschmar, 1999; Villalobos et al., 2001; Dyer et al., 2003; Trivedi et al., 2003; Villalobos and Pérez-Gallegos, 2008; Serrano et al., 2009; Gustafsson et al., 2011). In those published results, there is a general consensus that Pb(II) binding on different substrates occurs via an inner-sphere mode. However, details of the binding configuration and stoichiometry diverge widely among different studies. It is not surprising to see the discrepancy of surface binding configurations proposed from different studies, since a lack of structural constraints would result in non-unique descriptions of the data, as often found in previous studies (Christl and Kretzschmar, 1999; Reich et al., 2010; Gustafsson et al., 2011).

A variety of approaches have been used to add structural constraints to better describe sorption reactions, such as X-ray absorption fine structure (XAFS) spectroscopy (Koningsberger and Prins, 1988; Brown et al., 1995), Fourier transform infrared spectroscopy (FTIR) (Lefevre, 2004) and computation methods, like density functional theory (DFT) (Parr, 1983). XAFS spectroscopy is a powerful tool which provides the information of the local structure of the central element and therefore is widely used to derive the binding structures of surface complex

species. To date, numerous XAFS studies have been reported to investigate the sorption of Pb(II) on different substrates under wide environmental conditions, and those studies suggested that Pb(II) sorption on different substrate surface occurs in an inner-sphere mode, consistent with results based on macroscale batch experiment results mentioned above. In addition, it was also found that detailed binding configurations of Pb surface complex are related to solution pH. For example, Ostergren et al. (Ostergren et al., 2000b) investigated Pb(II) adsorption on the goethite surface, and they derived a surface Pb complex structure in a bidentate edge-sharing binding mode over a pH range from pH 5.0 to pH 7.0. In addition, their findings also suggested the presence of a new type of Pb surface species with a bidentate corner-sharing structure at pH 5.0. Such a pH dependence of the surface binding configuration was observed in another XAFS study using a ferrihydrite substrate (Trivedi et al., 2003). The bidentate edge-sharing binding structure at relatively higher pH was also confirmed in an earlier XAFS study by Bargar et al. (Bargar et al., 1997b), who investigated the Pb(II) adsorption on both goethite and hematite powder over a solution pH range from pH 6.0 to pH 8.0. The underlying mechanism for the pH dependence of Pb surface complex binding structure was unclear, although Ostergren et al. (Ostergren et al., 2000b) claimed that it could be due to the distinct proton affinity of different types of surface functional groups. Besides the solution pH, the presence of anionic ligands, including the phosphate (Tiberg et al., 2013), sulfate (Ostergren et al., 2000a), carbonate (Ostergren et al., 2000b) and chloride (Bargar et al., 1998), were also found to change the surface binding configuration through the formation of ternary surface complexes, which were observed to exert a synergistic effect on Pb(II) uptake on mineral surfaces.

Using XAFS spectroscopy, great improvements have been achieved in the understandings of surface binding configurations of Pb(II) on different substrates. However, the ability to uniquely

derive the stoichiometries of surface complexation reactions using XAFS spectroscopy is limited when there are potentially multiple surface sites exposed at a mineral surface with similar plausible binding configurations. In addition, the XAFS spectra is only sensitive to the local structure of the surface complex but insensitive to the structure of the substrate itself, which is subject to relaxation / modification to different extents depending on the physical/chemical history on the substrate surface (Eng et al., 2000; Park and Sposito, 2002; Trainor et al., 2002a; Geissbühler et al., 2004; Trainor et al., 2004; Catalano et al., 2007; Tanwar et al., 2007a; Fukuma et al., 2010; Ghose et al., 2010; Heberling et al., 2011). Therefore, in order to develop a unique set of surface complexation reaction stoichiometries, and examine the structure reactivity relationship, it requires knowledge of the interfacial structure including the binding configuration of the sorbate as well as the substrate surface structure. Crystal truncation rod (CTR) X-ray diffraction provides such capability when it is used to probe single crystal samples (Robinson and Tweet, 1992). To date, CTR has been used to investigate the surface structure of numerous (hydr)oxides in the presence of water (liquid form or water vapor), including the hematite ($1\bar{1}02$) (Catalano et al., 2007; Tanwar et al., 2007(a, b)), hematite (0001) (Trainor et al., 2004), corundum (Eng et al., 2000; Catalano, 2010), goethite (Ghose et al., 2010), calcite (Geissbühler et al., 2004; Heberling et al., 2011), and mica (Park and Sposito, 2002). The characterization of the surface structure of hydrated oxide samples provides the basis to extend the structural study from a clean surface to a surface reacted with aqueous ions, like heavy metals.

In the present paper, CTR diffraction was utilized to investigate the adsorption of Pb(II) on the hematite ($1\bar{1}02$) surface. Hematite was chosen, since it serves as a model substrate with similar types of surface functional groups as those exposed on other common forms of iron-(oxyhydr)oxides, such as goethite, lepidocrocite, and ferrihydrite, which play a key role in a

diversity of biogeochemical processes at the Earth's surface (Cornell and Schwertmann, 2003). The surface structure of the hydrated hematite ($1\bar{1}02$) has been well characterized using both theoretical and experimental approaches (Catalano et al., 2007; Tanwar et al., 2007(a, b); Lo et al., 2007). The choice of Pb(II) is due to its environmental concern as mentioned above. In addition, the adsorption of Pb(II) on different oxides has been extensively studied using XAFS spectroscopy, to which our results could be compared. By doing CTR analysis, we intend to provide a deeper insight into the metal adsorption mechanism on the hematite surface with a particular focus on the understandings of the relationship between the surface reactivity and the surface structure.

3.2 Methods and experiments

3.2.1 Sample preparations

A natural single crystal hematite (~2cm diameter) was oriented and cut parallel to the ($1\bar{1}02$) plane and grinded using a customized gig. Sample mis-cut is $<0.01^\circ$ based on the results of X-ray reflectivity measurements. The sample preparation protocol, based on a chemical mechanical polishing procedure (CMP), has been described by Tanwar et al. (Tanwar et al., 2007b). Briefly, the sample was first polished for 20 min using a commercial colloidal silica suspension (0.06 μm diameter) (TED PELLA, USA), which was buffered to pH 11.5 with NaOH. Then we switched to the raw colloidal silica suspension (pH 10.0) and continued polishing the surface for another 10 min. Following the polishing the sample is subject to a 1-hour base wash (crystal soaking in the NaOH solution of pH 10.5) and a 4-hour acid wash (crystal soaking in the HNO_3 solution of pH 2.0). Afterwards, the crystal was restored in de-ionized water before CTR measurements.

Metal solutions were prepared in a N₂ purged glove box to avoid CO₂ contamination. Reagent grade Pb(NO₃)₂ was dissolved in de-ionized water, which was de-gassed in advance by continual purge of pure N₂ (>99.999%) for 2 hours under a boiling condition. All metal solutions were diluted to 200 μM and carefully adjusted to pH 5.5(±0.1) using NaOH and HNO₃. Each metal solution was introduced to the hematite surface using a liquid cell designed for surface diffraction measurement. The liquid cell was described in detail elsewhere (Heberling et al., 2011). The thickness of water on top of the crystal surface was controlled by an adjustable gap between the crystal surface and a Kapton membrane. When the solution is first introduced a thick film (>5 mm) of solution was left atop the surface for 15 minutes. After this equilibration time the film thickness was reduced to several microns and maintained at this thickness throughout data collection. The quality of the liquid film was monitored through observing the film surface which should exhibit clear Newton's rings under visible light if the liquid film has a relatively uniform thickness. To avoid dehydration of the liquid film due to water escaping through the Kapton film, the liquid cell was capped with a Kapton dome that maintained a water-saturated He (relative humidity >90%) headspace.

3.2.2 CTR data collection

CTR measurements were performed at the bending magnet beamline 13BMC at the Advanced Photon Source (APS), Argonne National Laboratory. The energy of incoming X-ray beam was fixed at 13 keV by tuning the liquid nitrogen cooled double-crystal silicon (111) monochromator. The incoming beam was focused and collimated to 400 μm×250 μm using rhodium coated horizontal and the vertical mirrors and slits. A Kappa geometry Newport diffractometer (4S+2D) was used for sample and detector orientation with angles and

diffractometer coordinates defined according to You (You, 1999). X-ray intensity prior to the sample was monitored using a N₂ gas filled ion-chamber and scattered intensity was measured using a Dectris PILATUS 100K 2D pixel array detector with 195×487 pixels (vertical × horizontal) (Eikenberry et al., 2003). Nine CTRs, including the specular rod, were collected in order to probe both the lateral and vertical electron density of the surface. To collect non-specular CTR data, the incident angle of the beam relative to the sample surface was fixed at 2°, while an Omega scan was used to scan specular rod with the surface normal of the sample constrained to lie in the lab-frame horizontal plane.

The structure factor (magnitude) was extracted from each Pilatus image using the TDL software package (<http://cars9.uchicago.edu/ifeffit/tdl>). Each data point is subject to background subtraction, followed by corrections for active area, polarization, and Lorentz factors to account for the variance of the intercept between Ewald-sphere and the CTR as a function of Q according to the method by Schlepütz et al. (Schlepütz et al., 2005). Potential beam-induced damage to the sample surface was checked by repeating the collection of a CTR segment several times throughout the course of the measurements. We observed that “check rod” intensities remained within experimental errors indicative of no substantial surface damage.

3.2.3 Structure and termination of hematite ($1\bar{1}02$) surface

The structure of α -Fe₂O₃ (space group of R-3c) can be described in terms of a hexagonal close-packing of the oxygen with the iron occupying two-thirds of the octahedral holes. The lattice parameters of α -Fe₂O₃ (5.035 Å, 13.747 Å, 90°, 90°, 120°) as well as the bulk isotropic Debye-Waller factors have been reported previously (Finger and Hazen, 1980). The distortion of the octahedral structural unit in the bulk α -Fe₂O₃ structure produces two sets of Fe-O bond

lengths (1.95 Å and 2.11 Å). There are two dominant growth faces exposed on the natural α -Fe₂O₃ surface, the (0001) and (1 $\bar{1}$ 02) surface (Cornell and Schwertmann, 2003). The (1 $\bar{1}$ 02) surface, also named R-plane, could be denoted equivalently by the other two sets of miller indices in the hexagonal coordinate system: (01 $\bar{1}$ 2) and ($\bar{1}$ 012). For convenience, the hematite (1 $\bar{1}$ 02) surface can be re-indexed by defining a pseudo unit cell (5.038 Å, 5.434 Å, 7.3707 Å, 90°, 90°, 90°) as described in detail by Trainor et al. (Trainor, Eng and Robinson, 2002). The main advantage of the pseudo-cell is it places the c-axis parallel to the surface normal (\mathbf{c}_s), with the \mathbf{a}_s and \mathbf{b}_s axes defined within the plane of the surface. The re-indexed unit cell contains ten atom layers with a stoichiometric layer sequence of (O₂-Fe₂-O₂-Fe₂-O₂-O₂-Fe₂-O₂-Fe₂-O₂-R) along the \mathbf{c}_s axis, where **R** represents the stoichiometric (Fe₂O₃) repeat of the bulk material. The bottom five atom layers are symmetrically related to the top five layers via a glide plane (\mathbf{c}_s glide). Such a glide plane symmetry results in symmetry related surface terminations which are chemically equivalent but crystallographically distinct.

The surface termination of hematite (1 $\bar{1}$ 02) has been studied experimentally using hematite samples prepared under different conditions including ultra-high vacuum (UHV) annealing (Henderson et al., 1998), high temperature annealing in air (Catalano et al., 2007; Tanwar et al., 2007a) and chemical mechanical polishing procedures (CMP) (Tanwar et al., 2007b). It was found that the sample preparation condition has a great influence on the surface termination. For example, the stoichiometric (1 \times 1) hematite (1 $\bar{1}$ 02) sample is observed to produce a reduced (2 \times 1) surface when it is subject to an annealing in a ultra-high vacuum at 950 K (Henderson et al., 1998). However, sample preparations based on both air annealing and CMP favor the formation of a double-termination surface including the stoichiometric termination (usually named as full layer termination (FLT)) and the other so-called half layer termination (HLT) that

shares the same atomic layer sequence as the FLT but with a vacant surface Fe sites (Figure 3.1). In addition, results based on published CTR studies also indicated that the CMP protocols would favor the HLT surface (Tanwar et al., 2007b), while the air annealing procedures would result in a surface termination transformation to produce a surface dominated by the FLT (Tanwar et al., 2007a).

Figure 3.1 illustrates the top view and side view of the HLT and FLT structures. As shown in Figure 3.1 (panel A and panel B), the HLT consists of three types of surface functional groups ($^{\text{I}}\text{O}$, $^{\text{II}}\text{O}$ and $^{\text{III}}\text{O}$), while the FLT has only two types of surface functional groups ($^{\text{I}}\text{O}$ and $^{\text{III}}\text{O}$). Within the surface plane the Fe-octahedra form a zigzagging pattern of surface atoms parallel to the \mathbf{b}_s axis, as shown in Figure 3.1 (C and D). The geometrical relationship between two adjacent Fe octahedral units can be described by a \mathbf{b}_s glide plane passing through the in-plane lattice point $(\frac{3}{4}, 0)$ based on the re-index coordinated system.

3.2.4 Potential binding sites on the hematite ($1\bar{1}02$) surface

Based on previous XAFS studies we consider Pb(II) sorption to the hematite ($1\bar{1}02$) surface in an inner-sphere mode with a trigonal pyramid local structure (Bargar et al., 1997(a, b, c)). Both the HLT and the FLT have an equivalent number of $^{\text{I}}\text{O}$ groups within one unit cell, which are thought to dominate the surface reactivity (Catalano et al., 2008). Therefore, we assume that the Pb(II) could form an inner-sphere complex on either the HLT or the FLT surface. We only consider bidentate sites and exclude the monodentate and tridentate binding sites, which will result in Pb-Fe separations either too long or too short to be consistent with previous XAFS studies (Bargar et al., 1997b). In addition, edge-sharing sites involving $^{\text{III}}\text{O}$ on the HLT surface were not considered, since Pb binding at those sites would exert great steric constraints.

A comprehensive analysis was performed by refining the CTR data using structural models with different binding geometries, which are compiled in Table 3.1. The labeling rule for surface oxygens follows that illustrated in Figure 3.1 (C and D). Models based on Pb(II) binding at a single surface site were tested first. Then the examination of more complicated models involving multiple binding sites was followed if the fitting quality in the first stage is not desirable. We realized that there will be a large set of possible combinations of binding sites in the second stage of surface modeling. Therefore, we only consider the edge-sharing binding mode in each two-site model trial, since previous XAFS studies support Pb(II) adsorption to hematite substrates in an edge-sharing binding mode (Bargar et al., 1997b; Bargar et al., 2004).

3.2.5 Description of the CTR analysis

In the present study, CTR measurements were performed on a CMP-prepared hematite ($1\bar{1}02$) surface, which was found to expose with a mixture of the dominant HLT and the minor FLT, as found in Tanwar's study (Tanwar et al., 2007b). The c_s glide plane symmetry of the hematite structure mentioned above indicates that each chemically distinct surface termination has a corresponding symmetry related copy with a step height difference equivalent to $Nc_s/2$, where N is an odd integer and c_s is the lattice parameter. In order to account for the possible different surface relaxation for chemically distinct terminations, we performed the CTR modeling based on multi-unit cell structural models which explicitly include multiple chemically distinct surface terminations and their symmetry copies. Therefore, each structural model contains two symmetry related domains with each constituent domain consisting of clean surface terminations as well as Pb-bonded surface terminations. In each multi-unit cell structural model, weights for chemically distinct terminations were allowed to vary during fitting; weights for

symmetry related terminations were linked to maintain the same values and all individual weights were normalized to ensure a sum of unity. A question then is how the domains should be summed (coherently or incoherently). In this study, our best fits were obtained when the structure factors from symmetry related terminations are summed incoherently, but those for chemically distinct surface terminations are summed coherently. This approach is consistent with a surface morphology containing terrace and step features as illustrated in Figure 3.2.

The method for calculating structure factor along each CTR is described elsewhere (Robinson, 1986; Vlieg, 2000; Fenter, 2002). Each model trial was conducted by optimizing model parameters which include the atomic displacements, occupancies and isotropic Debye Waller factors for each atom. In-plane displacements were considered only for top two atomic layers, while the out-of-plane displacement was allowed to extend up to 6th atom layers. Surface atoms within the same layer were constrained to maintain equivalent out-of-plane displacements, but have in-plane displacements constrained by the \mathbf{b}_s glide plane.

To refine the sorbate positions (Pb and distal O) under the bidentate binding configuration, we defined two geometrical parameters, a rotation angle θ and a dihedral angle φ , as illustrated in Figure 3.3. Using these angles as fitting parameters allows the Pb and distal O positions to change while maintaining the geometrical relationship with the anchored surface oxygens (bidentate edge-sharing or corner-sharing binding configuration) as well as a trigonal pyramid local structure. To consider the distortion of the local coordination structure to result in asymmetric Pb-O bonds and O-Pb-O bond angles, the Pb atom is allowed to move along one Pb-O bond (vector A1O shown in Figure 3.3) within 0.2 Å, while the distal O could rotate within 20° about the axis on a bisect plane (plane OBC shown in Figure 3.3). The occupancy of the distal O was linked to that for Pb atom during model refinement. Using these constraints a robust

surface modeling could be achieved with up to two termination unit cells being optimized simultaneously. Therefore, each model trial was run to optimize parameters from only two terminations, this procedure was repeated for all terminations until a best fit self-consistent model result was obtained.

In a multi-unit cell structural model, we refined the weights for different types of surface terminations. The weight for the total FLT was fit in a range from 0.2 to 0.4 based on the constraint derived previously (Tanwar et al., 2007b); the percentages of different HLT surfaces (the clean surface and the Pb-bounded surfaces) were floated independently but the sum of the total weights for HLT surfaces is constrained such that $HLT + FLT = 1$. In addition, we incorporate interfacial water structure in the last step after the best fit model free of interfacial water is achieved, considering that the interfacial water has small contribution to the overall scattering factors. Two water layers with each layer containing two water molecules per unit cell were added to each termination of the best fit water-free model. Occupancy, the Debye Waller factors and out-of-plane displacements for two water molecules within the same layer were linked and their in-plane positions were constrained by the b_s glide symmetry as mentioned above.

3.2.6 Incorporation of bond valence constraints in the CTR analysis

The CTR modeling process was undertaken using GenX software (Björck, 2011), which employs a differential evolution algorithm to minimize the figure of merit (FOM) based on a normalize χ^2 value

$$\chi^2 = \sum_{i=1}^N \frac{\left[\frac{|F_i| - |F_{i,c}|}{e_i} \right]^2}{N-p} \quad (3.4)$$

In Equation 3.4, F_i is the experimental value for structure factor, $F_{i,c}$ is the calculated structure factor, e_i is the error of i^{th} data point, N is the number of data points, p is the number of fitting parameters. In the current study, a bond valence constraint was incorporated to compute a penalty factor (≥ 1) that scales the original FOM. The penalty factor is based on the chemical plausibility of the structure and calculated as

$$P = 1 + \sum_{j=1}^n |x_j - f_j| \quad (3.5)$$

where f_j represents the formal charge of atom j and x_j is the bond valence sum calculated for atom j during fitting. The bond-length bond-strength relationship proposed by Brown and Altermatt (Brown and Altermatt, 1985) was applied to calculate the valence contributed by each individual Fe-O and Pb-O bond as

$$s = e^{\frac{(r_0-r)}{B}} \quad (3.6)$$

In Equation 3.6, r_0 is the nominal length of a bond, which is tabulated for different metal-O bonds; B is a constant with a value of 0.37 representing the softness of the interaction between the two atoms; r is the actual bond length (Brown, 2009). It should be noted that we applied a r_0 value for Fe(III)-O bond of 1.759 Å as presented by Brown (Brown, 2009), but used an r_0 value for Pb(II)-O of 2.04 Å as suggested by Bargar et al. (Bargar et al., 1997a).

To account for the protonation of surface oxygens in the bond valence constraint, we apply the protonation schemes of the clean hydrated hematite (1 $\bar{1}$ 02) surface suggested by Tanwar et al. (Tanwar et al., 2007b). As for the Pb-bonded surface, we predicted the protonation schemes using the valences contributed by a proton and a hydrogen bond, which are of 0.68 to 0.88 v.u. and 0.13 to 0.25 v.u., respectively, as suggested by Bargar et al. (Bargar et al., 1997a). In addition, we assume a total coordination number of less than four for each surface oxygen. As a result, the valence contributed from the covalent hydrogen and/or the hydrogen bond will be

assigned whenever it could lead to a better bond valence saturation state. We apply a tolerance level (0.2 v.u.) for each bond valence sum when judging the bond valence penalty. Then an atom with a bond valence offset (compared to the associated atomic valence) within the tolerance level will be regarded as one making no contribution to the total bond valence penalty factor ($x_j - f_j = 0$ in Equation 3.5). It should be noted that the arbitrary tolerance level of 0.2 v.u. is chosen based on the bond valence difference (~ 0.2 v.u.) between two sets of Fe-O bonds (1.95 Å and 2.11 Å) as found in the unrelaxed bulk hematite structure.

It is apparent that a bond valence penalty factor equivalent to 1 indicates a bond valence saturation for all atoms, while a value higher than 1 indicates a bond valence non-saturation (either under-saturation or over-saturation). It was found that the best fit model derived without a bond valence constraint usually contains some atoms with serious bond valence non-saturation states due to unrealistic bond lengths or coordination numbers. On the contrary, using the bond valence constraint it is more likely to arrive at best fit models with physically realistic structures that also give rise to a good fit to the experimental data.

3.3 CTR modeling results

3.3.1 Model trials based on a single type of sorption site

As listed in Table 3.1, the model trials based on a single type of sorption site include one corner-sharing site and two edge-sharing sites for both the HLT and the FLT surfaces. Each model trial was run separately using constraints for model parameters described above. The first question arising is whether the corner-sharing sites are reactive or not, since this type of binding site was ruled out in previous XAFS studies using hematite substrates (Bargar et al., 1997b; Bargar et al., 2004) but confirmed to exist at lower pH (<5.0) based on XAFS studies using

ferrihydrite (Trivedi et al., 2003; Tiberg et al., 2013) and goethite (Ostergren et al., 2000b). The comparison of representative CTR profiles derived from models based on Pb(II) binding at the corner-sharing sites and the edge-sharing sites are depicted in Figure 3.4. It was found that the calculated (3 0 L) rod profile for the corner-sharing binding configurations showed significant discrepancy at numerous positions compared to the experimental data. For example, the O5O6 model produces a substantial drop of scattering intensity starting from near (3 0 2.0) and extending to around (3 0 3.8), forming a steep shoulder as opposed to a lobe clearly seen in the experimental data. In addition, the corner-sharing model O1O2 gave rise to a “complete” hump without splitting near (1 0 0.0), as opposed to the feature shown in the associated experimental data, which has two symmetric and well-separated humps, as shown in Figure 3.4. We also noticed that fitting qualities on (2 -1 L) and (2 1 L) are poor for models of both edge-sharing and corner-sharing binding sites. The specular rod profile (0 0 L) calculated based on the optimized O5O7 model is significantly distinct from the data at low L regions (<2.0). According to the qualitative comparison of optimized CTR profiles with the experimental data, we observed that structure model based on Pb(II) binding at the corner-sharing sites could not arrive at a good fit at all CTRs. In addition, a single edge-sharing binding mode, which, although predicted in previous XAFS spectroscopy studies (Bargar et al., 1997b; Ostergren et al., 2000b; Trivedi et al., 2003; Tiberg et al., 2013), could not produce a good fit according to our CTR modeling results. This motivates us to try a multi-site model to fit the CTR data. Our goal for the multi-site modeling is to identify the reactive edge-sharing sites on either HLT or FLT surfaces, and we ignored the presence of corner-sharing binding sites, since they were ruled out according to previous XAFS spectroscopy studies mentioned above. In the multi-site modeling processes, there are two possible combination rules depending on whether the potential reactive edge-

sharing sites are assigned to the same surface termination or not, as outlined in Table 3.1. The description of fitting results for model trials with different combination rules will be detailed in the following two sections.

3.3.2 Model trials based on two edge-sharing sites assigned to two termination surfaces

Further modeling analysis is based on the consideration of Pb(II) binding at one edge-sharing site on both the HLT and the FLT. As shown in Table 3.1, such a combination rule gives rise to four different modeling trials, including O1O3_O5O7, O1O3_O5O8, O1O4_O5O7 and O1O4_O5O8. The optimized CTR profiles for these models are compared to the experimental data in Figure 3.5. As shown in the Figure 3.5, models considering two edge-sharing sites did not lead to a significant improvement on the overall fitting quality compared to the modeling results for Pb(II) adsorption at a single type of edge-sharing site. The mismatches are most pronounced on the (3 0 L), (2 -1 L) and (2 1 L) rods. For example, the symmetric lobes near (3 0 ±2.5) were poorly reproduced in model O1O4_O5O7 and model O1O4_O5O8, as shown in Figure 3.5. The calculated CTR for model O1O3_O5O8 produces an obvious split hump feature near (3 0 3.1) instead of a single hump as seen in the experiment data. In addition, there are numerous places displaying a misfit due to the presence of a dip feature, such as (0 0 1.7) (observed in both model O1O4_O5O8 and model O1O4_O5O7), (2 2 -5.5) (observed in both model O1O4_O5O7 and O1O3_O5O7), and (2 1 3.8) (observed in model O1O4_O5O8). These misfits found at different rod positions serve as a qualitative indicator that the sorbate is registered incorrectly on the hematite (1 $\bar{1}$ 02) surface. It is apparent from the results of these modeling trials that a proper solution to the surface complexation structure in a metal/substrate system will rely not only on

the knowledge of a realistic binding configuration but also on the details of the site occupation pattern if there are multiple sites available.

3.3.3 Model trials based on two types of edge-sharing site on the same termination surface

Here we consider Pb(II) binding to two edge-sharing sites on the same surface termination. The CTR profiles based on this type of combination are shown in Figure 3.6. As shown in Figure 3.6, a significantly better fit was obtained using the O5O7_O5O8 model with a FOM value of 3.9, which is better than the results of models described above (>4.9) at a 95% confidence level in the Hamilton R-test (Hamilton, 1965). However, pronounced misfits were seen near $(0\ 0\ 1.8)$ with the calculated scattering intensity being significantly underestimated compared to the experimental data. In addition, the optimized $(3\ 0\ L)$ rod profile could not reproduce the symmetric lobes seen near $(3\ 0\ \pm 3.1)$ due to a significant shift towards $(3\ 0\ 0)$ by about 1 L unit.

Compared to O5O7_O5O8 model, the O1O3_O1O4 model gave rise to a much better fitting quality with a FOM as low as 2.2. The fit quality using O1O3_O1O4 model is significantly better than that O5O7_O5O8 model at a 95% confidence level in the Hamilton R-test. The improvement of the fitting quality for this model was clearly seen on $(3\ 0\ L)$, $(2\ -1\ 0)$ and $(2\ 1\ L)$ rods, where a variety of misfits were otherwise found in the previous model trials due to the occurrence of unexpected dips or mismatch of the bump features. The reproduction of two symmetric hump features observed at $(1\ 0\ L)$ rod was significantly improved in the current model trial. The best fit model suggests that those two types of edge-sharing binding sites on the HLT are potentially reactive surface sites for binding Pb(II) simultaneously in the studied system. However, it should be noted that on a HLT dominated surface, the Pb(II) sorption to the FLT probably could not be well resolved, since the total proportion of Pb-bonded FLT surface

should be very close to the model uncertainty. We need to perform a separated CTR study of Pb(II) adsorption to a FLT dominated hematite ($1\bar{1}02$) surface in order to identify the reactive binding site on the FLT surface (read Chapter 4 for details).

3.3.4 Influence of interfacial waters

Previous CTR studies (Eng et al., 2000; Trainor et al., 2002a; Fenter and Sturchio, 2004; Trainor et al., 2004; Tanwar et al., 2007b; Catalano et al., 2009; Catalano, 2010; Ghose et al., 2010; Gaigeot et al., 2012) have presented the evidence that the semi-ordering interfacial waters are physically present on top of oxide surfaces with low occupancy and high Debye Waller factors. It is widely accepted that interfacial waters, which are hydrogen bound with the oxide surface, create a transition zone with a different dielectric constant connecting the oxide surface and the bulk solution, and may serve as an important mechanism to stabilize the interfacial structure (Catalano et al., 2007a; Catalano et al., 2009; Catalano, 2010). In our modeling the influence of interfacial waters was tested by incorporating four oxygen atoms (two water layers) to the clean HLT and clean FLT unit cell using the best-fit model O1O3_O1O4, which was optimized without interfacial waters. To model the interfacial water structure, the occupancies, Debye Waller factors and the out-of-plane positions for two constituent oxygens within the same layer were linked to a same value, whereas the in-plane positions of two constituent oxygens were fit with the constraint of \mathbf{b}_s glide plane. After the optimization, the FOM value dropped from 2.2 to 1.9. A Hamilton R-test was performed to evaluate the improvement of the fit after adding interfacial water in the structural model. The hypothesis that the fit improved using a model involving interfacial water layers was rejected in the Hamilton R-test at 95% confidence level. Therefore, the CTR modeling results presented in this study could not lead to a reasonable

constraint of interfacial water molecules in the Pb(II)/hematite system. Such a finding is not surprising, considering that Pb atom has an electron density substantially higher than that of the oxygen and thus dominates the scattering intensity at oxide-fluid interface.

3.4 Discussions

3.4.1 Description of best-fit model

The best fit modeling results, as described in detail in Table 3.2, gave rise to a surface structure consisting of four surface terminations: 19% Pb-bonded HLT with Pb(II) binding at the edge-sharing site of type 1 (named as ES1 site, i.e. O_1O_3 and the symmetry related site O_2O_{4+y}); 25% Pb-bonded HLT with Pb(II) binding at the edge-sharing site of type 2 (named as ES2 site, i.e. O_1O_4 site and the symmetry related site O_2O_{3+x}); 27% clean hydroxylated HLT; and 29% clean hydroxylated FLT. The HLT to the FLT ratio of 71/29 in our modeling results is in good agreement with that reported in a previous CTR study of a clean hydroxylated hematite ($1\bar{1}02$) surface (Tanwar et al., 2007b).

3.4.1.1 Relaxation of surface structure

Based on our best fit model, we found the out-of-plane relaxations of the top six atomic layers from the HLT surfaces are comparable within model uncertainties, as shown in Figure 3.7. The general agreement of the atomic layer relaxation for Pb-bonded HLT and the clean HLT indicates that the Pb-adsorption induced surface relaxation is limited. In addition, we also compared the out-of-plane relaxation of the atomic layers in the clean HLT to that derived in Tanwar's best fit CTR model of a clean CMP-prepared hematite($1\bar{1}02$) surface (Tanwar et al., 2007b). As illustrated in Figure 3.7, our best fit model gave rise to the Layer-3 Fe atoms relaxing

towards substrate surface by 0.10 Å, whereas the Layer-4 O atoms recessing into the bulk structure by 0.14 Å. Such a relaxation pattern significantly expand the Layer 3-4 spacing by 0.24 Å, which is in sharp contrast to Tanwar's model, which suggested negligible change of the Layer 3-4 spacing. The different atomic relaxation pattern found in our model compared to Tanwar's model could be attributed to the different methods used to perform the model refinement, i.e. model refinement based on either average structural model in Tanwar's case or multi-unit cell structural model for this study. The refinement of an average structure model could not explicitly account for the different relaxation patterns for chemically different termination surfaces. In addition, we notice that the Layer-3 Fe and Layer-4 O relaxing in an opposite direction will lead to a slight contraction of the Fe-^{III}O bonds, which will increase the valence sum of ^{III}O from 1.58 v.u. based on the ideal structure to 1.72 v.u., a value closer to the bond valence saturation. However, the Layer-3 Fe and Layer-4 O without relaxation as suggested in Tanwar's best fit model would not change the Fe-^{III}O bond length, and would maintain the valence sum of ^{III}O atoms at the ideal value (1.58 v.u.). The ^{III}O group with a valence sum of 1.72 v.u. could be nearly saturated after accepting one hydrogen bond contributing a valence of 0.25 v.u., but the ^{III}O with a valence sum of 1.58 v.u. could not arrive at a bond valence saturation after considering the contribution of a hydrogen bond, which contributes valence typically ranging from 0.13 to 0.25 v.u.(Bargar et al., 1997a).

3.4.1.2 Surface complex structure of Pb(II) on hematite surface

As mentioned above, the best fit model gives rise to two types of Pb surface complexes with a bidentate edge-sharing binding configuration. The surface Pb atom is bound with two surface functional groups (^IO and ^{II}O groups) and one distal oxygen (not directly binding to the substrate

surface) forming a trigonal pyramid local structure. The trigonal pyramid structure is slightly distorted causing asymmetric Pb-O bond lengths (2.17, 2.27 and 2.37 Å for Pb binding at ES1 site; 2.20, 2.29 and 2.30 Å for Pb binding at ES2 site) and different O-Pb-O bond angles (71°, 80°, 80° for Pb binding at ES1 site; 68°, 68°, 70° for Pb binding at ES2 site). The coordination structures of those two surface complex species are illustrated in Figure 3.8. The average Pb-O bond lengths deduced from this study (2.26 Å and 2.27 Å) are in good agreement with those (2.28±0.01 Å) reported in previous XAFS studies (Bargar et al., 1997b; Bargar et al., 2004). The characteristic Pb-Fe separations are 3.32 Å and 3.64 Å corresponding to the ES1 site and the ES2 site, respectively. An XAFS study using hematite powder sample undertaken by Bargar et al (Bargar et al., 1997b) suggested a single Pb-Fe distance (3.28±0.02 Å), which is consistent with that for the ES1 site in the present study. Interestingly, Bargar et al. (Bargar et al., 2004) found that the Pb-Fe distance could not be uniquely resolved when using a single crystal hematite (1 $\bar{1}$ 02) sample, and the broad range of the Pb-Fe distance (3.34-3.86 Å) derived in that study was attributed to the data quality. However, the range of Pb-Fe values could also be caused by an un-identified surface complex species with a significantly larger Pb-Fe separation.

According to our CTR modeling results, the Pb-Fe distance of 3.64 Å (Pb surface complex at the ES2 site) is longer than assigned to edge sharing binding sites found in previous XAFS studies (Bargar et al., 1997b; Ostergren et al., 1999; Trivedi et al., 2003). This larger Fe-Pb separation is consistent with a smaller O-Fe-O bond angle for the ES2 site (74°) as compared to that for the ES1 site (85°), as shown in Figure 3.8. A study of density functional theory (DFT) provided quantum mechanical evidence of the Fe/Pb covalent interaction in a system of Pb(II) adsorption to the hematite (0001) surface (Mason et al., 2009). Inferred by the DFT results, the Pb surface complex binding at ES1 site with a smaller Pb-Fe separation may correspond to a

stronger Pb-Fe covalent interaction (adsorption energy gain). However, the overall binding energy is also determined by the structural distortion. As shown in Figure 3.6, O-Pb-O bond angles at both ES1 site and ES2 site are significantly smaller than that (109.5°) for an ideal trigonal pyramid coordination structure, which is due to the lone electron pair effect in Pb atom as revealed in previous quantum chemistry calculations (Jensen, 2002; Breza et al., 2003). Besides this common angle distortion from the ideal coordination structure, it should be noted that the surface Pb complexes at ES1 site display a greater angle distortion indicative of two O-Pb-O_{dist} angles (80°) much larger than the $^I\text{O-Pb-}^{II}\text{O}$ angle (71°). Our best fit angle parameters (rotation angle ϕ , Figure 3.3) indicated that the larger O-Pb-O_{dist} angle is caused by the rotation of Pb-O_{dist} off the ideal position by $11(\pm 2)^\circ$ towards solution side, which is necessary to release the steric constraint caused by the extremely short O-O separation ($<2.11 \text{ \AA}$) if the distal oxygen had occupied the original site without rotation. On the contrary, the angle distortion of the surface complex binding at the ES2 site is less severe with O-Pb-O bond angles close to each other within 2° , which probably means a lower energy cost for the strain caused by the O-Pb-O bond angle distortion. As for the overall surface binding energy of ES1 site and ES2 site, we, nevertheless, could not identify the high energy site through comparing site coverages, since the surface adsorption was probed using a metal solution of a mono-layer saturation concentration, and thus both sites should have achieved a Langmuir mono-layer saturation successively with similar CTR-derived occupancies (refer to next section for details).

Interestingly, previous XAFS studies also provide the evidence of Pb(II) sorption to iron-(oxyhydr)oxides (ferrihydrite and gothite) via a bidentate corner-sharing binding configuration at low pH (pH <5.0) (Ostergren et al., 2000b; Trivedi et al., 2003). That probably indicates that the protons compete with Pb(II) ions for the surface binding sites such that Pb-O bond involving the

surface oxygen groups ($^{\text{II}}\text{O}$ or $^{\text{III}}\text{O}$) with a higher proton affinity will break due to the protonation of that oxygen group at lower pH. Our CTR modeling results do not support the formation of the surface Pb complex with a corner-sharing binding configuration even at a relatively low pH (pH 5.5), and that may be induced by different substrate surface structures.

3.4.2 Relationship between the site coverage and the sorbate-sorbate distance

In this section, we explore the relationship between the site coverage and the sorbate-sorbate distance by performing site coverage simulations. The intrinsic b_s glide plane symmetry on the hematite ($1\bar{1}02$) plane determines that there are two symmetry sites per surface unit cell for each type of surface site resulting in four sites in total within one unit cell (considering ES1 and ES2 sites). Then in theory we could achieve a 400% site coverage (assuming 100% site coverage corresponds to one site occupied by a Pb sorbate per unit cell), if all four sites within one unit cell are occupied. However, occupation of all available surface sites within a single unit cell should be hindered by steric constraints. To study the steric constraints caused by occupied sites, site coverage simulations were performed based on occupying available surface sites randomly under constraints of different inter-site cutoff limits. A 20×20 super cell was defined for each simulation using site positions derived from the best fit CTR model. The simulations were performed at Pb-Pb cutoff limits ranging from 2.84 Å to 10.08 Å, which were identified from the site distribution pattern (Figure 3.9B). As illustrated in Figure 3.9A, the simulation results show, as expected, a trend of decreasing site coverage with increasing sorbate-sorbate cutoff limits. Interestingly, the CTR derived occupancy of 75% (normalized to the HLT) is in good agreement with the simulated site coverage corresponding to a cutoff of 5.42 Å (Figure 3.9 A). The site occupation pattern simulated at the 5.42 Å cutoff limit is illustrated in Figure 3.9D. We note that

a cutoff limit of 5.42 Å is only slightly smaller than the lattice parameter b_s (5.43 Å), which indicates that two adjacent occupied sites of the same type are allowed to be aligned in the y (b_s) direction. However, the case with two adjacent occupied site aligned in the x (a_s) direction is forbidden at this cutoff since that would result in a sorbate-sorbate distance as short as 5.04 Å (the associated lattice parameter a_s). In addition, we also realized that a cutoff limit of 5.42 Å could give rise to a 100% site coverage, had a super lattice formed, which contains columns of occupied sites of two different types alternating along the x axis direction as shown in Figure 3.9C, as an example. However, such a super lattice occupation pattern was not observed based on the CTR derived site occupancy that is significantly lower than 100% signifying random site occupation. Apparently, the site multiplicity (ES1 site and ES2 site) as well as the site degeneracy (symmetry related sites) greatly decreases the sorption capacity and therefore the sorbate-sorbate interaction serves as an important factor in dictating the surface site coverage. To test this idea further, we conducted another CTR measurement following the same procedures but loading a Pb(II) solution of higher concentration (400 μM) to react with the hematite surface. Significant variance of CTR profiles (data not shown) was not observed for the system with a higher Pb(II) concentration, indicating an apparent site saturation of Pb(II) sorption to CMP-prepared hematite ($1\bar{1}02$) surface being achieved under 200 μM.

Bargar et al. (Bargar et al., 2004) conducted an XPS measurement of Pb(II) adsorption to the hematite ($1\bar{1}02$) surface at pH 7.0, and the results indicated a site coverage of 7.2 atoms/nm², corresponding to ~200% site coverage (two occupied sites within one unit cell) after normalizing to the re-indexed lattice structure ($a=5.038$ Å, $b=5.434$ Å) of the hematite ($1\bar{1}02$). In addition, by using the grazing incidence XAFS, Bargar et al. presented an oligomeric surface Pb complex with a short Pb-Pb separation of ~3.69 Å. According to our simulation results, such an inter-

sorbate distance would give rise to a site coverage of ~110%, significantly lower than the value suggested by the XPS experiment. Note that our site simulation test is based on Pb(II) binding within a mono layer, which does not account for the possible surface binding configuration corresponding to oligomeric surface species. Our site coverage simulation test would greatly underestimate the total site coverage in the presence of oligomeric Pb species in the system. Hence, our simulation results provide an indirect evidence that lends support to Bargar's observation of the oligomeric Pb species at the hematite ($1\bar{1}02$) surface. We noticed that the only difference of the experimental conditions in the study by Bargar et al. is the solution pH (our Pb(II) solution is buffered to pH 5.5, compared to pH 7.0 used in Bargar's experiment). The polymerization of Pb at the mineral surface at higher pH ($\text{pH} > 7.0$) was also confirmed in a Pb(II) adsorption study on goethite powder using method based on macroscale batch experiments (Gunneriusson et al., 1994). Therefore, the solution pH may be the driving force to trigger the formation of oligomeric Pb species binding at mineral surface.

3.4.3 Surface complexation reactions of Pb(II) on hematite ($1\bar{1}02$) surface

Based on the best fit surface structural model, we predict the protonation schemes for surface functional groups using the bond valence constraints. As a reference, we used the initial protonation states of surface oxygen groups (doubly protonated $^{\text{I}}\text{O}$ groups and singly protonated $^{\text{II}}\text{O}$ group) from a previous CTR study by Tanwar et al. (Tanwar et al., 2007b) to discuss the possible proton release induced by Pb(II) adsorption. As outlined in Table 3.3, $^{\text{I}}\text{O}$ groups, doubly protonated initially, would release one proton upon Pb(II) adsorption to the surface. However, the protonation state of the $^{\text{II}}\text{O}$ groups does not change after Pb(II) binding to the surface, probably due to relatively long Pb- $^{\text{II}}\text{O}$ bonds ($> 2.29 \text{ \AA}$, Figure 3.8) that contribute a bond valence

(~0.4 v.u.), significantly less than that for a covalent hydrogen (0.68-0.88 v.u) (Bargar et al., 1997a). As a result, instead of substituting for a proton, Pb(II) bonding to an ^{II}O group will displace a coordinated hydrogen atom away from the associated ^{II}O to weaken the covalent hydrogen bond. In addition, the weak hydrogen bond associating with ^{II}O is missing after Pb(II) adsorption, as shown in Table 3.3. Although we could not provide direct evidence of the hydrogen bonding effect, we infer that the elimination of the weak hydrogen bond may be related to the deprotonation of the ^{I}O group, which should donate a hydrogen bond to the ^{II}O group when it is doubly protonated prior to Pb(II) adsorption at the surface. The protonation schemes for surface functional groups were also predicted by Ostergren et al. (Ostergren et al., 2000b) in an XAFS study of Pb(II) sorption to goethite surface. In that study, XAFS derived structure information was combined with bond valence constraints as well as steric consideration to predict the possible surface complexation reaction stoichiometries. Although they were not able to propose a unique surface complexation stoichiometry, the bidentate edge-sharing site (containing both ^{I}O and ^{II}O) were predicted to be plausible sites for binding Pb(II) with a protonation scheme consistent with that reported in this study. On the contrary, the findings presented here are different from that suggested by Bargar et al. in an XAFS study of Pb(II) sorption using hematite powder sample (Bargar et al., 1997b). In that study, the doubly coordinated oxygen group (^{II}O) was regarded as chemically inert for binding Pb(II), since the bond valence analysis predicted that the Pb(II) binding to such a group would result in a ^{II}O group with either bond valence oversaturation in a protonated state or bond valence under-saturation in a non-protonated state. Such a discrepancy regarding Pb surface complex species proposed in that XAFS study is not surprising, since the knowledge of the non-ideal surface structure could not be well constrained using the XAFS spectroscopy. Realizing that issue,

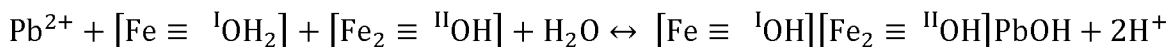
Bargar et al. examined the influence of Fe-O bond lengths on the results of bond-valence analysis by allowing for the variance of Fe-O bond length in a range from 1.95 to 2.12 Å. The bond valence analysis results indicated that the doubly coordinated H_2O group, which was predicted to be unreactive based on using an average Fe- H_2O bond length (2.26 Å), was found to be possible for binding Pb(II) if allowing for a relatively long Fe- H_2O bond.

In addition, it was found that the distal oxygen (O_{dist}) of the surface Pb complex could arrive at a bond valence saturation when it is doubly protonated with each proton contributing a valence of 0.68 v.u.. However, the protonation state of the distal oxygen should be pH dependent, and the deprotonation may not significantly change the associated Pb- O_{distal} bond since the bond valence loss due to the deprotonation of the distal oxygen could be balanced again through the other ways, such as hydrogen bonding interaction and strengthening the other covalent hydrogen bond. For example, the consideration of a singly protonated distal oxygen group is also possible, if the distal oxygen could accept one more hydrogen bond (0.25 v.u.) and contract the other covalent hydrogen bond to make it stronger (0.88 v.u.). Then the valence deficit is only 0.2 v.u. that could be further balanced by slightly contracting the Pb- O_{distal} bond by 0.1 Å. Such a slight displacement of the distal oxygen towards the Pb atom should make little influence on the variations of CTR profiles. Consistent with our results, surface complexation reaction stoichiometries with a hydroxylated Pb surface complex were proposed in previous XAFS studies (Bargar et al., 1997b; Ostergren et al., 2000b).

To date, there is no consensus opinion on the hydrolysis of the adsorbed Pb. Previous macro scale studies of Pb(II) sorption on different substrates proposed surface complexation stoichiometries with either non-hydroxylated Pb surface complex (Tiberg et al., 2013) and/or hydroxylated Pb surface complex (Gunneriusson et al., 1994) without further explanation. The

variance of proton release observed among different studies may be due to the hydrolysis of the adsorbed Pb as a function of solution pH. An XPS study of Pb(II) sorption on goethite (Abdel-Samad and Watson, 1998) provided spectroscopic evidence of the protonation schemes of surface functional groups as well as the hydrolysis of the adsorbed Pb as a function of pH. They found that a low pH condition would favor the Pb surface complex species with protonated Pb-bonded surface oxygen groups as well as nonhydroxylated adsorbed Pb, while a Pb surface complex species with deprotonated surface functional groups and the adsorbed Pb being hydroxylated is favored at a higher pH.

Using the protonation schemes of surface oxygen groups predicted in the bond valence analysis as well as an assumption of the hydrolysis of the distal oxygen, we proposed the reaction stoichiometry of Pb(II) adsorption to the HLT-dominated hematite ($1\bar{1}02$) surface (pH 5.5) as:



Note that the proposed surface complexation stoichiometry will be subject to change as a function of solution pH with higher pH probably inducing the further deprotonation of $^{\text{I}}\text{OH}$, $^{\text{II}}\text{OH}$ and Pb-OH groups.

3.5 Conclusions

CTR diffraction was used to characterize the adsorption of Pb(II) on a CMP-prepared hematite ($1\bar{1}02$) surface under *in situ* conditions at pH 5.5. The CTR results indicate a substrate surface consisting of 71% HLT and 29% FLT, which is in good agreement with that reported in a published CTR study of hydrated hematite ($1\bar{1}02$) surface (Tanwar et al., 2007b). The best-fit structural model indicates that Pb(II) adsorption on the HLT surface is via an inner-sphere mode

with a bidentate edge-sharing binding configuration. Two types of edge-sharing binding sites (ES1 and ES2) are identified to be reactive for binding Pb(II) with characteristic Pb-Fe distances of 3.32 Å and 3.64 Å, respectively. The local structure of the surface Pb complex is a distorted trigonal pyramid with an averaged Pb-O bond length of 2.26 Å, comparable to the results of previous XAFS studies. The detailed binding structure for the surface Pb complex at each site is different with the Pb surface complex at ES1 site displaying a more severe O-Pb-O bond angle distortion compared to the other site. Both the Pb-Fe separation as well as the distortion of surface binding structure may play a role in dictating the overall surface binding energy, which could, however, not be evaluated to distinguish the high/low energy site in this study due to the mono-layer saturation of Pb adsorbate achieved at the substrate surface.

The results of site coverage simulation tests gave rise to a decreasing trend of the simulated site coverage with the inter-site cutoff limits. The CTR-derived Pb occupancy agrees with the simulated surface site coverage obtained at 5.42 Å Pb-Pb cutoff limit, suggesting a random occupation of available surface sites. The site coverage simulation results also revealed that the sorbate-sorbate repulsion may exert some influence on the surface site coverage especially when the surface site coverage is approaching an apparent monolayer saturation.

Using the bond valence constraints as well as the best fit structural model derived from CTR analysis, we proposed a reaction stoichiometry for Pb(II) adsorption to the CMP-prepared hematite (1 $\bar{1}$ 02) surface. The proposed stoichiometry suggests two proton release which is due to the hydrolysis of the adsorbed Pb as well as the deprotonation of the surface functional group (^1O) upon Pb(II) bonding to that group.

3.6 Acknowledgements

This project is funded by DoD SERDP grant ER-1770. All the associated experiments were performed at beamline 13BMC of GeoSoilEnviroCARS (Sector 13), Advanced Photon Source (APS), Argonne National Laboratory. GSECARS is supported by the National Science Foundation - Earth Sciences (EAR-1128799) and Department of Energy - Geosciences (DE-FG02-94ER14466). Use of the Advanced Photon Source was supported by the U. S. Department of Energy, Office of Science, Office of Basic Energy Sciences, under Contract No. DE-AC02-06CH11357. We would also like to thank the Arctic Super Computer Center (ARSC) at University of Alaska Fairbanks for providing computation resource used in the surface modeling.

3.7 References

- Abdel-Samad H. and Watson P. R. (1998) An XPS study of the adsorption of lead on goethite (α -FeOOH). *Appl. Surf. Sci.* **136**, 46–54.
- Bargar J. R., Brown G. E. and Parks G. A. (1997a) Surface complexation of Pb(II) at oxide-water interfaces: I. XAFS and bond-valence determination of mononuclear and polynuclear Pb(II) sorption products on aluminum oxides. *Geochim. Cosmochim. Acta* **61**, 2617–2637. Available at: <http://www.sciencedirect.com/science/article/pii/S0016703797001245>.
- Bargar J. R., Brown G. E. and Parks G. A. (1997b) Surface complexation of Pb(II) at oxide-water interfaces: II. XAFS and bond-valence determination of mononuclear Pb(II) sorption products and surface functional groups on iron oxides. *Geochim. Cosmochim. Acta* **61**, 2639–2652. Available at: <http://www.sciencedirect.com/science/article/pii/S0016703797001257>.
- Bargar J. R., Brown G. E. and Parks G. A. (1998) Surface Complexation of Pb(II) at Oxide-Water Interfaces: III. XAFS Determination of Pb(II) and Pb(II)-Chloro Adsorption Complexes on Goethite and Alumina. *Geochim. Cosmochim. Acta* **62**, 193–207. Available at: <http://www.sciencedirect.com/science/article/pii/S0016703797003347>.
- Bargar J. R., Towle S. N., Brown G. E. and Parks G. A. (1997c) XAFS and Bond-Valence Determination of the Structures and Compositions of Surface Functional Groups and Pb(II) and Co(II) Sorption Products on Single-Crystal α -Al₂O₃. *J. Colloid Interface Sci.* **185**, 473–492. Available at: <http://www.sciencedirect.com/science/article/pii/S0021979796945749>.

- Bargar J. R., Trainor T. P., Fitts J. P., Chambers S. A. and Brown G. E. (2004) In Situ Grazing-Incidence Extended X-ray Absorption Fine Structure Study of Pb(II) Chemisorption on Hematite (0001) and (1-102) Surfaces. *Langmuir* **20**, 1667–1673.
- Björck M. (2011) Fitting with differential evolution: an introduction and evaluation. *J. Appl. Crystallogr.* **44**, 1198–1204. Available at: <http://dx.doi.org/10.1107/S0021889811041446>.
- Breza M., Biskupič S. and Manová A. (2003) On the structure of lead (II) complexes in aqueous solutions.: Part IV. Binuclear clusters. *Polyhedron* **22**, 2863–2867.
- Brown G. E. (2001) How Minerals React with Water. *Science* **294**, 67–69. Available at: <http://www.sciencemag.org/content/294/5540/67.short>.
- Brown G. E., Parks G. A. and O'Day P. A. (1995) Sorption at mineral-water interfaces: macroscopic and microscopic perspectives. *Miner. Surfaces* **5**, 129–183.
- Brown G. E. and Sturchio N. C. (2002) An overview of synchrotron radiation applications to low temperature geochemistry and environmental science. *Rev. Mineral. Geochemistry* **49**, 1–115.
- Brown I. D. (2009) Recent Developments in the Methods and Applications of the Bond Valence Model. *Chem. Rev.* **109**, 6858–6919. Available at: <http://pubs.acs.org/doi/abs/10.1021/cr900053k>.
- Brown I. D. and Altermatt D. (1985) Bond-valence parameters obtained from a systematic analysis of the Inorganic Crystal Structure Database. *Acta Crystallogr. Sect. B* **41**, 244–247. Available at: <http://dx.doi.org/10.1107/S0108768185002063>.
- Catalano J. G. (2010) Relaxations and Interfacial Water Ordering at the Corundum (110) Surface. *J. Phys. Chem. C* **114**, 6624–6630. Available at: <http://pubs.acs.org/doi/abs/10.1021/jp100455s>.
- Catalano J. G., Fenter P. and Park C. (2007) Interfacial water structure on the (0 1 2) surface of hematite: Ordering and reactivity in comparison with corundum. *Geochim. Cosmochim. Acta* **71**, 5313–5324.
- Catalano J. G., Fenter P. and Park C. (2009) Water ordering and surface relaxations at the hematite (110)--water interface. *Geochim. Cosmochim. Acta* **73**, 2242–2251.
- Catalano J. G., Park C., Fenter P. and Zhang Z. (2008) Simultaneous inner- and outer-sphere arsenate adsorption on corundum and hematite. *Geochim. Cosmochim. Acta* **72**, 1986–2004.
- Christl I. and Kretzschmar R. (1999) Competitive sorption of copper and lead at the oxide-water interface: Implications for surface site density. *Geochim. Cosmochim. Acta* **63**, 2929–2938. Available at: <http://www.sciencedirect.com/science/article/pii/S0016703799002665>.
- Cornell R. M. and Schwertmann U. (2003) *The iron oxides: structure, properties, reactions, occurrences and uses.*, John Wiley & Sons.
- Craig J. R., Rimstidt J. D., Bonnaffon C. A., Collins T. K. and Scanlon P. F. (1999) Surface water transport of lead at a shooting range. *Bull. Environ. Contam. Toxicol.* **63**, 312–319.

- Davis J. A. and Leckie J. O. (1978) Surface ionization and complexation at the oxide/water interface II. Surface properties of amorphous iron oxyhydroxide and adsorption of metal ions. *J. Colloid Interface Sci.* **67**, 90–107.
- Dyer J. A., Trivedi P., Scrivner N. C. and Sparks D. L. (2003) Lead Sorption onto Ferrihydrite. 2. Surface Complexation Modeling. *Environ. Sci. Technol.* **37**, 915–922. Available at: <http://pubs.acs.org/doi/abs/10.1021/es025794r>.
- Dzombak D. A. and Morel F. M. M. (1990) *Surface complexation modeling: hydrous ferric oxide.*, John Wiley & Sons.
- Eikenberry E. F., Brönnimann C., Hülsen G., Toyokawa H., Horisberger R., Schmitt B., Schulze-Briese C. and Tomizaki T. (2003) PILATUS: a two-dimensional X-ray detector for macromolecular crystallography. *Nucl. Instruments Methods Phys. Res. Sect. A Accel. Spectrometers, Detect. Assoc. Equip.* **501**, 260–266.
- Eng P. J., Trainor T. P., Brown G. E. J., Waychunas G. A., Newville M., Sutton S. R. and Rivers M. L. (2000) Structure of the Hydrated α -Al₂O₃ (0001) Surface. *Science* **288**, 1029–1033. Available at: <http://www.sciencemag.org/content/288/5468/1029.abstract>.
- Fenter P. A. (2002) X-ray Reflectivity as a Probe of Mineral-Fluid Interfaces: A User Guide. *Rev. Mineral. Geochemistry* **49**, 149–221. Available at: <http://ring.geoscienceworld.org/content/49/1/149.short>.
- Fenter P. and Sturchio N. C. (2004) Mineral--water interfacial structures revealed by synchrotron X-ray scattering. *Prog. Surf. Sci.* **77**, 171–258. Available at: <http://www.sciencedirect.com/science/article/pii/S0079681605000031>.
- Finger L. W. and Hazen R. M. (1980) Crystal structure and isothermal compression of Fe₂O₃, Cr₂O₃, and V₂O₃ to 50 kbars. *J. Appl. Phys.* **51**, 5362–5367.
- Fukuma T., Ueda Y., Yoshioka S. and Asakawa H. (2010) Atomic-scale distribution of water molecules at the mica-water interface visualized by three-dimensional scanning force microscopy. *Phys. Rev. Lett.* **104**, 16101.
- Gaigeot M.-P., Sprik M. and Sulpizi M. (2012) Oxide/water interfaces: how the surface chemistry modifies interfacial water properties. *J. Phys. Condens. Matter* **24**, 124106. Available at: <http://stacks.iop.org/0953-8984/24/i=12/a=124106>.
- Geissbühler P., Fenter P., DiMasi E., Srajer G., Sorensen L. B. and Sturchio N. C. (2004) Three-dimensional structure of the calcite--water interface by surface X-ray scattering. *Surf. Sci.* **573**, 191–203.
- Ghose S. K., Waychunas G. A., Trainor T. P. and Eng P. J. (2010) Hydrated goethite (α -FeOOH)(100) interface structure: Ordered water and surface functional groups. *Geochim. Cosmochim. Acta* **74**, 1943–1953. Available at: <http://www.sciencedirect.com/science/article/pii/S0039602804012531>.
- Goyer R. A. (1993) Lead toxicity: current concerns. *Environ. Health Perspect.* **100**, 177.
- Gunneriusson L., Lövgren L. and Sjöberg S. (1994) Complexation of Pb (II) at the goethite (α -FeOOH)/water interface: The influence of chloride. *Geochim. Cosmochim. Acta* **58**, 4973–4983.

- Gustafsson J. P., Tiberg C., Edkymish A. and Kleja D. B. (2011) Modelling lead(II) sorption to ferrihydrite and soil organic matter. *Environ. Chem.* **8**, 485–492.
- Hamilton W. C. (1965) Significance tests on the crystallographic $\{R\}$ factor. *Acta Crystallogr.* **18**, 502–510. Available at: <http://dx.doi.org/10.1107/S0365110X65001081>.
- Heberling F., Trainor T. P., Lützenkirchen J., Eng P., Denecke M. A. and Bosbach D. (2011) Structure and reactivity of the calcite–water interface. *J. Colloid Interface Sci.* **354**, 843–857. Available at: <http://www.sciencedirect.com/science/article/pii/S0021979710012336>.
- Henderson M. A., Joyce S. A. and Rustad J. R. (1998) Interaction of water with the (1×1) and (2×1) surfaces of α -Fe₂O₃(0 1 2). *Surf. Sci.* **417**, 66–81. Available at: <http://www.sciencedirect.com/science/article/pii/S0039602898006621>.
- Jensen J. O. (2002) Vibrational frequencies and structural determinations of Pb₄(OH)₄₄⁺. *J. Mol. Struct. THEOCHEM* **587**, 111–121. Available at: <http://www.sciencedirect.com/science/article/pii/S0166128002001021>.
- Jordan R. N., Yonge D. R. and Hathhorn W. E. (1997) Enhanced mobility of Pb in the presence of dissolved natural organic matter. *J. Contam. Hydrol.* **29**, 59–80. Available at: <http://www.sciencedirect.com/science/article/pii/S0169772296000873> [Accessed November 13, 2015].
- Koningsberger D. C. and Prins R. (1988) X-ray absorption: principles, applications, techniques of EXAFS, SEXAFS, and XANES.
- Koretsky C. (2000) The significance of surface complexation reactions in hydrologic systems: a geochemist's perspective. *J. Hydrol.* **230**, 127–171.
- Lee P. K., Baillif P. and Touray J. C. (1997) Geochemical behaviour and relative mobility of metals (Mn, Cd, Zn and Pb) in recent sediments of a retention pond along the A-71 motorway in Sologne, France. *Environ. Geol.* **32**, 142–152. Available at: <http://link.springer.com/10.1007/s002540050203> [Accessed November 13, 2015].
- Lefevre G. (2004) In situ Fourier-transform infrared spectroscopy studies of inorganic ions adsorption on metal oxides and hydroxides. *Adv. Colloid Interface Sci.* **107**, 109–123.
- Lin Z. (1996) Secondary mineral phases of metallic lead in soils of shooting ranges from Örebro County, Sweden. *Environ. Geol.* **27**, 370–375.
- Lo C. S., Tanwar K. S., Chaka A. M. and Trainor T. P. (2007) Density functional theory study of the clean and hydrated hematite (1-102) surfaces. *Phys. Rev. B* **75**, 75425. Available at: <http://link.aps.org/doi/10.1103/PhysRevB.75.075425>.
- Mason S. E., Iceman C. R., Tanwar K. S., Trainor T. P. and Chaka A. M. (2009) Pb (II) Adsorption on Isostructural Hydrated Alumina and Hematite (0001) Surfaces: A DFT Study. *J. Phys. Chem. C* **113**, 2159–2170.
- McKenzie R. M. (1980) The adsorption of lead and other heavy metals on oxides of manganese and iron. *Soil Res.* **18**, 61–73.

- Müller B. and Sigg L. (1992) Adsorption of lead(II) on the goethite surface: Voltammetric evaluation of surface complexation parameters. *J. Colloid Interface Sci.* **148**, 517–532. Available at: <http://www.sciencedirect.com/science/article/pii/002197979290187Q>.
- Nriagu J. O. (1990) The rise and fall of leaded gasoline. *Sci. Total Environ.* **92**, 13–28.
- Ostergren J. D., Bargar J. R., Brown G. E. and Parks G. A. (1999) Combined EXAFS and FTIR investigation of sulfate and carbonate effects on Pb(II) sorption to goethite (α -FeOOH). *J. Synchrotron Radiat.* **6**, 645–647. Available at: <http://dx.doi.org/10.1107/S0909049598017750>.
- Ostergren J. D., Brown G. E., Parks G. A. and Persson P. (2000a) Inorganic Ligand Effects on Pb(II) Sorption to Goethite (α -FeOOH): II. Sulfate. *J. Colloid Interface Sci.* **225**, 483–493. Available at: <http://www.sciencedirect.com/science/article/pii/S0021979799967024> [Accessed November 13, 2015].
- Ostergren J. D., Trainor T. P., Bargar J. R., Brown G. E. and Parks G. A. (2000b) Inorganic Ligand Effects on Pb(II) Sorption to Goethite (α -FeOOH): I. Carbonate. *J. Colloid Interface Sci.* **225**, 466–482. Available at: <http://www.sciencedirect.com/science/article/pii/S0021979799967012> [Accessed November 13, 2015].
- Park S.-H. and Sposito G. (2002) Structure of water adsorbed on a mica surface. *Phys. Rev. Lett.* **89**, 85501.
- Parr R. G. (1983) Density functional theory. *Annu. Rev. Phys. Chem.* **34**, 631–656.
- Piper D. and Restrepo J. F. C. (2013) Lead and Cadmium: Priorities for action from UNEP's perspective for addressing risks posed by these two heavy metals. *E3S Web Conf* **1**, 30004. Available at: <http://dx.doi.org/10.1051/e3sconf/20130130004>.
- Reich T. J., Das S., Koretsky C. M., Lund T. J. and Landry C. J. (2010) Surface complexation modeling of Pb (II) adsorption on mixtures of hydrous ferric oxide, quartz and kaolinite. *Chem. Geol.* **275**, 262–271.
- Robertson A. P. and Leckie J. O. (1997) Cation binding predictions of surface complexation models: Effects of pH, ionic strength, cation loading, surface complex, and model fit. *J. Colloid Interface Sci.* **188**, 444–472.
- Robinson I. K. (1986) Crystal truncation rods and surface roughness. *Phys. Rev. B* **33**, 3830–3836. Available at: <http://link.aps.org/doi/10.1103/PhysRevB.33.3830>.
- Robinson I. K. and Tweet D. J. (1992) Surface x-ray diffraction. *Reports Prog. Phys.* **55**, 599.
- Sandalinas C., Ruiz-Moreno S., López-Gil A. and Miralles J. (2006) Experimental confirmation by Raman spectroscopy of a Pb--Sn--Sb triple oxide yellow pigment in sixteenth-century Italian pottery. *J. Raman Spectrosc.* **37**, 1146–1153.
- Scheuhammer A. M. and Norris S. L. (1995) *A review of the environmental impacts of lead shotshell ammunition and lead fishing weights in Canada.*, Canadian Wildlife Service Ottawa, Ontario.

- Schlepütz C. M., Herger R., Willmott P. R., Patterson B. D., Bunk O., Brönnimann C., Henrich B., Hülsen G. and Eikenberry E. F. (2005) Improved data acquisition in grazing-incidence X-ray scattering experiments using a pixel detector. *Acta Crystallogr. Sect. A Found. Crystallogr.* **61**, 418–425.
- Serrano S., O'Day P. A., Vlassopoulos D., García-González M. T. and Garrido F. (2009) A surface complexation and ion exchange model of Pb and Cd competitive sorption on natural soils. *Geochim. Cosmochim. Acta* **73**, 543–558. Available at: <http://www.sciencedirect.com/science/article/pii/S0016703708006844>.
- Smuda J., Dold B., Friese K., Morgenstern P. and Glaesser W. (2007) Mineralogical and geochemical study of element mobility at the sulfide-rich Excelsior waste rock dump from the polymetallic Zn–Pb–(Ag–Bi–Cu) deposit, Cerro de Pasco, Peru. *J. Geochemical Explor.* **92**, 97–110. Available at: <http://www.sciencedirect.com/science/article/pii/S0375674206001993> [Accessed November 13, 2015].
- Stumm W., Hohl H. and Dalang F. (1976) Interaction of metal-ions with hydrous oxide surfaces. *Croat. Chem. Acta* **48**, 491–504.
- Tanwar K. S., Catalano J. G., Petitto S. C., Ghose S. K., Eng P. J. and Trainor T. P. (2007a) Hydrated α -Fe₂O₃ surface structure: Role of surface preparation. *Surf. Sci.* **601**, L59–L64.
- Tanwar K. S., Lo C. S., Eng P. J., Catalano J. G., Walko D. A., Brown G. E. J., Waychunas G. A., Chaka A. M. and Trainor T. P. (2007b) Surface diffraction study of the hydrated hematite surface. *Surf. Sci.* **601**, 460–474. Available at: <http://www.sciencedirect.com/science/article/pii/S0039602806010739>.
- Tiberg C., Sjöstedt C., Persson I. and Gustafsson J. P. (2013) Phosphate effects on copper (II) and lead (II) sorption to ferrihydrite. *Geochim. Cosmochim. Acta* **120**, 140–157.
- Trainor T. P., Chaka A. M., Eng P. J., Newville M., Waychunas G. A., Catalano J. G. and Brown G. E. J. (2004) Structure and reactivity of the hydrated hematite (0001) surface. *Surf. Sci.* **573**, 204–224. Available at: <http://www.sciencedirect.com/science/article/pii/S0039602804012531>.
- Trainor T. P., Eng P. J., Brown G. E. J., Robinson I. K. and Santis M. De (2002a) Crystal truncation rod diffraction study of α -Al₂O₃ surface. *Surf. Sci.* **496**, 238–250. Available at: <http://www.sciencedirect.com/science/article/pii/S003960280101617X>.
- Trainor T. P., Eng P. J. and Robinson I. K. (2002b) Calculation of crystal truncation rod structure factors for arbitrary rational surface terminations. *J. Appl. Crystallogr.* **35**, 696–701. Available at: <http://dx.doi.org/10.1107/S0021889802013985>.
- Trivedi P., Dyer J. A. and Sparks D. L. (2003) Lead Sorption onto Ferrihydrite. 1. A Macroscopic and Spectroscopic Assessment. *Environ. Sci. Technol.* **37**, 908–914. Available at: <http://pubs.acs.org/doi/abs/10.1021/es0257927>.
- Verma S. and Dubey R. S. (2003) Lead toxicity induces lipid peroxidation and alters the activities of antioxidant enzymes in growing rice plants. *Plant Sci.* **164**, 645–655.

- Villalobos M. and Pérez-Gallegos A. (2008) Goethite surface reactivity: A macroscopic investigation unifying proton, chromate, carbonate, and lead(II) adsorption. *J. Colloid Interface Sci.* **326**, 307–323. Available at: <http://www.sciencedirect.com/science/article/pii/S0021979708007686>.
- Villalobos M., Trotz M. A. and Leckie J. O. (2001) Surface Complexation Modeling of Carbonate Effects on the Adsorption of Cr(VI), Pb(II), and U(VI) on Goethite. *Environ. Sci. Technol.* **35**, 3849–3856. Available at: <http://pubs.acs.org/doi/abs/10.1021/es001748k>.
- Vlieg E. (2000) ROD: a program for surface X-ray crystallography. *J. Appl. Crystallogr.* **33**, 401–405. Available at: <http://dx.doi.org/10.1107/S0021889899013655>.
- Wang F., Chen J. and Forsling W. (1997) Modeling sorption of trace metals on natural sediments by surface complexation model. *Environ. Sci. Technol.* **31**, 448–453.
- You H. (1999) Angle calculations for a 4S+2D six-circle diffractometer. *J. Appl. Crystallogr.* **32**, 614–623.

Table 3.1 A complete description of different model trials in terms of binding sites, binding modes and possible protonation schemes

Models	Binding sites		Binding modes		Protonation schemes of surface functional groups*		FOM
	HLT	FLT	HL	FL	HL	FL	
O1O2	O ₁ O ₂ , O ₁ O _{2+y}	clean	CS	N/A	Pb-(^I OH) ₂ -(^{II} OH) ₂ -Fe ₂ -O ₂ - R	(^I OH ₂) ₂ -(^{III} OH) ₂ -Fe ₂ -O ₂ -Fe ₂ -O ₂ - R	5.0
O1O3	O ₁ O ₃ , O ₂ O _{4+x}	clean	ES	N/A	Pb-(^I OH ^I OH ₂)-(^{II} O ^{II} OH)-Fe ₂ -O ₂ - R	(^I OH ₂) ₂ -(^{III} OH) ₂ -Fe ₂ -O ₂ -Fe ₂ -O ₂ - R	6.0
O1O4	O ₁ O _{4+y} , O ₂ O _{3+x}	clean	ES	N/A	Pb-(^I OH ^I OH ₂)-(^{II} O ^{II} OH)-Fe ₂ -O ₂ - R	(^I OH ₂) ₂ -(^{III} OH) ₂ -Fe ₂ -O ₂ -Fe ₂ -O ₂ - R	5.8
O5O6	clean	O ₅ O ₆ , O ₅ O _{6+y}	N/A	CS	(^I OH ₂) ₂ -(^{II} OH) ₂ -Fe ₂ -O ₂ - R	Pb-(^I OH) ₂ -(^{III} OH) ₂ -Fe ₂ -O ₂ -Fe ₂ -O ₂ - R	4.9
O5O7	clean	O ₅ O _{7+x} , O ₆ O ₈	N/A	ES	(^I OH ₂) ₂ -(^{II} OH) ₂ -Fe ₂ -O ₂ - R	Pb-(^I OH ^I OH ₂)-(^{III} O ^{III} OH)-Fe ₂ -O ₂ -Fe ₂ -O ₂ - R	5.4
O5O8	clean	O ₅ O _{8+x} , O _{6+y} O ₇	N/A	ES	(^I OH ₂) ₂ -(^{II} OH) ₂ -Fe ₂ -O ₂ - R	Pb-(^I OH ^I OH ₂)-(^{III} O ^{III} OH)-Fe ₂ -O ₂ -Fe ₂ -O ₂ - R	5.2
O1O3_O5O7	O ₁ O ₃ , O ₂ O _{4+x}	O ₅ O _{7+x} , O ₆ O ₈	ES	ES	Pb-(^I OH ^I OH ₂)-(^{II} O ^{II} OH)-Fe ₂ -O ₂ - R	Pb-(^I OH ^I OH ₂)-(^{III} O ^{III} OH)-Fe ₂ -O ₂ -Fe ₂ -O ₂ - R	5.5
O1O3_O5O8	O ₁ O ₃ , O ₂ O _{4+x}	O ₅ O _{8+x} , O _{6+y} O ₇	ES	ES	Pb-(^I OH ^I OH ₂)-(^{II} O ^{II} OH)-Fe ₂ -O ₂ - R	Pb-(^I OH ^I OH ₂)-(^{III} O ^{III} OH)-Fe ₂ -O ₂ -Fe ₂ -O ₂ - R	5.4
O1O4_O5O7	O ₁ O _{4+y} , O ₂ O _{3+x}	O ₅ O _{7+x} , O ₆ O ₈	ES	ES	Pb-(^I OH ^I OH ₂)-(^{II} O ^{II} OH)-Fe ₂ -O ₂ - R	Pb-(^I OH ^I OH ₂)-(^{III} O ^{III} OH)-Fe ₂ -O ₂ -Fe ₂ -O ₂ - R	5.5
O1O4_O5O8	O ₁ O _{4+y} , O ₂ O _{3+x}	O ₅ O _{8+x} , O _{6+y} O ₇	ES	ES	Pb-(^I OH ^I OH ₂)-(^{II} O ^{II} OH)-Fe ₂ -O ₂ - R	Pb-(^I OH ^I OH ₂)-(^{III} O ^{III} OH)-Fe ₂ -O ₂ -Fe ₂ -O ₂ - R	5.2
O5O7_O5O8	clean	O ₅ O _{7+x} , O ₆ O ₈ , O ₅ O _{8+x} , O _{6+y} O ₇	N/A	ES	Pb-(^I OH ^I OH ₂)-(^{II} O ^{II} OH)-Fe ₂ -O ₂ - R	(^I OH ₂) ₂ -(^{III} OH) ₂ -Fe ₂ -O ₂ -Fe ₂ -O ₂ - R	3.9
O1O3_O1O4	O ₁ O ₃ , O ₂ O _{4+x} , O ₁ O _{4+y} , O ₂ O _{3+x}	clean	ES	N/A	Pb-(^I OH ^I OH ₂)-(^{II} O ^{II} OH)-Fe ₂ -O ₂ - R	(^I OH ₂) ₂ -(^{III} OH) ₂ -Fe ₂ -O ₂ -Fe ₂ -O ₂ - R	2.2

HL and FL represent the half layer termination and the full layer termination surfaces, respectively. CS, ES represent corner-sharing, edge-sharing binding mode, respectively. The naming rules for binding sites are followed as described in Figure 3.1 (C and D). A suffix with a term '+x' or '+y' in the binding sites denotes the associated atom after translating along **a_s** or **b_s** axis for one unit.

*The proposed protonation schemes are based on the bond valence analysis using the ideal surface structure. The protonation schemes in the real situation for the best fit model could be different from those for the ideal case (see the text for detail). **R** represents the stoichiometric repeat of the atom layers (O₂-Fe₂-O₂-Fe₂-O₂) along **c_s** axis.

Table 3.2 Best fit parameters based on CTR analysis on the model O1O3_O1O4

Layer	el	x	y	z	Δx (Å)	Δy (Å)	Δz (Å)	B_{iso} (Å ²)	Occ
HLT surface with Pb bounded at ES1 sites of 9.5% (-1%, +2%)									
^a i ₁	Pb	0.446	0.600	1.056	-	-	-	0.47 (-3E-1, 5E-1)	0.50
^a i ₀	O	0.090	0.833	1.041	-	-	-	0.64 (-4E-2, 9E0)	0.50
Layer-1	O	0.613	0.933	0.906	-0.199 (-2E-3, 1E-1)	-0.216 (-1E-3, 6E-2)	0.019 (-1E-1, 8E-2)	0.40	1.00
	O	0.887	0.433	0.906	0.199 (-2E-3, 1E-1)	-0.216 (-1E-3, 6E-2)	0.019 (-1E-1, 8E-2)	0.40	1.00
Layer-2	O	0.346	0.565	0.752	0.199 (-9E-2, 2E-3)	-0.216 (-9E-4, 9E-2)	0.015 (-2E-2, 8E-2)	0.40	1.00
	O	0.154	0.064	0.752	-0.199 (-9E-2, 2E-3)	-0.216 (-9E-4, 9E-2)	0.015 (-2E-2, 8E-2)	0.40	1.00
Layer-3	Fe	0.500	0.880	0.656	-	-	0.084 (-5E-2, 2E-2)	0.32	1.00
	Fe	0.000	0.379	0.656	-	-	0.084 (-5E-2, 2E-2)	0.32	1.00
Layer-4	O	0.847	0.737	0.580	-	-	-0.125 (-1E-2, 2E-1)	0.40	1.00
	O	0.653	0.236	0.580	-	-	-0.125 (-1E-2, 2E-1)	0.40	1.00
Layer-5	O	0.347	0.904	0.413	-	-	0.077 (-1E-1, 4E-2)	0.40	1.00
	O	0.153	0.403	0.413	-	-	0.077 (-1E-1, 4E-2)	0.40	1.00
Layer-6	Fe	0.000	0.761	0.357	-	-	0.016 (-2E-2, 6E-2)	0.32	1.00
	Fe	0.500	0.260	0.357	-	-	0.016 (-2E-2, 6E-2)	0.32	1.00
HLT surface with Pb bounded at ES2 sites of 12.5% (-1%, +1%)									
^a i ₁	Pb	0.341	1.271	1.044	-	-	-	0.95 (-7E-1, 5E-2)	0.50
^a i ₀	O	0.182	0.903	1.074	-	-	-	9.93 (-9E0, 7E-2)	0.50
Layer-1	O	0.613	0.985	0.918	-0.201 (-2E-4, 2E-2)	0.064 (-4E-2, 6E-2)	0.110 (-4E-2, 3E-2)	0.40	1.00
	O	0.887	0.485	0.918	0.201 (-2E-4, 2E-2)	0.064 (-4E-2, 6E-2)	0.110 (-4E-2, 3E-2)	0.40	1.00
Layer-2	O	0.346	0.627	0.770	0.201 (-3E-2, 6E-4)	0.120 (-1E-2, 4E-2)	0.144 (-1E-2, 2E-2)	0.40	1.00
	O	0.154	0.126	0.770	-0.201 (-3E-2, 6E-4)	0.120 (-1E-2, 4E-2)	0.144 (-1E-2, 2E-2)	0.40	1.00
Layer-3	Fe	0.500	0.880	0.658	-	-	0.097 (-2E-2, 8E-3)	0.32	1.00
	Fe	0.000	0.379	0.658	-	-	0.097 (-2E-2, 8E-3)	0.32	1.00
Layer-4	O	0.847	0.737	0.580	-	-	-0.127 (-9E-3, 7E-2)	0.40	1.00
	O	0.653	0.236	0.580	-	-	-0.127 (-9E-3, 7E-2)	0.40	1.00
Layer-5	O	0.347	0.904	0.419	-	-	0.117 (-3E-2, 2E-5)	0.40	1.00
	O	0.153	0.403	0.419	-	-	0.117 (-3E-2, 2E-5)	0.40	1.00
Layer-6	Fe	0.000	0.761	0.358	-	-	0.023 (-2E-2, 4E-2)	0.32	1.00
	Fe	0.500	0.260	0.358	-	-	0.023 (-2E-2, 4E-2)	0.32	1.00

Table 3.2 Continued

Clean HLT surface of 13.5% (-5%, +4%)									
Layer-1	O	0.693	0.933	0.876	0.201 (-2E-1, 3E-4)	-0.216 (-1E-3, 4E-1)	-0.201 (-2E-2, 2E-1)	0.40	1.00
	O	0.807	0.433	0.876	-0.201 (-2E-1, 3E-4)	-0.216 (-1E-3, 4E-1)	-0.201 (-2E-2, 2E-1)	0.40	1.00
Layer-2	O	0.346	0.565	0.739	0.201 (-2E-1, 4E-4)	-0.217 (-2E-4, 1E-1)	-0.084 (-8E-2, 6E-2)	0.40	1.00
	O	0.154	0.064	0.739	-0.201 (-2E-1, 4E-4)	-0.217 (-2E-4, 1E-1)	-0.084 (-8E-2, 6E-2)	0.40	1.00
Layer-3	Fe	0.500	0.880	0.657	-	-	0.089 (-2E-2, 1E-2)	0.32	1.00
	Fe	0.000	0.379	0.657	-	-	0.089 (-2E-2, 1E-2)	0.32	1.00
Layer-4	O	0.847	0.737	0.578	-	-	-0.139 (-8E-3, 6E-2)	0.40	1.00
	O	0.653	0.236	0.578	-	-	-0.139 (-8E-3, 6E-2)	0.40	1.00
Layer-5	O	0.347	0.904	0.419	-	-	0.115 (-4E-2, 2E-3)	0.40	1.00
	O	0.153	0.403	0.419	-	-	0.115 (-4E-2, 2E-3)	0.40	1.00
Layer-6	Fe	0.000	0.761	0.356	-	-	0.009 (-4E-2, 4E-2)	0.32	1.00
	Fe	0.500	0.260	0.356	-	-	0.009 (-4E-2, 4E-2)	0.32	1.00
Clean FLT surface of 14.5% (-5%, +4%)									
Layer-4	O	0.846	0.697	0.586	-0.006 (-9E-2, 1E-1)	-0.217 (-4E-4, 4E-1)	-0.081 (-1E-1, 8E-2)	0.40	1.00
	O	0.654	0.196	0.586	0.006 (-9E-2, 1E-1)	-0.217 (-4E-4, 4E-1)	-0.081 (-1E-1, 8E-2)	0.40	1.00
Layer-5	O	0.325	0.864	0.389	-0.110 (-4E-2, 3E-2)	-0.217 (-2E-4, 2E-1)	-0.103 (-3E-2, 4E-2)	0.40	1.00
	O	0.175	0.363	0.389	0.110 (-4E-2, 3E-2)	-0.217 (-2E-4, 2E-1)	-0.103 (-3E-2, 4E-2)	0.40	1.00
Layer-6	Fe	0.000	0.761	0.338	-	-	-0.126 (-3E-2, 4E-2)	0.32	1.00
	Fe	0.500	0.260	0.338	-	-	-0.126 (-3E-2, 4E-2)	0.32	1.00
Layer-7	O	0.694	0.535	0.248	-	-	-0.014 (-8E-2, 5E-2)	0.40	1.00
	O	0.806	0.035	0.248	-	-	-0.014 (-8E-2, 5E-2)	0.40	1.00
Layer-8	Fe	0.500	0.810	0.147	-	-	0.012 (-3E-2, 2E-2)	0.32	1.00
	Fe	0.000	0.310	0.147	-	-	0.012 (-3E-2, 2E-2)	0.32	1.00
Layer-9	O	0.153	0.667	0.104	-	-	0.049 (-8E-2, 4E-2)	0.40	1.00
	O	0.347	0.167	0.104	-	-	0.049 (-8E-2, 4E-2)	0.40	1.00

The coordinates are fractional based on the re-indexed unit cell parameters ($a=5.038 \text{ \AA}$, $b=5.434 \text{ \AA}$, $c=7.3707 \text{ \AA}$, $\alpha=90^\circ$, $\beta=90^\circ$, $\gamma=90^\circ$). Δx , Δy , and Δz are atomic displacements in \AA along directions of \mathbf{a}_s axis, \mathbf{b}_s axis, and \mathbf{c}_s axis respectively. The B_{iso} are isotropic Debye-Waller factors and Occ are occupancy parameters. The occupancies of all surface atoms were fixed at 100% in each individual termination. Only one site (Occ=0.5) was shown in the table for clarity, although two symmetry sites were explicitly considered during surface modeling. Numbers inside a parenthesis are the ranges of errors for the best fit parameter values calculated at a 95% confidence level. Note that those errors written in scientific notation do not follow a normal distribution an intrinsic feature for the differential evolution algorithm. Note results for symmetry related copy for each termination listed in the table (total weight=50%) were not included for simplicity. ^a \mathbf{i}_0 is the sorbate layer, and the distal oxygen ligand are represented as \mathbf{i}_1 .

Table 3.3 Bond valence analysis of sorbate, distal oxygen and surface functional groups based on the best fit model structure (valence in v.u.)

	Pb-(^I O, ^{II} O, O _{distal})	O _{distal}	^I O-(Pb,Fe)	^I O-Fe	^{II} O-(Pb,Fe)	^{II} O-Fe ₂
Best fit model	1.65	0.65	1.12	0.61	1.37	0.88
Protonation scheme	2HB (0.18)	2H (0.68) or 1H(0.88) + 1HB (0.25)	1H (0.88)	2H (0.70)	1H (0.68)	1H (0.88) + 1HB (0.24)
Bond valence sum	2.01	2.01 or 1.78	2.00	2.01	2.05	2.00

Bond valence analysis were performed on singly coordinated oxygen (^IO), double coordinated oxygen (^{II}O), distal oxygen coordinated with Pb only (O_{distal}), and Pb under either trigonal pyramid (3 coordinative ligands). H and HB represent the proton and hydrogen bond, respectively. Bond valence is arbitrarily assigned to a proton and a hydrogen bond associated with different group in order to approach the bond valence saturation state. The valence range for a proton (0.68-0.88 v.u) and a hydrogen bond (0.13-0.25 v.u) is used according to Bargar et al. (Bargar et al., 1997a).

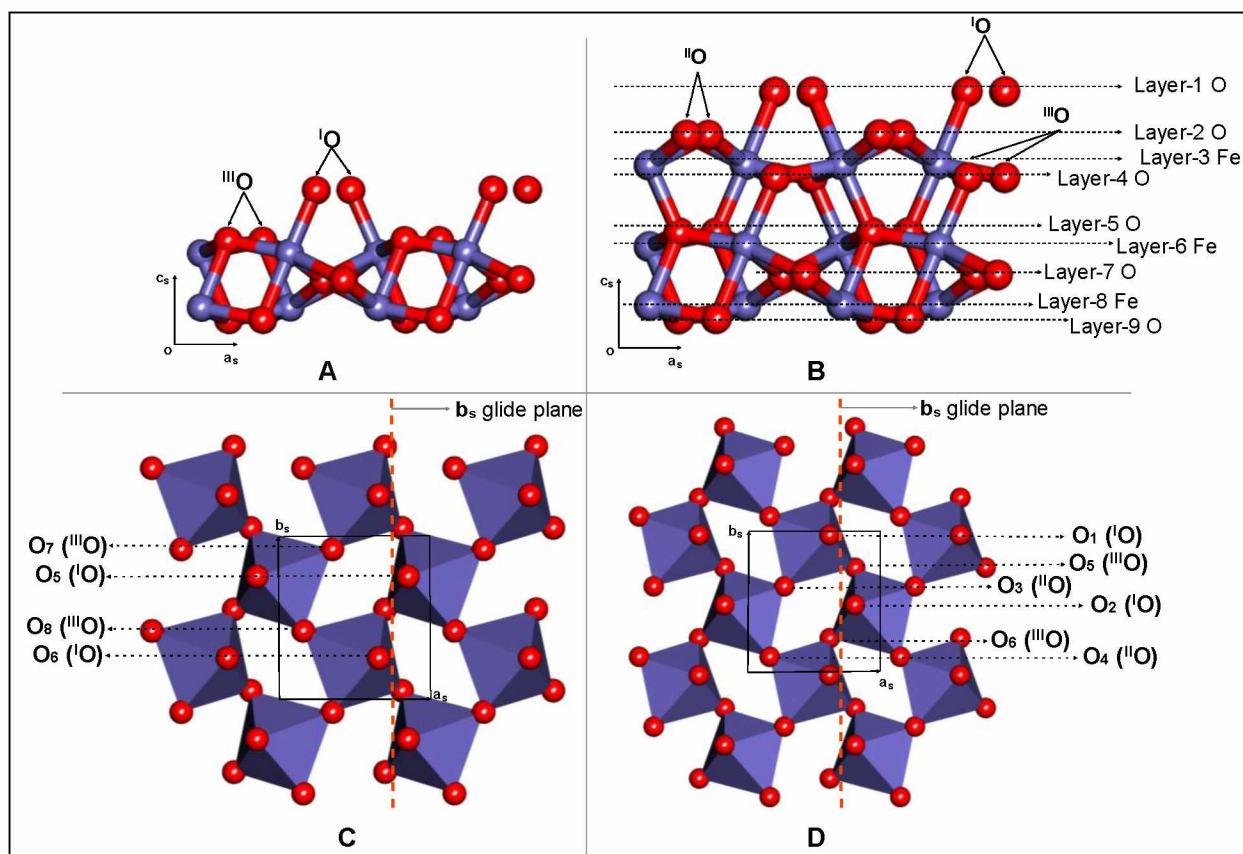


Figure 3.1 (A) Layer stacking sequence along the C_s axis for the full layer termination surface of hematite ($1\bar{1}02$); (B) Layer stacking sequence along the C_s axis for the half layer termination surface of hematite ($1\bar{1}02$); (C) polyhedral representation of the oxygen-terminated full layer termination surface of hematite ($1\bar{1}02$) (second octahedral layer and those beneath are not shown for clarity) ; (D) polyhedral representation of the oxygen-terminated half layer termination surface of hematite ($1\bar{1}02$) (second octahedral layer and those beneath are not shown for clarity). Lengths for unit cell edges are $a=5.038 \text{ \AA}$, $b=5.434 \text{ \AA}$ and $c=7.3707 \text{ \AA}$. The $^{\text{III}}\text{O}$, $^{\text{II}}\text{O}$, and $^{\text{I}}\text{O}$ represent oxygen triply, doubly and singly coordinated to iron, respectively. Each atom layer is labelled as “Layer-n E”, where n is integer from 1 and E is the element symbol for either O or Fe.

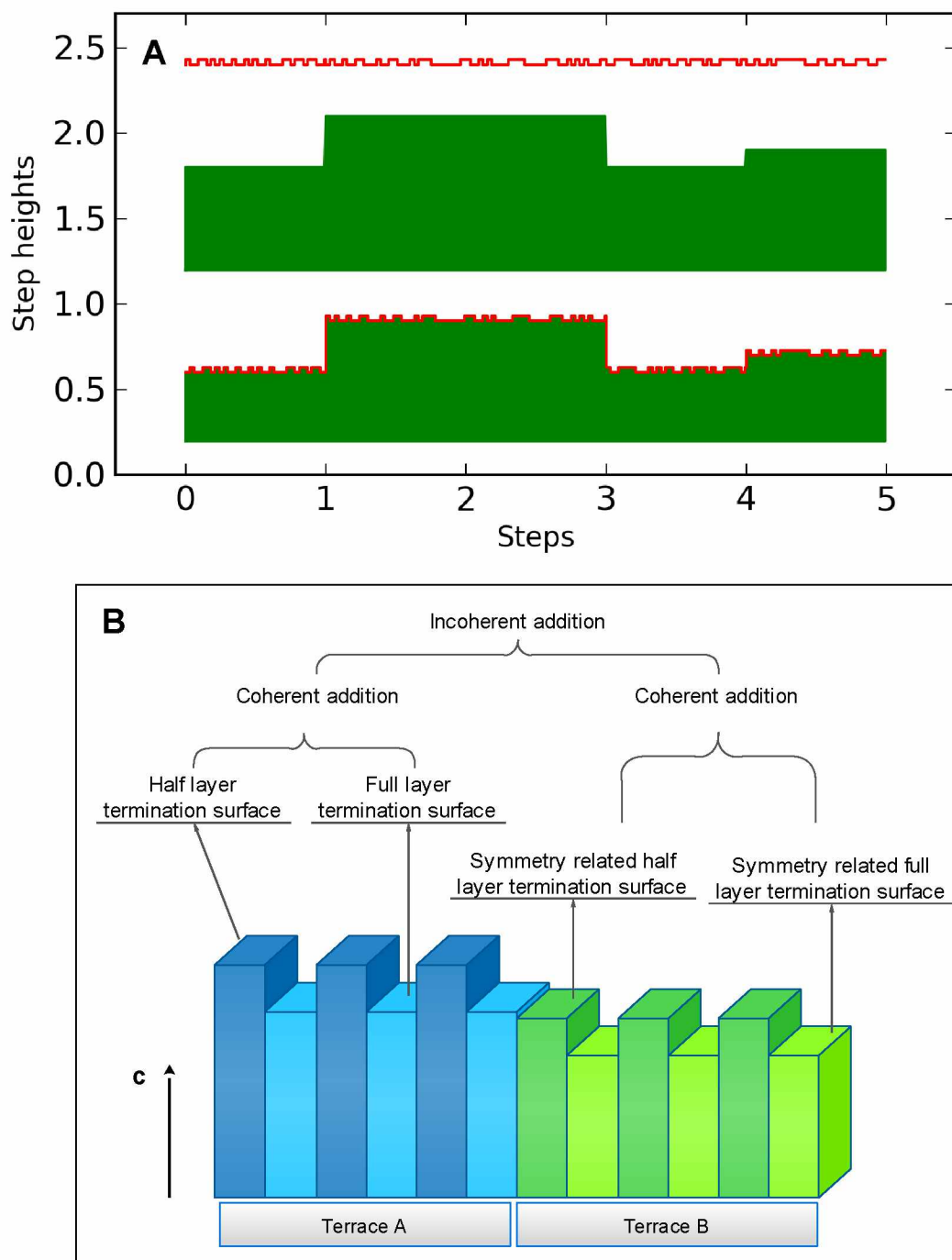


Figure 3.2 (A) Schematic diagram of surface topographic pattern (bottom part) formed by overlapping the termination fine steps (top part) on a surface with terraces of relatively large size (middle part). Step heights are numerical values demonstrating the relative height of steps without physical meaning. (B) A closer view of the step patterns on the CMP-hematite ($1\bar{1}02$) surface showing the relative step height difference between two symmetrically related terraces (Terrace A and Terrace B) as well as the rules for summing over the structure factors among different domains.

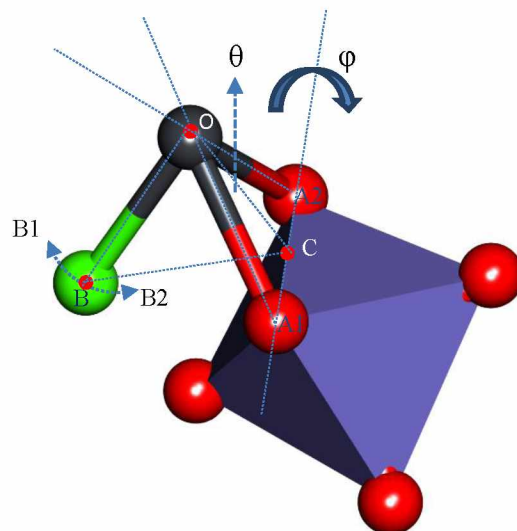


Figure 3.3 Schematic diagram of fitting parameters of Pb and distal oxygen in a bidentate edge-sharing binding mode. The Pb complex trigonal pyramid could rotate about axis A1A2 (A1 and A2 are positions for two anchored oxygen atoms) by ϕ , while the dihedral angle θ (A1OA2, O is the position of Pb atom) could vary in a range from 60° to 90° . To consider the distortion of Pb complex structure, Pb atom is allowed to slide along vector OA1, and distal oxygen could rotate freely on the OBC plane (B is the ideal position of the distal oxygen, and C is the center of A1A2). Red spheres are the surface oxygens, the gray sphere is Pb, the green sphere is the distal oxygen not directly bonded at substrate surface. Fe coordination structure is represented in an octahedral.

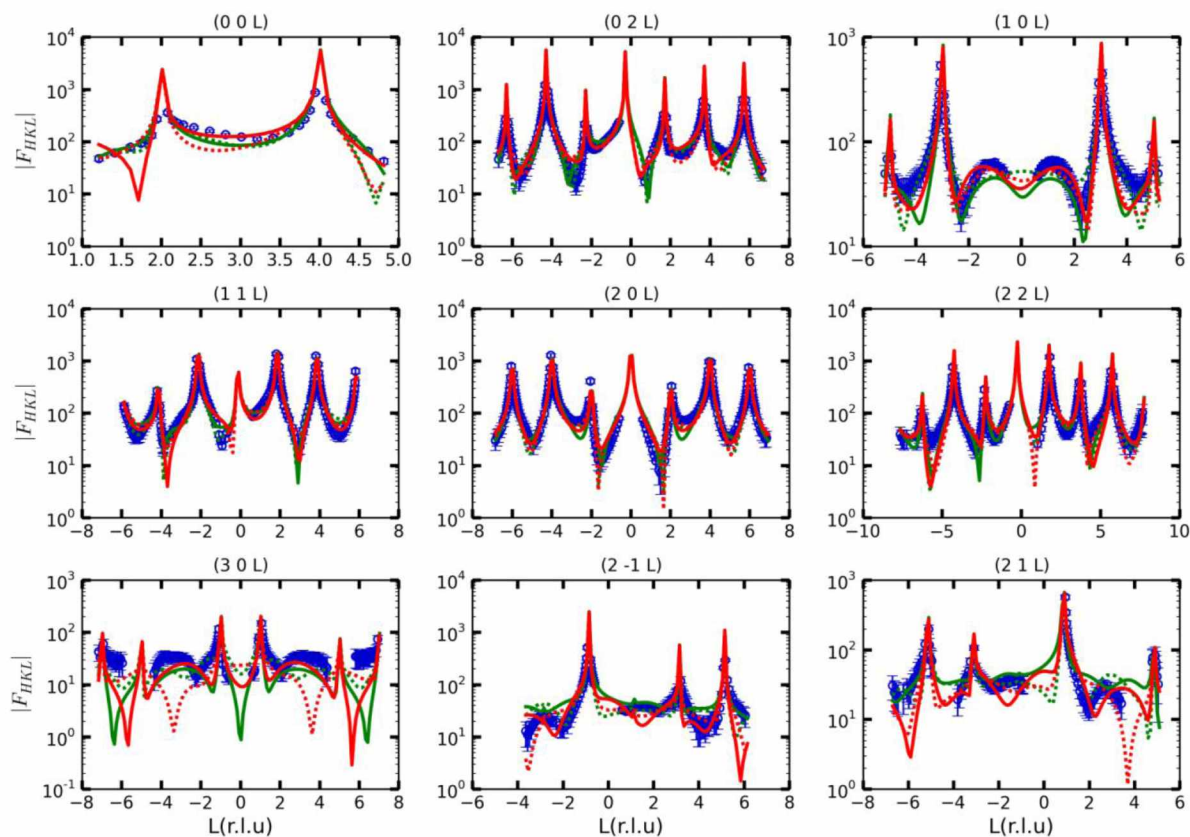


Figure 3.4 Experimental structure factors (F_{HKL}) as a function of perpendicular momentum transfer (L , in reciprocal lattice units) for the hematite ($1\bar{1}02$) surface reacted with $200\ \mu\text{M}$ Pb(II) at pH 5.5. The dash lines in green represent the calculated CTR profiles based on the best fit model O1O2, the solid lines in green represent the calculated CTR profiles based on the best fit model O1O3, the dash lines in red represent the calculated CTR profiles based on the best fit model O5O6, and the solid lines in red represent the calculated CTR profiles based on the best fit model O5O7.

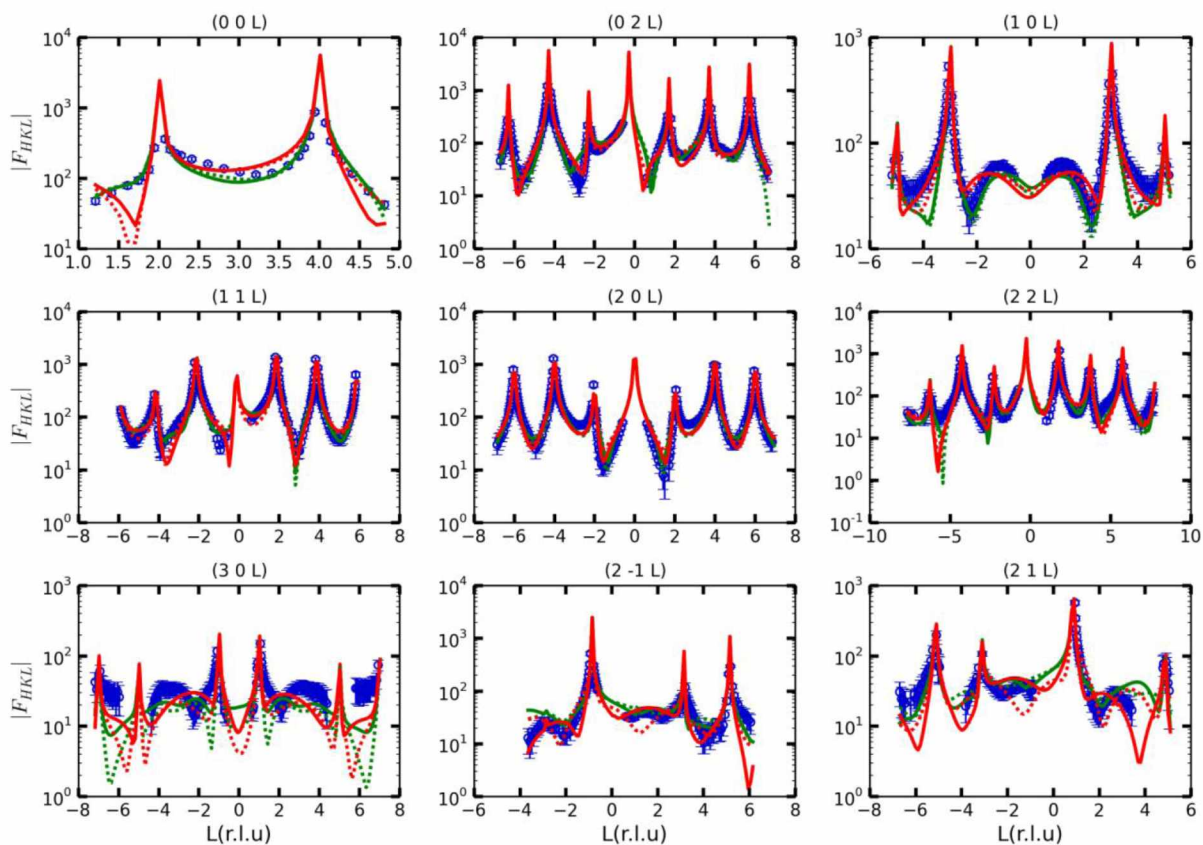


Figure 3.5 Experimental structure factors (F_{HKL}) as a function of perpendicular momentum transfer (L , in reciprocal lattice units) for the hematite ($1\bar{1}02$) surface reacted with $200\ \mu\text{M}$ Pb(II) at $\text{pH } 5.5$. The dash lines in green represent the calculated CTR profiles based on the best fit model O1O3_O5O7 , the solid lines in green represent the calculated CTR profiles based on the best fit model O1O3_O5O8 , the dash lines in red represent the calculated CTR profiles based on the best fit model O1O4_O5O7 , and the solid lines in red represent the calculated CTR profiles based on the best fit model O1O4_O5O8 .

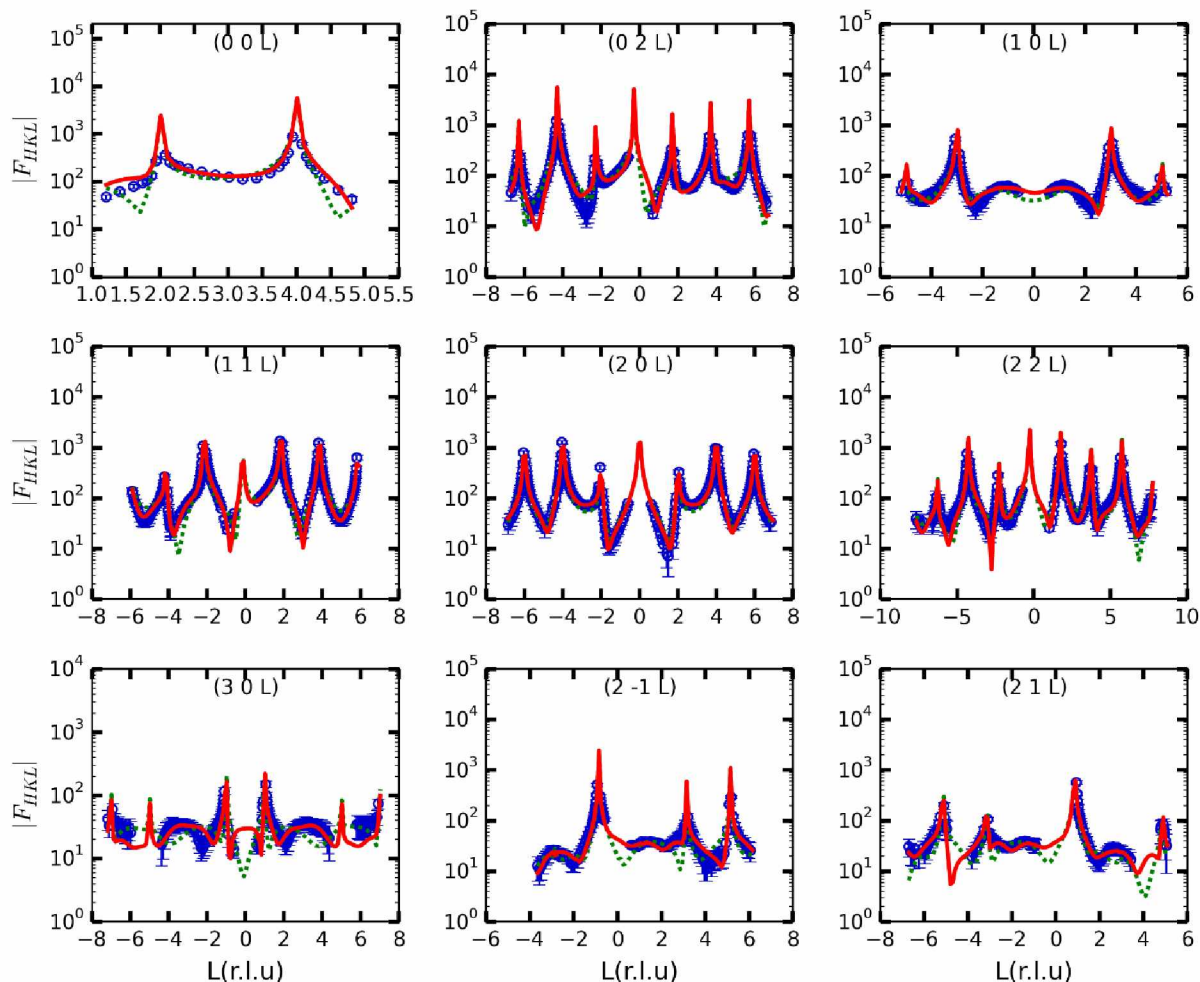


Figure 3.6 Experimental structure factors (F_{HKL}) as a function of perpendicular momentum transfer (L , in reciprocal lattice units) for the hematite ($1\bar{1}02$) surface reacted with $200\ \mu\text{M}$ Pb(II) at $\text{pH } 5.5$. The red solid lines represent the calculated CTR profiles based on the optimized model O1O3_O1O4 without interfacial water, and the green dashed lines represent the calculated CTR profiles based on the optimized model O5O7_O5O8.

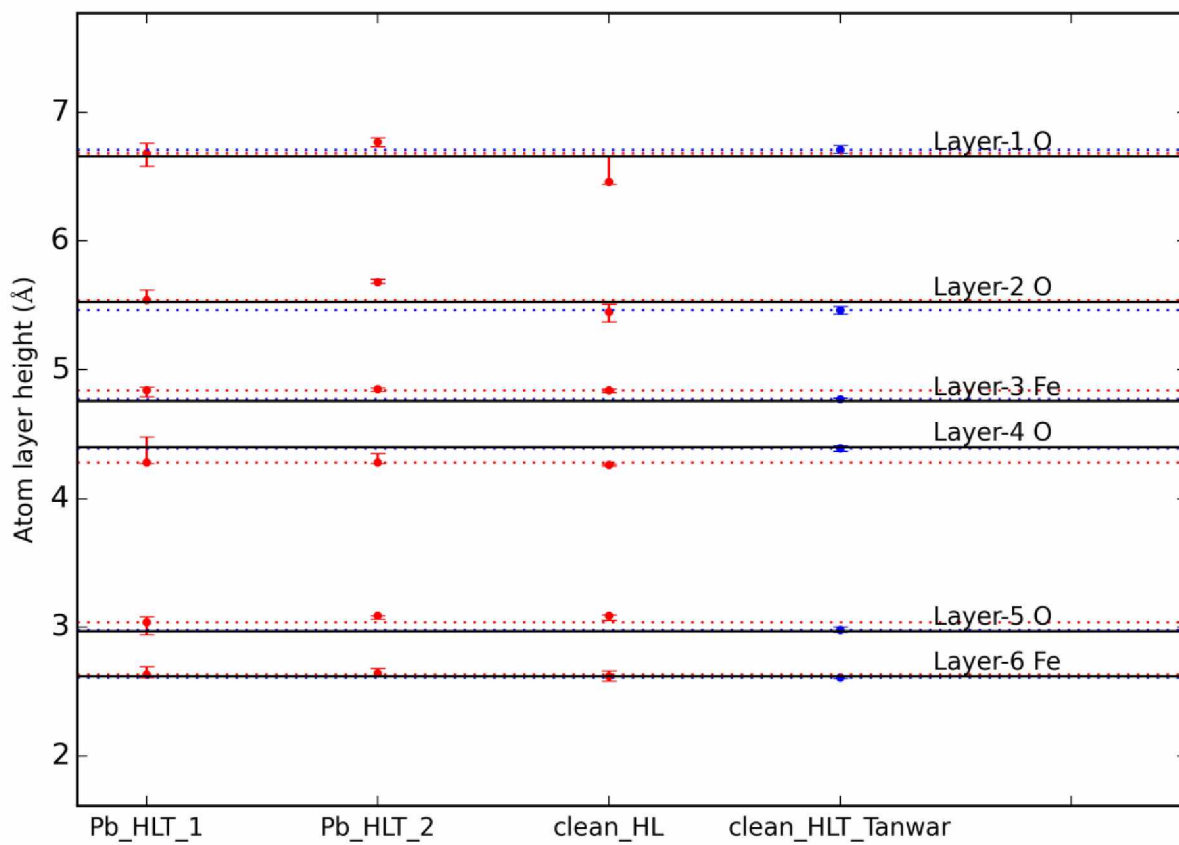


Figure 3.7 Comparison of layer heights of top six atomic layers for the clean (labeled as clean_HL) and Pb bonded HLT (labeled as Pb_HLT_1 for O1O3 site and Pb_HLT_2 for O1O4 site) based on the best fit structural from this study as well as those presented in Tanwar's best fit model (Tanwar et al., 2007b). The solid lines are based on the ideal atomic layer height in the un-relaxed structure. The dash lines in red are drawn based on the layer heights for Pb_HLT_1 and the dash lines in blue are drawn based on layer heights presented in Tanwar's mode.

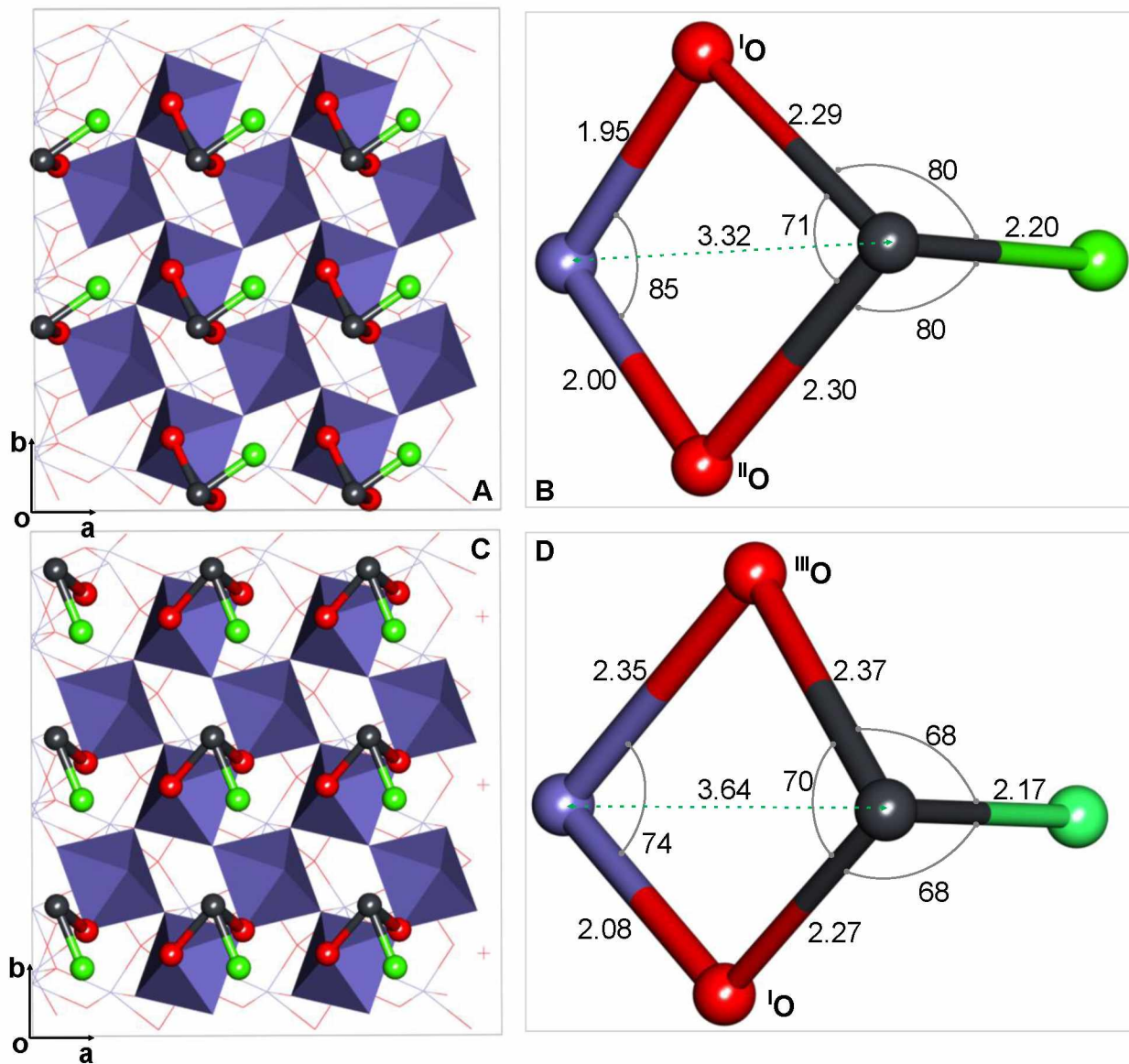


Figure 3.8 Structures of surface complex species with two types of edge-sharing binding configurations on the HL termination surface based on the best fit model. The top view of the interfacial structure for cases of Pb binding at site O1O3 (A) and site O1O4 (C) with first Fe layer visualized as octahedral and the local structure of surface complex species as ball and stick with green balls representing for distal oxygen, red balls surface binding oxygen, gray balls the Pb atom. Note that the symmetry related sites were not shown for clarity. The detailed structural information of the surface complex species at site O1O3 (B) and site O1O4 (D) in terms of bond angles ($^{\circ}$) and bond lengths (\AA). The near neighbor Fe atoms (blue balls) was showed as well. And the local structure of trigonal pyramid was oriented properly for a better view of geometric relationships.

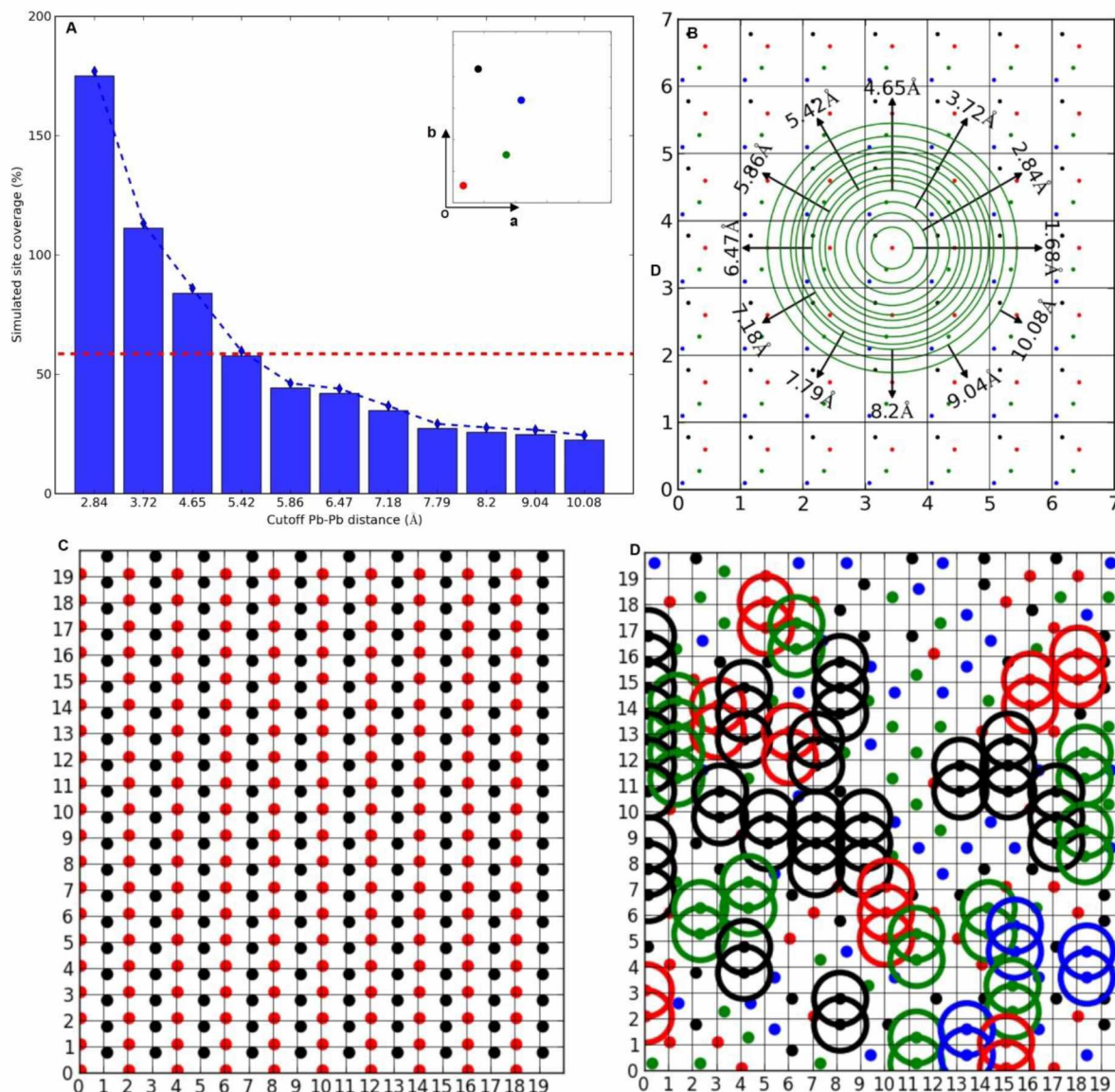


Figure 3.9 (A) The trend of simulated site coverage (%) as a function of cutoff Pb-Pb distances (Å) using the CTR derived reacted surface sites consisting of two pair of symmetric sites (embedded in A). The blue dash lines track the overall trend of simulated coverage over the cutoff Pb-Pb distance. (B) The inter site distances identified from a fully occupied super cell through drawing a variety of co-centered coordinated circles with radius representing the associated inter site distances. (C) An example of site occupation with a super lattice forming but still satisfying the cutoff Pb-Pb distance of 5.42 Å (see text for more explanation). Horizontal dash line in red marks the CTR derived site occupancies. (D) The simulated site occupation pattern associated with the cutoff Pb-Pb distance of 5.42 Å, where the circles in different colors highlight the adjacent sites of same type aligned vertically.

Chapter 4 Structural Study of Surface Complexation of Pb(II) on Annealed and Hydroxylated Hematite($1\bar{1}02$) Surface¹

Abstract

A structural study of Pb(II) adsorption on a high temperature-annealed hematite ($1\bar{1}02$) surface was undertaken using crystal truncation rod (CTR) X-ray diffraction. The best fit CTR model suggests that Pb(II) adsorption on the surface is via an inner-sphere binding mode with a bidentate edge-sharing configuration. The local structure of the Pb surface complex is a distorted trigonal pyramid with an average Pb-O bond length of 2.27 Å, in good agreement with that reported in previous XAFS studies. Pb(II) adsorption at three different possible bidentate sites, 2 different edge-sharing sites, and a corner-sharing site were tested separately in the surface modeling. It was determined that only one edge-sharing site was occupied. This preferred edge-sharing binding site has an O-O edge that appears to better match the binding structure of the Pb(II) complex compared to the other type of edge-sharing site. A bond valence analysis was employed as an extra constraint in the modeling of the CTR data to assure the steric feasibility of the optimized surface complex structure. Under-coordinated surface oxygens were brought to bond valence saturation state by assignment of a protonation scheme. Following this approach a possible stoichiometry of Pb(II) adsorption to the hematite ($1\bar{1}02$) surface was proposed. The proposed stoichiometry indicates that the primary source of proton release is through the deprotonation of surface functional groups ($^{\text{I}}\text{O}$ and $^{\text{III}}\text{O}$) which are chemically bound to Pb.

¹ Qiu C., Majs F., Eng P. J., Stubbs J. and Trainor T. P. (2015) Structural Study of Surface Complexation of Pb(II) on Annealed and Hydroxylated Hematite($1\bar{1}02$) surface. Prepared for submission to *Geochimica et Cosmochimica Acta*.

4.1 Introduction

Pb contamination is a serious environmental issue owing to its notorious toxic effect on organisms (Goyer, 1993; Verma and Dubey, 2003) as well as its widespread usage including the historic use as anti-knocking fuel additive (Nriagu, 1990), paint pigment (Sandalinas et al., 2006), and its current applications in the battery industry (Piper and Restrepo, 2013) and the manufacture of ammunition (Scheuhammer and Norris, 1995; Lin, 1996; Craig et al., 1999). The geochemical properties of Pb in aqueous environments is dictated to a great extent by its sorption to the surface of a variety of natural sorbents, such as Al/Fe-(oxyhydr)oxides, which exhibit wide occurrence in the environment, and serve as effective scavengers of trace metals (McKenzie, 1980; Cornell and Schwertmann, 2003). Specifically, Fe-(oxyhydr)oxides, existing in great abundance in nature, are among the most effective natural substrates for the uptake of aqueous ions.

Previous macroscale batch experiment studies have presented evidences supporting the strong binding of Pb(II) to Fe-(oxyhydr)oxide surfaces in an inner-sphere mode (Müller and Sigg, 1992; Christl and Kretzschmar, 1999; Villalobos et al., 2001; Dyer et al., 2003; Villalobos and Pérez-Gallegos, 2008; Serrano et al., 2009; Gustafsson et al., 2011). In macroscale uptake studies, different surface complexation reactions are tested by using a variety of surface complexation models(SCMs) to fit the experimental sorption data (Davis et al., 1978; Davis and Leckie, 1978). The difficulty of using SCMs lies in the lack of structural details of surface binding configurations, such that it is frequently found that surface complexation modeling based on different sets of stoichiometric reactions could, however, produce an equivalently good fit to the same dataset (Reich et al., 2010; Gustafsson et al., 2011). Such an ambiguity of using SCMs could be effectively solved if the associated surface binding structures could be obtained using

some spectroscopic techniques sensitive to sorbate coordination structures, such as the X-ray adsorption fine structure (XAFS) spectroscopy. Some successful cases of using XAFS-derived binding structures as constraints in the SCM studies have been reported for Pb(II) adsorption to goethite (Ponthieu et al., 2006) and ferrihydrite (Dyer et al., 2003; Tiberg et al., 2013).

The XAFS technique can be employed to achieve structural information, such as identity of near-neighbor atoms, inter-atomic distances and coordination number, which can be further used to derive potential sorbate binding structures (Koningsberger and Prins, 1988; Brown et al., 1995). Consistent with results of batch adsorption experiments, numerous XAFS studies gave rise to molecular-scale structural evidences of inner-sphere Pb surface complex species, which exhibit different binding configurations on a variety of Fe-(oxyhydr)oxides, including hematite (Bargar et al., 1997a; Lenhart et al., 2001; Bargar et al., 2004), goethite (Roe et al., 1991; Ostergren et al., 2000a; Ostergren et al., 2000b) and ferrihydrite (Trivedi et al., 2003; Tiberg et al., 2013). It was found that the binding structure of Pb(II) sorption to Fe-(oxyhydr)oxide surfaces is a function of the substrate type. For example, an XAFS study of Pb(II) adsorption to the goethite and hematite powders suggested the formation of a mononuclear bidentate edge-sharing Pb complex specie on both substrate surfaces (Bargar et al., 1997a). However, under comparable experimental conditions using a single crystal hematite substrate, oligomeric Pb surface complex species were found (Bargar et al., 2004). In addition, the binding configuration of Pb(II) is also related to solution pH. Ostergren et al. (Ostergren et al., 2000a) investigated Pb(II) adsorption on goethite surface using XAFS spectroscopy, and they derived two types of surface Pb complex species, including one with a bidentate edge-sharing binding mode found over a pH range from pH 5.0 to pH 7.0, and the other one in a bidentate corner-sharing binding mode that is only present at pH 5.0. Such a pH dependence of surface binding configuration was

also confirmed in another XAFS study using a ferrihydrite substrate (Trivedi et al., 2003). The underlying mechanism is unclear, although Ostergren et al. (Ostergren et al., 2000a) claimed that it could be attributed to the distinct proton affinity of different types of surface functional groups. Besides the solution pH, the presence of anion ligands, such as phosphate (Tiberg et al., 2013), sulfate (Ostergren et al., 2000b), carbonate (Ostergren et al., 2000a) and chloride (Bargar et al., 1998), were also found to change the binding structure of surface Pb complexes through forming the associated ternary complexes.

Although the XAFS technique could be used to derive detailed surface complexation structures, it is difficult to rely on XAFS spectroscopy to arrive at a unique surface binding configuration, especially when there are multiple potential reactive surface sites with similar binding structures. The main limitation of using XAFS-derived structural information lies in its incapability of resolving the detailed geometrical relationship between the sorbate and the substrate, since the XAFS spectra is only sensitive to the local structure of a sorbate species. As a result, some ambiguities could be confronted when using the cation-cation distance to derive the surface binding structures. For example, a relatively large Pb-Fe separation could be assigned to either a bidentate corner-sharing binding mode or a monodentate binding mode (Trivedi et al., 2003), whereas a relatively shorter Pb-Fe separation could be interpreted as a surface complex species with either a mononuclear bidentate edge-sharing binding configuration or a binuclear tridentate binding configuration (Ostergren et al., 2000a; Ostergren et al., 2000b). The assignment of a unique surface binding structure could become even more difficult when considering the displacements of surface atoms at substrate-fluid interface as observed in a number of surface diffraction studies of different oxides (Chiarello and Sturchio, 1995; Sturchio

et al., 1997; Eng et al., 2000; Trainor et al., 2002a; Trainor et al., 2004; Tanwar, Lo, et al., 2007; Ghose et al., 2010; Fenter et al., 2013).

A unique identification of reactive sites as well as the associated surface complexation structure requires a technique, which is sensitive to the entire interfacial structure. CTR technique provides such a capability, when it is used to probe the surface of a single crystal substrate (Robinson and Tweet, 1992). The CTR profiles are sensitive to the interfacial structure of a substrate, which is modified through atomic displacements as well as the adsorption of “foreign” ions at surface. In the current study, CTR technique was utilized to explore the structural details of Pb(II) adsorption on the hematite ($1\bar{1}02$) surface. The hematite ($1\bar{1}02$) was chosen, since it serves as a model substrate with similar types of surface functional groups as those exposed on the surface of more common forms of Fe-(oxyhydr)oxides, such as goethite, lepidocrocite, and ferrihydrite, which play a key role in a diversity of biogeochemical processes at the Earth’s surface (Cornell and Schwertmann, 2003). In addition, the clean hydrated hematite ($1\bar{1}02$) surface structure has been extensively studied based on both the experimental approach (Catalano et al., 2007; Tanwar et al., 2007a; Tanwar et al., 2007b) and the theoretical computation (Lo et al., 2007). As found in previous CTR studies (Catalano et al., 2007; Tanwar et al., 2007a; Tanwar et al., 2007b), hematite ($1\bar{1}02$) surface could display two chemically distinct surface terminations when it is subject to two surface preparation protocols, i.e. the wet chemical mechanical polishing (CMP) and the surface annealing process. Using CTR technique, we have investigated the surface complexation of Pb(II) on a CMP-prepared hematite($1\bar{1}02$) surface, and the present study is a continual work to examine Pb(II) adsorption to an annealed hematite ($1\bar{1}02$) surface. By comparing results of Pb(II) binding on different surface

terminations of hematite($1\bar{1}02$), we intent to provide deeper insight into the relationship between the surface structure and the surface reactivity.

4.2 Methods and experiments

4.2.1 Sample preparation

A natural single crystal hematite sample was first cut into a small piece with a size of around 2 cm² and a thickness of around 0.5 cm. Then the sample was carefully grinded along ($1\bar{1}02$) lattice plane using a customized gig. Following that the sample surface was further polished following CMP procedures, as detailed elsewhere (Tanwar et al., 2007b). Briefly, the sample was first polished for 20 min using a commercial colloidal silica suspension (0.06 μm diameter) (TED PELLA, USA), which was buffered to pH 11.5 using a NaOH solution. Then we switched to the raw colloidal silica suspension (pH 10.0) and continued to polish the surface for another 10 min, which is followed by 1-hour base wash (crystal soaking in NaOH solution of pH 10.5) and 4-hour acid wash (crystal soaking in HNO₃ solution of pH 2.0). The CMP-prepared sample was then annealed in a furnace of 550 °C for 24 hours under an ambient atmosphere. The annealed sample was cooled in a dessicator overnight prior to reacting with metal solutions.

Metal solutions were prepared in a glove box purged with N₂ gas to avoid CO₂ contamination from the atmosphere. To make metal solutions, reagent grade Pb(NO₃)₂ was dissolved in de-ionized water de-gassed in advance by continuous purge of N₂ gas for 2 hours under a boiling condition. All metal solutions were diluted to 200 μM and carefully adjusted to pH 5.5(\pm 0.1) using NaOH and HNO₃. The surface reaction was initiated by introducing each metal solution to the sample surface using a liquid cell, which was designed specifically for *in situ* surface reactions. The liquid cell was described in detail elsewhere (Heberling et al., 2011). The

thickness of water on top of the crystal surface can be controlled by an adjustable gap between the crystal surface and a Kapton membrane. When the solution is first introduced a thick film (>5 mm) of solution was left atop the surface for 15 minutes. After this equilibration time the film thickness was reduced to several microns and maintained at this thickness throughout the data collection. The quality of the liquid film was monitored through observing the film surface, which should display clear Newton's rings under visible light if the thin liquid film has a relatively uniform thickness. To avoid dehydration of the liquid film due to water escaping through the Kapton film, the liquid cell was capped with a Kapton film dome with water-saturated He (relative humidity >90%) flowing through the dome headspace.

4.2.2 Beamline experiments

CTR measurements were carried out at the undulator beamline 13IDC at Advance Photon Source, Argonne National Laboratory. The energy of incoming X-ray beam was fixed at 13 keV using a liquid nitrogen cooled double single crystal silicon (111) monochromator. X-ray beam was focused and collimated to $360\ \mu\text{m} \times 40\ \mu\text{m}$ (horizontal \times vertical) using two sets of focusing mirrors (horizontal and vertical), which are made of Pt-coated silicon (111) single crystal. A Kappa geometry Newport diffractometer (4S+2D) was used for sample and detector orientation with angles and diffractometer coordinates defined according to You (You, 1999). X-ray intensity prior to the sample was monitored using a N_2 gas filled ion-chamber and the scattering intensity was measured using a Dectris PILATUS 100K 2D pixel array detector with 195×487 pixels (vertical \times horizontal) (Eikenberry et al., 2003). Nine CTRs, including the specular rod, were collected in order to probe both the lateral and vertical electron density of the surface. To collect non-specular CTR data, the incident angle of the beam relative to the sample surface was

fixed at 2° , while an Omega scan was used to scan specular rod with the surface normal of the sample constrained to lie in the lab-frame horizontal plane.

The structure factor (magnitude) was extracted from each Pilatus image using the TDL software package (<http://cars9.uchicago.edu/ifeffit/tld>). Each data point is subject to background subtraction, followed by corrections for active area, polarization, and Lorentz factors to account for the variance of the intercept between Ewald-sphere and the CTR as a function of Q according to the method by Schlepütz et al. (Schlepütz et al., 2005). Potential beam-induced damage to the sample surface was checked by repeat of the collection of a CTR segment several times throughout the course of the measurements. We observed that “check rod” intensities remained within experimental errors indicative of no substantial surface damage.

4.2.3 Structure and terminations of hematite ($1\bar{1}02$) surface

The lattice structure of α -Fe₂O₃ (space group of R-3c) has a hexagonal close-packing of oxygen with iron occupying two-thirds of the octahedral hole. The lattice parameters (5.035 Å, 13.747 Å, 90°, 90°, 120°) as well as the bulk isotropic Debye-Waller factors of α -Fe₂O₃ was reported previously (Finger and Hazen, 1980). In the bulk α -Fe₂O₃ structure, the Fe octahedral structural unit is distorted with two sets of Fe-O bonds (1.95 Å and 2.11 Å). Two dominant growth faces exposed on a natural α -Fe₂O₃ surface are (0001) and ($1\bar{1}02$), respectively (Cornell and Schwertmann, 2003). For convenience, the hematite ($1\bar{1}02$) surface can be re-indexed by defining a pseudo unit cell as described in detail by Trainor et al. (Trainor et al., 2002b). The main advantage of the pseudo-cell is that it places the c-axis parallel to the surface normal (\mathbf{c}_s), with the \mathbf{a}_s and \mathbf{b}_s axes defined within the plane of the surface. After re-indexation, the lattice structure could be defined by a new set of lattice parameters (5.038 Å, 5.434 Å, 7.3707 Å, 90°,

90°, 90°), which maintains in-plane translation symmetry and requires a slab repeated vector $V_r = [-2/3 \ 2/3 \ -1/3]$ to define the out of plane translation symmetry.

The surface termination pattern of hematite ($1\bar{1}02$) has been the focus of numerous studies, which suggest that the sample preparation scheme plays a key role in determining the surface termination pattern. For example, a high temperature annealing at 950 K under the (ultra-high vacuum) UHV would lead to transformation of a stoichiometric (1×1) surface to a reduced (2×1) surface (Henderson et al., 1998). However, when the hematite ($1\bar{1}02$) is annealed in air a stoichiometric (1×1) surface (often named as full layer termination (FLT)) is favored as observed in previous CTR studies (Catalano et al., 2007; Tanwar et al., 2007b). Interestingly, when the hematite ($1\bar{1}02$) surface is subject to CMP procedures, a chemically distinct termination (named as half layer termination (HLT)) become dominant at the surface. The atomic layer sequence of the FLT follows as **O₂-Fe₂-O₂-Fe₂-O₂-O₂-Fe₂-O₂-Fe₂-O₂-R** along the **c_s** axis, where the **R** is the stoichiometric repeat of Fe₂O₃ in the mineral structure. Compared to the stoichiometric FLT, the HLT displays a similar atomic layer sequence along **c_s** direction but with a vacancy of surface Fe sites corresponding to **O₂-X-O₂-Fe₂-O₂-O₂-Fe₂-O₂-Fe₂-O₂-R**, where the **X** represents the missing Fe sites.

4.2.4 Surface functional groups in the hematite ($1\bar{1}02$) surface

The top view and side view of the HLT and the FLT are illustrated in Figure 4.1. As shown in Figure 4.1 (panel A and panel B), the HLT consists of three types of surface functional groups (^IO, ^{II}O and ^{III}O), whereas the FLT contains only two types of surface functional groups (^IO and ^{III}O). Each surface functional group was assigned a unique name following a naming rule, which is based on suffixing the symbol ‘O’ with an integer number starting from 1 and symbols (“±x”

or “±y”) representing the in-plane lattice translations (along \mathbf{a}_s or \mathbf{b}_s axis) if necessary, as illustrated in Figure 4.1 (panel C and panel D). Note that inherent symmetry operations in the hematite ($1\bar{1}02$) structure produce Fe octahedral units with different orientations alternating along the \mathbf{b}_s direction as shown in Figure 4.1 (panel C and panel D). The geometrical relationship between two adjacent Fe octahedral units is defined by a \mathbf{b}_s glide plane passing through the in-plane surface lattice point at $(\frac{3}{4}, 0)$ in the re-indexed surface coordinate system. As a result, surface functional groups are present in pairs (Figure 4.1 A and B), which maintain a \mathbf{b}_s glide symmetry relationship as described above. Besides the \mathbf{b}_s glide plane symmetry, another glide plane symmetry is also found in the hematite ($1\bar{1}02$) structure with a direction parallel to the \mathbf{c}_s axis. Such a \mathbf{c}_s glide plane symmetry determines that there are existing two symmetry related terminations offset by $(N+0.5)\mathbf{c}_s$ in height, where N is an integer and \mathbf{c}_s (7.37 Å) is the lattice parameter.

4.2.5 Potential binding sites on hematite ($1\bar{1}02$) surface

With the surface functional groups defined as above, potential surface sites could be identified, including bidentate corner-sharing sites, bidentate edge-sharing sites and tridentate sites. However, our CTR modeling is limited to cases of Pb(II) binding at bidentate sites, since the Pb surface complexes at either a tridentate site or a mono-dentate site will give rise to a Pb-Fe separation too short or too long to be consistent with binding structures presented in previous XAFS studies (Bargar et al., 1997a; Bargar et al., 2004). In addition, we did not consider the surface Pb complex species on the HLT, since an annealed surface has a dominant FLT with a weight of >80%, and thus it is safe to ignore the minor portion of Pb adsorbate binding to the HLT in the CTR modeling. As a result, we tested three structural models in total corresponding

to Pb(II) binding to three types of surface sites on the FLT, namely the bidentate corner-sharing site (O_1O_2 and O_1O_{2+y}), the bidentate edge-sharing site of type 1 (O_1O_{3+x} and O_2O_4) and the bidentate edge-sharing site of type 2 (O_1O_{4+x} and $O_{2+y}O_3$). Note we employed a naming rule above for each surface site through concatenating the names of the associated constituent oxygen groups, and each type of site consists of two symmetry sites due to the presence of the b_s glide plane symmetry at the surface mentioned above. To make the following discussion easier, we also assign an arbitrary name to each structural model under consideration, i.e. model CS for the bidentate corner-sharing mode, model ES1 for the bidentate edge-sharing mode of type 1, model ES2 for the bidentate edge-sharing mode of type 2. The details of the binding configuration for Pb adsorbate in each model are listed in Table 4.1.

4.2.6 Description of the CTR analysis

4.2.6.1 Calculation of structure factor for a multi-unit cell model

The CTR scattering intensity is proportional to the magnitude of the structure factor $|F_T|$, which is calculated using the method that has been well described elsewhere (Robinson, 1986; Vlieg, 2000; Fenter, 2002). In this study, the model refinement is performed based on a multi-unit cell model, which explicitly contains different types of surface terminations. As shown in our CTR study of the clean annealed hematite ($1\bar{1}02$) surface (referring to Chapter 2), the annealing leads to the projection of the near surface Fe atoms from one HLT unit cell to occupy the vacant surface Fe sites in another HLT unit cell resulting in the termination transformation to the FLT. We found that the termination transformation is incomplete in the annealing process, resulting in an annealed surface containing both the HLT (<20%) and the FLT (>80%). Interestingly, our best fit CTR model further inferred that the annealed surface displays two

symmetry related domains offset by $(N+0.5)c_s$ in height (N is any integer and c_s is the lattice parameter), as illustrated in Figure 4.2. The best fit CTR modeling results of a clean hematite ($1\bar{1}02$) surface indicate that each domain contains three terminations, including 8% HLT, 13.5% long FLT, and 28.5% short FLT, where the long FLT and the short FLT are symmetry related through a c_s glide plane mentioned above. Note that a long(short) FLT on one domain is a crystallographically equivalent copy of a short(long) FLT on the other symmetry related domain, as illustrated in Figure 4.2. As a result, the total weights for symmetry related FLT's are equivalent across the substrate surface. In this two-domain/multi-termination model structure, the calculation of the total structure factor is performed through a specific coherence rule, where the structure factors from different domains are added up incoherently while the structure factors of the terminations within the same domain are summed over coherently. The CTR work of a clean annealed surface builds the basis for performing CTR modeling of an annealed hematite ($1\bar{1}02$) surface reacted with Pb(II) in this study. Based on the surface structural model of a clean annealed substrate described above, the total structure factors of a Pb-bonded annealed hematite ($1\bar{1}02$) surface could be calculated through summing over the structure factor for each constituent termination using the coherence rule defined above.

4.2.6.2 Procedure of CTR model refinement

The surface modeling is performed throughout two different phases. In the first phase, the model structure consists of three terminations within each domain, i.e. clean HLT surface, Pb(II) reacted short FLT surface and Pb reacted long FLT surface, respectively. In this phase, termination weights were constrained from the best fit CTR modeling results for the clean annealed hematite ($1\bar{1}02$) surface, as mentioned above. During the model refinement, Pb-bonded

short FLT and clean HLT were optimized independently considering that Pb-bonded long FLT is symmetrically related to Pb-bonded short FLT. In this three-termination structural model, Pb occupancy on the FLT is allowed to float for optimization. In the second phase, the clean FLT surface is separated from the Pb-bonded FLT surface to consider the possible atom relaxation induced by Pb(II) adsorption. As a consequence, the types of the surface termination increase to five, including the clean HLT surface, the Pb(II)-reacted short FLT surface, the clean short FLT surface, the Pb(II)-reacted long FLT surface and the clean long FLT surface, respectively. Weights for Pb-bonded FLT were calculated from the Pb occupancy obtained from the first phase. Likewise, we linked symmetry related terminations (two types of clean FLT, and two types Pb-bonded FLT) during model refinement. As a result, three chemically distinct terminations (clean HLT, clean long FLT, and Pb-bonded long FLT) were optimized independently in the second phase.

Each model trial was run by optimizing model parameters, including the atomic displacements, atomic occupancies and isotropic atomic Debye Waller factors. To decrease the number of fitting variables, the in-plane displacement was considered only for top two atomic layers, while the out-of-plane relaxation could be extended up to 6th atomic layers. Two surface atoms within the same atomic layer were grouped by considering an equivalent out-of-plane movement and using the b_s glide plane symmetry to constrain the in-plane displacements, as mentioned above. To refine the sorbate positions (Pb and distal O) under a bidentate binding configuration, we defined two geometrical parameters, a rotation angle θ and a dihedral angle φ , as illustrated in Figure 4.3. We set a reference to define the rotation angle such that a 0° rotation angle corresponds to a binding structure with Pb adsorbate, the near-neighboring Fe atom and two anchored oxygen atoms are coplanar in the consideration of an edge-sharing binding site

(Figure 4.3). In a corner-sharing binding configuration, 0° rotation angle is defined in a binding structure when the plane formed by the Pb adsorbate and two anchored oxygen atoms is perpendicular to the crystalline plane of $(1\bar{1}02)$. Using these angles as fitting parameters allows the Pb and distal O positions to change while maintaining the geometrical relationship with the anchored surface oxygens (bidentate edge-sharing or corner-sharing binding configuration) as well as a trigonal pyramid local structure. To consider the possible distortion of the local coordination structure, the Pb atom is allowed to slide along one Pb-O bond (vector AIO shown in Figure 4.3) within 0.2 \AA , while the distal O could rotate off the ideal position within 20° on the bisecting plane OBC , as illustrated in Figure 4.3. The occupancy of the distal O was linked to that for Pb atom in the model refinement. Using these constraints a robust surface modeling could be achieved with up to two termination surfaces being optimized simultaneously.

Therefore, each fit was run to optimize parameters for up to two terminations, and this procedure was repeated to cover all terminations until a best fit self-consistent model result was obtained. It should be noted that the isotropic Debye Waller factors of surface atoms in each model run were fixed to bulk values since they were found insensitive to the overall fitting quality. In addition, the interfacial water layers were only considered for the clean substrate surface (both the FLT and the HLT) and were not fit until all the other model parameters were optimized after a complete run cycle for a water-free structural model, since the semi-ordering interfacial waters should make minor contributions to the overall structure factors.

4.2.6.3 Bond valence constraint in the CTR analysis

CTR model refinement was performed using differential evolution (DE) algorithm to minimize the figure of merit (FOM) based on a normalized χ^2 value calculated following Equation

4.4, where F_i represents for the experimental values of the scattering intensity, $F_{i,c}$ the scattering intensity calculated using the method described above, e_i the experimental errors, N the total number of data points, p the total number of fitting parameters.

$$\chi^2 = \sum_{i=1}^N \frac{\left[\frac{|F_i - F_{i,c}|}{e_i} \right]^2}{N-p} \quad (4.4)$$

As described by Björck (Björck, 2011), a converged global minimum FOM could be achieved using the DE algorithm. However, we realized that an optimized model corresponding to the mathematical minimum FOM value does not ensure a physically realistic structure. Therefore, we intent to apply an extra constraint during the surface modeling. Bond valence rule has been proved as a useful tool to predict the chemical plausibility of a specific surface structure model as well as protonation states of surface functional groups, as suggested in numerous publications (Bargar et al., 1995; Bargar et al., 1996; Bargar et al., 1997a; Bargar et al., 1997b; Bargar et al., 1998; Bargar et al., 1999a; Bargar et al., 1999b; Ostergren et al., 2000a; Ostergren et al., 2000b). In the current study, bond valence rule was incorporated into the CTR analysis as an extra constraint to guide the refinement of each model structure. During model fitting, a penalty factor $P(\geq 1)$ was generated as a scaling factor to the original FOM value. The penalty factor P is calculated using the following equation,

$$P = 1 + \sum_{j=1}^n |x_j - f_j| \quad (4.5)$$

where f_j represents for the formal charge of atom j , and x_j the bond valence sum calculated for atom j during fitting. The bond length bond strength equation shown as Equation 4.6,

$$s = e^{\frac{(r_0 - r)}{B}} \quad (4.6)$$

was utilized to calculate the valence for each individual covalent bond (Fe(III)-O bond or Pb(II)-O bond in the current study) as proposed by Brown (Brown and Altermatt, 1985; Brown, 2009).

In Equation 4.6, r_0 is the nominal length of a bond of unit valence, which has been well tabulated for different Metal-O bonds; B is a constant with a value of 0.37 representing the softness of the interaction between the two atoms; r is the actual bond length. It should be noted that we applied a r_0 value for Fe(III)-O bond ($r_0=1.76 \text{ \AA}$) presented by Brown (Brown, 2009), and used a r_0 value for Pb-O bond ($r_0=2.04 \text{ \AA}$) suggested by Bargar et al. (Bargar et al., 1997b).

To account for the protonation/deprotonation of under-coordinated surface oxygen groups, we apply an arbitrary rule that an under-coordinated oxygen is allowed to coordinate with up to two covalent hydrogens (protons) as well as up to two hydrogen bonds but must have a total coordination number not exceeding four in the consideration of four empty electron orbitals in an oxygen atom. As a result, the valence from the covalent hydrogen and the hydrogen bond will be assigned whenever that could result in a better bond valence saturation state. The valences contributed by a covalent hydrogen bond and a hydrogen bond are of 0.68 to 0.88 v.u. and of 0.13 to 0.25 v.u. respectively, as suggested by Bargar et al. (Bargar et al., 1997b).

Based on the bond valence constraint defined above, a penalty value equivalent to 1 indicates a bond valence saturation state, while a value higher than 1 indicates a bond valence non-saturation (either under-saturation or over-saturation). By comparison, it was found that the surface modeling undertaken without a bond valence constraint usually leads to a best-fit model with some atoms having a significant over-saturated or under-saturated bond valence sum, whereas with the bond valence constraint in a CTR modeling it is more likely to attain an optimized model, which not only makes a decent fit to the experimental data, but also has a realistic interfacial structure with atoms achieving bond valence saturation. In addition, we applied a tolerance level (0.2 v.u) in the calculation of the penalty factor for each atom. The tolerance level of 0.2 v.u. is arbitrarily chosen based on the bond valence difference ($\sim 0.2 \text{ v.u.}$)

between two sets of Fe-O bonds (1.95 Å and 2.11 Å) as found in the unrelaxed bulk hematite structure. Then the contribution of the penalty factor from an atom will be ignored if the bond valence non-saturation state for that atom is within the tolerance level, i.e. $|x_j - f_j| < 0.2$ v.u..

4.3 CTR modeling results

Three CTR modeling trials were undertaken based on Pb(II) adsorption at three different bidentate sites on the FLT surface, as listed in Table 4.1. The calculated CTR profiles based on the optimized models are compared in Figure 4.4. As shown in Figure 4.4, the calculated structure factors for the model CS deviates significantly from the experimental data points producing numerous misfits on different rod profiles; for example near (2 2 -5.1), (2 2 3.1) and the whole 30L rod. As for the model ES1, significant misfits were seen at positions near (0 0 3.0), (0 0 5.0) and (2 2 -3). Analogous to model CS, the structure factors in the 30L rod according to the optimized model ES1 were significantly underestimated as well. On the contrary, an excellent fit was obtained in model ES2, which greatly improves the misfits observed in the other two models especially in 30L and 00L rods, as shown in Figure 4.4. Based on the qualitative comparison of fits for three different models, we proposed that the most probable binding configuration of Pb(II) on an annealed hematite ($1\bar{1}02$) surface is through a bidentate edge-sharing mode at two symmetry related surface sites (O_1O_{4+x} and $O_{2+y}O_3$).

The best modeling results based on the model ES2 are compiled in Table 4.2. The optimized ES2 model structure consists of two symmetry related domains (1:1 ratio) with each domain containing different terminations, including 9% clean HLT, 12% long FLT (of which 7.5% is occupied by Pb adsorbate) and 29% short FLT (of which 18% is occupied by Pb adsorbate). In addition, we found that the interfacial waters could not be well constrained since the model

uncertainties for both Debye Waller factors and occupancies were extremely high, as shown in Table 4.2.

4.4 Discussion

4.4.1 Description of best-fit model

4.4.1.1 Relaxation of surface structure

The surface modeling based on a multi-termination structural model provides an opportunity to examine the structural difference between a clean surface termination and a Pb(II) reacted surface termination. As shown in Figure 4.5, the atomic layer heights in the clean FLT derived in this study are consistent with those reported in a previous CTR study of clean annealed hematite ($1\bar{1}02$) (Tanwar et al., 2007a) within model errors. In addition, our best fit model shows a good agreement of layer heights for the top five atomic layers between the clean FLT and the Pb-bonded FLT surface except for Layer-2 O and Layer-3 Fe, which display opposite relaxations, as illustrated in Figure 4.5. In the Pb-bonded FLT, Layer-2 O ($+0.109(\pm 0.004)$ Å) and Layer-3 Fe ($-0.059(\pm 0.006)$ Å) display a relaxation in opposite directions resulting in a large expansion ($+0.168(\pm 0.01)$ Å) of Layer 2-3 (O-Fe). On the contrary, in the clean FLT we found a significant contraction ($-0.174(\pm 0.16)$ Å) of Layer 2-3 (O-Fe) caused by Layer-2 O recessing into bulk structure ($-0.080(\pm 0.1)$ Å) as well as Layer-3 Fe relaxing towards surface ($0.094(\pm 0.06)$ Å). Note that the model uncertainties for atomic layer heights in the clean FLT are generally larger than those in the Pb-bonded FLT, which could be related to the significantly lower proportion of the clean FLT compared to the Pb-bonded FLT.

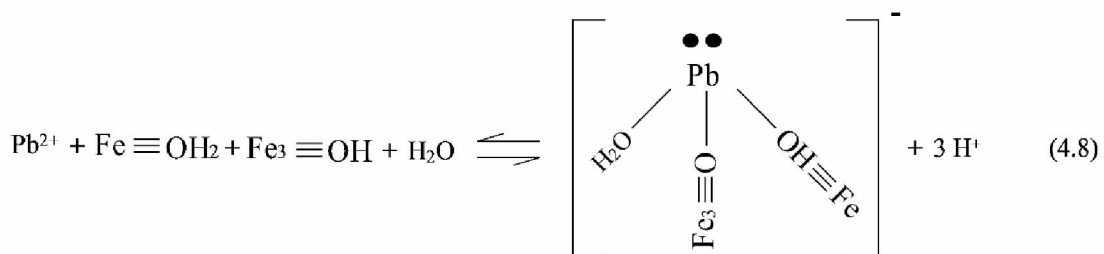
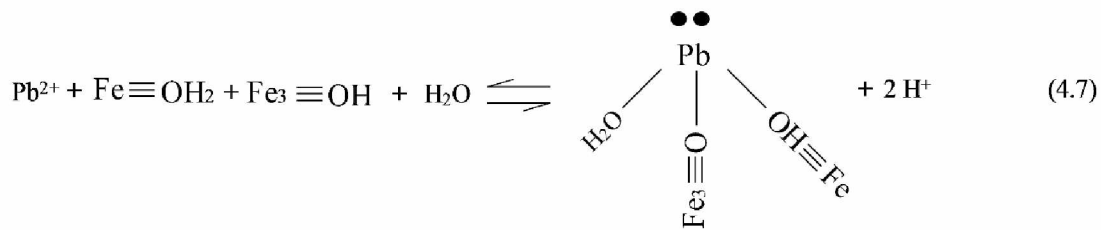
4.4.1.2 Pb complex structure on the FLT

The best fit structural model gave rise to a surface Pb complex species binding via a bidentate edge-sharing mode at two symmetry sites of O_1O_{4+x} and $O_{2+y}O_3$ (named as ES2 sites in hereafter) on the FLT. As illustrated in Figure 4.6B, the local structure of Pb complex is a distorted trigonal pyramid with three Pb-O bonds, two of which (Pb-^IO and Pb-^{III}O) are identical in length (2.30 Å). The shorter Pb-O bond (2.20 Å) is associated with the distal oxygen oriented towards the solution. The O-Pb-O angles associated with the distal oxygen ($78(\pm 4)^\circ$) is significantly larger than the ^IO-Pb-^{III}O angle ($68(\pm 2)^\circ$) indicative of bond angle distortion. In addition, as illustrated in Figure 4.6A, the distal oxygen occupies a position over the valley formed by four adjacent Fe octahedral units, which is more sterically feasible compared to a position when the distal oxygen bends to the other side of the O-Pb-O plane.

The best fit surface complex structure proposed here is also consistent with those reported in previous XAFS studies (Bargar et al., 1997a; Bargar et al., 1998; Bargar et al., 2004) in terms of coordination number (CN=3) and average Pb-O bond lengths (2.24 to 2.30 Å). However, the Pb-Fe separation in the current study is 3.53 Å (Figure 4.6B), significantly larger than those derived from the XAFS studies using hematite powder sample (3.27-3.36 Å) (Bargar et al., 1997a). That could be related to the exposure of multiple types of edge-sharing sites at hematite surface depending on the surface morphology. A hematite substrate in a powder form could expose more types of edge-sharing sites for binding Pb(II), and the short Pb-Fe separation found in that XAFS study may represent the Pb complex species binding to a different bidentate edge-sharing site than the ES2 site found in this study.

4.4.2 Bond valence analysis and the surface complexation reaction stoichiometry

The results of bond valence analysis on the best fit structural model are listed in Table 4.3. As shown in Table 4.3, to arrive at a bond valence saturation state, two protons are required for the ^IO group. The doubly protonated ^IO group will be deprotonated upon Pb(II) sorption to the group producing a singly protonated ^IO group that accepts one hydrogen bond (0.20 v.u.). In addition, the singly protonated ^{III}O group will be subject to a deprotonation as well upon Pb(II) adsorption. However, we noticed that the under-saturated Pb-bonded ^{III}O group (a bond valence deficit of 0.19 v.u.) could not be saturated by accepting a hydrogen bond, since a Pb-bonded ^{III}O group has achieved the maximum coordination number of four. Although we cannot evaluate the bond valence error for the Pb-bonded ^{III}O group, we found that a bond valence deficit of 0.19 v.u. is within the pre-defined arbitrary bond valence tolerance level (0.2 v.u.) suggesting a plausible state. Different from the surface oxygen groups, distal oxygen could have two possible protonation schemes to arrive at a bond valence saturation state. In the first protonation scheme, the distal oxygen is associating with two protons with each proton donating 0.68 v.u., as compared to the other one, where the distal oxygen is singly protonated (0.88 v.u.) and accepts two extra hydrogen bonds (0.24 v.u.).



Using the predicted protonation schemes of different oxygen groups, we proposed two surface complexation reaction stoichiometries, which represent Pb(II) binding at ES2 sites with and without being subject to hydrolysis (Equation 4.7 and 4.8). Similar reaction stoichiometry was also proposed by Bargar et al., who used XAFS-derived structural information as a constraint in the bond valence analysis for developing the surface complexation reaction stoichiometry (Bargar et al., 1997a). Using bond valence constraints, Bargar et al. predicted a doubly protonated $^{\text{I}}\text{O}$ group as well as a deprotonation of that group upon Pb(II) adsorption consistent with our results. As for the $^{\text{III}}\text{O}$ group, Bargar et al. predicted a non-protonated state prior to Pb(II) sorption to this group, which is different from a singly protonated $^{\text{III}}\text{O}$ group presented in this study. In addition, Bargar's bond valence analysis results also suggested that the primary proton release is due to the deprotonation of $^{\text{I}}\text{O}$ group as well as the hydrolysis of the Pb adsorbate. Apparently, Bargar et al. ignored the other possible protonation scheme of the distal oxygen corresponding to a doubly protonated distal oxygen, which is likely to occur at a relatively low pH. It should be noted that the protonation schemes predicted in that XAFS paper lacks structural evidence of the substrate surface. In the XAFS paper, the estimation of the bond valence sum of a surface oxygen group is based on an unrelaxed surface structure rather than a relaxed surface structure, since XAFS technique is insensitive to the substrate surface structure. In light of that, we believe that the bond valence analysis results based on the CTR-derived model structure is superior to deriving more realistic protonation schemes for oxygen groups. However, it should be noted that the bond valence analysis results based on the best fit structural model presented here could not identify a unique protonation scheme for the distal oxygen due to the ambiguity of assigning protons and/or hydrogen bonds to that group as mentioned above. A unique identification of the protonation scheme for the distal oxygen would rely on future studies

based on a combination of the molecular-scale experimental approaches (like XAFS and CTR) and macroscale batch uptake experiments.

4.4.3 Exploration of the relationship between surface reactivity and structure

According to the best fit model structure presented in this study, Pb(II) binding at the ES2 site could reproduce the experimental data much better compared to cases of Pb(II) binding at the other two sites, i.e. ES1 site (including two symmetry site pair of O_1O_{3+x} and O_2O_4) and CS site (including two symmetry site pair of O_1O_2 and O_1O_{2+y}). In this section, we intent to explore the structure/reactivity relationship through comparing the structural details of Pb(II) binding at each site in terms of steric feasibility. The following discussions build on the local structure of Pb complex species at Fe-(oxyhydr)oxide surfaces derived in previous XAFS studies (John R. Bargar, G.E. Brown, et al., 1997; Bargar et al., 2004), which suggest a trigonal pyramid coordination structure with Pb-O bond lengths of $\sim 2.26 \text{ \AA}$. In addition, in order to predict the plausibility of a Pb coordination structure we applied a cutoff limit (72°) for O-Pb-O bond angles according to the observations in a series of semi-empirical quantum-chemical computations, which proposed the optimized complex structures for aqueous Pb complex species (in a form of binuclear cluster $[\text{Pb}_2(\text{OH})_n]^{q+}$) bearing O-Pb-O angles less than 72° (Breza et al., 2003).

The site heterogeneity (bidentate edge-sharing sites) at hematite ($1\bar{1}02$) surface is attributed to the distortion of Fe-octahedral unit that gives rise to different types of bidentate edge-sharing sites bearing characteristic O-Fe-O angles ($85^\circ - 103^\circ$) as well as O-O edge lengths ($2.77 \text{ \AA} - 3.04 \text{ \AA}$). As mentioned above, ES1 and ES2 sites represent two sterically more feasible sites exposed on the FLT hematite ($1\bar{1}02$) surface. To compare the binding configuration of Pb(II) adsorption at these two sites requires the knowledge of the relaxed substrate surface structure,

which is, nonetheless, unknown for Pb(II) binding at ES1 site. To make the comparison fair, unrelaxed hematite ($1\bar{1}02$) surface structures (the FLT) were used as a first approximation to explore the possible trend of site preference for Pb(II) binding. And we assume a regular trigonal pyramid structure for the Pb coordination structure (equivalent Pb-O bond lengths and O-Pb-O angles). In addition, we applied two geometrical constraints to uniquely calculate the positions of Pb sorbate and its distal oxygen, i.e. rotation angle equaling to 0° (Figure 4.3) and three Pb-O bonds with a bond length of 2.26 Å. It should be noted that the first geometrical constraint is based on the best fit model structure of Pb(II) binding at ES2 site, which shows a rotation angle of $-5(\pm 3)^\circ$ statistically consistent with a 0° rotation angle. And the other constraint of Pb-O bond length of 2.26 Å has its basis on surface complex structures presented in previous XAFS studies (Bargar et al., 1997a; Bargar et al., 2004).

Under those constraints described above, the binding structures of Pb(II) adsorption at two different sites were uniquely calculated. As shown in Figure 4.7B, the surface binding structure of Pb(II) sorption at ES1 site requires a O-Pb-O bond angle of 85° in order to maintain a trigonal pyramid local structure with Pb-O bonds of 2.26 Å. Such a O-Pb-O bond angle is much larger than those ($<72^\circ$) predicted in previous semiempirical quantum-chemical studies (Breza et al., 2003). The Pb surface complex with such a large O-Pb-O bond angle should be energetically unfavorable due to the effect of lone electron pair of Pb atom (Shimoni-Livny et al., 1998). In addition, we found that the Pb surface complex species of a larger O-Pb-O bond angle would “pull” the Pb adsorbate and its distal oxygen closer to the associated O-O edge, corresponding to a smaller Pb-Fe separation (2.89 Å) that induces a severe steric constraint with unrealistic short O-O separations (1.96 Å), as shown in Figure 4.7D. On the contrary, Pb(II) binding at ES2 site is sterically more feasible with reasonable O-O separations (>2.69 Å) and smaller O-Pb-O bond

angles (76°) corresponding to a larger separation (3.27 \AA) between Pb adsorbate and its near-neighbor Fe atom, as shown in Figure 4.7A. Interestingly, the Pb-Fe separation of 3.27 \AA calculated from the Pb(II) binding structure at ES2 site is consistent with those reported in previous XAFS studies (John R. Bargar, G.E. Brown, et al., 1997; Bargar et al., 2004), and the O-Pb-O bond angle (76°) for the Pb/ES2 site structure is fairly close to those ($<72^\circ$) proposed in published quantum chemical studies mentioned above. We found that the distinction of Pb(II) binding structure at ES1 and ES2 sites lies in the difference in the associated O-O edge length. The ES1 site has a longer O-O edge (3.04 \AA) than that for ES2 site (2.78 \AA), as shown in Figure 4.7(A, B). As a result, to maintain a trigonal pyramid local structure with Pb-O bonds of 2.26 \AA , the O-Pb-O bond angles in the Pb/ES1 structure have to be enlarged as a compromise for a longer O-O edge. In the case of Pb/ES2 structure, a shorter O-O edge corresponds to a binding structure with smaller O-Pb-O bond angles, which are responsible for an effective alleviation of the steric constraints encountered in the Pb/ES1 structure attributed to a larger separation of the Pb adsorbate and its distal oxygen from the surface oxygens.

Compared to edge-sharing sites, Pb(II) adsorption through bridging two terminal oxygen groups (CS site) should be sterically more feasible, since the Pb and distal O would occupy a position significantly above the surface oxygen groups. However, we notice that the O-O corner-linkage of the CS site experienced an elongation to 3.05 \AA according to our best fit model structure of Pb-bonded FLT. Pb(II) adsorption to such a long O-O corner-linkage would correspond to a Pb surface complex species with a steric infeasible coordination structure with a large O-Pb-O bond angle (85°). The formation of a stable Pb surface complex species (O-Pb-O bond angles of 72°) at the CS site requires a O-O corner linkage as short as 2.66 \AA . Note that such a short O-O corner linkage cannot be achieved by displacing two terminal oxygens in the

constraint of b_s glide plane symmetry, since two symmetry related terminal oxygens within each unit cell would be separated at least by a distance of 2.72 \AA ($c_s/2$) when they sit on the b_s glide plane through some in-plane movement (Figure 4.1D). The other possible reason to render CS sites less reactive could be related to a larger Pb-Fe separation (weaker Pb-Fe interaction), as revealed in a previous DFT study of Pb adsorption on hematite (0001) surface undertaken by Mason et al. (Mason et al., 2009).

The results of structural comparisons of Pb(II) binding at different surface sites are consistent with Pb surface complex species on the annealed hematite ($1\bar{1}02$) surface derived from the CTR modeling, and the results also provide a sound evidence of the relationship between the surface reactivity and the structure of surface sites. According to the structural comparisons of Pb(II) adsorption to different bidentate sites, it seems that the surface binding configuration of Pb(II) on hematite ($1\bar{1}02$) surface is determined by a balance among different factors, such as steric feasibility and lone electron pair effect of Pb atom. A stable Pb surface complex will require a binding configuration with physically realistic O-O separations as well as suitable O-Pb-O bond angles. In addition, we also propose here that the analysis of the ion sorption to an unrelaxed substrate surface could be used as a first approximation to guide the prediction of the binding preference for different potential surface sites, as long as a detailed knowledge of the substrate surface terminations as well as the coordination structure of the studied element is available.

4.5 Conclusions

The surface complexation of Pb(II) on an annealed hematite ($1\bar{1}02$) surface was explored through CTR diffraction. The best fit model indicates that Pb(II) is preferentially bound to the ES2 sites on the FLT surface in an inner-sphere mode. The optimized binding structure is a

distorted trigonal pyramid with an average Pb-O bond length of 2.27 Å in good agreement with previous XAFS studies. Pb(II) adsorption at the other binding sites were not observed indicative of the binding preference of Pb(II) at ES2 sites.

To explain the site preference observed in this study, the structural details of Pb(II) binding at different sites were compared to provide insights into the relationship between the surface structure and the surface reactivity. It was found that the reactive ES2 sites bear a shorter O-O edge allowing for the adsorption of Pb(II) with reasonable O-Pb-O bond angles and O-O separations, as opposed to ES1 sites, which have an O-O edge apparently too long to form a stable Pb complex due to a severe steric constraint corresponding to unreasonably short O-O separation (<2.0 Å). The structural details presented in the current study provide a sound evidence that the surface reactivity for Pb(II) binding is determined to a great extent by the surface structure. The energetically more favorable sites should bear local structures, which not only have a better structural match to the coordination structure of an adsorbate, but also provide a more desirable coordination environment to minimize the strain caused by steric constraints.

The results of bond valence analysis suggested that one $^{\text{I}}\text{O}$ group and one $^{\text{III}}\text{O}$ group would release one proton upon Pb bonding to those groups, while the counterpart groups ($^{\text{I}}\text{O}$ and $^{\text{III}}\text{O}$ unbounded with Pb atom) will remain doubly protonated and singly protonated, as observed for a clean hydrated hematite ($1\bar{1}02$) surface. The proton stoichiometry regarding to the distal oxygen could not be uniquely predicted using bond valence analysis, since either a doubly protonated distal oxygen or a singly protonated distal oxygen associating with an extra weak hydrogen bond could arrive at a bond valence saturation state. The proton stoichiometry of the distal oxygen is probably related to the solution pH with a low pH favoring a doubly protonated distal oxygen group and a high pH favoring the deprotonation of the group. The structural details

generated in the present study improve the understanding the surface complexation of Pb(II) on the hematite (1102) surface, which can be used as a basis in further studies of the macroscale surface complexation modeling of the Pb(II) sorption behavior on iron oxide samples over wide experimental conditions.

4.6 Acknowledgements

This project is funded by DoD SERDP grant ER-1770. All the associated experiments were performed at beamline 13BMC of GeoSoilEnviroCARS (Sector 13), Advanced Photon Source (APS), Argonne National Laboratory. GSECARS is supported by the National Science Foundation - Earth Sciences (EAR-1128799) and Department of Energy - Geosciences (DE-FG02-94ER14466). Use of the Advanced Photon Source was supported by the U. S. Department of Energy, Office of Science, Office of Basic Energy Sciences, under Contract No. DE-AC02-06CH11357. We would also like to thank the Arctic Super Computer Center (ARSC) at University of Alaska Fairbanks for providing computation resource used in the surface modeling.

4.7 References

- Bargar J. R., Brown G. E. and Parks G. A. (1997a) Surface complexation of Pb(II) at oxide-water interfaces: II. XAFS and bond-valence determination of mononuclear Pb(II) sorption products and surface functional groups on iron oxides. *Geochim. Cosmochim. Acta* **61**, 2639–2652. Available at: <http://www.sciencedirect.com/science/article/pii/S0016703797001257> [Accessed November 27, 2015].
- Bargar J. R., Brown G. E. and Parks G. A. (1998) Surface Complexation of Pb(II) at Oxide-Water Interfaces: III. XAFS Determination of Pb(II) and Pb(II)-Chloro Adsorption Complexes on Goethite and Alumina. *Geochim. Cosmochim. Acta* **62**, 193–207. Available at: <http://www.sciencedirect.com/science/article/pii/S0016703797003347>.
- Bargar J. R., Brown G. E. and Parks G. A. (1995) XAFS study of Pb (II) sorption at the α -Al₂O₃-water interface. *Phys. B Condens. Matter* **208-209**, 455–456. Available at: <http://www.sciencedirect.com/science/article/pii/0921452694007228>.

- Bargar J. R., Persson P. and Jr. G. E. B. (1999a) Outer-sphere adsorption of Pb(II)EDTA on goethite. *Geochim. Cosmochim. Acta* **63**, 2957–2969. Available at: <http://www.sciencedirect.com/science/article/pii/S0016703799002641>.
- Bargar J. R., Reitmeyer R. and Davis J. A. (1999b) Spectroscopic Confirmation of Uranium(VI)-Carbonato Adsorption Complexes on Hematite. *Environ. Sci. Technol.* **33**, 2481–2484. Available at: <http://pubs.acs.org/doi/abs/10.1021/es990048g>.
- Bargar J. R., Towle S. N., Brown G. E. and Parks G. A. (1997b) XAFS and Bond-Valence Determination of the Structures and Compositions of Surface Functional Groups and Pb(II) and Co(II) Sorption Products on Single-Crystal α -Al₂O₃. *J. Colloid Interface Sci.* **185**, 473–492. Available at: <http://www.sciencedirect.com/science/article/pii/S0021979796945749>.
- Bargar J. R., Towle S. N., Jr. G. E. B. and Parks G. A. (1996) Outer-sphere Pb(II) adsorbed at specific surface sites on single crystal α -alumina. *Geochim. Cosmochim. Acta* **60**, 3541–3547. Available at: <http://www.sciencedirect.com/science/article/pii/0016703796002220>.
- Bargar J. R., Trainor T. P., Fitts J. P., Chambers S. A. and Brown G. E. (2004) In Situ Grazing-Incidence Extended X-ray Absorption Fine Structure Study of Pb(II) Chemisorption on Hematite (0001) and (1-102) Surfaces. *Langmuir* **20**, 1667–1673.
- Björck M. (2011) Fitting with differential evolution: an introduction and evaluation. *J. Appl. Crystallogr.* **44**, 1198–1204. Available at: <http://dx.doi.org/10.1107/S0021889811041446>.
- Breza M., Biskupič S. and Manová A. (2003) On the structure of lead (II) complexes in aqueous solutions.: Part IV. Binuclear clusters. *Polyhedron* **22**, 2863–2867.
- Brown G. E., Parks G. A. and O'Day P. A. (1995) Sorption at mineral-water interfaces: macroscopic and microscopic perspectives. *Miner. Surfaces* **5**.
- Brown I. D. (2009) Recent Developments in the Methods and Applications of the Bond Valence Model. *Chem. Rev.* **109**, 6858–6919. Available at: <http://pubs.acs.org/doi/abs/10.1021/cr900053k>.
- Brown I. D. and Altermatt D. (1985) Bond-valence parameters obtained from a systematic analysis of the Inorganic Crystal Structure Database. *Acta Crystallogr. Sect. B* **41**, 244–247. Available at: <http://dx.doi.org/10.1107/S0108768185002063>.
- Catalano J. G., Fenter P. and Park C. (2007) Interfacial water structure on the (0 1 2) surface of hematite: Ordering and reactivity in comparison with corundum. *Geochim. Cosmochim. Acta* **71**, 5313–5324.
- Chiarello R. P. and Sturchio N. C. (1995) The calcite (10 $\bar{1}$ 4) cleavage surface in water: Early results of a crystal truncation rod study. *Geochim. Cosmochim. Acta* **59**, 4557–4561.
- Christl I. and Kretzschmar R. (1999) Competitive sorption of copper and lead at the oxide-water interface: Implications for surface site density. *Geochim. Cosmochim. Acta* **63**, 2929–2938. Available at: <http://www.sciencedirect.com/science/article/pii/S0016703799002665>.
- Cornell R. M. and Schwertmann U. (2003) *The iron oxides: structure, properties, reactions, occurrences and uses.*, John Wiley & Sons.

- Craig J. R., Rimstidt J. D., Bonnaffon C. A., Collins T. K. and Scanlon P. F. (1999) Surface water transport of lead at a shooting range. *Bull. Environ. Contam. Toxicol.* **63**, 312–319.
- Davis J. A., James R. O. and Leckie J. O. (1978) Surface ionization and complexation at the oxide/water interface: I. Computation of electrical double layer properties in simple electrolytes. *J. Colloid Interface Sci.* **63**, 480–499.
- Davis J. A. and Leckie J. O. (1978) Surface ionization and complexation at the oxide/water interface II. Surface properties of amorphous iron oxyhydroxide and adsorption of metal ions. *J. Colloid Interface Sci.* **67**, 90–107.
- Dyer J. A., Trivedi P., Scrivner N. C. and Sparks D. L. (2003) Lead Sorption onto Ferrihydrite. 2. Surface Complexation Modeling. *Environ. Sci. Technol.* **37**, 915–922. Available at: <http://pubs.acs.org/doi/abs/10.1021/es025794r>.
- Eikenberry E. F., Brönnimann C., Hülsen G., Toyokawa H., Horisberger R., Schmitt B., Schulze-Briese C. and Tomizaki T. (2003) PILATUS: a two-dimensional X-ray detector for macromolecular crystallography. *Nucl. Instruments Methods Phys. Res. Sect. A Accel. Spectrometers, Detect. Assoc. Equip.* **501**, 260–266.
- Eng P. J., Trainor T. P., Brown G. E. J., Waychunas G. A., Newville M., Sutton S. R. and Rivers M. L. (2000) Structure of the Hydrated α -Al₂O₃ (0001) Surface. *Science (80-.)*. **288**, 1029–1033. Available at: <http://www.sciencemag.org/content/288/5468/1029.abstract>.
- Fenter P. A. (2002) X-ray Reflectivity as a Probe of Mineral-Fluid Interfaces: A User Guide. *Rev. Mineral. Geochemistry* **49**, 149–221. Available at: <http://rimg.geoscienceworld.org/content/49/1/149.short>.
- Fenter P., Kerisit S., Raiteri P. and Gale J. D. (2013) Is the Calcite-Water Interface Understood? Direct Comparisons of Molecular Dynamics Simulations with Specular X-ray Reflectivity Data. *J. Phys. Chem. C* **117**, 5028–5042. Available at: <http://dx.doi.org/10.1021/jp310943s>.
- Finger L. W. and Hazen R. M. (1980) Crystal structure and isothermal compression of Fe₂O₃, Cr₂O₃, and V₂O₃ to 50 kbars. *J. Appl. Phys.* **51**, 5362–5367.
- Ghose S. K., Waychunas G. A., Trainor T. P. and Eng P. J. (2010) Hydrated goethite (α -FeOOH)(100) interface structure: Ordered water and surface functional groups. *Geochim. Cosmochim. Acta* **74**, 1943–1953. Available at: <http://www.sciencedirect.com/science/article/pii/S0039602804012531>.
- Goyer R. A. (1993) Lead toxicity: current concerns. *Environ. Health Perspect.* **100**, 177.
- Gustafsson J. P., Tiberg C., Edkymish A. and Kleja D. B. (2011) Modelling lead(II) sorption to ferrihydrite and soil organic matter. *Environ. Chem.* **8**, 485–492.
- Heberling F., Trainor T. P., Lützenkirchen J., Eng P., Denecke M. A. and Bosbach D. (2011) Structure and reactivity of the calcite--water interface. *J. Colloid Interface Sci.* **354**, 843–857. Available at: <http://www.sciencedirect.com/science/article/pii/S0021979710012336>.
- Henderson M. A., Joyce S. A. and Rustad J. R. (1998) Interaction of water with the (1×1) and (2×1) surfaces of α -Fe₂O₃(0 1 2). *Surf. Sci.* **417**, 66–81. Available at: <http://www.sciencedirect.com/science/article/pii/S0039602898006621>.

- Koningsberger D. C. and Prins R. (1988) X-ray absorption: principles, applications, techniques of EXAFS, SEXAFS, and XANES.
- Lenhart J. J., Bargar J. R. and Davis J. A. (2001) Spectroscopic Evidence for Ternary Surface Complexes in the Lead(II)–Malonic Acid–Hematite System. *J. Colloid Interface Sci.* **234**, 448–452. Available at: <http://www.sciencedirect.com/science/article/pii/S0021979700973454>.
- Lin Z. (1996) Secondary mineral phases of metallic lead in soils of shooting ranges from Örebro County, Sweden. *Environ. Geol.* **27**, 370–375.
- Lo C. S., Tanwar K. S., Chaka A. M. and Trainor T. P. (2007) Density functional theory study of the clean and hydrated hematite (1-102) surfaces. *Phys. Rev. B* **75**, 75425. Available at: <http://link.aps.org/doi/10.1103/PhysRevB.75.075425>.
- Mason S. E., Iceman C. R., Tanwar K. S., Trainor T. P. and Chaka A. M. (2009) Pb (II) Adsorption on Isostructural Hydrated Alumina and Hematite (0001) Surfaces: A DFT Study. *J. Phys. Chem. C* **113**, 2159–2170.
- McKenzie R. M. (1980) The adsorption of lead and other heavy metals on oxides of manganese and iron. *Soil Res.* **18**, 61–73.
- Müller B. and Sigg L. (1992) Adsorption of lead(II) on the goethite surface: Voltammetric evaluation of surface complexation parameters. *J. Colloid Interface Sci.* **148**, 517–532. Available at: <http://www.sciencedirect.com/science/article/pii/002197979290187Q>.
- Nriagu J. O. (1990) The rise and fall of leaded gasoline. *Sci. Total Environ.* **92**, 13–28.
- Ostergren J. D., Trainor T. P., Bargar J. R., Brown G. E. and Parks G. A. (2000a) Inorganic Ligand Effects on Pb(II) Sorption to Goethite (α -FeOOH): I. Carbonate. *J. Colloid Interface Sci.* **225**, 466–482. Available at: <http://www.sciencedirect.com/science/article/pii/S0021979799967012> [Accessed November 13, 2015].
- Ostergren J. D., Brown G. E., Parks G. A. and Persson P. (2000b) Inorganic Ligand Effects on Pb(II) Sorption to Goethite (α -FeOOH): II. Sulfate. *J. Colloid Interface Sci.* **225**, 483–493. Available at: <http://www.sciencedirect.com/science/article/pii/S0021979799967024> [Accessed November 13, 2015].
- Piper D. and Restrepo J. F. C. (2013) Lead and Cadmium: Priorities for action from UNEP's perspective for addressing risks posed by these two heavy metals. *E3S Web Conf* **1**, 30004. Available at: <http://dx.doi.org/10.1051/e3sconf/20130130004>.
- Ponthieu M., Juillot F., Hiemstra T., Van Riemsdijk W. H. and Benedetti M. F. (2006) Metal ion binding to iron oxides. *Geochim. Cosmochim. Acta* **70**, 2679–2698.
- Reich T. J., Das S., Koretsky C. M., Lund T. J. and Landry C. J. (2010) Surface complexation modeling of Pb (II) adsorption on mixtures of hydrous ferric oxide, quartz and kaolinite. *Chem. Geol.* **275**, 262–271.
- Robinson I. K. (1986) Crystal truncation rods and surface roughness. *Phys. Rev. B* **33**, 3830–3836. Available at: <http://link.aps.org/doi/10.1103/PhysRevB.33.3830>.

- Robinson I. K. and Tweet D. J. (1992) Surface X-ray diffraction. *Reports Prog. Phys.* **55**, 599. Available at: <http://stacks.iop.org/0034-4885/55/i=5/a=002>.
- Roe A. L., Hayes K. F., Chisholm-Brause C., Brown G. E. J., Parks G. A., Hodgson K. O. and Leckie J. O. (1991) In situ X-ray absorption study of lead ion surface complexes at the goethite-water interface. *Langmuir* **7**, 367–373.
- Sandalinas C., Ruiz-Moreno S., López-Gil A. and Miralles J. (2006) Experimental confirmation by Raman spectroscopy of a Pb--Sn--Sb triple oxide yellow pigment in sixteenth-century Italian pottery. *J. Raman Spectrosc.* **37**, 1146–1153.
- Scheuhammer A. M. and Norris S. L. (1995) *A review of the environmental impacts of lead shotshell ammunition and lead fishing weights in Canada.*, Canadian Wildlife Service Ottawa, Ontario.
- Schleppütz C. M., Herger R., Willmott P. R., Patterson B. D., Bunk O., Brönnimann C., Henrich B., Hülsen G. and Eikenberry E. F. (2005) Improved data acquisition in grazing-incidence X-ray scattering experiments using a pixel detector. *Acta Crystallogr. Sect. A Found. Crystallogr.* **61**, 418–425.
- Serrano S., O'Day P. A., Vlassopoulos D., García-González M. T. and Garrido F. (2009) A surface complexation and ion exchange model of Pb and Cd competitive sorption on natural soils. *Geochim. Cosmochim. Acta* **73**, 543–558. Available at: <http://www.sciencedirect.com/science/article/pii/S0016703708006844>.
- Shimoni-Livny L., Glusker J. P. and Bock C. W. (1998) Lone Pair Functionality in Divalent Lead Compounds. *Inorg. Chem.* **37**, 1853–1867. Available at: <http://pubs.acs.org/doi/abs/10.1021/ic970909r>.
- Sturchio N. C., Chiarello R. P., Cheng L., Lyman P. F., Bedzyk M. J., Qian Y., You H., Yee D., Geissbuhler P., Sorensen L. B., Liang Y. and Baer D. R. (1997) Lead adsorption at the calcite-water interface: Synchrotron X-ray standing wave and X-ray reflectivity studies. *Geochim. Cosmochim. Acta* **61**, 251–263. Available at: <http://www.sciencedirect.com/science/article/pii/S0016703796003262>.
- Tanwar K. S., Catalano J. G., Petitto S. C., Ghose S. K., Eng P. J. and Trainor T. P. (2007a) Hydrated α -Fe₂O₃ surface structure: Role of surface preparation. *Surf. Sci.* **601**, L59–L64.
- Tanwar K. S., Lo C. S., Eng P. J., Catalano J. G., Walko D. A., Brown G. E. J., Waychunas G. A., Chaka A. M. and Trainor T. P. (2007b) Surface diffraction study of the hydrated hematite surface. *Surf. Sci.* **601**, 460–474. Available at: <http://www.sciencedirect.com/science/article/pii/S0039602806010739>.
- Tiberg C., Sjöstedt C., Persson I. and Gustafsson J. P. (2013) Phosphate effects on copper (II) and lead (II) sorption to ferrihydrite. *Geochim. Cosmochim. Acta* **120**, 140–157.
- Trainor T. P., Chaka A. M., Eng P. J., Newville M., Waychunas G. A., Catalano J. G. and Brown G. E. J. (2004) Structure and reactivity of the hydrated hematite (0001) surface. *Surf. Sci.* **573**, 204–224. Available at: <http://www.sciencedirect.com/science/article/pii/S0039602804012531>.

- Trainor T. P., Eng P. J., Brown G. E. J., Robinson I. K. and Santis M. De (2002a) Crystal truncation rod diffraction study of α -Al₂O₃ surface. *Surf. Sci.* **496**, 238–250. Available at: <http://www.sciencedirect.com/science/article/pii/S003960280101617X>.
- Trainor T. P., Eng P. J. and Robinson I. K. (2002b) Calculation of crystal truncation rod structure factors for arbitrary rational surface terminations. *J. Appl. Crystallogr.* **35**, 696–701. Available at: <http://dx.doi.org/10.1107/S0021889802013985>.
- Trivedi P., Dyer J. A. and Sparks D. L. (2003) Lead Sorption onto Ferrihydrite. 1. A Macroscopic and Spectroscopic Assessment. *Environ. Sci. Technol.* **37**, 908–914. Available at: <http://pubs.acs.org/doi/abs/10.1021/es0257927>.
- Verma S. and Dubey R. S. (2003) Lead toxicity induces lipid peroxidation and alters the activities of antioxidant enzymes in growing rice plants. *Plant Sci.* **164**, 645–655.
- Villalobos M. and Pérez-Gallegos A. (2008) Goethite surface reactivity: A macroscopic investigation unifying proton, chromate, carbonate, and lead(II) adsorption. *J. Colloid Interface Sci.* **326**, 307–323. Available at: <http://www.sciencedirect.com/science/article/pii/S0021979708007686>.
- Villalobos M., Trotz M. A. and Leckie J. O. (2001) Surface Complexation Modeling of Carbonate Effects on the Adsorption of Cr(VI), Pb(II), and U(VI) on Goethite. *Environ. Sci. Technol.* **35**, 3849–3856. Available at: <http://pubs.acs.org/doi/abs/10.1021/es001748k>.
- Vlieg E. (2000) ROD: a program for surface X-ray crystallography. *J. Appl. Crystallogr.* **33**, 401–405. Available at: <http://dx.doi.org/10.1107/S0021889899013655>.
- You H. (1999) Angle calculations for a 4S+2D six-circle diffractometer. *J. Appl. Crystallogr.* **32**, 614–623.

Table 4.1 A complete list of structural models tested in the surface modeling

Models	Binding sites		Binding modes		Protonation schemes	
	HLT	FLT	HLT	FLT	HLT	FLT
CS	clean	O ₁ O ₂ , O ₁ O _{2+y}	N/A	CS	(^I OH ₂) ₂ -(^{II} OH) ₂ -Fe ₂ -R	Pb-(^I OH) ₂ -(^{III} OH) ₂ -Fe ₂ -R
ES1	clean	O ₁ O _{3+x} , O ₂ O ₄	N/A	ES	(^I OH ₂) ₂ -(^{II} OH) ₂ -Fe ₂ -R	Pb-(^I OH ^I OH ₂)-(^{III} O ^{III} OH)-Fe ₂ -R
ES2	clean	O ₁ O _{4+x} , O _{2+y} O ₃	N/A	ES	(^I OH ₂) ₂ -(^{II} OH) ₂ -Fe ₂ -R	Pb-(^I OH ^I OH ₂)-(^{III} O ^{III} OH)-Fe ₂ -R

Note: The binding sites are defined using naming rules described in the text. CS and ES are symbols representative of the corner-sharing binding mode, the edge-sharing binding mode, respectively. The proposed protonation schemes are based on the bond valence analysis for the ideal surface structures.

Table 4.2 Atomic displacements, Debye Waller factors and occupancies for different domains in the best fit model structure

Layer	el	x	y	z	Δx (Å)	Δy (Å)	Δz (Å)	B_{iso} (Å ²)	Occ
Clean HLT surface with weight of 9% (-1%, +2%)									
^a w ₁	O	0.865	0.085	1.176	-	-	-	3.23 (-2E0, 7E0)	0.60 (-6E-1, 3E-3)
^a w ₀	O	0.635	0.585	1.176	-	-	-	3.23 (-2E0, 7E0)	0.60 (-6E-1, 3E-3)
2	O	0.633	0.993	0.884	-0.100 (-4E-4, 2E-1)	0.107 (-2E-1, 2E-3)	-0.140 (-7E-3, 1E-1)	0.40	1.00
	O	0.867	0.493	0.884	0.100 (-4E-4, 2E-1)	0.107 (-2E-1, 2E-3)	-0.140 (-7E-3, 1E-1)	0.40	1.00
4	O	0.324	0.585	0.770	0.090 (-2E-1, 1E-2)	-0.107 (-1E-3, 2E-1)	0.146 (-1E-1, 1E-3)	0.40	1.00
	O	0.176	0.084	0.770	-0.090 (-2E-1, 1E-2)	-0.107 (-1E-3, 2E-1)	0.146 (-1E-1, 1E-3)	0.40	1.00
5	Fe	0.500	0.880	0.665	-	-	0.147 (-1E-1, 2E-4)	0.32	1.00
	Fe	0.000	0.379	0.665	-	-	0.147 (-1E-1, 2E-4)	0.32	1.00
6	O	0.847	0.737	0.580	-	-	-0.124 (-9E-3, 5E-2)	0.40	1.00
	O	0.653	0.236	0.580	-	-	-0.124 (-9E-3, 5E-2)	0.40	1.00
7	O	0.347	0.904	0.396	-	-	-0.050 (-9E-2, 6E-2)	0.40	1.00
	O	0.153	0.403	0.396	-	-	-0.050 (-9E-2, 6E-2)	0.40	1.00
Pb reacted long FLT with weight of 7.5% (-1%, +1%)									
^b i ₁	Pb	0.95	0.416	1.22	-	-	-	0.42 (-2E-1, 7E-2)	0.50
^b i ₀	O	0.59	0.657	1.23	-	-	-	0.84 (-2E-1, 1E0)	0.50
1	O	0.103	0.774	1.093	-0.251 (-1E-4, 2E-2)	-0.176 (-1E-2, 2E-2)	-0.028 (-1E-2, 1E-2)	0.40	1.00
	O	0.397	0.274	1.093	0.251 (-1E-4, 2E-2)	-0.176 (-1E-2, 2E-2)	-0.028 (-1E-2, 1E-2)	0.40	1.00
2	O	0.665	0.950	0.918	0.059 (-1E-2, 1E-2)	-0.126 (-2E-2, 2E-2)	0.109 (-4E-3, 4E-3)	0.40	1.00
	O	0.835	0.450	0.918	-0.059 (-1E-2, 1E-2)	-0.126 (-2E-2, 2E-2)	0.109 (-4E-3, 4E-3)	0.40	1.00
3	Fe	-0.009	0.820	0.847	-0.043 (-5E-3, 6E-3)	-0.053 (-1E-2, 2E-2)	-0.059 (-6E-3, 6E-3)	0.32	1.00
	Fe	0.509	0.320	0.847	0.043 (-5E-3, 6E-3)	-0.053 (-1E-2, 2E-2)	-0.059 (-6E-3, 6E-3)	0.32	1.00
4	O	0.306	0.605	0.759	-	-	0.068 (-1E-2, 5E-3)	0.40	1.00
	O	0.194	0.104	0.759	-	-	0.068 (-1E-2, 5E-3)	0.40	1.00
5	Fe	0.500	0.880	0.639	-	-	-0.042 (-6E-3, 6E-3)	0.32	1.00
	Fe	0.000	0.379	0.639	-	-	-0.042 (-6E-3, 6E-3)	0.32	1.00

Table 4.2 Continued

Layer	el	x	y	z	Δx (Å)	Δy (Å)	Δz (Å)	B_{iso} (Å ²)	Occ
Clean long FLT with weight of 4.5% (-1%, +1%)									
^a w ₁	O	0.054	0.574	1.418	-	-	-	0.84 (-4E-2, 9E0)	0.60 (-5E-1, 3E-4)
^a w ₀	O	0.446	0.074	1.418	-	-	-	0.84 (-4E-2, 9E0)	0.60 (-5E-1, 3E-4)
1	O	0.173	0.826	1.117	0.100 (-2E-1, 6E-4)	0.107 (-2E-1, 2E-3)	0.147 (-2E-1, 3E-4)	0.40	1.00
	O	0.327	0.326	1.117	-0.100 (-2E-1, 6E-4)	0.107 (-2E-1, 2E-3)	0.147 (-2E-1, 3E-4)	0.40	1.00
2	O	0.648	0.978	0.892	-0.024 (-7E-2, 1E-1)	0.028 (-1E-1, 8E-2)	-0.080 (-7E-2, 1E-1)	0.40	1.00
	O	0.852	0.478	0.892	0.024 (-7E-2, 1E-1)	0.028 (-1E-1, 8E-2)	-0.080 (-7E-2, 1E-1)	0.40	1.00
3	Fe	0.019	0.830	0.868	0.095 (-7E-2, 6E-3)	0.001 (-1E-1, 1E-1)	0.094 (-6E-2, 5E-2)	0.32	1.00
	Fe	0.481	0.330	0.868	-0.095 (-7E-2, 6E-3)	0.001 (-1E-1, 1E-1)	0.094 (-6E-2, 5E-2)	0.32	1.00
4	O	0.306	0.605	0.765	-	-	0.112 (-1E-1, 4E-2)	0.40	1.00
	O	0.194	0.104	0.765	-	-	0.112 (-1E-1, 4E-2)	0.40	1.00
5	Fe	0.500	0.880	0.639	-	-	-0.046 (-8E-2, 8E-2)	0.32	1.00
	Fe	0.000	0.379	0.639	-	-	-0.046 (-8E-2, 8E-2)	0.32	1.00

The coordinates are fractional based on the re-indexed unit cell parameters ($a=5.038$ Å, $b=5.434$ Å, $c=7.3707$ Å, $\alpha=90^\circ$, $\beta=90^\circ$, $\gamma=90^\circ$). Δx , Δy , and Δz are atomic displacements in Å along directions of \mathbf{a}_s axis, \mathbf{b}_s axis, and \mathbf{c}_s axis respectively. The B_{iso} are isotropic Debye-Waller factors and Occ are occupancy parameters. The occupancies of all surface atoms were fixed at 100% in each individual domain with the domain weight being optimized during the modeling. Only one site was shown in Pb-bonded long FLT for clarity, although two symmetry sites were explicitly considered during surface modeling. The other two terminations (Pb-bonded short FLT (18%) and clean short FLT (11%)), symmetrically related to Pb-bonded long FLT and clean LFL respectively, are not listed. The Numbers inside a parenthesis are the ranges of errors for the best fit parameter values calculated at a 95% confidence level. Note that those errors written in scientific notation do not follow a normal distribution an intrinsic feature for the differential evolution algorithm.

^a \mathbf{i}_0 is the sorbate layer, and the distal oxygen layer is represented as \mathbf{i}_1 .

Table 4.3 The results of bond valence analysis of the best fit model structure (valence in v.u.)

	Pb-(^I O ₁ , ^{III} O ₂ , O _{distal})	O _{distal}	O _{distal}	^I O ₁ -(Pb, Fe)	^I O ₂ -Fe	^{III} O ₃ -(Pb, Fe ₃)	^{III} O ₄ -Fe ₃
Best fit model	1.64	0.65	0.65	1.15	0.65	1.81	1.30
Protonation scheme	2HB (0.18)	2H (0.68)	1H (0.88) + 2HB (0.24)	1H (0.68) + 1HB (0.20)	2H (0.68)	-	1H (0.70)
Bond valence sum	2.00	2.01 v.u	2.01 v.u	2.03 v.u	2.01	1.81	2.00

Bond valence analysis were performed on singly coordinated oxygen (^IO₁ and ^IO₂), triply coordinated oxygen (^{III}O₁ and ^{III}O₂), distal oxygen coordinated with Pb only (O_{distal}). H and HB represent the proton and hydrogen bond, respectively. Two types of protonation schemes for the distal oxygen corresponding to the adsorbed Pb associating with a aquo group or a hydroxyl group due to hydrolysis. Bond valence is arbitrarily assigned to a proton and a hydrogen bond associated with different group in order to approach the bond valence saturation state. The valence range for a proton (0.68-0.88 v.u) and a hydrogen bond (0.13-0.25 v.u) is used according to Bargar et al. (Bargar et al., 1997b).

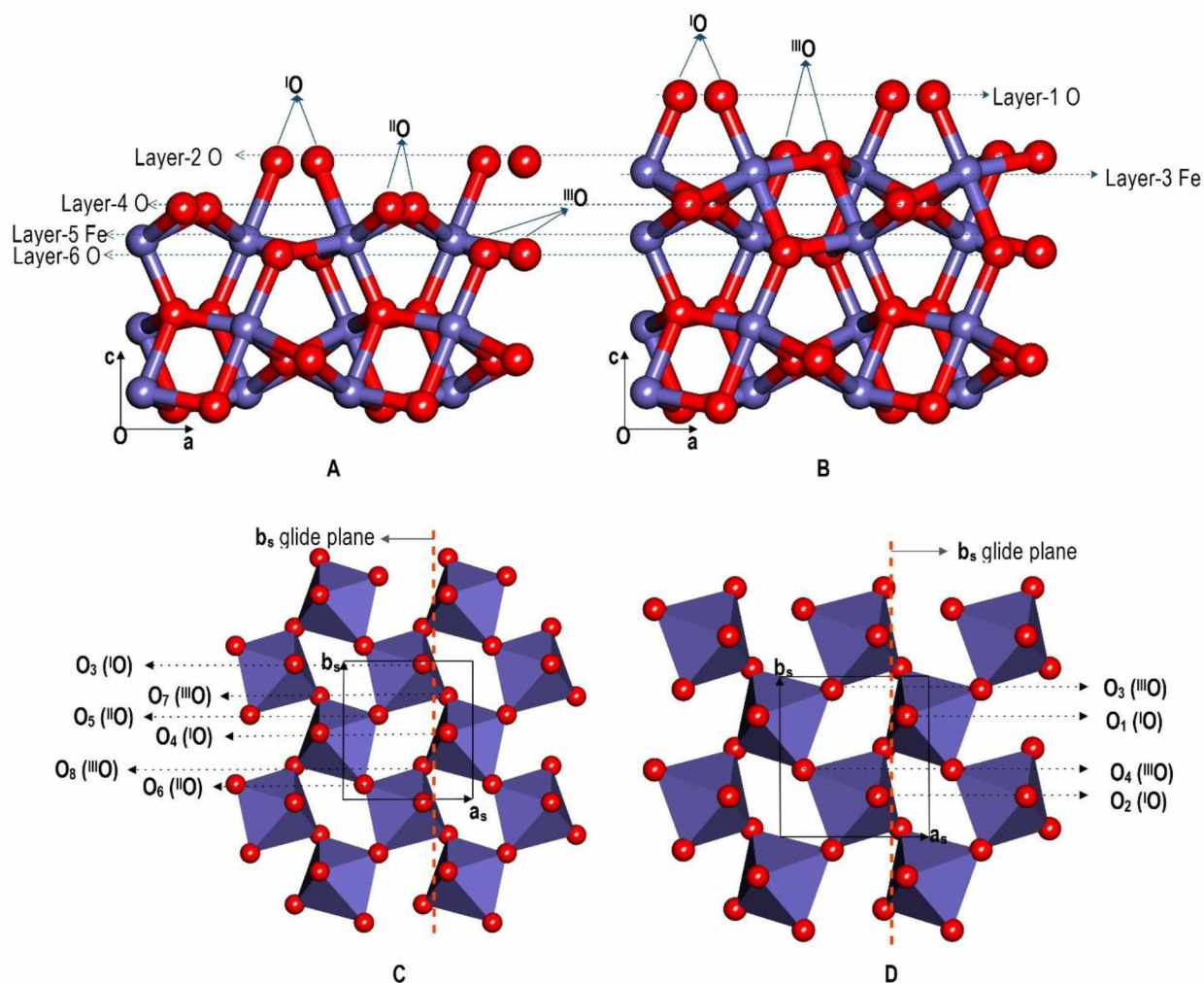


Figure 4.1 (A) Layer stacking sequence along the c_s axis for the HLT surface of hematite ($1\bar{1}02$); (B) Layer stacking sequence along the c_s axis for the FLT surface of hematite ($1\bar{1}02$); (C) polyhedral representation of the oxygen-terminated HLT surface of hematite ($1\bar{1}02$) (second octahedral layer and those beneath are not shown for clarity) ; (D) polyhedral representation of the oxygen-terminated FLT surface of hematite ($1\bar{1}02$) (second octahedral layer and those beneath are not shown for clarity). Lengths for unit cell edges are $a=5.038$ Å, $b=5.434$ Å and $c=7.3707$ Å. The $^{\text{III}}\text{O}$, $^{\text{II}}\text{O}$, and $^{\text{I}}\text{O}$ represent oxygen triply, doubly and singly coordinated to iron, respectively. Top six atomic layers are labeled. Note Layer-1 O and Layer-3 Fe belong to FLT only, while the other four atomic layers are shared by both terminations. The surface functional groups are named as “ O_n ” with the subscripts n starting from 1. The red dash lines represent for the b_s glide planes.

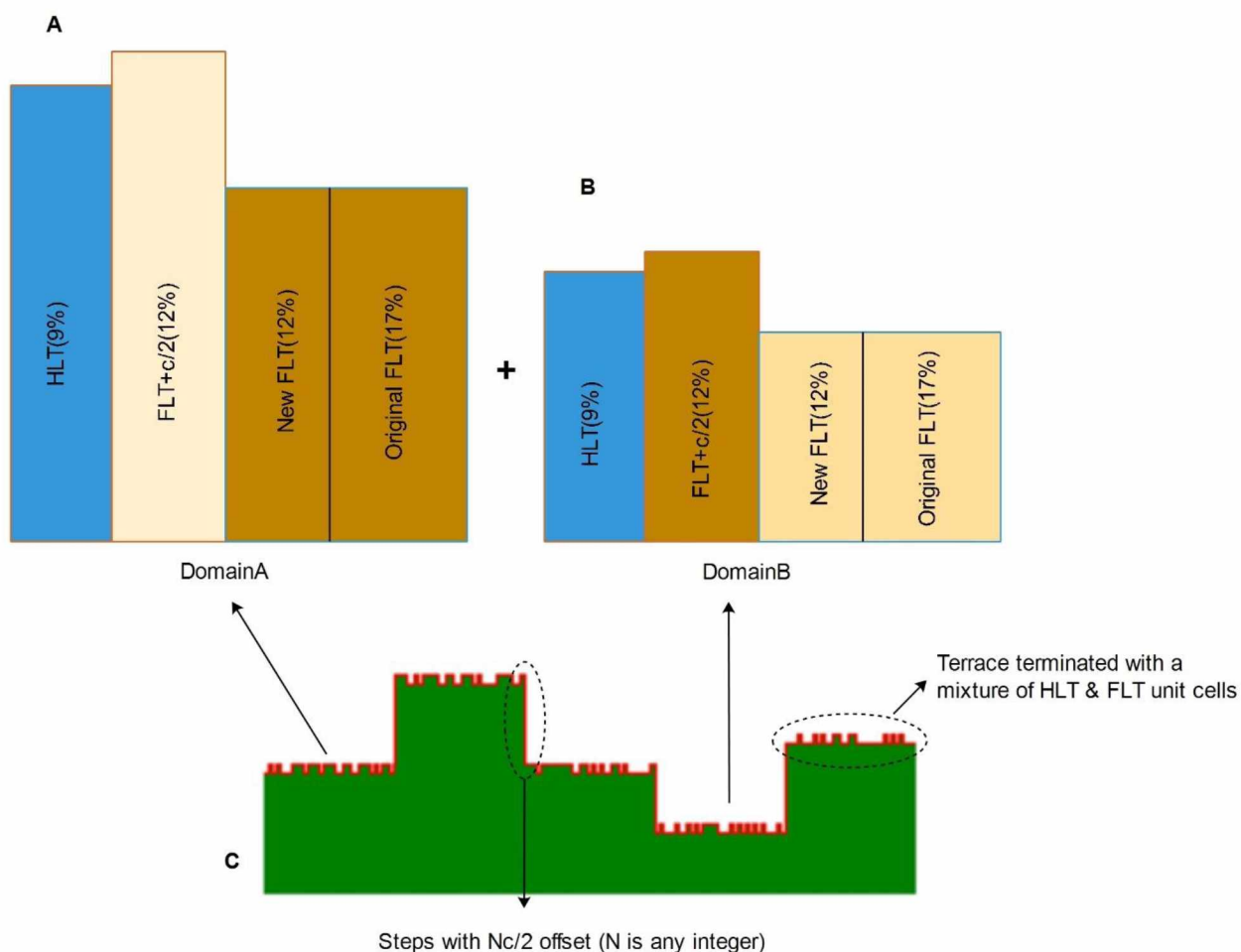


Figure 4.2 A schematic diagram of the mechanism of surface termination transformations on an annealed hematite ($1\bar{1}02$) based on the best fit model for the clean annealed hematite ($1\bar{1}02$) surface. In this diagram, the surface terminations of the same type (chemically and crystallographically equivalent) are painted in the same color. The surface termination pattern of an annealed surface is illustrated as Panel A and Panel B, which represent for two symmetry related domains with equivalent weight percentage (50%). The weights for different terminations are denoted on each domain. Note that although the surface termination transformation result in an unequal weight for two types of FLT on each domain, the total weight of each type of FLT is equivalent to each other when the summation is performed across two symmetry domains. Our best fit model supports a surface morphology, which is characterized by presence of domains, which are separated by steps with $Nc/2$ offset (N is any integer, and c is the lattice parameter), as illustrated in Panel C. On each domain, there are multiple surface terminations with characteristic termination heights. The rule for summing over the structure factors within domain size follows coherent addition while the structure factors over the domain size are summed up based on incoherent addition rule.

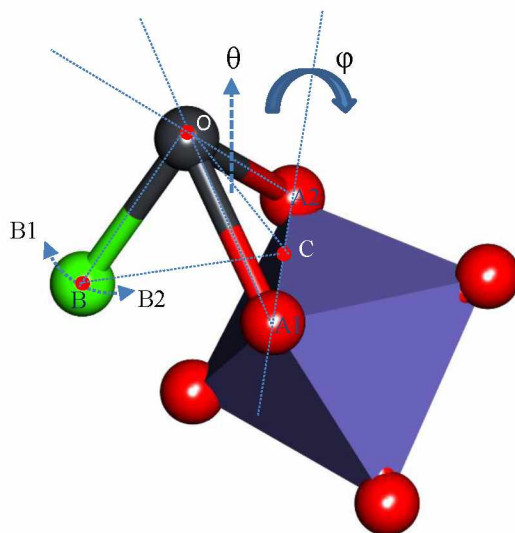


Figure 4.3 Schematic diagram of fitting parameters of Pb and distal oxygen in a bidentate edge-sharing binding mode. The Pb complex trigonal pyramid could rotate about axis A1A2 (A1 and A2 are positions for two anchored oxygen atoms) by ϕ , while the dihedral angle θ (A1OA2, O is the position of Pb atom) could vary in a range from 60° to 90° . To consider the distortion of Pb complex structure, Pb atom is allowed to slide along vector A1O, and distal oxygen could rotate freely on the OBC plane (B is the ideal position of the distal oxygen, and C is the center of A1A2). Red spheres are the surface oxygens, the gray sphere is Pb, the green sphere is the distal oxygen not directly bonded at substrate surface. Fe coordinative structure is represented in an octahedral.

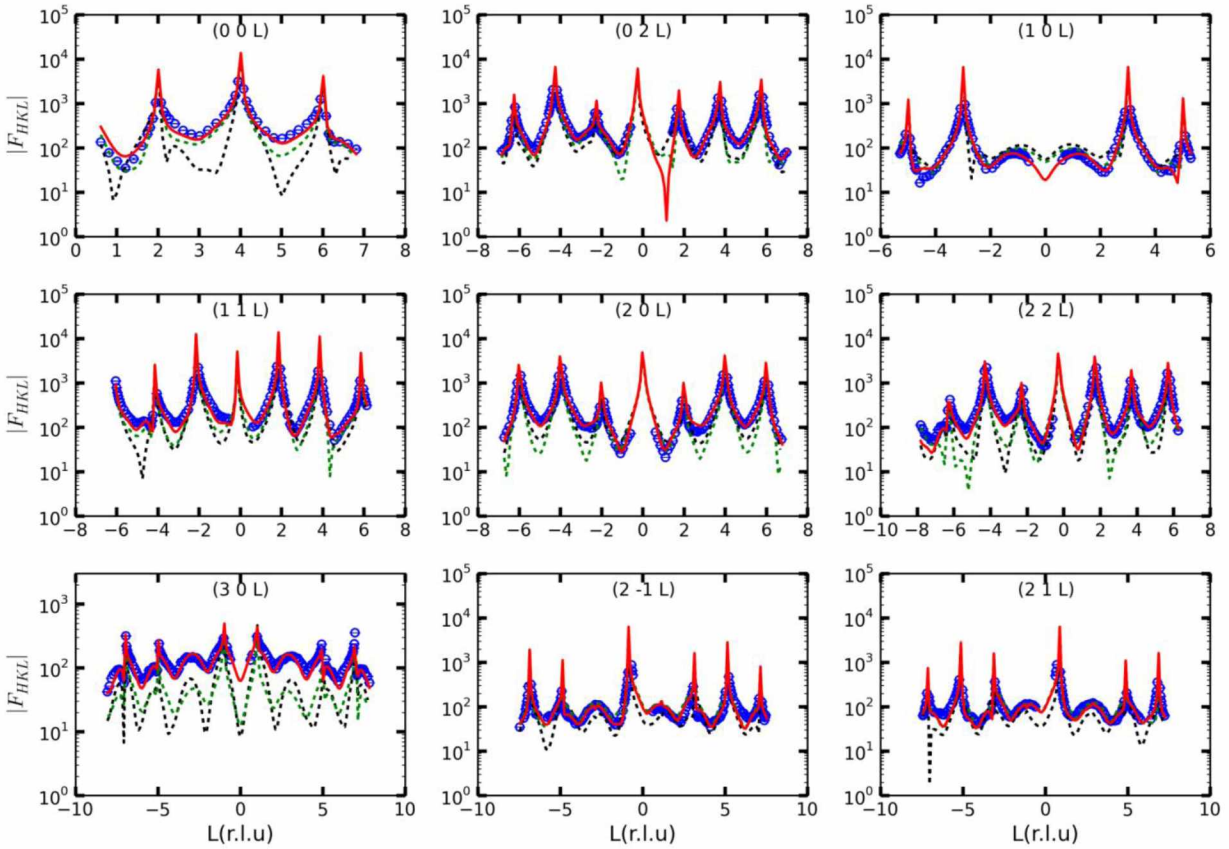


Figure 4.4 Experimental structure factors (blue open circles) (F_{HKL}) as a function of perpendicular momentum transfer (L , in reciprocal lattice units) for the annealed hematite ($1\bar{1}02$) surface reacted with $200\ \mu\text{M}$ Pb(II) at $\text{pH } 5.5$. The green dash lines represent the calculated CTR profiles based on the optimized model CS, the black dash lines represent the calculated CTR profiles based on the optimized model ES1, and the red solid lines represent the calculated CTR profiles based on the optimized model ES2 (best fit model).

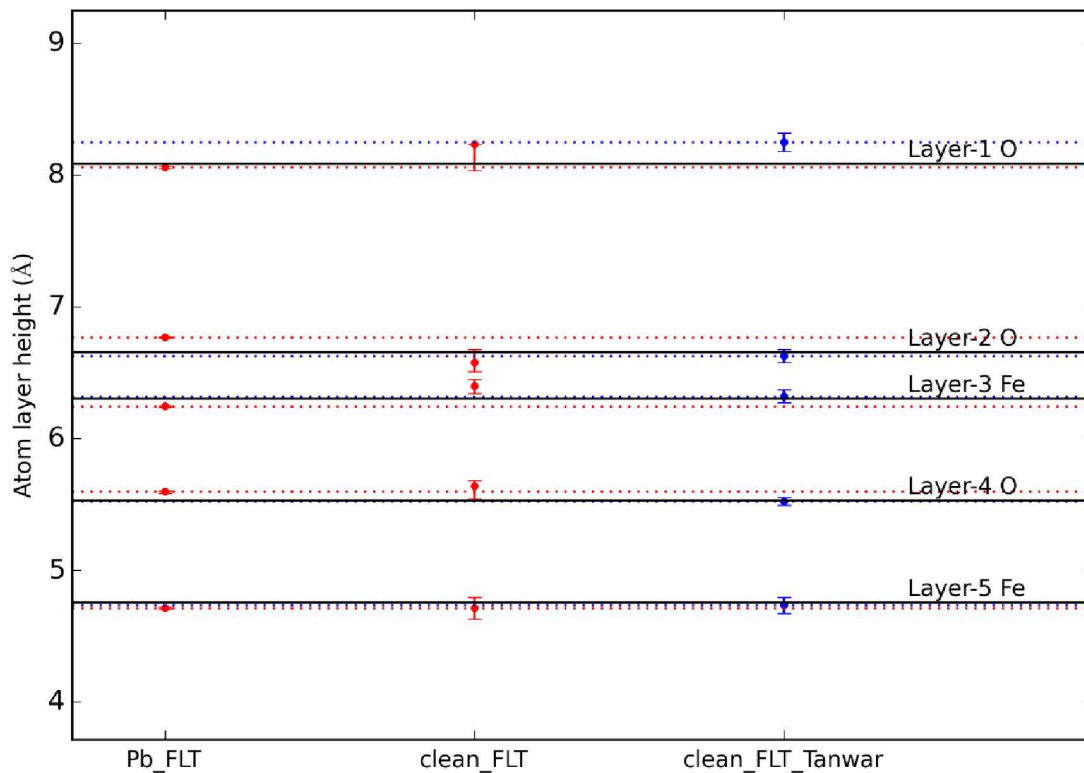


Figure 4.5 Comparison of atomic layer heights for the Pb-bonded FLT surface (Pb_FLT), clean FLT surface (clean_FLT) in this study and the clean FLT surface reported by Tanwar et al. (Tanwar et al., 2007a) (clean_FLT_Tanwar). The uncertainties were illustrated as error bars for each point. The black solid lines show the atom layer heights in the ideal surface structure. For comparison purpose, the red dot lines are drawn based on the results of Pb_FLT from the current study, and blue dot lines are based on Tanwar's model.

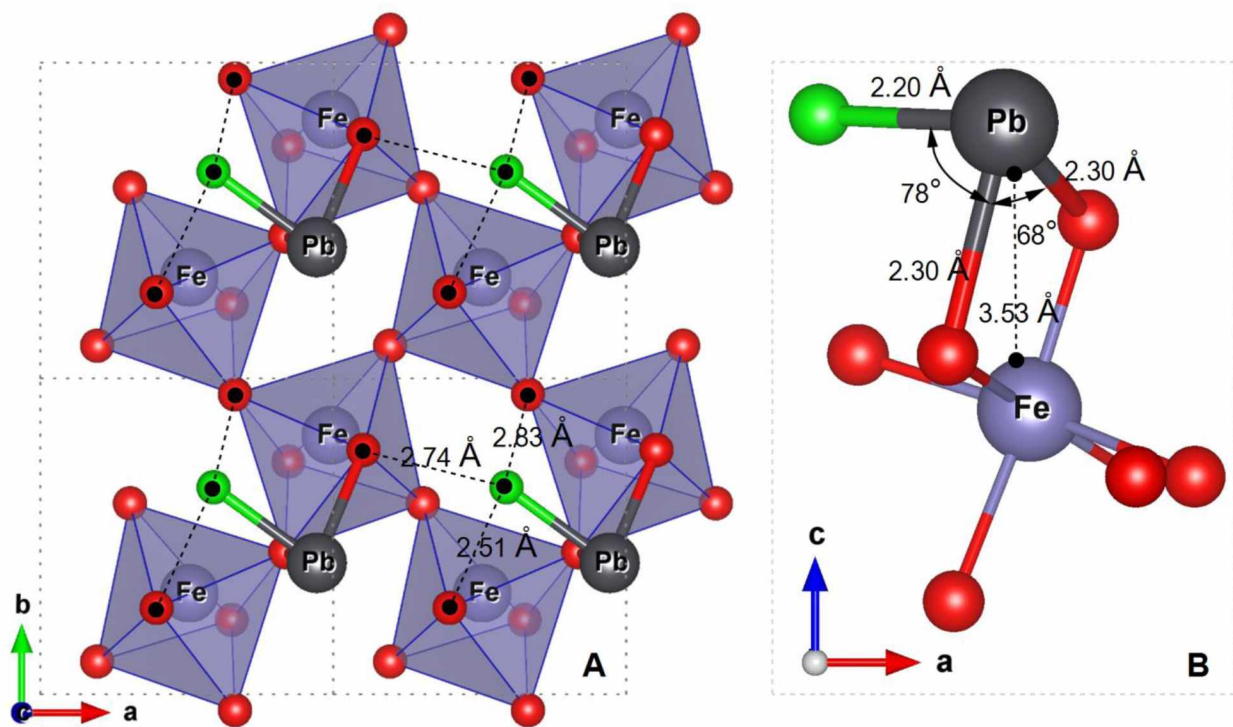


Figure 4.6 (A) The top view of the best fit model structure of Pb surface complex species binding at ES2 sites on the FLT surface within 2 by 2 unit cells. The top Fe layers are displayed as octahedra, and deeper atoms are not shown for clarity. The cations are labeled as element symbols, while the oxygen anions are represented as red balls for surface oxygen groups as well as green balls for distal oxygen atoms. Some O-O separations are highlighted at the surface as dashed lines. (B) The structural details of the surface complex species at ES2 sites in terms of bond angles and bond lengths. The near neighbor Fe atoms (blue balls) was shown as well. And the local structure of trigonal pyramid was oriented properly for a better view of geometric relationships.

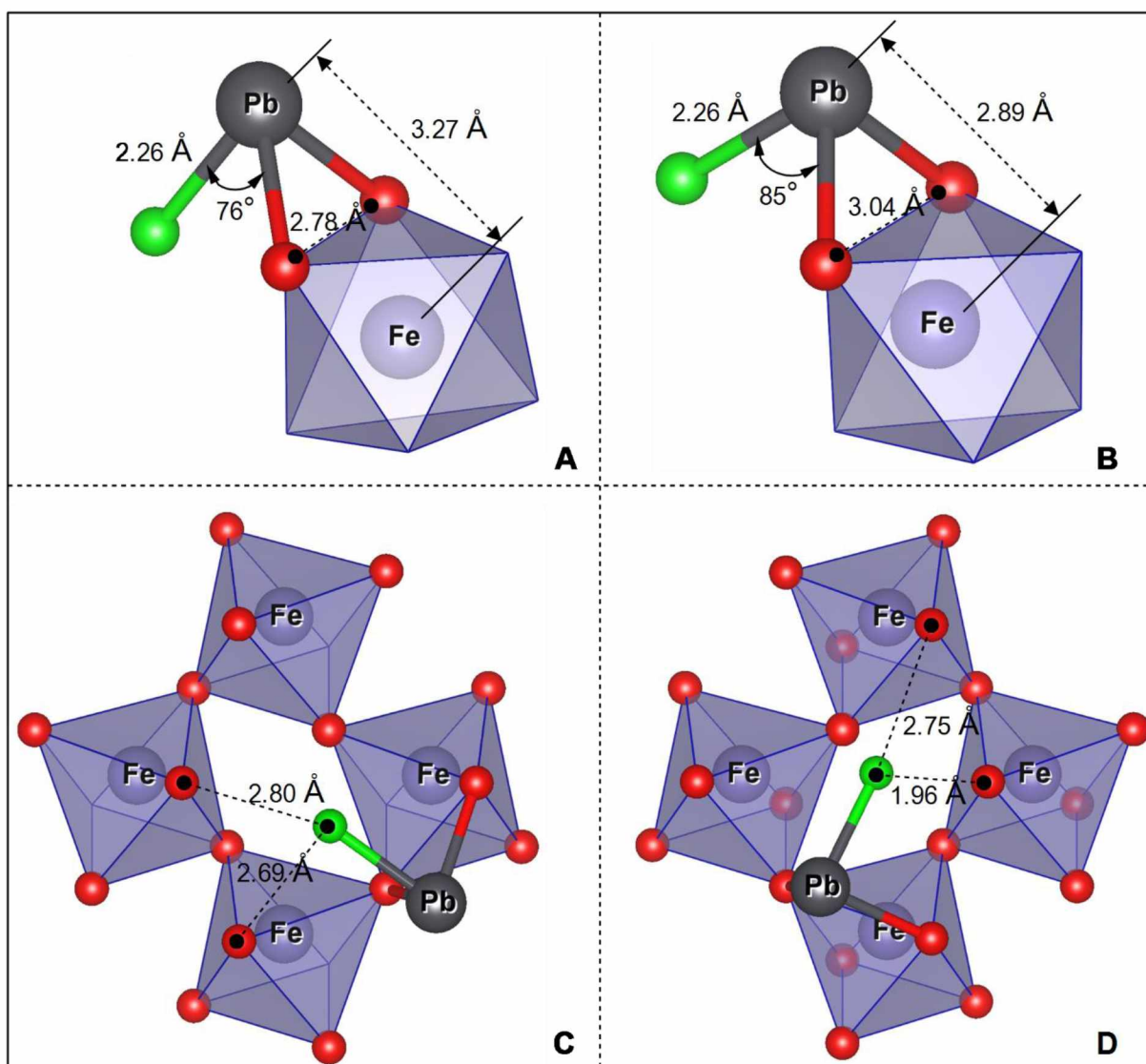


Figure 4.7 Structural comparison of Pb(II) binding to ES1 sites (B and D) and ES2 sites (A and C) assuming an unrelaxed FLT surface in the geometrical constraints of Pb-O bonds of 2.26 Å as well as a 0° rotation angle (see text for details). Four adjacent surface Fe octahedral units are shown on the top view in Panel C and Panel D, where the O-O separations (dashed lines) between the distal oxygen (green balls) and two terminal oxygens are shown to highlight the potential steric constraints. Panel A and Panel B display the geometrical relationship between the Pb surface complex species and the associated Fe octahedral in terms of O-Pb-O bond angles, the Pb-O bond length, O-O edge lengths and Pb-Fe separations. The structure is properly oriented for better visibility. Cations (Fe and Pb) are labeled as the associated element symbols, the structural surface oxygen atoms are shown as red balls.

Chapter 5 Structural Study of Sb(V) Adsorption on Hematite ($1\bar{1}02$) Using Crystal Truncation Rod X-ray Scattering¹

Abstract

In the present study, *in situ* adsorption of Sb(V) on a single crystal hematite ($1\bar{1}02$) surface was explored using crystal truncation rod X-ray diffraction (CTR). The best fit CTR model indicates that Sb(V) adsorbs at the surface via an inner-sphere mode, forming a tridentate binding geometry consisting of an edge-sharing and a corner-sharing binding configurations. It was found that the Sb octahedral local structure was distorted producing six Sb-O bonds with bond lengths ranging from 2.00 to 2.21 Å. The Sb-Fe distance (3.05 Å) derived from the present study is comparable to that published in previous XAFS studies. The chemical plausibility of the proposed structure was further verified by performing a bond valence analysis, which also deduced a protonation scheme. In addition, a simple but novel approach was developed to perform simulations to reveal the relationship between the site coverage and the inter-sorbate distance. The simulation results are compared to the CTR-derived site coverage suggesting an inter-site distance of ~ 5.0 Å at the apparent surface site saturation. The results of site simulation tests provided important insights into the steric and electrostatic effects, which are potential factors in controlling surface adsorption.

¹ Qiu C., Majs F., Eng P. J., Stubbs J. and Trainor T. P. (2015) Structural Study of Sb(V) Adsorption on Hematite ($1\bar{1}02$) Using Crystal Truncation rod X-ray Scattering. Prepared for submission to Environmental Science & Technology.

5.1 Introduction

Recently, concerns over antimony (Sb) contamination have aroused increasing attentions in the community of environmental science due to its wide applications and potential toxicity to humans. Sb is widely applied in the fabrication of commercial products for different purposes, such as its use as fire retardant and catalyst in plastic products, lubricant in automobile breaking lining and hardener in Pb alloy used for the manufacture of acid-lead storage battery and ammunition products (Filella et al., 2002a; Wilson et al., 2010). The increasing demand of Sb has stimulated the Sb mining activity, which produces growing amount of Sb around the world. It was reported that Sb is the 9th most exploited metal with annual production of 140000 mg (Scheinost et al., 2006). Environmental concerns on Sb lies in its toxicity that includes respiratory irritation, pneumoconiosis, antimony spots on the skin and gastrointestinal symptoms due to occupational exposure (Sundar and Chakravarty, 2010). In addition, antimony therapeutic for the treatment of leishmaniasis and schistosomiasis (Rawcliffe, 2000) was found to cause the toxic side effects relating to cardiotoxicity and pancreatitis (Herwaldt and Berman, 1992; Franco et al., 1995). Furthermore, antimony trioxide (Sb_2O_3) is classified as potentially carcinogenic (Group 2B) to humans by the International Agency for Research on Cancer (IARC, 1990). USEPA has added Sb to the list of the contaminants of priority interest, and it set the maximum contamination level of Sb in drinking water as 6 $\mu\text{g/L}$ (USEPA, 2009).

Sb falls into the category of metalloid in the periodic table with three oxidation states, including Sb^0 , Sb(III) and Sb(V). Sb^0 is readily oxidized to Sb(III) under the ambient environmental conditions, although further oxidation of Sb(III) to Sb(V) is observed to be kinetically controlled by the coexisting ions in the aqueous system (Ilgen et al., 2014), and Sb(III) adsorption to natural sorbents, such as pyrite, goethite, was found to greatly facilitate the

Sb(III) oxidation (Leuz et al., 2006; Xi et al., 2013; Kong et al., 2015). In light of that, Sb speciation in the natural environment is dominated by the Sb(V), which exists as Sb(OH)_6^- over a wide pH range (pH 4.0 to pH 12.0) (Filella et al., 2002b), although Sb(III) could become prevailing under some reducing environmental systems (Mitsunobu, et al., 2010a).

It is generally accepted that surface adsorption on natural substrates, such as Fe/Al-(oxyhydr)oxides, is the main mechanism controlling the environmental fate and transport of Sb (Mitsunobu, et al., 2010b; Resongles et al., 2013). Recently, increasing studies are available focusing on Sb adsorption behavior using a diversity of techniques, including methods based on batch adsorption experiments (Leuz et al., 2006; Martínez-Lladó et al., 2008; Cai et al., 2015), the X-ray spectroscopic technique (XAFS) (Scheinost et al., 2006; Mitsunobu, et al., 2010b; Ilgen and Trainor, 2012; Guo et al., 2014) and theoretical computation (like DFT) (Mason et al., 2012; Ramadugu and Mason, 2015). The studies using batch adsorption experiments demonstrated that the Sb(V) adsorption to the iron oxy(hydr)oxide samples is via an inner-sphere binding mode. For example, Leuz et al. (Leuz et al., 2006) studied Sb(V) adsorption on goethite surface using surface complexation modeling method, and their findings suggested that Sb(V) adsorbed on the goethite surface in a mononuclear bidentate binding mode. Such a binding mode was confirmed in a later study undertaken by Martnez-Lladó et al. (Martínez-Lladó et al., 2008) using the same method. Interestingly, a more recent paper (Vithanage et al., 2013), which examined the Sb(V) sorption behavior on a more complicated substrate, iron-oxide-rich red earth soil sample, proposed that Sb(V) adsorption on the substrate is under a bidentate binuclear binding mode besides the one found in the studies of Leuz and Martnez-Lladó. The lack of molecular structural information on the substrate surface used in those studies makes it difficult to make a further identification of those two Sb(V) surface complex species. Such a perplexed

situation was also encountered by Cai et al. (Cai et al., 2015), who investigated the Sb(V) sorption to iron-oxide-coated sands synthesized in laboratory. Surprisingly, in that study Cai et al. proposed two Sb(V) surface complex species corresponding to monodentate binding mode and outer-sphere binding mode, respectively, which were not reported before. Apparently, results based on the method using surface complexation modeling is insufficient to derive surface binding configurations without a detailed knowledge of the substrate surface structure, since the model fitting is not sensitive to the surface binding structure, and thus a different set of binding configuration is also possible to produce a statistically equivalent fit to the same experimental adsorption data. Hence, detailed insights into the surface binding configurations relies on other techniques, which are sensitive to the binding structure, such as X-ray adsorption fine structure (XAFS) spectroscopy.

The inner-sphere binding mode deduced from batch adsorption studies is consistent with that revealed by XAFS studies, which provided further information on the binding structure. For example, Guo et al. (Guo et al., 2014) presented a bidentate edge-sharing mode for Sb(V) adsorption on hydrous ferric oxide based on a relatively short Sb-Fe distance (3.0-3.19 Å). Such an edge-sharing binding mode was also found on a goethite sample with a Fe-Sb distance of 3.08-3.11 Å (Mitsunobu, et al., 2010b). In that study, Sb(V) sorption to ferrihydrite sample was also studied as a comparison, and it was found that besides the edge-sharing, the corner-sharing binding mode was observed as well on ferrihydrite sample corresponding to a longer Sb-Fe distance (3.51-3.55 Å). In line with the results of XAFS studies using iron oxyhydroxides synthesized in laboratory, EXAFS analysis of shooting range soil samples (Scheinost et al., 2006; Ackermann et al., 2009) and downstream sediment samples close to a historical Sb mining site (Ritchie et al., 2013) also gave rise to two types of Sb(V) surface complex species

with both edge-sharing and corner-sharing binding configurations probably due to a mixture of different types of iron oxyhydroxides coexisting in the soil sample. The different binding configurations observed in XAFS studies implied that there exist on iron (hydr)oxide surfaces at least two types of reactive sites for binding Sb(V) corresponding to surface complex species with different Sb-Fe separations. The heterogeneity pertaining to Sb(V) adsorption on the iron oxyhydroxide surfaces could also be the reason responsible for different desorption rates observed by McComb et al. (McComb et al., 2007), who conducted a desorption test of Sb(V) from amorphous iron oxide particle sample and speculated the presence of at least two binding sites with different binding strength.

XAFS technique could provide some direct structure information, such as the coordination number, the bond length and the chemical identity of neighboring atoms (Koningsberger and Prins, 1988; Brown et al., 1995). However, the analysis of XAFS data could also lead to ambiguity if there are multiple reactive binding sites available, especially when each site shares a similar coordination environment making the sorbate bound to those sites undistinguishable. In addition, the surface structure of the substrate used in an XAFS study is usually not well understood, and thus it is unlikely to identify the reactive binding sites on the substrate surface. As a result, structural information derived from XAFS analysis only represents the average surface binding structure, and the deduction of site specific surface complexation reactions is difficult largely due to lack of the well characterized structural details of substrate surface. To overcome these obstacles, we require a technique, which could be used to well resolve the geometrical relationship between the sorbate and the substrate surface. Crystal truncation rod (CTR) X-ray diffraction provides such capability, when it is used to probe the surface adsorption of an aqueous sorbate to a single crystal substrate with an abrupt surface, since CTRs are diffuse

streaks of scattering intensities running along surface normal, which are extremely sensitive to the interfacial structure (Robinson and Tweet, 1992). In the present paper, CTR technique was used to characterize the Sb(V) adsorption mechanism on the single crystal hematite($1\bar{1}02$) surface, which has been extensively studied before using both the experimental approach and the theoretical computation (Catalano et al., 2007; Tanwar et al., 2007b; Lo et al., 2007). To the best of our knowledge, Sb(V) adsorption on hematite sample was not studied before using an experimental approach, thus our study will fill the knowledge gap and, by presenting structural details of surface complexation, will improve the understanding of the structure-reactivity relationship regarding to the surface adsorption on mineral substrates of toxic elements.

5.2 Methods and experiments

5.2.1 Sample preparation

A natural single crystal hematite sample was first cut into small chips with a proper size (rounded shape with a radius of ~ 2 cm and a thickness of ~ 0.5 cm), which were then grinded and polished parallel to ($1\bar{1}02$) plane. Prior to CTR measurements, the single crystal samples were further polished following chemical mechanical polishing (CMP) procedures as described elsewhere (Tanwar et al., 2007b). Briefly, the sample was first polished for 20 min using commercial colloidal silica suspension ($0.06 \mu\text{m}$ diameter) (TED PELLA, USA), which was pre-buffered to pH 11.5 using NaOH solution. Then we switched to the raw colloidal silica suspension (pH 10.0) to further polish the surface for another 10 min, which is followed successfully by 1-hour base wash (crystal soaking in NaOH solution of pH 10.5) and 4-hour acid wash (crystal soaking in HNO_3 solution of pH 2.0). We found that a single crystal sample prepared that way has a low mis-cut ($<0.01^\circ$) surface with a good surface quality (small

roughness) suitable for CTR measurements. Sb(V) solutions (200 μM) were made inside a N_2 (>99.999%) filled glove box to avoid the influence of CO_2 in the atmosphere. To make Sb(V) solutions, antimonate salt ($\text{KSb}(\text{OH})_6$) was dissolved using degassed water, prepared by purging N_2 (>99.999%) through de-ionized water under the boiling condition for 2 hours. The solution pH was carefully adjusted to pH 5.5(± 0.2) using HCl and NaOH. Sb(V) solutions were stored inside the glove box prior to CTR measurements.

To monitor the surface reaction under *in situ* conditions, Sb(V) solutions were introduced to the hematite surface via a liquid cell, which utilized a Kapton membrane to trap a liquid film over the sample surface. The liquid cell was described in detail elsewhere (Heberling et al., 2011). To initiate the surface reaction, 30 mL Sb(V) solution was pumped through the liquid cell at a speed of 2 mL/min and with a larger film gap (2000 μm) between the sample surface and the Kapton membrane to favor the surface equilibrium. Then the system was left equilibrating for another 15 min with the film gap open. Afterwards, the film gap was pulled down to make a close contact of the Kapton membrane to the crystal surface. By using liquid cell, we are capable of making a liquid film with a thickness of several micrometers throughout the CTR measurement. The quality of the liquid film was monitored through observing the film surface, which should exhibit clear Newton's rings if the liquid film has a relatively uniform thickness. To avoid dehydration of liquid film due to water escaping through the Kapton film, the liquid cell was capped with a Kapton film dome with water-saturated He (relative humidity >90%) flowing through the dome headspace.

5.2.2 Beamline experiments

CTR measurements were conducted at the bending magnet beamline 13BMC at the Advanced Photon Source (APS), Argonne National Laboratory. The energy of the incident X-ray beam was fixed to 13 keV using a liquid nitrogen cooled double-crystal silicon (1 1 1) monochromator. The beam was focused to a proper size (250 μm by 400 μm) for CTR measurements using vertical and horizontal focusing mirrors, which are Si single crystal (1 1 1) coated with Pt to reject harmonics. A Kappa geometry Newport diffractometer (4S+2D) was used for sample and detector orientation with angles and diffractometer coordinates defined according to You (You, 1999). X-ray intensity prior to the sample was monitored using N_2 gas filled ion-chambers and scattered intensity was measured using a Dectris PILATUS 100K 2D pixel array detector with 195 \times 487 pixels (vertical \times horizontal) (Eikenberry et al., 2003). Nine CTRs, including the specular rod, were collected in order to probe both the lateral and vertical electron density of the surface. To collect non-specular CTR data, the incident angle of the beam relative to the sample surface was fixed at 2° , while Omega scan was used to scan specular rod with the surface normal of the sample in a horizontal position.

During the CTR measurement, a small subset of rod was repeatedly collected along with the full rods to monitor the possible beam induced damage to the surface. Noticeable variation of intensity was not observed in those “check” rods, indicating a stable surface throughout the CTR measurement. In the end, a full CTR dataset was collected consisting of 9 CTRs in total with >1500 unique data points. The structure factor (magnitude) of each data point was extracted from each Pilatus image using TDL software package (<http://cars9.uchicago.edu/ifeffit/tld>). Then, each data point is subject to background subtraction, followed by further corrections for active area, polarization, and Lorentz factors to account for the variance of the intercept between

Ewald-sphere and CTR as a function of Q according to the method by Schlepütz et al. (Schlepütz et al., 2005).

5.2.3 Hematite ($1\bar{1}02$) crystallographic property

The crystal structure of a hematite (α -Fe₂O₃) belongs to the R-3c space group, and can be defined by a hexagonal close packing of oxygen with iron occupying two-thirds of the octahedral holes. The lattice parameter of α -Fe₂O₃ (5.035 Å, 13.747 Å, 90°, 90°, 120°) as well as the bulk isotropic Debye-Waller factors was previously reported (Finger and Hazen, 1980). The distortion of Fe octahedral in α -Fe₂O₃ results in two sets of Fe-O bonds with bond length of 1.95 Å and 2.11 Å, respectively. For convenience, the hematite ($1\bar{1}02$) surface can be re-indexed by defining a pseudo unit cell (5.038 Å, 5.434 Å, 7.3707 Å, 90°, 90°, 90°) as described in detail by Trainor et al. (Trainor et al., 2002). The main advantage of the pseudo-cell is that it places the c -axis parallel to the surface normal (\mathbf{c}_s), with the \mathbf{a}_s and \mathbf{b}_s axes defined within the plane of the surface. The re-indexed unit cell contains ten atom layers with a stoichiometric layer sequence of **(O₂-Fe₂-O₂-Fe₂-O₂-O₂-Fe₂-O₂-Fe₂-O₂-R)** along the \mathbf{c}_s axis, where **R** represents the stoichiometric (Fe₂O₃) repeat of the bulk material. The bottom five atom layers are symmetrically related to the top five layers via a glide plane (\mathbf{c}_s glide). Such a glide plane symmetry results in symmetry related unit cells, which are chemically equivalent but crystallographically distinct.

The termination of the hematite ($1\bar{1}02$) has been extensively studied using both experimental and theoretical approaches (Henderson et al., 1998; Catalano et al., 2007; Tanwar et al., 2007a; Tanwar et al., 2007b; Lo et al., 2007). In those studies, it was found that the chemical identity of the surface termination is largely determined by the sample preparation scheme. For example,

the stoichiometric (1×1) hematite ($1\bar{1}02$) sample prepared under ultra-high vacuum annealing at 950 K is observed to produce a reduced (2×1) surface (Henderson et al., 1998). However, when prepared using the wet chemical mechanical polishing (CMP) procedures the surface is dominated by the so-called half-layer termination (HLT); similar to the stoichiometric (1×1) surface but with the surface Fe sites vacant (Figure 5.1 B and D) (Tanwar et al., 2007b). Interestingly, after the CMP-prepared surface was annealed at 500 °C in the ambient atmosphere for 3 h the surface was observed to be dominated by a (hydrated) stoichiometry termination (>70%), as found by Tanwar et al. (Tanwar et al., 2007a). This implies a termination transformation from the HLT to the stoichiometry termination (called full layer termination (FLT) hereafter) in the annealing process. The CTR evidence of surface termination transformation was also suggested in a DFT study undertaken by Lo et al. (Lo et al., 2007), who claimed that the FLT is thermodynamically more favorable than the HLT at higher temperature, and the HLT is stable only at lower temperature.

The HLT and the FLT on a hematite ($1\bar{1}02$) surface display a different set of surface functional groups. As shown in Figure 5.1, on the FLT surface, there exist only two types of surface functional groups (singly coordinated oxygen $^{\text{I}}\text{O}$ and triply coordinated oxygen $^{\text{III}}\text{O}$), whereas on the HLT another type of surface functional group (the doubly coordinated oxygen $^{\text{II}}\text{O}$) exists as well besides those two found in the FLT. As depicted in Figure 5.1 (C and D), hematite ($1\bar{1}02$) surface (both the HLT and the FLT) displays a topographical pattern with surface atoms zigzagging along a direction parallel to the \mathbf{b}_s axis. Two types of Fe octahedral units with different orientations alternate on the surface, which form interstitials. The geometrical relationship between two types of Fe octahedral units could be depicted by a \mathbf{b}_s glide plane crossing the surface lattice point $(\frac{3}{4}, 0)$ based on the re-indexed unit cell.

5.2.4 Potential binding sites and the step features on the hematite surface

The potential bidentate and tridentate binding sites are identified on both the HLT and the FLT of hematite ($1\bar{1}02$) surface, as listed in Table 5.1. An arbitrary naming rule was applied to distinguish different surface sites. According to the rule, each site is referred to with a unique name composing of labels for the constituent surface oxygens. Each surface oxygen was represented with the letter “O” subscripted by an integer starting from 1. The associated in-plane translation symmetry operation was defined by suffixing the number with “ $\pm x$ ” or “ $\pm y$ ”, which use the letter “x” or “y” to label the translation symmetry along x or y axis with the “+” or “-” signs specifying the associated translation direction. Note that we ignored the monodentate binding mode in this study, since it was not observed in previous XAFS studies (Scheinost et al., 2006; Mitsunobu et al., 2010b; Guo et al., 2014). In addition, we noticed that Sb(V) adsorption with a bidentate edge-sharing sites would lead to extremely small O-O separations ($<2.0\text{\AA}$) between the distal oxygen (bonding to Pb only) and the surface oxygen. Such short O-O distances will result in a strong electrostatic repulsion, and make the bidentate edge-sharing sites energetically unfavorable for Sb(V) binding. In light of that, bidentate edge-sharing binding sites were excluded as well for surface modeling. As a result, surface modeling work in the current study was limited to six model trials (Table 5.1) corresponding to bidentate corner-sharing, tridentate corner-sharing/edge-sharing and tridentate face-sharing binding configurations on both the HLT and the FLT.

5.2.5 CTR theory

CTRs are diffuse streaks of scattering intensities running along a direction parallel to the surface normal, and the variation of the scattering intensity along each CTR is attributed to the

abrupt termination of a surface plane (Robinson and Tweet, 1992). The atoms in the surface slab are usually subject to slight displacements from the bulk structure to compromise for the under-coordination of surface functional groups. In addition, interfacial processes occurring at the mineral-water interface, such as the surface complexation reactions, could significantly modify the surface structure. In light of that, the structure factors along each CTR are expressed as a coherent sum of the bulk structure and the surface slab. The CTR theory has been described in detail before (Robinson, 1986; Robinson and Tweet, 1992; Vlieg, 2000; Fenter, 2002), and a general mathematic expression of a structure factor could be written as Equation 5.1, where the S is the overall scaling factor, R is the roughness factor using β roughness model described by Robinson (Robinson, 1986), F_b is the bulk structure factor, F_{CTR} is the CTR form factor, and F_{sc} is the surface structure factor.

$$F_T = SR(F_b F_{CTR} + F_{sc}) \quad (5.1)$$

$$F_{CTR} = \frac{1}{1 - e^{-i2\pi L}} \quad (5.2)$$

$$F_b = \sum_{j=1}^n \theta_j f_j \exp(iQ \cdot r_j) \exp[-B_j(|Q|/4\pi)^2] \quad (5.3)$$

F_b is calculated by summing over each atom within one unit cell, which is a function of the atomic form factor (f_j), the atomic occupancy (θ_j), and isotropic atomic Debye Waller factor (B_j); the relative phase difference is expressed as the dot product of the position vector of each atom (r_j) and the momentum transfer (Q), as expressed in Equation 5.3. The CTR form factor F_{CTR} is calculated using Equation 5.2, which is scaled to F_b to account for the effect of semi-infinite bulk unit cells stacking along c_s direction. F_{sc} is expressed using a similar equation as F_b , but it needs to be multiplied by an additional phase factor ($\exp(i2\pi l)$) to account for the phase difference due to the layer height difference between the bulk slab and the surface slab. It should be noted that the calculations of the structure factor using a re-indexed unit cell requires some extra

corrections to the perpendicular momentum transfer L , which are correctly handled according to the approach described by Trainor et al. (Trainor et al., 2002).

5.2.6 CTR analysis

5.2.6.1 Structure factor calculation in a multi-unit cell model

In this study, we used the multi-unit cell model for the structure refinement. In a multi-unit cell model, different terminations are explicitly defined as compared to an average structural model, which contains only one unit cell subject to structural refinement. As proposed in a previous CTR study (Tanwar et al., 2007b), a CMP-prepared hematite ($1\bar{1}02$) surface contains up to 72% HLT, which is balanced by the FLT taking up ~28% of the substrate surface. We noticed that Tanwar employed the CTR modeling based on an average structural model that gave rise to a partially occupied top Fe layer, which implies a mixture of HLT and FLT with the FLT relatively lower than the HLT. Therefore, Tanwar's average structural model could be transformed equivalently to a multi-unit cell structural model to explicitly consider for the HLT and the FLT, as described in Figure 5.1 A and B. In addition, we notice that the existence of c_s glide plane symmetry in the hematite structure makes it possible to have two symmetry related terminations associating with each type of termination. Those two symmetry related terminations are chemically equivalent but crystallographically distinct with a height offset of $(N+1/2)c$, where N is any integer and c is the lattice parameter 7.3707 \AA in the re-indexed coordinated system. To account for the symmetry related terminations, we introduce a concept of domain in our model, which could be physically interpreted as a terrace, on which multiple terminations are docked. The terraces are separated by steps with a step height of $Nc/2$ (N is any integer). Note that two terraces are symmetry related to each other when separating by $Nc/2$ with N being an

odd number, whereas two terraces are equivalent copies (both chemically and crystallographically) when separating by $Nc/2$ with N an even number. With terminations and domains defined as above, our multi-unit cell models consist of two domains with each domain containing two types of surface terminations (the HLT and the FLT).

We need a coherent rule for the calculation of structure factor in a multi-unit cell model. We noticed that a reasonable fit could be achieved only when the structure factors from the surface terminations on the same domain are added up coherently but structure factors from two domains are summed incoherently. Such a coherence rule for structure factor addition is probably related to the relatively large coherence length of the X-ray beam in a 3rd generation synchrotron beamline, which is roughly 5 μm if considering a 1 \AA X-ray beam (Als-Nielsen and McMorrow, 2011). Therefore, the structure factor addition rule applied here implies that the termination boundary within the same domain should be within the X-ray coherence length, whereas the domain size should be larger than the X-ray coherence length. The surface morphology based on the domain and termination features described above is illustrated as a schematic diagram in Figure 5.2.

5.2.6.2 Constraints on the fitting parameters

CTR analysis is performed to fit calculated structure factors against the experimental data using GenX program based on the differential evolution optimization algorithm as described by Björck (Björck, 2011). The fitting parameters include the atomic displacements, atomic occupancy, and atomic isotropic Debye Waller factors. Each surface atom layer was grouped such that the atoms within the same layer have equivalent occupancy, Debye Waller factor and the out of plane movement. The in-plane movement of atoms within the same layer was

constrained using the b_s glide plane symmetry mentioned above. The out of plane relaxation of top five surface atomic layers were optimized, whereas the in-plane movement was limited to the top two atom layers. We found that the Debye Waller factors of surface atoms are insensitive during model refinement, and thus they were fixed to bulk values.

To resolve the surface binding structure of Sb(V) on hematite($1\bar{1}02$) surface, we performed the model refinement for surface Sb complex species under different binding configurations. In the refinement of a model with a specific binding configuration, a robust fit would require a constraint to maintain the geometrical relationship between the sorbate and the associated binding site during model fitting. To address that, we introduced two sets of geometrical parameters for bidentate and tridentate binding configurations, respectively. In the case of structural refinement in a bidentate binding mode, two geometrical parameters, the rotation angle (θ) and the dihedral angle (ϕ), are defined and optimized. As shown in Figure 5.3A, Sb position could be uniquely computed with those two angles. A less distorted surface complex structure will require the dihedral angle ϕ closer to the ideal value (90°), and a slight offset of the dihedral angle within 10° is allowed to consider for the possible angle distortion. In the bidentate mode, there are four distal oxygens (bonding to the adsorbed Sb and being oriented towards solution side), and the positions of those distal oxygens are computed through the Sb position as well as two surface oxygen groups bonding to Sb. In the case of a tridentate binding mode, the positions for sorbates, the Sb atom and three distal oxygens, are directly computed through positions of three anchored oxygens at the surface. The geometrical solution in a tridentate binding configuration is illustrated in Figure 5.3B. Briefly, the position of a dummy-point is calculated such that this dummy-point form an equilateral triangle with two of the anchored oxygens and is nearest to the third anchored oxygen. The equilateral triangle, composing two surface anchored

oxygens and one dummy-point, will be used to compute the sorbate positions (Sb and three distal oxygens) in a constraint of an octahedral coordination structure. We noticed that it is too rigid to rely on the pure geometric solution to compute the sorbate positions in the case of tridentate binding mode, since all the sorbate atoms will have no freedom to change their positions, but will be solely determined by the positions of anchored surface atoms. In light of that, we introduce three correction parameters (dx, dy and dz), which are small in magnitude ($<0.1 \text{ \AA}$) and used to allow extra displacements of Sb atom and three distal oxygens. As a result, the calculated sorbate positions (x, y and z) will be corrected by (dx, dy, dz), respectively. We found that refinement of sorbate positions using aforementioned geometrical constraints is more robust, since the total fitting parameters for sorbate positions reduce to 2 in a bidentate mode and 3 in a tridentate mode. The other advantage of using geometrical constraint is that the local coordination structure could be maintained during model fitting.

The occupancy as well as the Debye Waller factors of sorbates were optimized as well. The occupancy of all sorbates are linked to have a same value, while the Debye Waller factors for Sb and distal oxygens are optimized independently. Sb binding at two symmetry sites are grouped such that these chemically equivalent sorbates have an equivalent occupancy and Debye Waller factor, but their positions are related to each other through the \mathbf{b}_s glide plane symmetry as mentioned above.

5.2.6.3 Incorporation of bond valence constraint into CTR analysis

A stable surface complex structure should have a bond valence saturation state for the composing atoms. Therefore, the under-saturated surface species, such as the surface oxygen atoms and the distal oxygen, should achieve a bond valence saturation state through atomic

displacement, protonation, or surface adsorption. To make a more effective surface modeling, we employ a bond valence constraint during fitting, such that structures with atoms having serious bond valence non-saturation states could be effectively screened out. As proposed by Brown (Brown and Altermatt, 1985), the valence contributed by a covalent chemical bond could be calculated using an empirical equation written as Equation 5.4, where r is the associated bond length continually being updated during fitting, r_0 the nominal length of a chemical bond of unit valence, which has been well tabulated for different Metal-O bonds (Brown, 2009), and B is a constant with a value of 0.37 representing the softness of the interaction between the two atoms.

$$s = e^{\frac{(r_0-r)}{B}} \quad (5.4)$$

However, a calculation of bond valence involving proton is practically impossible due to the fact that proton is a weak scatter of X-ray and does not contribute to X-ray scattering intensity.

Hence, to account for the possible protonation, under-coordinated oxygen (assuming maximum coordination number of 4) was arbitrarily assigned a protonation scheme with a covalent hydrogen and a hydrogen bond donating a bond valence of 0.68-0.88 v.u and 0.13-0.25 v.u, respectively (Bargar et al., 1997). Different protonation schemes will be tested under the constraints of the maximum coordination number of 4 for each oxygen atom, and the protonation scheme leading to the best bond valence saturation state will be used. With the rule to assign protonation scheme defined as above, bond valence sum for each atom is calculated. The absolute offset of the calculated bond valence sum from the associated formal charge was summed as a bond valence penalty factor scaled to the original figure of merit (FOM), which was calculated based on a normalized χ^2 equation. The modified χ^2 equation is described in Equation 5.5, where the pre-factor is the bond valence penalty factor (≥ 1) (x_j is the calculated bond valence sum, and f_j is the associated formal charge of atom_j) and the rest part is the

normalized χ^2 equation with F_i representing the experimental value for structure factor, $F_{i,c}$ the calculated structure factor, e_i the error of i^{th} data point, N the number of data points, p the number of fitting parameters.

$$\chi^2 = (1 + \sum_{j=1}^n |x_j - f_j|) \sum_{i=1}^N \frac{\left[\frac{|F_i - F_{i,c}|}{e_i} \right]^2}{N-p} \quad (5.5)$$

It should be noted that it is impossible to obtain the statistical errors for the bond valence sum calculated for each atom, since the bond valence sum is determined by the associated interatomic distances, which are not directly optimized in the process of surface model refinement.

Therefore, we predefine an arbitrary tolerance level (0.2 v.u.) in the calculation of bond valence penalty factor. A bond valence sum offset ($|x_j - f_j|$) within the tolerance level will be waived to be counted for computing the bond valence penalty factor.

5.3 CTR modeling results

5.3.1 Description of CTR profiles based on different models

5.3.1.1 Models regarding to Sb-bonded FLT

As shown in Table 5.1, Model1, Model2 and Model3 represent structural models with Sb(V) binding on the FLT corresponding to three different binding configurations. The optimized CTR profiles for these models were compared to the experimental data in Figure 5.4. As shown in Figure 5.4, the structure factors near (0 0 2.5) calculated based on all three models are significantly underestimated compared to the experimental data. The misfit was also observed at higher L of (0 0 L) rod for Model3. Besides the specular rod, the misfits were also observed on numerous off-specular rods. For example, all three models gave rise to extremely sharp dips near (2 2 -5.7), where the data points display a relatively flat shape. In addition, significant mismatch was seen at relatively lower L of the negative side of (1 1 L) rod, where the models produced a

similar dip feature but shifting significantly towards (1 1 0). Such a misfit due to the large shift of dip feature was also seen at low L on both positive and negative sides of (2 0 L) rod in the case of Model3. According to the qualitative comparison described above, it seems that Sb(V) is less likely to associate with the FLT surface under the experimental conditions used in this study.

5.3.1.2 Models regarding to Sb-bonded HLT

Model4, Model5 and Model6 are three models, which consider the Sb(V) binding to the HLT under three different binding configurations, as illustrated in Table 5.1. The optimized CTR profiles are compared to the experimental data in Figure 5.5. As shown in Figure 5.5, the CTRs calculated based on Model6 could not well reproduce the experimental data at numerous positions. For example, abnormal sharp dips were observed near (1 1 -4), (1 1 2.5), (2 2 -6) and (2 -1 1), and large shifting of anti-Bragg valley was observed near (2 0 1) and (2 0 -1).

On the contrary, both Model4 and Model5 gave rise to a significantly better fit to the experimental data, which not only remove abnormal dips seen in the other models, but also improve the misfit at anti-Bragg valleys, as seen in the other models. However, the fit based on the Model4 gave rise to a large FOM (710.32), which signifies a high bond valence penalty factor. Thus, Model5 is the only model capable of reproducing the CTR intensity variants well as well as resisting the bond valence penalty test during model refinement. Afterwards, two water layers were incorporated into the Model5 to consider the possible influence of interfacial water. It was found that the fitting quality was improved to some extent after adding interfacial water layers with a slight decrease of FOM value from 2.38 to 2.25. However, the improvement of the fit after adding interfacial water was rejected in a Hamilton R test at a 95% confidence level (Hamilton, 1965). Hence, the results of Hamilton R test indicated that interfacial water could not

be well resolved in the studied system, which is consistent to the large uncertainties of occupancy and Debye Waller factors observed for interfacial waters.

It should be noted that the best fit structural model presented above could not completely exclude the possibility of Sb(V) adsorption on the FLT surface, since FLT surface only takes up 22% of the substrate surface, which is probably too low to probe the Sb species associating with the FLT. A solution to that is to perform a separated CTR measurement of Sb(V) adsorption on a FLT dominated surface through annealing CMP-prepared hematite ($1\bar{1}02$) surface, which is undergoing in our group.

5.3.1.3 Description of best fit structure model

The best fit modeling results, including atomic displacements of surface atoms, sorbate positions, atomic occupancy and the Debye Waller factors, are compiled in Table 5.2. The best fit model suggests a surface structure with 22% of clean FLT and 78% of Sb-bonded HLT. The proportion ratio of FLT to HLT is in good agreement with that (72/28 HLT/FLT ratio) reported in a published CTR paper (Tanwar et al., 2007b). As shown in Figure 5.6, the best fit structural model gave rise to a Sb surface complex binding on the HLT surface in a tridentate mode with a corner-sharing/edge-sharing binding configuration. The Sb surface complex has a coordination structure of a distorted octahedron with asymmetric Sb-O bond lengths (2.00 Å, 2.05 Å, 2.15 Å and 2.21 Å) and a nearest Sb-Fe separation of 3.05 Å. The distortion arises from two relatively longer Sb-O bonds associating with ^{16}O groups, compared to the other Sb-O bonds (one associating with ^{18}O group and three associating with distal oxygens) that are nearly equivalent in length (~ 2.0 Å). Significant changes were observed for layer spacing on a Sb-bonded HLT compared to the unrelaxed HLT surface structure. As illustrated in Figure 5.6C, substantially

larger expansion of layer spacing (38%) was found for Layer 3-4 compared to Layer 5-6 (17%). On the contrary, Layer 1-2 (-8%), Layer 2-3 (-2%) and Layer 4-5 (-10%) experienced a slight contraction. The change of layer spacing in the Sb-bonded hydrated hematite($1\bar{1}02$) surface structure implies that the electron density at the substrate surface was altered. However, we cannot distinguish whether the variance of layer spacing is induced by the Sb adsorption or it is caused as a result of surface relaxation in the clean hydrated surface structure.

5.4 Discussions

5.4.1 Implications of the mechanism controlling the surface binding configuration

A surface binding configuration with a distorted coordination structure is less energetically favorable, since the structural distortion would cause strain. In this study, we found a severe structural distortion of Sb coordination structure with a set of Sb-O bond lengths ranging from 2.00 to 2.21 Å. We realized that the Sb coordination structure would become less distorted if the Sb atom could move towards $^{\text{I}}\text{O}$ groups, since that will produce a shorter Sb- $^{\text{I}}\text{O}$ bonds. However, we notice that Sb moving closer to $^{\text{I}}\text{O}$ groups would result in a smaller Sb-Fe separation accordingly. Hence, in our system, it appears that the energy cost associated with the electrostatic repulsion caused by placing Sb closer to Fe atom exceeds that arising from the strain due to the coordination structure distortion. Similar findings were presented in a DFT study of Sb(V) binding at three tridentate sites on the hematite (0001) undertaken by Mason et al. (Mason et al., 2012), who observed a site preference trend, which is in direct relevance to the Sb-Fe distance, *i.e.* Sb binding at a site with larger Sb-Fe separation is energetically more favorable. The electrostatic repulsion between Sb and Fe was also highlighted by Bolanz et al. (Bolanz et al., 2013), who studied the possible isomorphic substitution of Sb(V) to structural Fe(III) site in

the transformation products of 2-line ferrihydrite, including hematite, goethite and ferrihydrite, as a function of Sb(V) concentration. Interestingly, it was found that the presence of Sb(V) decreased the hematite transformation product, but favored the goethite and ferrihydrite transformation products. Bolanz et al. proposed a mechanism of the isomorphic substitution of Sb(V) to structural Fe(III) in goethite and ferrihydrite, while they claimed that the strong electrostatic repulsion should significantly impede the isomorphic substitution of Sb(V) to structural Fe(III) site in the hematite structure, since each Fe(III) octahedral unit in the hematite structure has a face-sharing neighbor, corresponding to a short cation-cation separation ($<3.0 \text{ \AA}$). Similar findings were also reported by Mitsunobu et al. (Mitsunobu et al., 2013), who highlight that the immobilization mechanism of Sb(V) through isomorphic substitution in the process of structural transformation of ferrihydrite to more crystalline iron oxy(hydr)oxide products could be more effective than pure surface adsorption. Results presented in those reports are consistent to our best fit Sb(V) binding structure on the hematite ($1\bar{1}02$) surface, which has a tridentate corner-sharing/edge-sharing (not face-sharing) binding configuration with two relatively longer Sb-O bonds that distort the Sb coordination structure leading to a relatively large Sb-Fe separation (3.05 \AA), and probably weaker electrostatic repulsion. And we also want to claim that although the isomorphic substitution represents a more effective mechanism to immobilize Sb(V) as mentioned by Mitsunobu et al. (Mitsunobu et al., 2013), the retention of Sb(V) through surface adsorption is probably more prevailing in the environment, since natural sorbents are usually already formed before accepting Sb(V) contaminated effluents.

5.4.2 Comparison to previous DFT and XAFS studies

The best fit Sb(V) binding structure model presented here is in good agreement with that found in a recent DFT study of Sb(V) adsorption on α -Al₂O₃ ($1\bar{1}02$) surface (isostructural to hematite ($1\bar{1}02$) surface) undertaken by Ramadugu and Mason (Ramadugu and Mason, 2015). In that DFT study, the adsorption energy was computed for Sb(V) binding on the substrate surface under different binding configurations, and it was found that the most energetically favorable Sb surface complex is associated with, consistent to our best fit model, a tridentate binding site that bridges two terminal oxygen groups and one extra oxygen group from deeper atomic layers. In addition, those Sb complex species with edge-sharing binding configurations have optimized structures corresponding to significantly larger DFT adsorption energy, which was attributed to adsorption-induced surface relaxations of oxygen groups from deeper layer of the surface.

Our best fit Sb(V) binding structure on the hematite ($1\bar{1}02$) surface is also comparable to that proposed in previous XAFS studies. For example, Guo et al. (Guo et al., 2014) suggested a bidentate mononuclear edge-sharing binding for adsorbed Sb(V) on hydrous ferric oxide surface based on the Sb-Fe separation of 3.00-3.19 Å. Similar Fe-Sb distance (3.10 Å) was reported for a shooting range soil sample by Scheinost et al. (Scheinost et al., 2006). Interestingly, in the shooting range soil sample, Scheinost et al. identified another Sb(V) complex, which has a larger Sb-Fe separation (3.56 Å) indicative of corner-sharing binding mode. A mixture of two types of Sb surface complex species was also observed in a downstream sediment sample collected from a place adjacent to a historic Sb mining site (Ritchie et al., 2013). Those two Sb surface complex species probably represent Sb associating with different types of iron oxy(hydr)oxides coexisting in the soil sample, as evidenced in another XAFS study undertaken by Mitsunobu et al. (Mitsunobu et al., 2010b), who conducted EXAFS measurements of Sb(V) adsorption using

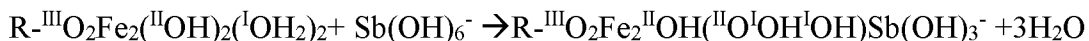
synthesized ferrihydrite and goethite samples. In that study, it was found that Sb(V) adsorption on ferrihydrite is via two binding structures (edge-sharing and corner-sharing modes with Sb-Fe distances of 3.1-3.11 Å and 3.51-3.55 Å, respectively), whereas in the goethite sample the Sb(V) was observed to only bind at edge-sharing sites corresponding to the Sb-Fe distance of 3.08-3.11Å. The crystallinity could be one reason responsible for the difference of binding configurations observed for ferrihydrite and goethite. Goethite is highly crystallized with well-ordered crystal structure, as opposed to ferrihydrite, which is poorly crystallized iron hydroxide with a more randomly ordered surface morphology responsible for a higher possibility to expose different types of reactive surface sites for Sb(V) binding.

The Sb-Fe separation derived in this study (3.05 Å) is in good agreement with those XAFS spectroscopy results (3.00-3.19 Å for edge-sharing mode). However, it should be noted that our best fit structure gave rise to a Sb complex species with a tridentate corner-sharing/edge-sharing binding configuration, rather than a bidentate edge-sharing binding configuration as implied in those XAFS studies. As mentioned above, Sb(V) bound to the hematite($1\bar{1}02$) surface under a bidentate edge-sharing binding configuration should be unfavorable due to the high steric constraint arising from abnormal short O-O separation between the distal oxygen and the surface oxygen, which is also confirmed in the DFT study mentioned above. Such an ambiguity in the binding mode could be avoided if the entire surface structure is resolved, which, however, is difficult when using XAFS spectroscopy, since the structure of substrate surface used is usually not well characterized.

5.4.3 Protonation schemes of interfacial oxygen

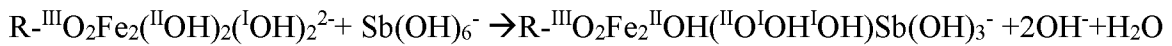
Using bond valence rule described above, protonation schemes could be predicted for surface functional groups in the best fit surface complex structure. The protonation schemes for different surface functional groups are listed in Table 5.3. As shown in Table 5.3, the $^I\text{O}_1$ atom has a bond valence sum of 1.05 v.u. prior to protonation, which could be saturated by associating with one covalent hydrogen (0.70 v.u.) and one hydrogen bond (0.25 v.u.). The counterpart surface oxygen $^I\text{O}_2$ is bonded to Sb with a shorter bond length, which corresponds to a larger bond valence (1.15 v.u.). As a result, $^I\text{O}_2$ could achieve a bond valence saturation by accepting one covalent hydrogen bond (0.85 v.u.), and does not require to accept a hydrogen bond making $^I\text{O}_2$ a hydrogen bond donor only. As for the ^{II}O groups, $^{II}\text{O}_3$ (bound with Sb) should be non-protonated and accept a hydrogen bond of valence 0.25 v.u., whereas $^{II}\text{O}_4$ (unbounded with Sb) should be singly protonated (0.88 v.u.) and accept one extra hydrogen bond with a valence of 0.25 v.u.. The ^{III}O groups, having a bond valence sum of 1.66 v.u., would only accept a hydrogen bond to achieve a near bond valence saturation state (valence sum=1.91 v.u.). In addition, as listed in Table 5.4, all three distal oxygens associating with Sb (bond valence of 0.93 v.u. contributed from the associated Sb-O bond) are singly protonated with each proton contributing 0.88 v.u., and would accept one more hydrogen bond with a bond valence of 0.19 v.u. to arrive at the bond valence saturation.

With the protonation schemes of surface oxygen groups described above, a stoichiometric reaction could be written as follows,



The protonation schemes for the clean hematite (1 $\bar{1}$ 02) surface in the reaction was based on the previous CTR work (Tanwar et al., 2007b) and DFT calculation (Lo et al., 2007). Interestingly,

the stoichiometry outlined above does not predict any proton/hydroxyl release, which seems to imply a pH independence of Sb(V) adsorption on the hematite surface. The proton/hydroxyl stoichiometry proposed here were also reported previously in results based on the macroscale adsorption experiments (Leuz et al., 2006; Martínez-Lladó et al., 2008; Vithanage et al., 2013). However, it should be noted that the proton and hydroxyl stoichiometry in the reaction is also determined by the protonation states of surface oxygen on the clean surface as a function of solution pH. Thus, the ^IO group could be less protonated or even non-protonated under a relatively higher pH. For example, considering a singly protonated ^IO groups, the stoichiometric reaction should be re-written as,



In this scenario, due to the production of OH⁻, a higher solution pH will favor the surface complexation reaction proceeding towards the reactant side leading to the desorption of the adsorbed Sb(V) under alkaline conditions. This stoichiometric reaction is consistent with pH adsorption edge results presented in previous studies (Leuz et al., 2006; Martínez-Lladó et al., 2008; Vithanage et al., 2013), which showed a maximum uptake at low pH but a decline of uptake at higher pH. Compared to those two stoichiometries, the Sb(V) adsorption on hematite ($1\bar{1}02$) surface in our system is more likely to take the first one, since the Sb(V) solution is buffered to pH 5.5, which should make the surface functional groups well protonated considering the pH corresponding to the pHPZC of the hematite surface is relatively high (>7.0) (Kosmulski, 2002).

5.4.4 Relationship between site coverage and the inter-site distance

To explore surface site coverage as a function of Sb(V) concentration, another CTR measurement was conducted with a Sb(V) solution of higher concentration (400 μM) attempting to achieve a mono layer saturation. However, little variation of CTR scattering intensity was observed (data not shown) when an elevated Sb(V) concentration was used in the CTR measurement, that implies an apparent mono layer saturation state at the concentration of 200 μM .

In this section, we presented a simple approach (site coverage simulation test) to explore the relationship between the site coverage and the inter site distance. To explain the observed apparent mono layer saturation, we proposed a hypothesis that is “when the surface sites are gradually being occupied, the adsorbed Sb will be closer to each other potentially inducing a higher Sb-Sb electrostatic repulsion to impede the site occupation”.

The conduction of site coverage simulation test requires the knowledge of the positions of reactive binding sites that were attained from the best fit CTR model. On the HLT of hematite ($1\bar{1}02$) surface, symmetry sites within each unit cell were allowed to be occupied with an equivalent chance. Simulation tests were run on a 20×20 super cell by repeatedly occupying the surface sites on a random basis at a cutoff limit of inter-sorbate distance, which needs to be pre-defined. After each simulation is completed, the number of occupied sites as well as the unoccupied sites were counted to further calculate the site coverage, which is the simulated site coverage corresponding to the associated cutoff limit. Different site simulation tests were run with cutoff limits ranging from 3.6 \AA to 11.01 \AA , which were identified from the site distribution pattern as shown in Figure 5.7B. The site coverage simulation results (Figure 5.7A) demonstrate, as expected, a decreasing trend of site occupancy with the cutoff distance limit. Interestingly, the

CTR derived occupancy of Sb(V) on the surface is around 75% (normalized to the HLT only, and 100% occupancy represents one site occupied per unit cell) in good agreement with the simulated site coverage at the 5.03 Å cutoff limit.

We noticed that a cutoff limit of 5.03 Å will allow each type of symmetry site to be occupied freely in vertical, horizontal and diagonal directions except for two cases. In the first case, two sites within a same unit cell were occupied simultaneously, and in the other case, two adjacent sites were vertically aligned with the bottom site sitting further away from the unit cell origin (represented by red dots in the Figure 5.7) and the top one closer to the unit cell origin (blue dots in the Figure 5.7). The site occupation pattern in either case will result in an inter-site distance < 3.6 Å, which would give rise to the theoretical mono layer saturation (200% occupancy), as predicted in the site coverage simulation results. As shown in Figure 5.7E, a mono layer saturation with Sb-Sb separation of 3.6 Å will undergo a strong steric constraint due to the extremely short O-O (< 0.3 Å) between distal oxygens bonding to vertically adjacent sorbates. We proposed a mechanism to release such a high steric constraint by allowing two adjacent sorbate to be aligned vertically sharing one oxygen as shown in Figure 5.7 F. As a result, a linkage structure connecting vertically adjacent sorbates running parallel along the \mathbf{b}_s direction would be produced. Such a site occupation pattern was, nonetheless, not observed in our system. Furthermore, we noticed that a surface site occupation pattern with one type of symmetry sites being occupied and the other counterpart surface sites being unoccupied would result in a 100% site coverage at the 5.03 Å cutoff limit that is higher than the result based on random occupation. Hence, it seems that the random occupation of surface sites breaks the site symmetry (\mathbf{b}_s glide plane) found in the clean substrate surface leading to a decrease in the site coverage that is probably controlled by both the steric and the electrostatic effect.

5.5 Conclusions

CTR study was performed to investigate Sb(V) adsorption on hematite ($1\bar{1}02$) surface under *in situ* conditions. The best fit structural model indicated that Sb(V) adsorption on the HLT surface is via an inner-sphere tridentate binding mode with the tridentate site composing of one O-O edge and two O-O linkages with one bridging two terminal oxygen groups (^IO) and the other one bridging one ^IO and one ^{II}O . The distortion of the Sb octahedral local structure with Sb- ^IO bonds significantly stretching by ~ 0.15 Å compared to the other Sb-O bonds is probably a compromise for maintaining a larger Sb-Fe separation to minimize the associated electrostatic repulsion. The Sb-Fe distance (3.05 Å) derived from the present study is comparable to those reported in published XAFS studies, which also identified a Sb(V) species on poorly crystallized substrates (like ferrihydrite) along with a larger Sb-Fe separation (~ 3.5 Å) indicative of corner-sharing binding structure.

The bond valence analysis was undertaken to evaluate the chemical plausibility of the best fit CTR model structure. It was found that all surface oxygen groups as well as sorbates could arrive at a bond valence saturation state within 0.2 v.u. after proper assignment of covalent hydrogen and/or hydrogen bond to under-coordinated oxygen groups. Using the predicted protonation schemes of oxygen groups, a unique surface complexation stoichiometry was generated, which suggests an pH independence of Sb(V) adsorption on hematite($1\bar{1}02$) surface in an acidic solution. We also highlight the possibility of a different proton stoichiometry under a different solution pH, which is directly related to the change of the protonation schemes of surface oxygen groups.

The site coverage simulation tests were conducted to address the influence of possible electrostatic repulsion between adsorbed Sb atoms on the surface site coverage. It was found that

the CTR-derived occupancy matches to the simulated site coverage at 5.03 Å cutoff limit. In addition, the results of site coverage simulation tests also suggested that the steric constraint as well as the Sb-Sb electrostatic repulsion are two potential factors in determining the Sb(V) uptake to iron oxide surfaces.

5.6 Acknowledgements

This project is funded by DoD SERDP grant ER-1770. All the associated experiments were performed at beamline 13BMC of GeoSoilEnviroCARS (Sector 13), Advanced Photon Source (APS), Argonne National Laboratory. GSECARS is supported by the National Science Foundation - Earth Sciences (EAR-1128799) and Department of Energy - Geosciences (DE-FG02-94ER14466). Use of the Advanced Photon Source was supported by the U. S. Department of Energy, Office of Science, Office of Basic Energy Sciences, under Contract No. DE-AC02-06CH11357. We would also like to thank the Arctic Super Computer Center (ARSC) at University of Alaska Fairbanks for providing computation resource used in the surface modeling.

5.7 References

- Ackermann S., Gieré R., Newville M. and Majzlan J. (2009) Antimony sinks in the weathering crust of bullets from Swiss shooting ranges. *Sci. Total Environ.* **407**, 1669–1682.
- Als-Nielsen J. and McMorrow D. (2011) *Elements of modern X-ray physics.*, John Wiley & Sons.
- Bargar J. R., Towle S. N., Brown G. E. and Parks G. A. (1997) XAFS and Bond-Valence Determination of the Structures and Compositions of Surface Functional Groups and Pb(II) and Co(II) Sorption Products on Single-Crystal α -Al₂O₃. *J. Colloid Interface Sci.* **185**, 473–492. Available at: <http://www.sciencedirect.com/science/article/pii/S0021979796945749>.
- Björck M. (2011) Fitting with differential evolution: an introduction and evaluation. *J. Appl. Crystallogr.* **44**, 1198–1204. Available at: <http://dx.doi.org/10.1107/S0021889811041446>.

- Bolanz R. M., Blaess U., Ackermann S., Ciobota V., Roesch P., Tarcea N., Popp J. and Majzlan J. (2013) The effect of antimonate, arsenate, and phosphate on the transformation of ferrihydrite to goethite, hematite, ferroxhyte, and tripuhyite. *Clays Clay Miner.* **61**, 11–25.
- Brown G. E., Parks G. A. and O'Day P. A. (1995) Sorption at mineral-water interfaces: macroscopic and microscopic perspectives. *Miner. Surfaces* **5**.
- Brown I. D. (2009) Recent Developments in the Methods and Applications of the Bond Valence Model. *Chem. Rev.* **109**, 6858–6919. Available at: <http://pubs.acs.org/doi/abs/10.1021/cr900053k>.
- Brown I. D. and Altermatt D. (1985) Bond-valence parameters obtained from a systematic analysis of the Inorganic Crystal Structure Database. *Acta Crystallogr. Sect. B* **41**, 244–247. Available at: <http://dx.doi.org/10.1107/S0108768185002063>.
- Cai Y., Li L. and Zhang H. (2015) Kinetic modeling of pH-dependent antimony (V) sorption and transport in iron oxide-coated sand. *Chemosphere* **138**, 758–764.
- Catalano J. G., Fenter P. and Park C. (2007) Interfacial water structure on the (0 1 2) surface of hematite: Ordering and reactivity in comparison with corundum. *Geochim. Cosmochim. Acta* **71**, 5313–5324.
- Eikenberry E. F., Brönnimann C., Hülsen G., Toyokawa H., Horisberger R., Schmitt B., Schulze-Briese C. and Tomizaki T. (2003) PILATUS: a two-dimensional X-ray detector for macromolecular crystallography. *Nucl. Instruments Methods Phys. Res. Sect. A Accel. Spectrometers, Detect. Assoc. Equip.* **501**, 260–266.
- Fenter P. A. (2002) X-ray Reflectivity as a Probe of Mineral-Fluid Interfaces: A User Guide. *Rev. Mineral. Geochemistry* **49**, 149–221. Available at: <http://rimg.geoscienceworld.org/content/49/1/149.short>.
- Filella M., Belzile N. and Chen Y. (2002a) Antimony in the environment: a review focused on natural waters: I. Occurrence. *Earth-Science Rev.* **57**, 125–176.
- Filella M., Belzile N. and Chen Y. (2002b) Antimony in the environment: a review focused on natural waters: II. Relevant solution chemistry. *Earth-Science Rev.* **59**, 265–285.
- Finger L. W. and Hazen R. M. (1980) Crystal structure and isothermal compression of Fe₂O₃, Cr₂O₃, and V₂O₃ to 50 kbars. *J. Appl. Phys.* **51**, 5362–5367.
- Franco M. A., Barbosa A. C., Rath S. and Dorea J. G. (1995) Antimony oxidation states in antileishmanial drugs. *Am. J. Trop. Med. Hyg.* **52**, 435–437.
- Guo X., Wu Z., He M., Meng X., Jin X., Qiu N. and Zhang J. (2014) Adsorption of antimony onto iron oxyhydroxides: Adsorption behavior and surface structure. *J. Hazard. Mater.* **276**, 339–345.

- Hamilton W. C. (1965) Significance tests on the crystallographic $\{R\}$ factor. *Acta Crystallogr.* **18**, 502–510. Available at: <http://dx.doi.org/10.1107/S0365110X65001081>.
- Heberling F., Trainor T. P., Lützenkirchen J., Eng P., Denecke M. A. and Bosbach D. (2011) Structure and reactivity of the calcite--water interface. *J. Colloid Interface Sci.* **354**, 843–857. Available at: <http://www.sciencedirect.com/science/article/pii/S0021979710012336>.
- Henderson M. A., Joyce S. A. and Rustad J. R. (1998) Interaction of water with the (1×1) and (2×1) surfaces of α -Fe₂O₃(0 1 2). *Surf Sci.* **417**, 66–81. Available at: <http://www.sciencedirect.com/science/article/pii/S0039602898006621>.
- Herwaldt B. L. and Berman J. D. (1992) Recommendations for treating leishmaniasis with sodium stibogluconate (Pentostam) and review of pertinent clinical studies. *Am. J. Trop. Med. Hyg.* **46**, 296–306.
- IARC (1990) Some organic solvents, resin monomers and related compounds, pigments and occupational exposures in paint manufacture and painting. *IARC Monogr. Eval. Carcinog. risks to humans* **47**.
- Ilgen A. G., Majs F., Barker A. J., Douglas T. A. and Trainor T. P. (2014) Oxidation and mobilization of metallic antimony in aqueous systems with simulated groundwater. *Geochim. Cosmochim. Acta* **132**, 16–30.
- Ilgen A. G. and Trainor T. P. (2012) Sb(III) and Sb(V) Sorption onto Al-Rich Phases: Hydrous Al Oxide and the Clay Minerals Kaolinite KGa-1b and Oxidized and Reduced Nontronite NAu-1. *Environ. Sci. Technol.* **46**, 843–851.
- Kong L., Hu X. and He M. (2015) Mechanisms of Sb(III) Oxidation by Pyrite-Induced Hydroxyl Radicals and Hydrogen Peroxide. *Environ. Sci. Technol.* **49**, 3499–3505.
- Koningsberger D. C. and Prins R. (1988) X-ray absorption: principles, applications, techniques of EXAFS, SEXAFS, and XANES. Wiley-Interscience.
- Kosmulski M. (2002) The pH-dependent surface charging and the points of zero charge. *J. Colloid Interface Sci.* **253**, 77-87. Available at: <http://www.sciencedirect.com/science/article/pii/S0021979702984900>
- Leuz A. K., Mönch H. and Johnson C. A. (2006) Sorption of Sb (III) and Sb (V) to goethite: influence on Sb (III) oxidation and mobilization. *Environ. Sci. Technol.* **40**, 7277–7282.
- Lo C. S., Tanwar K. S., Chaka A. M. and Trainor T. P. (2007) Density functional theory study of the clean and hydrated hematite (1-102) surfaces. *Phys. Rev. B* **75**, 75425. Available at: <http://link.aps.org/doi/10.1103/PhysRevB.75.075425>.

- Martínez-Lladó X., de Pablo J., Giménez J., Ayora C., Martí V. and Rovira M. (2008) Sorption of antimony(V) onto synthetic goethite in carbonate medium. *Solvent Extr. Ion Exch.* **26**, 289–300.
- Mason S. E., Trainor T. P. and Goffinet C. J. (2012) DFT study of Sb(III) and Sb(V) adsorption and heterogeneous oxidation on hydrated oxide surfaces. *Comput. Theor. Chem.* **987**, 103–114. Available at: <http://www.sciencedirect.com/science/article/pii/S2210271X11006062>.
- McComb K. A., Craw D. and McQuillan A. J. (2007) ATR-IR Spectroscopic Study of Antimonate Adsorption to Iron Oxide. *Langmuir* **23**, 12125–12130. Available at: <http://pubs.acs.org/doi/abs/10.1021/la7012667>.
- Mitsunobu S., Muramatsu C., Watanabe K. and Sakata M. (2013) Behavior of Antimony(V) during the Transformation of Ferrihydrite and Its Environmental Implications. *Environ. Sci. Technol.* **47**, 9660–9667.
- Mitsunobu S., Takahashi Y. and Terada Y. (2010a) μ -XANES Evidence for the Reduction of Sb(V) to Sb(III) in Soil from Sb Mine Tailing. *Environ. Sci. Technol.* **44**, 1281–1287.
- Mitsunobu S., Takahashi Y., Terada Y. and Sakata M. (2010b) Antimony(V) Incorporation into Synthetic Ferrihydrite, Goethite, and Natural Iron Oxyhydroxides. *Environ. Sci. Technol.* **44**, 3712–3718.
- Ramadugu S. K. and Mason S. E. (2015) DFT Study of Antimony (V) Oxyanion Adsorption on α -Al₂O₃ (1-102). *J. Phys. Chem. C* **119**, 18149–18159.
- Rawcliffe C. (2000) Antimony in medical history. *BMJ* **320**, 879.
- Resongles E., Casiot C., Elbaz-Poulichet F., Freydier R., Bruneel O., Piot C., Delpoux S., Volant A. and Desoeuvre A. (2013) Fate of Sb(V) and Sb(III) species along a gradient of pH and oxygen concentration in the Carnoules mine waters (Southern France). *Environ. Sci. Impacts* **15**, 1536–1544.
- Ritchie V. J., Ilgen A. G., Mueller S. H., Trainor T. P. and Goldfarb R. J. (2013) Mobility and chemical fate of antimony and arsenic in historic mining environments of the Kantishna Hills district, Denali National Park and Preserve, Alaska. *Chem. Geol.* **335**, 172–188.
- Robinson I. K. (1986) Crystal truncation rods and surface roughness. *Phys. Rev. B* **33**, 3830–3836. Available at: <http://link.aps.org/doi/10.1103/PhysRevB.33.3830>.
- Robinson I. K. and Tweet D. J. (1992) Surface x-ray diffraction. *Reports Prog. Phys.* **55**, 599.
- Scheinost A. C., Rossberg A., Vantelon D., Xifra I., Kretzschmar R., Leuz A.-K., Funke H. and Johnson C. A. (2006) Quantitative antimony speciation in shooting-range soils by EXAFS spectroscopy. *Geochim. Cosmochim. Acta* **70**, 3299–3312. Available at: <http://www.sciencedirect.com/science/article/pii/S0016703706001451>.

- Schlepütz C. M., Herger R., Willmott P. R., Patterson B. D., Bunk O., Brönnimann C., Henrich B., Hülsen G. and Eikenberry E. F. (2005) Improved data acquisition in grazing-incidence X-ray scattering experiments using a pixel detector. *Acta Crystallogr. Sect. A Found. Crystallogr.* **61**, 418–425.
- Sundar S. and Chakravarty J. (2010) Antimony toxicity. *Int. J. Environ. Res. Public Health* **7**, 4267–4277.
- Tanwar K. S., Catalano J. G., Petitto S. C., Ghose S. K., Eng P. J. and Trainor T. P. (2007a) Hydrated α -Fe₂O₃ surface structure: Role of surface preparation. *Surf. Sci.* **601**, L59–L64.
- Tanwar K. S., Lo C. S., Eng P. J., Catalano J. G., Walko D. A., Brown G. E. J., Waychunas G. A., Chaka A. M. and Trainor T. P. (2007b) Surface diffraction study of the hydrated hematite surface. *Surf. Sci.* **601**, 460–474. Available at: <http://www.sciencedirect.com/science/article/pii/S0039602806010739>.
- Trainor T. P., Eng P. J. and Robinson I. K. (2002) Calculation of crystal truncation rod structure factors for arbitrary rational surface terminations. *J. Appl. Crystallogr.* **35**, 696–701. Available at: <http://dx.doi.org/10.1107/S0021889802013985>.
- United States Environmental Protection Agency (2009) List of drinking water contaminants and their maximum contaminant levels.
- Vithanage M., Rajapaksha A. U., Dou X., Bolan N. S., Yang J. E. and Ok Y. S. (2013) Surface complexation modeling and spectroscopic evidence of antimony adsorption on iron-oxide-rich red earth soils. *J. Colloid Interface Sci.* **406**, 217–224.
- Vlieg E. (2000) ROD: a program for surface X-ray crystallography. *J. Appl. Crystallogr.* **33**, 401–405. Available at: <http://dx.doi.org/10.1107/S0021889899013655>.
- Wilson S. C., Lockwood P. V., Ashley P. M. and Tighe M. (2010) The chemistry and behaviour of antimony in the soil environment with comparisons to arsenic: a critical review. *Environ. Pollut. (Oxford, U. K.)* **158**, 1169–1181.
- Xi J., He M., Wang K. and Zhang G. (2013) Adsorption of antimony (III) on goethite in the presence of competitive anions. *J. Geochemical Explor.* **132**, 201–208.
- You H. (1999) Angle calculations for a 4S+2D six-circle diffractometer. *J. Appl. Crystallogr.* **32**, 614–623.

Table 5.1 Potential binding sites on hematite ($1\bar{1}02$) surface and goodness-of-fit for different models

Termination patterns	Binding sites	Binding configurations	Binding modes	Model trials	FOM ^a
FLT	O_5O_6, O_5O_{6+y}	Corner-sharing	Bidentate	Model1	10.08
	O_5O_{7+y}, O_6O_8	Edge-sharing	Bidentate	Excluded	-
	O_5O_{8+x}, O_6O_{7-y}	Edge-sharing	Bidentate	Excluded	-
	$O_5O_{6+y}O_7, O_5O_6O_{8+x}$	Corner/edge-sharing	Tridentate	Model2	6.94
	$O_5O_{7+x}O_{8+x}, O_6O_{7-y}O_8$	Face-sharing	Tridentate	Model3	9.88
HLT	O_1O_2, O_1O_{2+y}	Corner-sharing	Bidentate	Model4	710.32
	O_1O_3, O_2O_{4+x}	Edge-sharing	Bidentate	Excluded	-
	O_1O_{4+y}, O_2O_{3+x}	Edge-sharing	Bidentate	Excluded	-
	$O_1O_2O_3, O_{1-y}O_2O_{4+x}$	Corner/edge-sharing	Tridentate	Model5	2.25
	$O_1O_3O_{4+y}, O_2O_{3+x}O_{4+x}$	Face-sharing	Tridentate	Model6	10.73

^a The FOM has been scaled by the bond valence penalty factor

Table 5.2 Best fit structural parameters based on the model with tridentate corner-sharing/edge-sharing binding mode

Layer	el	x	y	z	Δx (Å)	Δy (Å)	Δz (Å)	B_{iso} (Å ²)	Occ
Sb bonded HLT surface with weight of 39% (-4%, +2%)									
^a w ₂	O	0.173	0.157	1.656	-	-	-	0.60 (-1E-4, 9E0)	0.20 (-2E-1, 6E-1)
^a w ₁	O	1.327	0.657	1.656	-	-	-	0.60 (-1E-4, 9E0)	0.20 (-2E-1, 6E-1)
^b i ₃	O	0.608	0.626	1.272	-	-	-	1.00	0.37 (-3E-2, 2E-2)
^b i ₂	O	0.160	0.725	1.146	-	-	-	1.00	0.37 (-3E-2, 2E-2)
^b i ₁	O	0.328	0.295	1.107	-	-	-	1.00	0.37 (-3E-2, 2E-2)
^b i ₀	Sb	0.484	0.609	1.014	-	-	-	0.22 (-2E-2, 5E-1)	0.37 (-3E-2, 2E-2)
1	O	0.659	0.933	0.896	0.032 (-7E-2, 8E-2)	-0.217 (-3E-5, 5E-2)	-0.053 (-1E-1, 5E-2)	0.40	1.00
	O	0.841	0.433	0.896	-0.032 (-7E-2, 8E-2)	-0.217 (-3E-5, 5E-2)	-0.053 (-1E-1, 5E-2)	0.40	1.00
2	O	0.340	0.567	0.755	0.172 (-8E-2, 3E-2)	-0.207 (-1E-2, 1E-1)	0.035 (-7E-2, 6E-2)	0.40	1.00
	O	0.160	0.066	0.755	-0.172 (-8E-2, 3E-2)	-0.207 (-1E-2, 1E-1)	0.035 (-7E-2, 6E-2)	0.40	1.00
3	Fe	0.500	0.880	0.651	-	-	0.048 (-8E-3, 1E-5)	0.32	1.00
	Fe	0.000	0.379	0.651	-	-	0.048 (-8E-3, 1E-5)	0.32	1.00
4	O	0.847	0.737	0.585	-	-	-0.088 (-1E-2, 5E-3)	0.40	1.00
	O	0.653	0.236	0.585	-	-	-0.088 (-1E-2, 5E-3)	0.40	1.00
5	O	0.347	0.904	0.411	-	-	0.061 (-2E-2, 2E-5)	0.40	1.00
	O	0.153	0.403	0.411	-	-	0.061 (-2E-2, 2E-5)	0.40	1.00
Clean FLT surface of 11% (-4%, +2%)									
^a w ₂	O	1.010	0.001	0.838	-	-	-	0.60 (-2E-4, 9E0)	0.80 (-8E-1, 6E-5)
^a w ₁	O	0.490	0.501	0.838	-	-	-	0.60 (-2E-4, 9E0)	0.80 (-8E-1, 6E-5)
1	O	0.823	0.697	0.571	-0.121 (-8E-2, 3E-1)	-0.217 (-1E-5, 4E-1)	-0.194 (-3E-2, 3E-1)	0.40	1.00
	O	0.677	0.196	0.571	0.121 (-8E-2, 3E-1)	-0.217 (-1E-5, 4E-1)	-0.194 (-3E-2, 3E-1)	0.40	1.00
2	O	0.338	0.864	0.380	-0.047 (-2E-1, 1E-1)	-0.217 (-3E-4, 4E-1)	-0.168 (-5E-2, 3E-1)	0.40	1.00
	O	0.162	0.363	0.380	0.047 (-2E-1, 1E-1)	-0.217 (-3E-4, 4E-1)	-0.168 (-5E-2, 3E-1)	0.40	1.00
3	Fe	0.000	0.761	0.352	-	-	-0.020 (-1E-1, 8E-2)	0.32	1.00
	Fe	0.500	0.260	0.352	-	-	-0.020 (-1E-1, 8E-2)	0.32	1.00
4	O	0.694	0.535	0.258	-	-	0.062 (-3E-1, 1E-1)	0.40	1.00
	O	0.806	0.035	0.258	-	-	0.062 (-3E-1, 1E-1)	0.40	1.00

Table 5.2 Continued

Layer	el	x	y	z	Δx (Å)	Δy (Å)	Δz (Å)	B_{iso} (Å ²)	Occ
5	Fe	0.500	0.810	0.137	-	-	-0.061 (-2E-2, 8E-2)	0.32	1.00
	Fe	0.000	0.310	0.137	-	-	-0.061 (-2E-2, 8E-2)	0.32	1.00

The coordinates are fractional based on the re-indexed unit cell parameters ($a=5.038$ Å, $b=5.434$ Å, $c=7.3707$ Å, $\alpha=90^\circ$, $\beta=90^\circ$, $\gamma=90^\circ$). Δx , Δy , and Δz are atomic displacements in Å along directions of \mathbf{a}_s axis, \mathbf{b}_s axis, and \mathbf{c}_s axis respectively. The B_{iso} are isotropic Debye-Waller factors and Occ are occupancy parameters. The occupancies of all surface atoms were fixed at 100% in each individual domain with the domain weight being optimized during the modeling.

Note results associated symmetry related terminations (total weight=50%) were not shown in this table.

Only one site was shown in the table for clarity, although two symmetry sites were explicatively considered during surface modeling. Numbers inside a parenthesis are the ranges of errors for the best fit parameter values calculated at a 95% confidence level. Note that those errors do not have a normal distribution since the optimization is performed based on the differential evolution algorithm.

^a \mathbf{w}_1 and \mathbf{w}_2 represent the two interfacial water molecules

^b \mathbf{i}_0 is the sorbate layer, and the distal oxygen layers are represented as \mathbf{i}_1 , \mathbf{i}_2 and \mathbf{i}_3

Table 5.3 Bond valence analysis of surface species based on the best fit structure model

Surface Species	Original bond valence sum (v.u)	Protonation scheme and hydrogen bonding		Bond valence sum after adding H or H bond (v.u)	Chemical plausibility
		Number of H	Number of H bond		
Fe≡O ₁ —Sb	1.05	1 (0.70)	1 (0.25)	2.00	Plausible
Fe≡O ₂ —Sb	1.15	1 (0.85)	0	2.00	Plausible
Fe ₂ ≡O ₃ —Sb	1.65	0	1 (0.25)	1.90	Plausible
Fe ₂ ≡O ₄	0.84	1 (0.88)	1 (0.25)	1.97	Plausible
Fe ₃ ≡O _{5,6}	1.66	0	1 (0.25)	1.91	Plausible
O _{dist} —Sb	0.93	1(0.88)	1 (0.19)	2.00	Plausible

The numbers inside the parenthesis are bond valence arbitrarily assigned to a covalent hydrogen (H) or a hydrogen bond (H bond) to obtain a bond valence sum closest to the saturation state. The ranges of the valence for a H and a H bond are 0.68-0.88 v.u and 0.13-0.25 v.u, respectively as suggested by Bargar (Bargar et al., 1997).

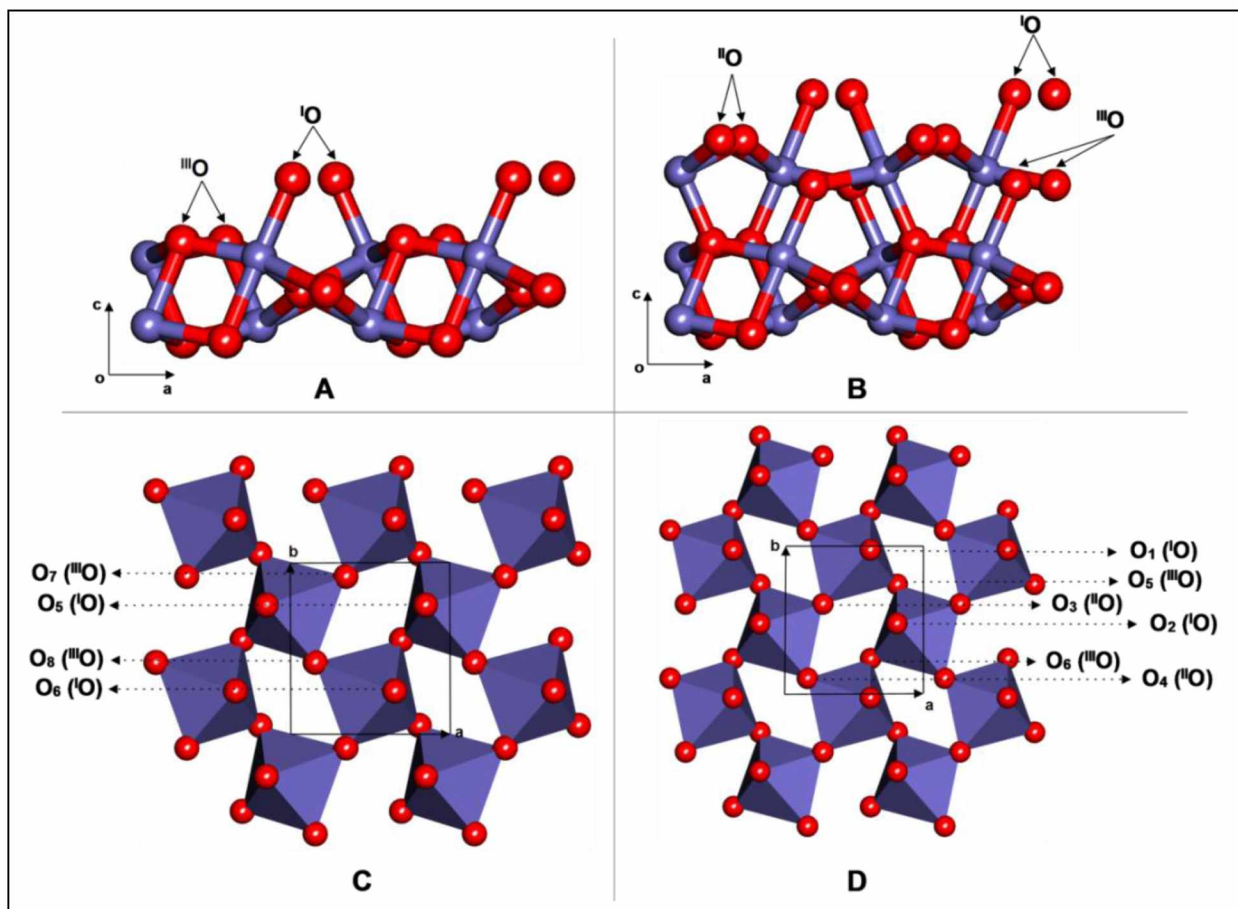


Figure 5.1 Layer stacking sequence along the C_s axis for the stoichiometric termination surface of hematite ($1\bar{1}02$) (A) and the half layer termination surface of hematite ($1\bar{1}02$) (B). Polyhedral representation of the oxygen-terminated full layer termination surface of hematite ($1\bar{1}02$) (C) and half layer termination surface of hematite ($1\bar{1}02$) (D) (second octahedral layer and those beneath are not shown for clarity). Lengths for unit cell are $a=5.038 \text{ \AA}$, $b=5.434 \text{ \AA}$ and $c=7.3707 \text{ \AA}$. The $^{\text{III}}\text{O}$, $^{\text{II}}\text{O}$, and $^{\text{I}}\text{O}$ represent oxygen triply, doubly and singly coordinated to iron in the structure, respectively. Names of surface functional groups were shown for both half layer termination surface (O_1 to O_6) and the stoichiometric termination surface (O_6 to O_8). Note that the first atom layer in the stoichiometric termination surface overlaps with the fourth atom layer in the half layer termination surface, and thus O_5 and O_6 represent either atoms in the fourth atom layer in the half layer termination surface or atoms in the first atom layer in the stoichiometric termination surface.

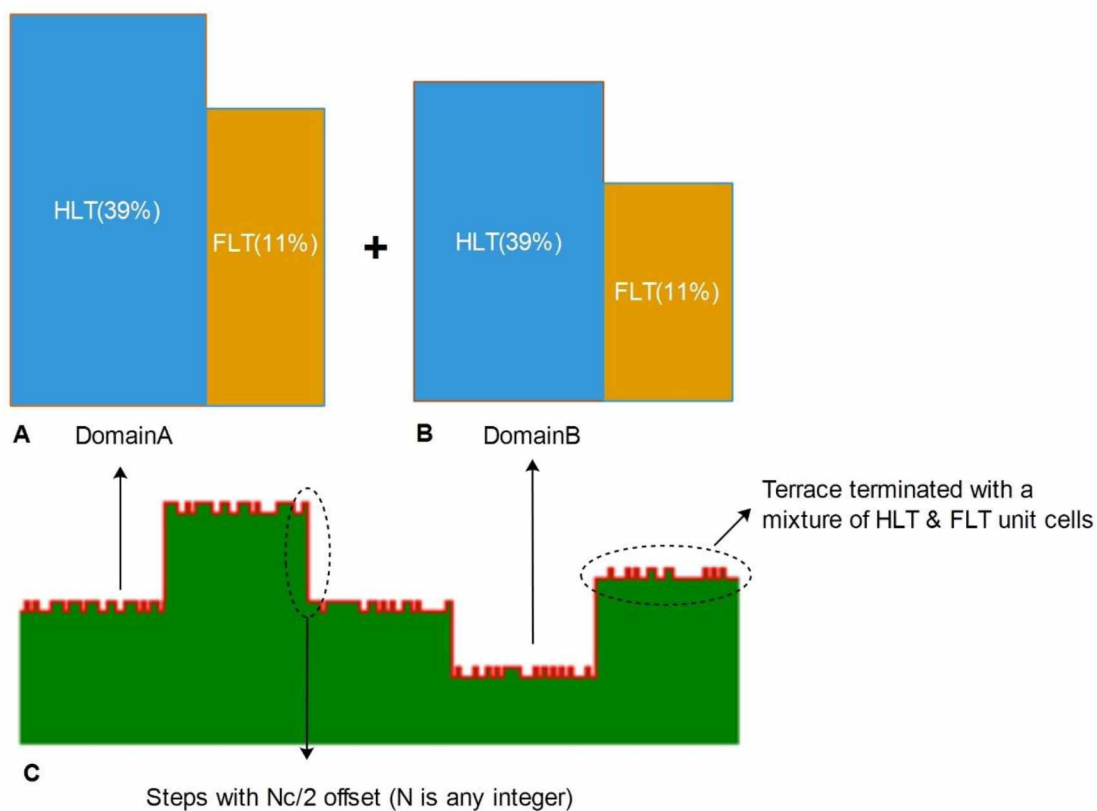


Figure 5.2 Schematic diagram of surface topographic pattern (C) formed by a mixture of HLT and FLT on different terraces (either DomainA or DomainB). The DomainA is symmetry related to DomainB. The weight percentage for each termination is based on the results of the best fit model.

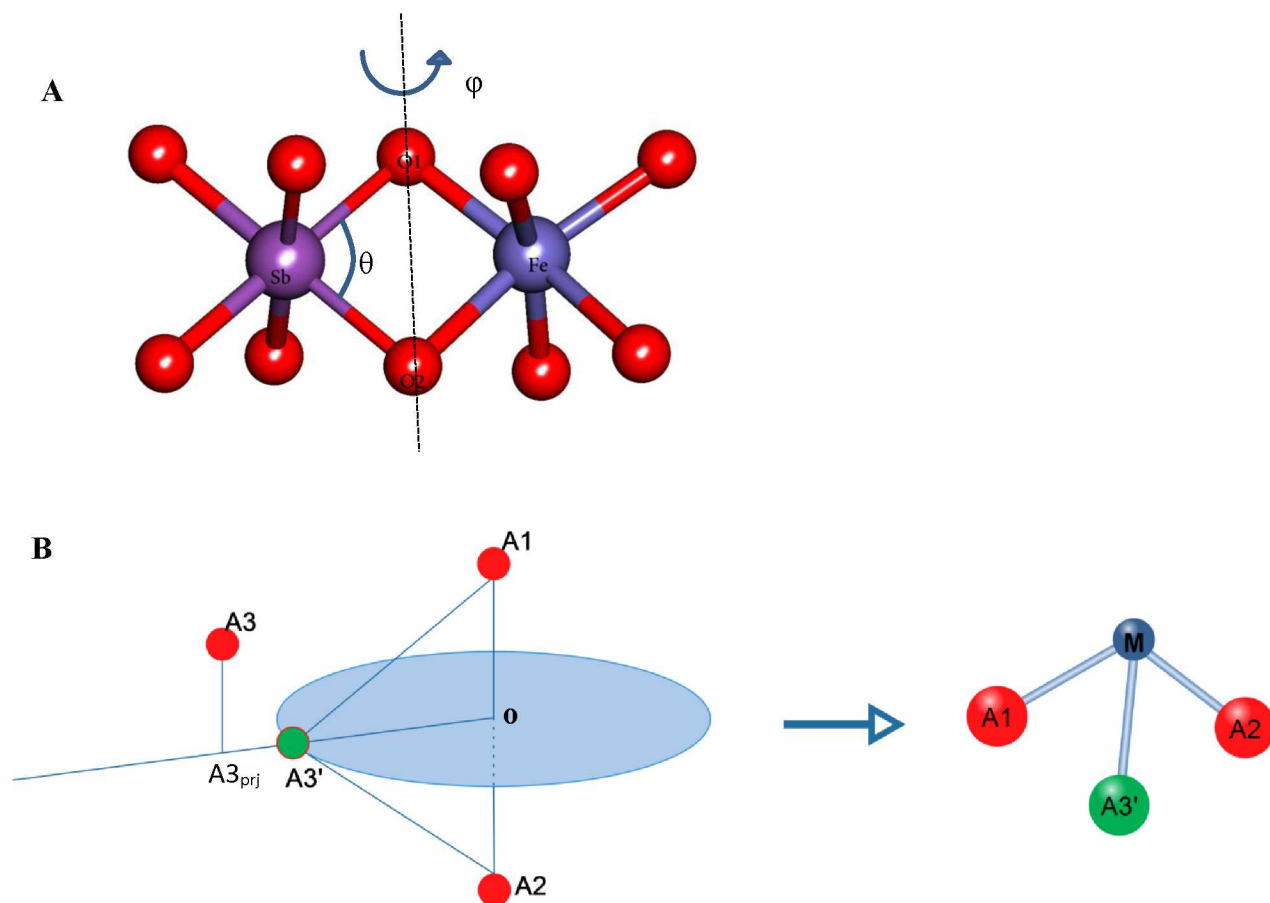


Figure 5.3 (A) Geometrical solution of Sb position in a bidentate edge-sharing binding mode (O1O2 as the binding site) through two angles, rotation angle ϕ (rotating about O1O2 axis), dihedral angle θ (angle O1-Sb-O2 floated in a range from 80° to 100° during model refinement). (B) Geometrical solution of Sb position in a tridentate binding mode (A1A2A3 as the binding site). A bisecting plane through center point of A1A2 (\mathbf{o}) is used to find a dummy point $A3'$, which forms an equilateral triangle with A1 and A2, and is nearest to A3. To locate $A3'$, a circle centering at \mathbf{o} on the bisecting plane is drawn with a radius, which makes each point on the circle form an equilateral triangle with A1 and A2. Then A3 is projected on the bisecting plane to point $A3_{prj}$, which is connected to point \mathbf{o} . Then $\mathbf{o}A3_{prj}$ will cross the dummy point $A3'$ on the circle. With dummy point $A3'$ computed, the position for Sb (shown as blue ball labeled as M) as well as positions for the other three distal oxygens (not shown) could be calculated by knowing the dihedral angles (O-Sb-O) is 90° .

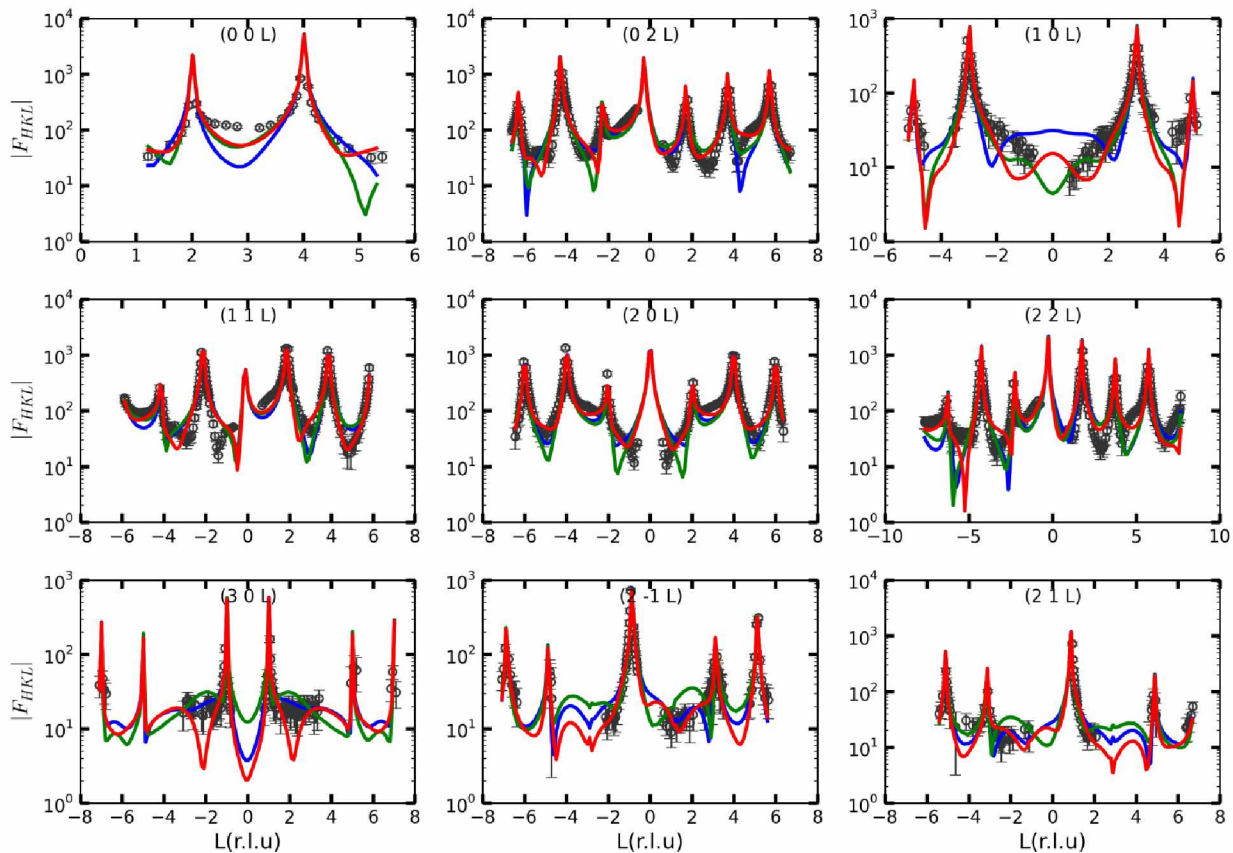


Figure 5.4 Experimental (gray circles) and model-based structure factors (F_{HKL}) as a function of perpendicular momentum transfer (L , in reciprocal lattice units) for the hematite ($1\bar{1}02$) surface reacted with $200\ \mu\text{M}$ Sb(V) at $\text{pH } 5.5$. The solid lines in green represent the calculated CTR profiles based on the best fit model Model1, the solid lines in blue represent the calculated CTR profiles based on the best fit model Model2, the solid lines in red represent the calculated CTR profiles based on the best fit model Model3.

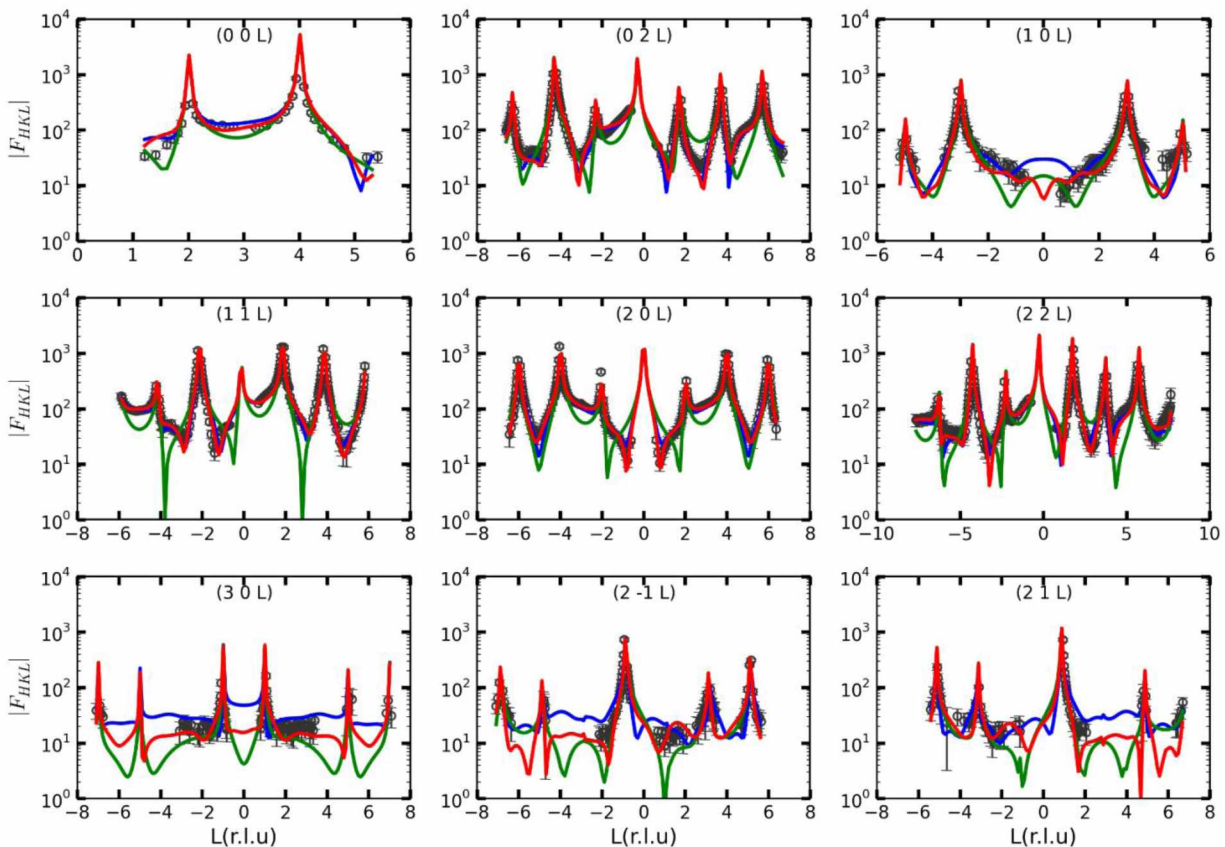


Figure 5.5 Experimental (gray circles) and model-based structure factors (F_{HKL}) as a function of perpendicular momentum transfer (L , in reciprocal lattice units) for the hematite ($1\bar{1}02$) surface reacted with $200\ \mu\text{M}$ Sb(V) at $\text{pH } 5.5$. The solid lines in green represent the calculated CTR profiles based on the best fit model Model4, the solid lines in blue represent the calculated CTR profiles based on the best fit model Model6, the solid lines in red represent the calculated CTR profiles based on the best fit model Model5.

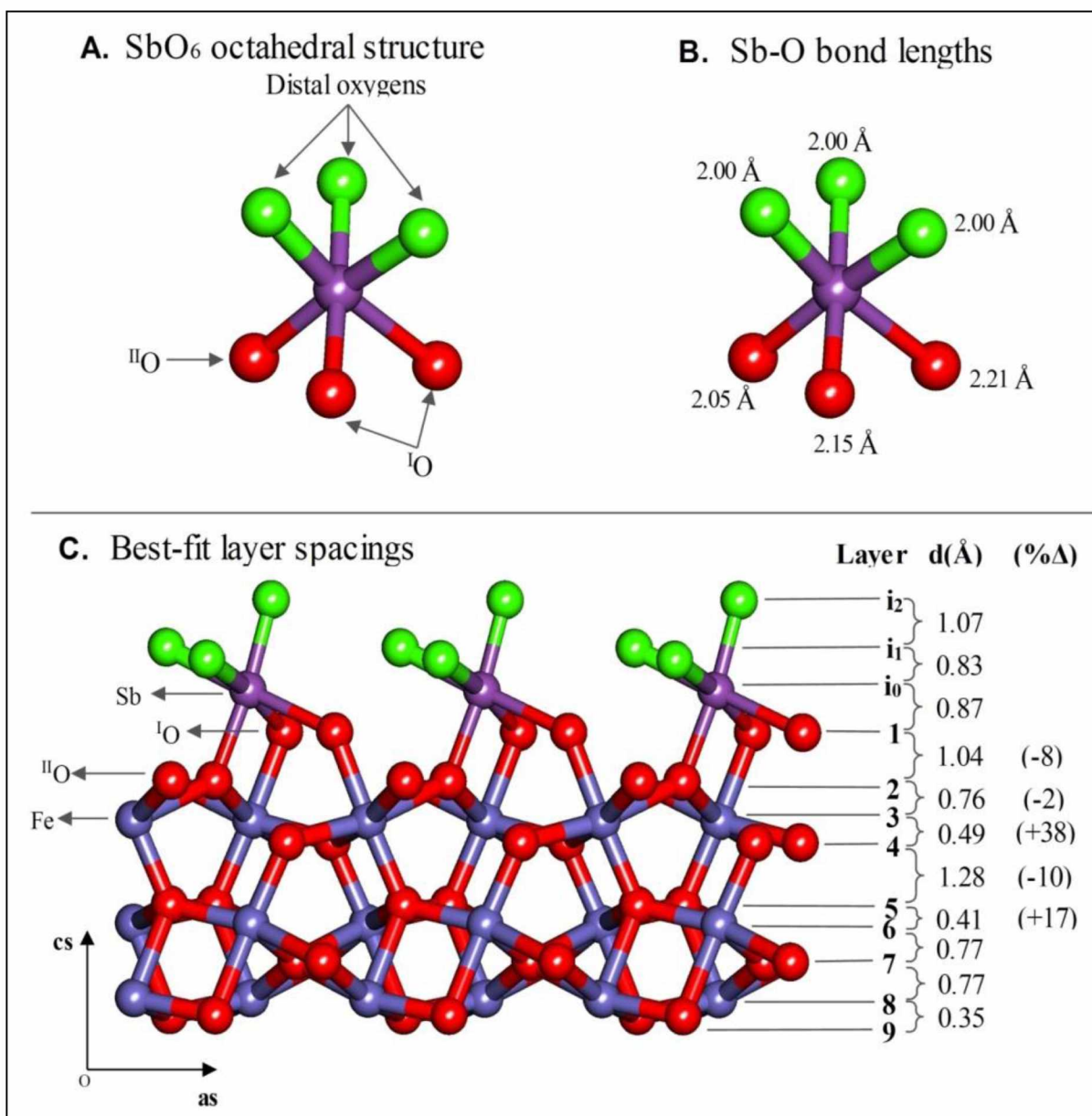


Figure 5.6 (A) Octahedral local structure of Sb(V) surface complex in the best fit model structure; (B) bond lengths of the Sb(V) surface complex; (C) Atom layer spacing values for Sb(V) modified half layer termination surface based on the best fit model structure for Model5. Sb octahedral structure in (A) and (B) were oriented properly for better visualization compared to that in (C).

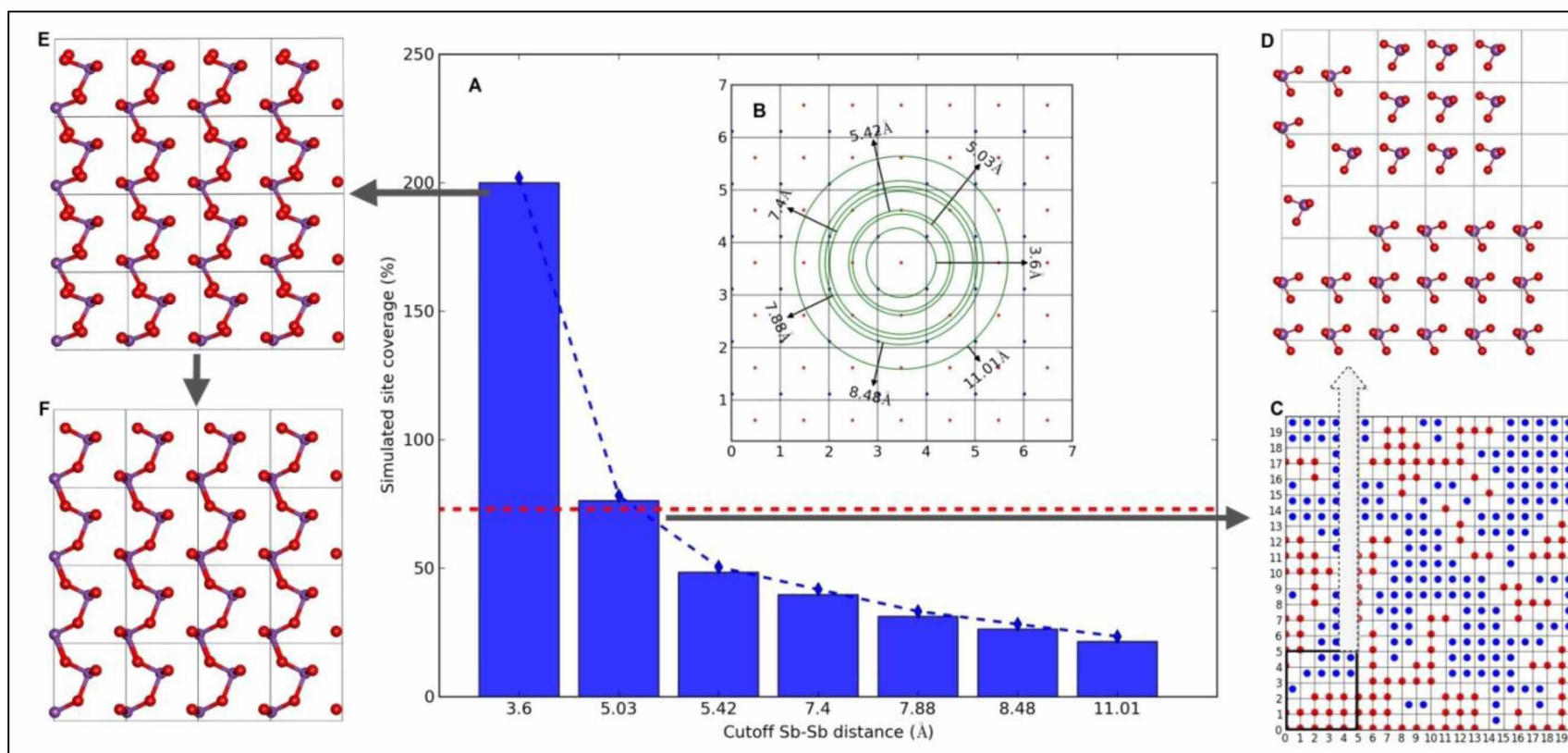
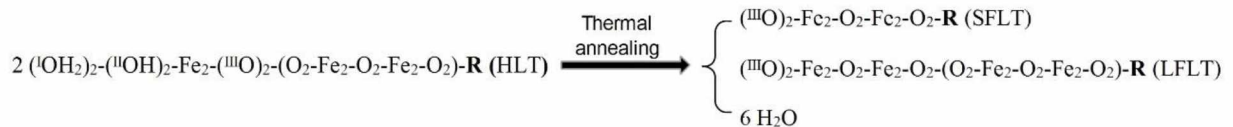


Figure 5.7 Results of site simulation test with (A) a bar chart showing the trend of simulated site coverages over the cutoff Sb-Sb distance, (B) radial chart of co-centered circles showing all cutoff Sb-Sb distances tested in the site simulation, (C) site occupation pattern obtained for the cutoff limit of 5.03 Å corresponding to the CTR derived site occupancy, (D) a subset of the site occupation pattern from (C) with the atomic structure of the substrate being visualized, (E) top view of an atomic structure of a surface with the theoretical mono layer saturation, (F) hypothetical mechanism for the re-organization of atoms to relieve steric strain by sharing one oxygen for the adjacent Sb(V) species aligned along the y direction. Note that the red dash line highlights the site coverage derived from the CTR analysis.

Chapter 6 Conclusions

6.1 Surface termination transformation mechanism from the HLT to the FLT

The best fit CTR modeling results of an annealed hematite ($1\bar{1}02$) surface suggested a mixture of two types of domains with each domain containing three surface terminations, corresponding to the HLT, the short FLT and the long FLT, respectively. The best fit CTR model also implies a surface termination transformation from the HLT to the FLT through near-surface Fe atoms projection to occupy the surface vacant Fe sites in the HLT. The associated stoichiometric equation for that process could be written as follows,



In the best fit modeling results, it was found that the termination weight of the short FLT is nonequivalent to that of the long FLT within each domain. However, the consideration of two symmetry related domains (1:1 ratio) will lead to the change of the types of the FLT when referring to a same height reference, *i.e.* a short (long) FLT on one domain is chemically and crystallographically equivalent to the long (short) FLT on the symmetry domain. In light of that, the sum of the termination weights for two types of FLT are equivalent when the summation is performed globally across the whole surface. We compared our best fit model structure (the FLT) to two published results (Catalano et al., 2007; Tanwar et al., 2007), and found that the atomic layer heights from different studies are comparable within model uncertainties. An AFM image of the annealed sample ($3 \mu\text{m} \times 3 \mu\text{m}$ scan size) gives rise to a relatively smooth surface with a root-mean-square roughness of 1.75 \AA . The AFM-derived surface roughness value is very

close to that ($\sim 1.65 \text{ \AA}$) calculated from a CTR-derived single domain structure (containing three terminations) suggesting that the domain size is probably comparable to the scan size used in collecting the AFM image.

In addition, our best fit CTR model reveals an interfacial hydrogen bonding network that bridges interfacial water layers and the substrate surface. The dipole orientation predicted in the constraint of a tetrahedral hydrogen-bonded water structure implies that the 1st layer water molecule would bridge two terminal ¹O groups through accepting hydrogen bonds, and the 2nd water layer would be hydrogen bonded to the 1st layer waters through donating hydrogen bonds.

In conclusion, the presence of multiple terminations at hematite ($1\bar{1}02$) surface implies the necessity of characterizing the surface reactivity of both terminations for binding aqueous ions. Therefore, when studying surface adsorption chemistry based on macroscale batch experiments, multiple surface complexation reactions may be required in order to obtain a more realistic and better characterization of the metal adsorption behaviors over wide experimental conditions.

6.2 Surface adsorption mechanism of Pb(II) and Sb(V) on the hematite ($1\bar{1}02$)

The surface complexation reaction at mineral-water interface is an important process to scavenge heavy metals and other toxic elements from different aquatic environments. The adsorption of ions at mineral-water interface is a function of different factors, such as the electrostatic effect, the steric effect and solution chemistry. The aqueous speciation of an ion is determined by solution chemistry, whereas the binding configuration of an ion on a mineral surface is to a great extent dictated by the surface structure. In this project, we take advantage of the well-characterized hematite ($1\bar{1}02$) surface structure to investigate the surface binding structure of Pb(II) and Sb(V) using high-resolution CTR technique, and we also rely on the

multi-termination feature of the hematite ($1\bar{1}02$) surface to achieve a better understanding of the structure-reactivity relationship.

6.2.1 Influence of substrate structure on the surface binding mechanism

The surface structures of the HLT and the FLT are different in that the HLT has three types of surface functional groups (single ($I\text{O}$), double ($II\text{O}$) and triply ($III\text{O}$) coordinated oxygen), while the FLT surface contains only $I\text{O}$ and $III\text{O}$ groups. Although the difference in the types of surface functional groups, both termination surfaces share an analogous set of surface binding sites, including one bidentate corner-sharing site, two types of bidentate edge-sharing sites, two types of tridentate sites (face-sharing and corner-sharing/edge-sharing), as illustrated in Figure 6.1 and Figure 6.2.

The knowledge of structural details of a clean substrate enables a site-specific analysis of the surface binding configuration in the CTR modeling process. The best fit CTR modeling results for Pb(II)/hematite ($1\bar{1}02$) systems indicate a site preference of Pb(II) binding to only edge-sharing sites that have relatively small O-Fe-O bond angles, including ES1 and ES2 sites on the HLT and the ES1 site on the FLT (Figure 6.1 and Figure 6.2). An edge-sharing site with a large O-Fe-O bond angle is not a favorable site, and the possible reason is that a Pb surface complex binding at that site would be left unstable corresponding to a binding structure with extremely long(weak) Pb-O bonds ($>2.5 \text{ \AA}$). The CTR-derived surface Pb complexes at reactive bidentate edge-sharing sites displayed a distorted trigonal pyramid coordination structure with average Pb-O bond lengths ($\sim 2.25 \text{ \AA}$) consistent to those reported in previous XAFS studies (Roe et al., 1991; Bargar et al., 1995; Bargar et al., 1997; Bargar et al., 1998; Ostergren et al., 1999; Trivedi et al., 2003; Bargar et al., 2004). In addition, our CTR results indicated that three Pb surface

complex species have characteristic Fe-Pb separations, which are found to be correlated to the associated O-Fe-O bond angles. For example, ES1 sites of the FLT (Figure 6.2) and ES2 sites of the HLT (Figure 6.1) display relatively small O-Fe-O bond angles, i.e. 76° and 74° corresponding to Pb-Fe separations of 3.64 \AA and 3.53 \AA , respectively. On the contrary, surface Pb complexes binding at ES1 sites of the HLT display a much smaller Pb-Fe separation (3.32 \AA) in line with a larger O-Fe-O bond angle (85°). Interestingly, previous XAFS studies mentioned above reported a set of consistent Fe-Pb separations ($\sim 3.35 \text{ \AA}$) corresponding to the Pb(II) sorption in an edge-sharing binding mode on different iron-(oxyhydr)oxide surfaces. Therefore, the CTR-derived Fe-Pb separations for the Pb complex binding at ES1 site of the HLT are comparable to those XAFS derived Fe-Pb separations. It is possible that those Pb complex species with larger Fe-Pb separations identified only in our CTR studies could have been missed in those XAFS studies especially when XAFS experiments were performed using iron-(oxyhydr)oxide substrates of a powder form.

Most of the iron-(oxyhydr)oxides (like goethite, hematite) share a distorted Fe octahedral structural unit containing 12 O-Fe-O bond angles (corresponding to 12 edge-sharing sites) that could be roughly divided into four sets with bond angles close to 78° , 86° , 90° and 103° , respectively. The iron-(oxyhydr)oxide substrates in a powder form could expose multiple types of edge-sharing sites with the associated characteristic O-Fe-O bond angles depending on the surface morphology. Our CTR results have ruled out the possibility of Pb(II) sorption to an edge-sharing site with a O-Fe-O angle as high as 103° due to the reason mentioned above, while those edge-sharing sites with smaller O-Fe-O bond angles ($78\text{-}90^\circ$) are potentially reactive sites for binding Pb(II). Then it will be difficult for the XAFS technique to distinguish Pb complex species binding at those edge-sharing sites if those characteristic Pb-Fe separations are very

close. As a result, the derived Pb complex structure presented in those XAFS studies is probably an average structure accounting for different types of surface complex species.

The site preference as observed in our CTR modeling results is eventually determined by the overall binding energy that is a function of different factors, such as covalent interactions, steric constraints as well as electrostatic effects. A DFT study of Pb(II) adsorption on hematite (0001) surface revealed that covalent interaction between Pb and Fe stabilizes the Pb surface complex species. In light of that, it seems that a surface site with a larger O-Fe-O bond angle will favor the formation of a Pb surface complex corresponding to a smaller Fe-Pb separation, and thus those sites may represent the energetically more favorable site due to the stronger Fe-Pb covalent interaction. However, our CTR modeling results indicated that the ES2 site (with the biggest O-Fe-O angle) on the FLT is chemically inert in binding Pb(II). As discussed above, Pb(II) binding at ES2 site on the FLT is unfavorable due to the formation of an unstable Pb complex with extremely large Pb-O bond length ($>2.5 \text{ \AA}$), as illustrated in Figure 6.3B. Interestingly, we also notice that the Pb complex with large Pb-O bond lengths could have been relaxed to shorten the Pb-O bond length to $\sim 2.25 \text{ \AA}$ by moving the Pb atom towards the Fe atom that makes a smaller Fe-Pb separation (Figure 6.3A). However, the extra displacement of Pb atom towards Fe atom will result in a much larger O-Pb-O angle ($>90^\circ$, Figure 6.3A), which is energetically unfavorable due to the lone electron pair effect of Pb atom, as found in numerous published results of Pb coordination structures optimized using theoretical computation tools under different systems (Breza Martin; Manova, 1995; Breza and Manová, 1999; Breza, 2002; Breza et al., 2003; Claudio et al., 2003; Davidovich et al., 2009; Breza et al., 2010). Therefore, it appears that the details of Pb(II) binding configurations are determined not only by the Fe-Pb covalent interaction but also by the coordination chemistry of Pb, which is affected by the lone electron

pair (2s). The Fe-Pb covalent interaction, which is energetically favorable, will favor the Pb binding at a bidentate site with larger O-Fe-O bond angle, whereas the lone electron pair effect will not allow a Pb coordination structure with large O-Pb-O bond angles.

Using a bond valence analysis, protonation schemes of under-coordinated surface functional groups were predicted based on the best fit surface complex structures. The bond valence analysis results suggested that Pb(II) bonding to an oxygen group may or may not release one proton accordingly depending on the associated proton affinity. For example, Pb(II) adsorption at ES1 sites (consisting of ^IO and ^{II}O groups) on the FLT displaces one proton from each constituent oxygen group leading to two proton release. However, we found that Pb(II) adsorption at both ES1 and ES2 sites on the HLT only displaces one proton originally bounded with ^IO group and leaves unchanged the protonation scheme of ^{II}O group (singly protonated). The bond valence excess due to the formation of the new Pb- ^{II}O bond (~ 0.5 v.u.) upon Pb binding at the surface was balanced by the decrease of the valence contributed from the covalent hydrogen bond (from 0.88 v.u. to 0.68 v.u.) as well as the disappearing of a weak hydrogen bond (0.24 v.u.). The difference in the change of protonation scheme upon Pb(II) binding to surface sites may represent the strength of proton affinity on different surface functional groups. It should be noted that a protonated oxygen group with a high proton affinity (smaller O-H distance) could probably resist the deprotonation at higher pH rendering this oxygen group a weak Bronsted acid. However, the surface oxygen group with high proton affinity could not be used as an indicator to come to a conclusion of low reactivity for binding cations, since the bonded cation may just weaken rather than replace the covalent hydrogen bond, as revealed in our bond valence analysis results. In addition, the hydrolysis of the distal oxygen only bonding to Pb may occur according to the bond valence analysis results, although a different protonation

scheme consistent with a doubly protonated distal oxygen could be used as well to arrive at a bond valence saturation. It was found the deprotonation of the aqua group to a hydroxyl group will result in a stronger covalent hydrogen bond and the formation an extra weak hydrogen bond to balance the valance loss. Published XAFS results derived surface complexation reactions, which suggest the hydrolysis of the distal oxygen (Bargar et al., 1997a; Bargar et al., 1997b; Ostergren et al., 2000a; Ostergren et al., 2000b). Macroscale batch experiments found that the number of protons release due to Pb(II) adsorption on the goethite surface is in a range from 1 to 2 (Müller and Sigg, 1992). The variance of number for the proton release may imply multiple surface complexation reactions with different proton stoichiometries as well as the extent of the hydrolysis of the distal oxygen as a function of solution pH. Although different proton stoichiometries were observed in different batch experiment studies, the Pb(II) adsorption display a general cation uptake pattern on oxide surfaces, *i.e.* sorption capacity decease with solution pH corresponding to the proton release upon Pb(II) adsorption at substrate surface (Davis and Leckie, 1978; Barrow et al., 1981; Hayes and Leckie, 1987; Müller and Sigg, 1992; Rose and Bianchi-Mosquera, 1993; Gunneriusson et al., 1994; Christl and Kretzschmar, 1999; Palmqvist et al., 1999; Kovačević et al., 2000; Müller and Duffek, 2001; Villalobos et al., 2001; Appel and Ma, 2002; Tonkin et al., 2002; Dyer et al., 2003; Serrano et al., 2005; Ponthieu et al., 2006; Villalobos and Pérez-Gallegos, 2008; Reich et al., 2010).

6.2.2 Surface binding mechanism of Sb(V) to the hematite ($1\bar{1}02$) surface

Sb(V) displays an uniform coordination structure over a broad solution chemistry, *i.e.* existing as an oxyanion species $\text{Sb}(\text{OH})_6^-$ with the central Sb atom coordinating with six hydroxyl groups in an octahedral local structure (Filella et al., 2002; Wilson et al., 2010). Sb(V)

carries more positive charges than Pb(II), and unlike Pb(II) displaying covalent interactions with structural Fe atom (Mason et al., 2009), there is no covalent interaction between Sb and Fe atom as found in another DFT study by Mason et al. (Mason et al., 2012). In light of that, it is more likely for Sb(V) to bind at the iron oxide surface in a binding mode with larger Sb-Fe separations.

Our best fit CTR model indicated that Sb(V) is chemically bonded to the CMP-prepared hematite ($1\bar{1}02$) surface (dominant HLT) through a tridentate binding configuration. In the tridentate binding structure, Sb(V) associates with two $^{\text{I}}\text{O}$ groups as well as one $^{\text{II}}\text{O}$ group forming a binuclear corner-sharing/edge-sharing binding configuration. The coordination structure of Sb(V) sorption at the surface is a distorted octahedral with an average Sb-O bond length of 2.07 Å and Sb-Fe separation of 3.05 Å in good agreement with published XAFS studies (Scheinost et al., 2006; Ackermann et al., 2009; Mitsunobu et al., 2010; Ritchie et al., 2013; Guo et al., 2014). We found that the complexation structure with Sb(V) binding at the bidentate corner-sharing site could also fit the experimental CTR data well but with a high FOM value attributed from the high bond valence penalty factor. The optimized binding structure under the bidentate corner-sharing mode gave rise to the position of Sb atom similar to that in the case of the best fit tridentate binding configuration, but the position of one distal oxygen being too close to one surface oxygen. Compared to the bidentate corner-sharing mode, Sb(V) binding at the surface via a tridentate corner-sharing/edge-sharing mode probably represents an energetically more favorable surface complex species with a better steric feasibility. However, it should be noted that such a tridentate binding mode may not represent the binding configuration of Sb(V) as observed in natural soil samples, since the soil sample is usually of fine particles in both

crystalline form or amorphous form, which could comprise some edge-sharing sites (for example at step edges) with steric feasibility.

The bond valence analysis results suggest that Sb(V) adsorption at surface is via ligand exchange process, where the hydroxyl group (OH^-) coordinating with the aqueous Sb(V) initially will “grab” a covalent hydrogen from a surface oxygen group producing a H_2O releasing from surface, and at the same time the surface functional oxygen will coordinate with Sb(V) becoming a part of the Sb coordination structure. The proposed surface complexation stoichiometry does not involve proton or hydroxyl on either reactant side or product side, but that does not necessarily mean a pH independence of surface complexation reaction. The surface functional groups will experience a deprotonation at a high pH, where the free aqueous hydroxyl (OH^-) species compete for covalent hydrogen of surface oxygen groups with coordinated hydroxyl group in aqueous $\text{Sb}(\text{OH})_6^-$ species. As a result, the sorption capacity of Sb(V) on substrate surface will decrease accordingly at a higher pH, as found in numerous published studies based on macroscale batch adsorption experiments (Leuz et al., 2006; Martínez-Lladó et al., 2008; Vithanage et al., 2013).

6.3 Implication of site coverage simulation results

In this study, we performed site coverage simulations to explore the relationship between the inter-site distance and the site coverage. The simulation results of Sb(V) adsorption on the HLT hematite ($1\bar{1}02$) surface suggest a Sb-Sb separation of 5.03 Å corresponding to an apparent monolayer saturation limit with site coverage of 75%. It was also found that further uptake of Sb(V) at the substrate surface will be impeded due to the steric constraint attributed to the abnormally short O-O separation between distal oxygens. In addition, the Sb(V)-Sb(V) repulsion

at a smaller inter-site distance (next level is 3.6 Å) may also play a role in hampering a further uptake of Sb(V) at the substrate surface. Likewise, the site simulation tests of Pb(II) adsorption on the HLT hematite (1 $\bar{1}$ 02) surface gave rise to a larger inter-site distance (5.42 Å) at the apparent monolayer saturation limit with a site coverage of 58%. Further uptake of Pb(II) is probably hampered by the cation-cation repulsion induced by placing two occupied Pb(II) closer than 5.42 Å (the next inter-site distance cutoff limit is 4.65 Å), since the steric constraint between oxygens were not found at the cutoff limit of 4.65 Å. Interestingly, comparing both the Pb(II) adsorption and the Sb(V) adsorption case, it seems that the occupied Sb(V) species are allowed to be closer to each other than Pb(II) species, although Sb(V) carries more positive charges and should be subject to more severe cation-cation repulsion. Thus, it seems more reasonable for surface Sb complexes to be separated further apart to alleviate the cation-cation repulsion. However, it is unfair to make direct comparison using pure inter-site distance, considering the Sb(V) and Pb(II) bear different ionic radius (0.98 Å for Pb(II) and 0.60 Å for Sb(V)) (Shannon, 1976). If we compare the effective inter-sorbate distance r_e (inter-sorbate distance-2×ionic radius), the r_e (3.83 Å) for Sb(V)-Sb(V) is larger than that (3.46 Å) for Pb(II)-Pb(II), that is consistent with the higher charge density of Sb(V).

Our site coverage simulation tests underscore the potential significance of the electrostatic repulsion among occupied sites in affecting the site coverage. In traditional surface complexation models, the electrostatic effect is taken into account for sorbates in the process of moving ions from bulk solution across the electric diffuse layer and finally register on some electrostatic plane (like 0-plane, 1-plane) depending on the binding mode (inner-sphere or outer-sphere). However, the electrostatic force between near-neighboring sorbates are not considered in the surface complexation models. The greatest issue encountered in using a surface complexation

model lies in its difficulty in extrapolating the model parameters derived under one set of conditions to broader experimental conditions. For example, Dyer et al. found that a unique set of surface complexation constants could not be derived in fitting the adsorption data of Pb(II) on 2-line ferrihydrite surfaces over a pH range from 3.5 to pH 6.5, and some corrections to the reaction constants are necessary in order to reproduce the sorption data across all the pH conditions (Dyer et al., 2003). Therefore, a more accurate characterization of the sorption chemistry of aqueous ions at mineral surface will rely on a more robust surface complexation model that could deal with the electrostatic influence from the nearby sorbates as a function of site coverage.

6.4 The future direction in the environmental interfacial chemistry

Fundamental understandings of surface adsorption of aqueous ions to different environmental substrates is a challenge, since there is no single technique available now, which is sufficient to derive a complete picture of heterogeneous reactions at mineral-water interface in nature.

In light of that, the future direction in the study of heterogeneous processes occurring at mineral-water interfaces from different perspectives should rely on a combination of different techniques, including the modern synchrotron X-ray techniques (like CTR, XAFS), the traditional surface complexation modeling (like CD-MUSIC), and high resolution electron microscopy (TEM and SEM). It will be even better if those experiment-based techniques could be coupled with theoretical computation theory (like DFT). By combining different techniques, I believe that a significant leap forward could be made in the field of environmental geochemistry to better address the following two questions: (1) what's the relationship between the substrate surface structure and the surface reactivity; (2) how to make use of information

derived from in-lab systems to develop a robust model to better predict the environmental fate and transport of aqueous contaminants in the real environment.

6.5 References

- Ackermann S., Gieré R., Newville M. and Majzlan J. (2009) Antimony sinks in the weathering crust of bullets from Swiss shooting ranges. *Sci. Total Environ.* **407**, 1669–1682.
- Appel C. and Ma L. (2002) Concentration, pH, and surface charge effects on cadmium and lead sorption in three tropical soils. *J. Environ. Qual.* **31**, 581–589.
- Bargar J. R., Brown G. E. and Parks G. A. (1997a) Surface complexation of Pb(II) at oxide-water interfaces: I. XAFS and bond-valence determination of mononuclear and polynuclear Pb(II) sorption products on aluminum oxides. *Geochim. Cosmochim. Acta* **61**, 2617–2637. Available at: <http://www.sciencedirect.com/science/article/pii/S0016703797001245>.
- Bargar J. R., Brown G. E. and Parks G. A. (1997b) Surface complexation of Pb(II) at oxide-water interfaces: II. XAFS and bond-valence determination of mononuclear Pb(II) sorption products and surface functional groups on iron oxides. *Geochim. Cosmochim. Acta* **61**, 2639–2652. Available at: <http://www.sciencedirect.com/science/article/pii/S0016703797001257> [Accessed November 27, 2015].
- Bargar J. R., Brown G. E. and Parks G. A. (1998) Surface Complexation of Pb(II) at Oxide-Water Interfaces: III. XAFS Determination of Pb(II) and Pb(II)-Chloro Adsorption Complexes on Goethite and Alumina. *Geochim. Cosmochim. Acta* **62**, 193–207. Available at: <http://www.sciencedirect.com/science/article/pii/S0016703797003347>.
- Bargar J. R., Brown G. E. and Parks G. A. (1995) XAFS study of Pb (II) sorption at the α -Al₂O₃-water interface. *Phys. B Condens. Matter* **208-209**, 455–456. Available at: <http://www.sciencedirect.com/science/article/pii/0921452694007228>.
- Bargar J. R., Trainor T. P., Fitts J. P., Chambers S. A. and Brown G. E. (2004) In Situ Grazing-Incidence Extended X-ray Absorption Fine Structure Study of Pb(II) Chemisorption on Hematite (0001) and (1-102) Surfaces. *Langmuir* **20**, 1667–1673.
- Barrow N. J., Bowden J. W., Posner A. M. and Quirk J. P. (1981) Describing the adsorption of copper, zinc and lead on a variable charge mineral surface. *Soil Res.* **19**, 309–321.
- Breza M. (2002) On the Structure of Lead(II) Complexes in Aqueous Solutions. III. Hexanuclear Clusters. *Collect. Czechoslov. Chem. Commun.* **67**, 219.
- Breza M., Biskupič S. and Manová A. (2003) On the structure of lead (II) complexes in aqueous solutions.: Part IV. Binuclear clusters. *Polyhedron* **22**, 2863–2867.
- Breza M., Bučinský L., Šoralová S. and Biskupič S. (2010) On the origin of the hemidirected geometry of tetracoordinated lead(II) compounds. *Chem. Phys.* **368**, 14–19. Available at: <http://www.sciencedirect.com/science/article/pii/S030101040900384X>.

- Breza M. and Manová A. (1999) On the structure of lead(II) complexes in aqueous solutions. II: Tetranuclear clusters. *Polyhedron* **18**, 2085–2090. Available at: <http://www.sciencedirect.com/science/article/pii/S0277538799001047>.
- Breza Martin; Manova A. (1995) On the structure of Lead(II) complexes in aqueous solutions. I. Trinuclear Clusters. *Collect. Czechoslov. Chem. Commun.* **60**, 527.
- Catalano J. G., Fenter P. and Park C. (2007) Interfacial water structure on the (0 1 2) surface of hematite: Ordering and reactivity in comparison with corundum. *Geochim. Cosmochim. Acta* **71**, 5313–5324.
- Christl I. and Kretzschmar R. (1999) Competitive sorption of copper and lead at the oxide-water interface: Implications for surface site density. *Geochim. Cosmochim. Acta* **63**, 2929–2938. Available at: <http://www.sciencedirect.com/science/article/pii/S0016703799002665>.
- Claudio E. S., Godwin H. A. and Magyar J. S. (2003) Fundamental Coordination Chemistry, Environmental Chemistry, and Biochemistry of Lead(II). In *Progress in Inorganic Chemistry* John Wiley & Sons, Inc. pp. 1–144. Available at: <http://dx.doi.org/10.1002/0471267287.ch1>.
- Davidovich R. L., Stabila V., Marinin D. V., Voit E. I. and Whitmire K. H. (2009) Stereochemistry of lead(II) complexes with oxygen donor ligands. *Coord. Chem. Rev.* **253**, 1316–1352. Available at: <http://www.sciencedirect.com/science/article/pii/S0010854508001719>.
- Davis J. A. and Leckie J. O. (1978) Surface ionization and complexation at the oxide/water interface II. Surface properties of amorphous iron oxyhydroxide and adsorption of metal ions. *J. Colloid Interface Sci.* **67**, 90–107.
- Dyer J. A., Trivedi P., Scrivner N. C. and Sparks D. L. (2003) Lead Sorption onto Ferrihydrite. 2. Surface Complexation Modeling. *Environ. Sci. Technol.* **37**, 915–922. Available at: <http://pubs.acs.org/doi/abs/10.1021/es025794r>.
- Filella M., Belzile N. and Chen Y.-W. (2002) Antimony in the environment: a review focused on natural waters: II. Relevant solution chemistry. *Earth-Science Rev.* **59**, 265–285.
- Gunneriusson L., Lövgren L. and Sjöberg S. (1994) Complexation of Pb (II) at the goethite (α -FeOOH)/water interface: The influence of chloride. *Geochim. Cosmochim. Acta* **58**, 4973–4983.
- Guo X., Wu Z., He M., Meng X., Jin X., Qiu N. and Zhang J. (2014) Adsorption of antimony onto iron oxyhydroxides: Adsorption behavior and surface structure. *J. Hazard. Mater.* **276**, 339–345.
- Hayes K. F. and Leckie J. O. (1987) Modeling ionic strength effects on cation adsorption at hydrous oxide/solution interfaces. *J. Colloid Interface Sci.* **115**, 564–572.
- Kovačević D., Pohlmeier A., Özbaş G., Narres H.D. and Kallay M. J. N. (2000) The adsorption of lead species on goethite. *Colloids Surfaces A Physicochem. Eng. Asp.* **166**, 225–233.
- Leuz A. K., Mönch H. and Johnson C. A. (2006) Sorption of Sb (III) and Sb (V) to goethite: influence on Sb (III) oxidation and mobilization. *Environ. Sci. Technol.* **40**, 7277–7282.

- Martínez-Lladó X., de Pablo J., Giménez J., Ayora C., Martí V. and Rovira M. (2008) Sorption of antimony(V) onto synthetic goethite in carbonate medium. *Solvent Extr. Ion Exch.* **26**, 289–300.
- Mason S. E., Iceman C. R., Tanwar K. S., Trainor T. P. and Chaka A. M. (2009) Pb (II) Adsorption on Isostructural Hydrated Alumina and Hematite (0001) Surfaces: A DFT Study. *J. Phys. Chem. C* **113**, 2159–2170.
- Mason S. E., Trainor T. P. and Goffinet C. J. (2012) DFT study of Sb(III) and Sb(V) adsorption and heterogeneous oxidation on hydrated oxide surfaces. *Comput. Theor. Chem.* **987**, 103–114. Available at: <http://www.sciencedirect.com/science/article/pii/S2210271X11006062>.
- Mitsunobu S., Takahashi Y., Terada Y. and Sakata M. (2010) Antimony(V) Incorporation into Synthetic Ferrihydrite, Goethite, and Natural Iron Oxyhydroxides. *Environ. Sci. Technol.* **44**, 3712–3718.
- Müller B. and Duffek A. (2001) Similar adsorption parameters for trace metals with different aquatic particles. *Aquat. Geochemistry* **7**, 107–126.
- Müller B. and Sigg L. (1992) Adsorption of lead(II) on the goethite surface: Voltammetric evaluation of surface complexation parameters. *J. Colloid Interface Sci.* **148**, 517–532. Available at: <http://www.sciencedirect.com/science/article/pii/002197979290187Q>.
- Ostergren J. D., Bargar J. R., Brown G. E. and Parks G. A. (1999) Combined EXAFS and FTIR investigation of sulfate and carbonate effects on Pb(II) sorption to goethite (α -FeOOH). *J. Synchrotron Radiat.* **6**, 645–647. Available at: <http://dx.doi.org/10.1107/S0909049598017750>.
- Ostergren J. D., Brown G. E., Parks G. A. and Persson P. (2000a) Inorganic Ligand Effects on Pb(II) Sorption to Goethite (α -FeOOH): II. Sulfate. *J. Colloid Interface Sci.* **225**, 483–493. Available at: <http://www.sciencedirect.com/science/article/pii/S0021979799967024> [Accessed November 13, 2015].
- Ostergren J. D., Trainor T. P., Bargar J. R., Brown G. E. and Parks G. A. (2000b) Inorganic Ligand Effects on Pb(II) Sorption to Goethite (α -FeOOH): I. Carbonate. *J. Colloid Interface Sci.* **225**, 466–482. Available at: <http://www.sciencedirect.com/science/article/pii/S0021979799967012> [Accessed November 13, 2015].
- Palmqvist U., Ahlberg E., Lövgren L. and Sjöberg S. (1999) Competitive metal ion adsorption in goethite systems using in situ voltammetric methods and potentiometry. *J. Colloid Interface Sci.* **218**, 388–396.
- Ponthieu M., Juillot F., Hiemstra T., Van Riemsdijk W. H. and Benedetti M. F. (2006) Metal ion binding to iron oxides. *Geochim. Cosmochim. Acta* **70**, 2679–2698.
- Reich T. J., Das S., Koretsky C. M., Lund T. J. and Landry C. J. (2010) Surface complexation modeling of Pb (II) adsorption on mixtures of hydrous ferric oxide, quartz and kaolinite. *Chem. Geol.* **275**, 262–271.

- Ritchie V. J., Ilgen A. G., Mueller S. H., Trainor T. P. and Goldfarb R. J. (2013) Mobility and chemical fate of antimony and arsenic in historic mining environments of the Kantishna Hills district, Denali National Park and Preserve, Alaska. *Chem. Geol.* **335**, 172–188.
- Roe A. L., Hayes K. F., Chisholm-Brause C., Brown G. E. J., Parks G. A., Hodgson K. O. and Leckie J. O. (1991) In situ X-ray absorption study of lead ion surface complexes at the goethite-water interface. *Langmuir* **7**, 367–373.
- Rose A. W. and Bianchi-Mosquera G. C. (1993) Adsorption of Cu, Pb, Zn, Co, Ni, and Ag on goethite and hematite; a control on metal mobilization from red beds into stratiform copper deposits. *Econ. Geol.* **88**, 1226–1236.
- Scheinost A. C., Rossberg A., Vantelon D., Xifra I., Kretzschmar R., Leuz A.-K., Funke H. and Johnson C. A. (2006) Quantitative antimony speciation in shooting-range soils by EXAFS spectroscopy. *Geochim. Cosmochim. Acta* **70**, 3299–3312. Available at: <http://www.sciencedirect.com/science/article/pii/S0016703706001451>.
- Serrano S., Garrido F., Campbell C. G. and García-González M. T. (2005) Competitive sorption of cadmium and lead in acid soils of Central Spain. *Geoderma* **124**, 91–104.
- Shannon R. D. (1976) Revised effective ionic radii and systematic studies of interatomic distances in halides and chalcogenides. *Acta Crystallogr. Sect. A Cryst. Physics, Diffraction, Theor. Gen. Crystallogr.* **32**, 751–767.
- Tanwar K. S., Catalano J. G., Petitto S. C., Ghose S. K., Eng P. J. and Trainor T. P. (2007) Hydrated α -Fe₂O₃ surface structure: Role of surface preparation. *Surf. Sci.* **601**, L59–L64.
- Tonkin J. W., Balistrieri L. S. and Murray J. W. (2002) Modeling metal removal onto natural particles formed during mixing of acid rock drainage with ambient surface water. *Environ. Sci. Technol.* **36**, 484–492.
- Trivedi P., Dyer J. A. and Sparks D. L. (2003) Lead Sorption onto Ferrihydrite. 1. A Macroscopic and Spectroscopic Assessment. *Environ. Sci. Technol.* **37**, 908–914. Available at: <http://pubs.acs.org/doi/abs/10.1021/es0257927>.
- Villalobos M. and Pérez-Gallegos A. (2008) Goethite surface reactivity: A macroscopic investigation unifying proton, chromate, carbonate, and lead(II) adsorption. *J. Colloid Interface Sci.* **326**, 307–323. Available at: <http://www.sciencedirect.com/science/article/pii/S0021979708007686>.
- Villalobos M., Trotz M. A. and Leckie J. O. (2001) Surface Complexation Modeling of Carbonate Effects on the Adsorption of Cr(VI), Pb(II), and U(VI) on Goethite. *Environ. Sci. Technol.* **35**, 3849–3856. Available at: <http://pubs.acs.org/doi/abs/10.1021/es001748k>.
- Vithanage M., Rajapaksha A. U., Dou X., Bolan N. S., Yang J. E. and Ok Y. S. (2013) Surface complexation modeling and spectroscopic evidence of antimony adsorption on iron-oxide-rich red earth soils. *J. Colloid Interface Sci.* **406**, 217–224.
- Wilson S. C., Lockwood P. V., Ashley P. M. and Tighe M. (2010) The chemistry and behaviour of antimony in the soil environment with comparisons to arsenic: a critical review. *Environ. Pollut. (Oxford, U. K.)* **158**, 1169–1181.

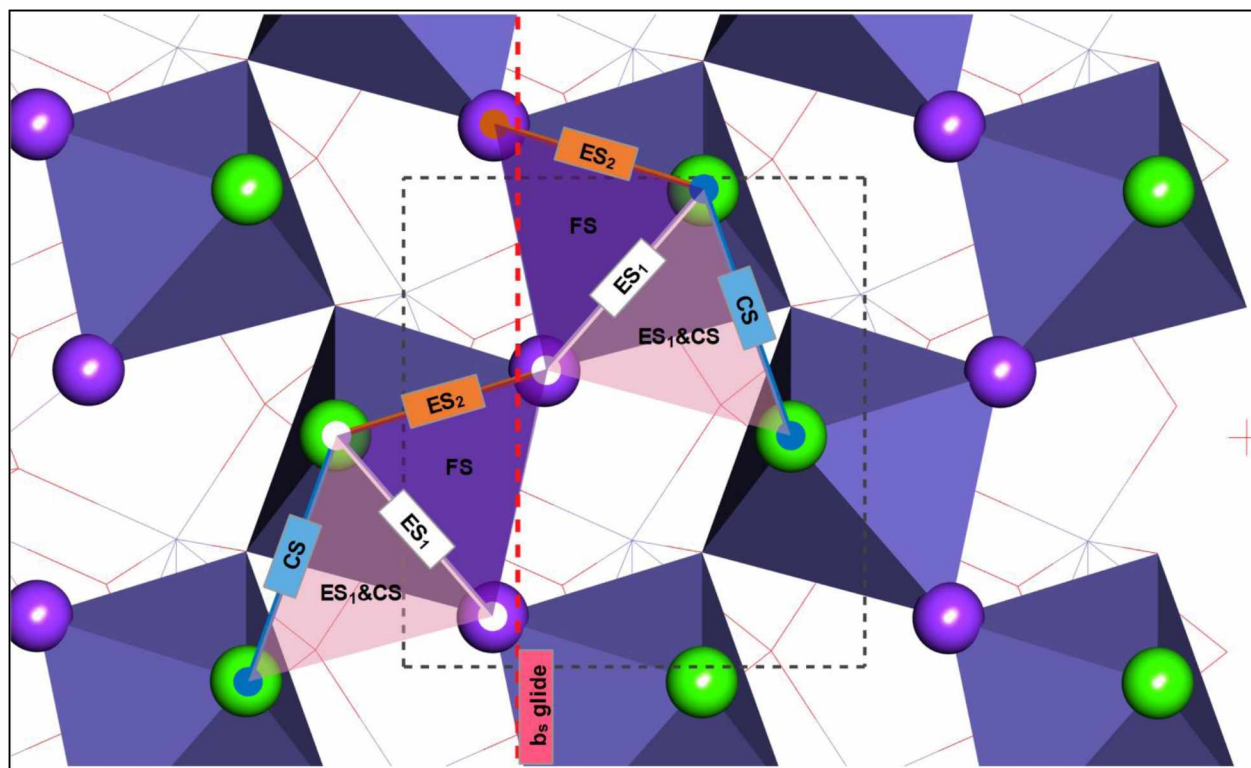


Figure 6.1 Topographic structure of the HLT surface with different types of surface binding sites identified, consisting of the bidentate edge-sharing site of type 1 (ES₁) and type 2 (ES₂), the bidentate corner-sharing site (CS), the face-sharing tridentate site (FS) and the tridentate site bridging ES₁ and CS site. One unit cell was highlighted with dash lines in black. The dash line in red represented the *b_s* glide plane. The top Fe atoms are visualized as octahedra in blue, the green spheres are singly coordinated oxygen groups, and the purple spheres are doubly coordinated oxygen groups. The other atoms and Fe-O bonds are shown as points and lines for clarity.

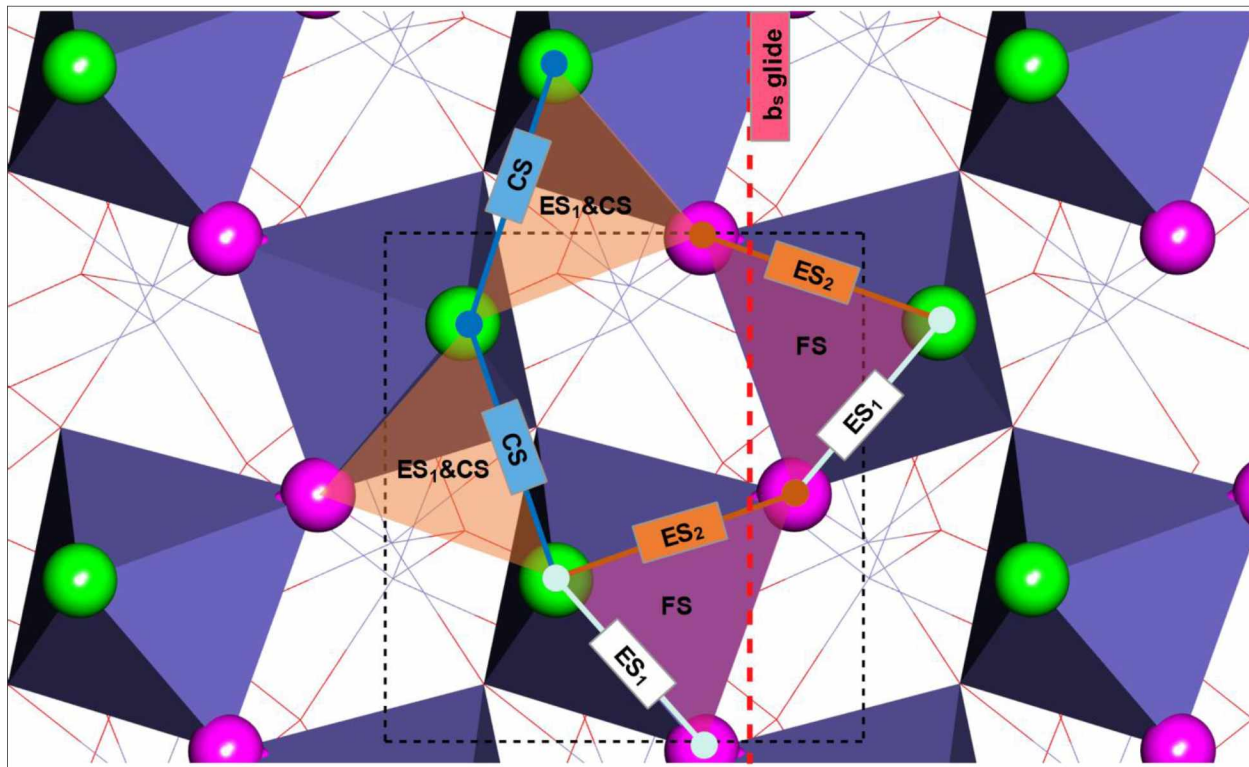


Figure 6.2 Topographic structure of the FLT surface with different types of surface binding sites identified, consisting of the bidentate edge-sharing site of type 1 (ES₁) and type 2 (ES₂), the bidentate corner-sharing site (CS), the face-sharing tridentate site (FS) and the tridentate site bridging ES₁ and CS site. One unit cell was highlighted with dash lines in black. The dash line in red represented the b_s glide plane. The top Fe atoms are visualized as octahedra in blue; the green spheres are singly coordinated oxygen groups, and the pink spheres are triply coordinated oxygen groups. The other atoms and Fe-O bonds are shown as points and lines for clarity.

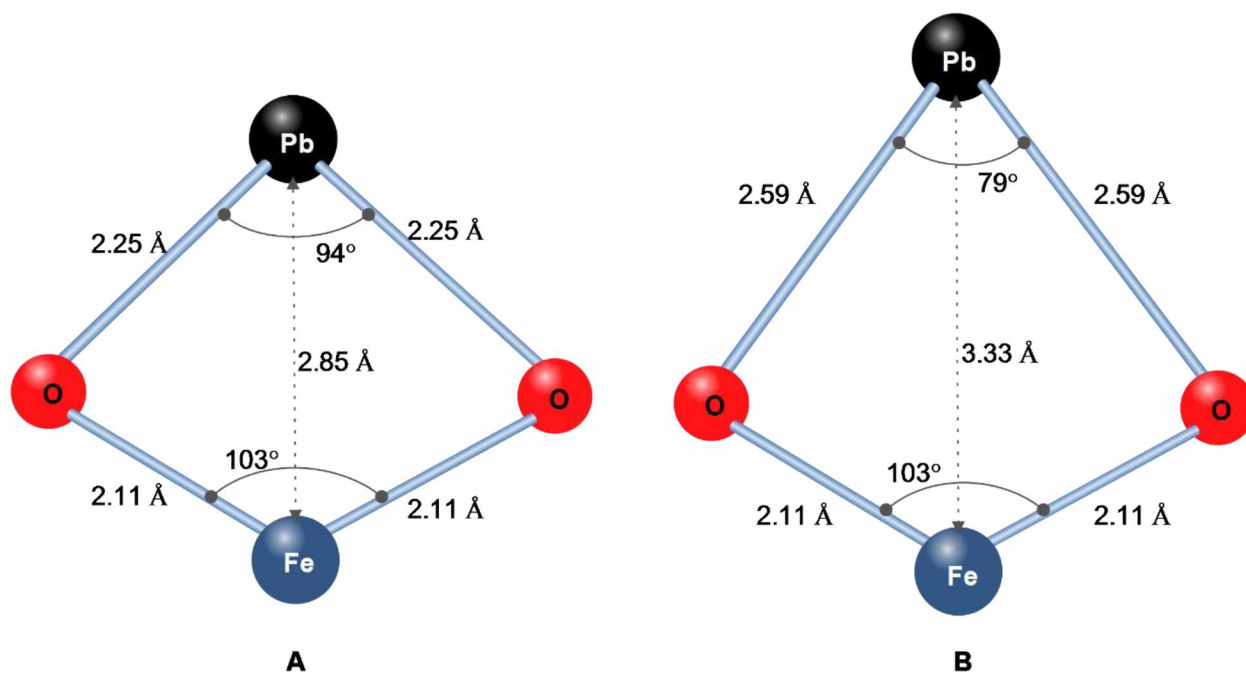


Figure 6.3 Schematic diagrams of Pb(II) binding at the ES2 site on the FLT under two different situations with (A) in a geometrical constraint of reasonable Pb-O bond length (2.25 Å) and (B) in a geometrical constraint of reasonable O-Pb-O bond angle (79°) and Pb-Fe separation (3.33 Å) derived from XAFS studies.